Na prawach rękopisu

Wrocław University of Science and Technology

Faculty of Mechanical and Power Engineering

PhD Dissertation

Agnieszka Kujawska

Heat transfer processes in thermosyphon employing nanofluid

Supervisor: prof. dr hab. inż. Zbigniew Królicki
Co-supervisor: dr hab. inż. Bartosz Zajaczkowski, prof. uczelni

Wrocław, 2019

Acknowledgements

The research presented in this thesis would not have been completed without a support of a number of people, whom I would like to acknowledge.

First, I would like to thank my supervisors Prof. Zbigniew Królicki and Prof. Bartosz Zajączkowski for their advice and guidance during the whole PhD studies, which thought me how to survive in Academia. I am grateful to both of them for their patience during checking drafts of this thesis and all publications along the way. Constructive suggestions I received helped me to clean my thoughts and to improve presentation of the results.

My sincere thanks also go to Dr.-Ing. habil. Matthias H. Buschmann for hosting me at Institut für Luft- und Kältetechnik gemeinnützige GmbH (ILK) in Dresden where I conducted a large amount of experimental work for this dissertation as a visiting scientist. All discussions and received advices have been a great help in preparing this thesis. I would also like to thank the staff of ILK for their help during daily work. This research stay was supported financially by Nanouptake COST Action CA15119 (grants no COST-STSM-CA15119-37694 and 39240) which I appreciatively acknowledge.

Taking part in Nanouptake COST Action CA15119 provided me with great opportunities to attend the conferences, training schools, and short stays abroad. I would like to acknowledge my research stay at Jaume I University (grant ref. COST-STSM-CA15119-35922) and support of all team members. Your help with experimental work and openness was invaluable.

My special thanks are extended to mgr inż. Michał Woluntarski from Institute of Electronic Materials in Warsaw for long-term cooperation on graphene oxide nanofluids, mgr Magdalena Romaniec for her professionalism in performing SEM analysis, and mgr Adrian Chlanda from Warsaw University of Technology for AFM analysis. I wish to acknowledge the great help with surface tension measurements provided by Dr inż. Gaweł Żyła and inż. Michał Wanic from Rzeszów University of Technology, Prof. Patrice Estellé from Université Rennes 1 for viscosity and contact angle measurements, Prof. Angel and Gabriele Huminic from Transilvania University of Brasov for their contribution to measurements of dynamic contact angle, and all teams in Nanotension project.

I thank my colleagues and officemates I had during this PhD journey, especially Stanisława Hałon, Karolina Wojtasik, Tomasz Hałon and Zbigniew Rogala. You cheered up the daily office routine. I highly appreciate all discussions and ideas that appeared over the last four years. I am also grateful to Piotr Wolski for his help in laboratory.

Last but not least, I thank my family without whom I would not be here. Special thanks go to my husband who has always been supportive and helped me to get through difficult moments. I thank my parents and grandparents for their endless love, support and encouragement over the years. I wish to acknowledge many more family members, friends, and workmates, but I cannot list you all here. Still, I cannot thank you enough for enriching my experiences and teaching me a lot, not only about science but life in general.

Contents

List of Figures

List of Tables

Nomenclature

Abbreviations	
AFM	Atomic Force Microscope
Au1	Gold nanofluid stabilized with PVP
Au2	Gold nanofluid stabilized with KOH
CHF	Critical Heat Flux
CMC	Critical Micelle Concentration
CNT	Carbon nanotubes
DLS	Dynamic Light Scattering
DSC	Differential Scanning Calorimetry
FR	Filling ratio
GO	Graphene oxide nanofluid
HEC	Hydroxyethyl cellulose (polymeric surfactant)
HTC	Heat transfer coefficient
IA	Inclination angle
mpd	Waiting period (refers to geyser boiling)
mph	Threshold value (refers to geyser boiling)
NH	Nanohorn nanofluid
PEO	Poly(ethylene oxide) (polymeric surfactant)
PVP	Polyvinylpyrrolidone (polymer)
SDBS	Sodium dodecylbenzenesulfonate (surfactant)
SDS	Sodium dodecyl sulfate (surfactant)
SEM	Scanning Electron Microscope
SLS	Sodium laureth sulfate (surfactant)
TEM	Transmission Electron Microscope

Symbols		
Symbol	**Name**	**Unit**
A	surface area	m^2
C_P	specific heat capacity	J/kg K
d_i	inner diameter	m
d_o	outer diameter	m
h	height of thermosyphon	m
Δh	latent heat of vaporization	J/kg
k	thermal conductivity	W/m^2K
L	length	m
$\dot{m}$	mass flux	kg/s^{-1}
p	pressure	Pa
p_i	pressure transmitter	-
q	heat flux density	W/m^2
R	thermal resistance	K/W
r	radius	m
Ra	roughness	μm
Q	heat flux	W
T	temperature	K
t	temperature	°C
V	volume	m^3
$\dot{V}$	volume flux	m^3/s^{-1}
β	heating rate	$K{\cdot}s^{-1}$
θ	contact angle	rad
μ	dynamic viscosity	Pa ·s
ρ	density	kg/m^3
σ	surface tension	N/m
σ_{SD}	standard deviation,	-
τ	time	s
ϕ	volume concentration	kg/m^3

Subscripts	
ad	advancing (contact angle)
atm	atmospheric
bf	base fluid
c	condenser
ci	inlet of cooling water
e	evaporator
ei	inlet of heating water
eff	effective parameter
i	inlet
l	liquid
max	maximum
min	minimum
nf	nanofluid
np	nanoparticles
o	outlet
re	receiving (contact angle)
ref	reference liquid
s	solid
sat	saturated
th	thermosyphon
v	vapor
w	wall

Chapter 1

Introduction

Thermosyphons and heat pipes are one of the most effective heat transfer devices known nowadays. Due to simultaneous phase changes in the evaporation-condensation cycle, apparent thermal conductivity of thermosyphons is several orders of magnitude higher than those of metals like copper or silver [164]. The first reported thermosyphon was the Perkins tube which transported heat from the furnace to the steam boiler evaporator in the middle of XIX century [52]. Since that time, thermosyphons are used in various applications, such as geothermal systems, preservation of permafrost, snow melting and deicing, nuclear reactors, heat exchangers, cooling of electronics, or solar energy storage systems [52, 123, 164, 166, 226, 219].

Two-phase closed thermosyphon consists of a pressurized container divided into three parts: evaporator where heat absorption takes place, isolated adiabatic section and condenser where heat is released. The sealed pipe is filled with a working fluid. As the external source of heat is supplied to the evaporator, vapor is generated in the working fluid gathered in the lower part of the device. Bubbles grow in the fluid and flow through the adiabatic section to the upper part – the condenser section. The vapor condenses and heat is released to the external cooling medium. The condensate form a falling film or rivulets that return to the boiling pool in the evaporator due to gravity forces. For this reason, the evaporation section is always located below the condenser. The device must be positioned either vertically or slightly inclined. This separates thermosyphons from heat pipes with capillary structures (condensate return to the evaporator is carried out using capillary, osmotic or electrostatic forces) or oscillating heat pipes (movement of liquid slugs interspersed with vapor bubbles is a result of pressures difference).

Decades of research exhausted possibilities of further improvement based on pure liquids or mixtures. Common heat transfer fluids, such as water or glycols seem to reach their operational limits. One of the most promising solutions for overcoming underlying heat and mass transfer limitations is the introduction of nanofluids.

Nanofluids are defined as suspensions of nanoobjects with at least one dimension smaller than 100 nm [31], while nanoparticles indicate nanoobjects with all spatial dimensions smaller than 100 nm [1]. The term *nanoparticle* is commonly used for both - nanoobject and nanoparticle [31, 100, 117], and is used in similar context in this thesis.

Capacities and thermal performances of thermosyphons are limited by thermodynamic properties of working fluids. The primary reason of creating suspensions with nanoparticles is to improve thermal conductivity of the base fluid - thermal conductivity of metallic solids is an order of magnitude higher than that of traditional heat transfer fluids, e.g. water or ethylene glycol. Attempts with micro-sized particles did not succeed due to prob-

lems with stability and clogging. In 1984, Yang and Maa [224] reported the first known study on boiling of suspensions with nano-sized particles. In 1993, Grimm [65] patented in Germany suspensions of aluminum particles with sizes between 80nm and 1μm and concentrations from 0.5 to 10 vol.% as a method for thermal conductivity enhancement [136]. The concept of *nanofluids* was introduced 2 years later (in 1995) by Choi and Eastman [38] from Argonne National Laboratory of USA. They published theoretical discussion on thermal conductivity copper nanofluid.

Since the 1990s, the interest in nanofluids is continuously increasing. They are attractive due to improved thermal properties, increased surface to volume ratio, reduced erosion, and great potential in numerous and intensively investigated fields, such as microelectronics, heat transfer systems, medical applications, and so on [45, 136].

In thermal sciences, the most investigated property of nanofluids is thermal conductivity. Although literature reports exceptionally high values, it does not simply translate to enhanced thermal capacity of heat transfer devices. During phase transitions other properties of both working fluid and heater surface affect heat transfer. Limited information in literature hints the need for shifting research to real applications which involve multiple processes at the same time.

Despite the raising number of studies, the impact of nanoparticles on thermophysical properties and phase change performance of suspensions is still inconclusive. In specific situations nano-additives work particularly well, while in other cases their impact is disputable. The influence of chemical stabilizers commonly used to improve stability of the suspensions is often neglected although they change working fluid properties. Different models attempt to describe enhanced heat transfer mechanisms, propose explanations to underlying mechanisms, but they have not been verified. Without understanding of behavior and relations between various factors and parameters, proper mathematical model cannot be developed. Drawing meaningful conclusions requires larger number of comparable experiments.

This dissertation summarizes the work conducted on nanofluids and surfactant solution used as working fluids in a two-phase closed thermosyphon with focus on the boiling process. Working fluids were chosen to address above mentioned research concerns. The list includes:

- two gold nanofluids with the same nanoparticles but different stabilizers (PVP polymer (polyvinylpyrrolidone) and potassium hydroxide KOH),
- different carbon-based nanofluids, including nanofluid based on single wall carbon nanohorns stabilized with sodium dodecyl sulfate (SDS), and graphene oxide nanofluid with and without addition of SDS,
- silica nanofluid stabilized with potassium hydroxide,
- water solution of sodium dodecyl sulfate,
- distilled water.

Gold shows the highest thermal conductivity of the metals and thus is considered as one of the most interesting materials for nanofluids. Single wall carbon nanohorns stand out for high specific surface area, up to several hundreds of square meters per gram [145]. Silica has film-forming properties and undergoes polymerization. It should improve deposited layer what is consider as one of the most important mechanisms for heat

transfer enhancement. Graphene oxide is interesting due to its extremely high thermal conductivity, large surface area and mechanical strength. The existence of graphene was predicted nearly 40 years ago but for the first time it was isolated in 2004 by Andre Geim and Konstantin Novoselov (2010 Nobel prize winners). Graphene oxide is a promising material, but it is unknown how its flakes behave during boiling and if they interact with the surface of heat exchanger.

Sodium dodecyl sulfate is an anionic surfactant commonly used for stabilization of nanofluids. Its suspension with the same concentration as in investigated nanofluid was used to study the effect caused by nanoparticles themselves and the stabilizer separately. Chosen working fluids show uncommon diversity and allow for observation of different properties and their influence on the results.

Literature review (Chapters 2 and 3) underlines that there is a lack of studies comparing broad range of working fluids under comparable operating conditions in a thermosyphon. Among carbon-based nanofluids, no studies on graphene oxide or nanohorns were conducted. Only one paper analyzed the silica nanofluid in thermosyphon and it is focused on the functionalization effect. No investigations of sodium dodecyl sulfate or any other surfactant on thermosyphon efficiency were available. Some hints could be find in the literature discussing pure boiling processes or determining single thermophysical properties. Still, further research was required in all these fields to fully understand mechanisms behind nanofluids behavior. The mentioned lacks in knowledge determined the scope of this dissertation.

Under some specific conditions, thermosyphon operates under geyser boiling regime. This phenomenon often remains unrecognized and is still not well understood. Usage of highly precise pressure transmitters located along the device allowed for observation and analysis of time-dependent behavior. Effect on geyser boiling seems to be negligible small on the averaged thermal performance of the device. However, it causes high mechanical loads and may be dangerous for thermosyphons usually installed in systems that are respected to work for long periods of time. The literature review (section 3.2) showed that almost no study on influence of nanofluids and surfactant solution were available. Research presented in this thesis fills this gap.

1.1 Scientific thesis and objectives of the dissertation

Scientific thesis of the dissertation

Operating parameters of a thermosyphon can be controlled by means of properly selected and prepared working fluid - a nanofluid. Nanoparticles and surfactant change properties of the base fluid influencing the boiling process and overall heat transfer efficiency.

Thermal resistance at the heater wall influences an overall heat transfer efficiency of the device. Deposition of nanoparticles into porous layers on the heater wall is the key mechanism leading to heat transfer improvement.

Under specific working conditions, a pseudo steady-state boiling regime - geyser boiling may occur. The frequency and the intensity of geyser events can be controlled by means of appropriate working fluid selection, i.e. properly determined composition of a base fluid, nanoparticles, and surfactant.

Objectives of the dissertation

The main aim of this dissertation is to analyze the influence of nanofluids (understood as a composition of base fluid, nanoparticles and optional stabilizer) on heat transfer and boiling behavior in a two-phase closed thermosyphon.

Objectives of the thesis:

1. Analysis of parameters and nanofluids properties affecting the boiling process in a thermosyphon. Characterization of selected nanofluids (Chapters 3 and 4).

2. Enhancement of the heat flux transported by a thermosyphon in the range of low thermal loads by means of appropriately selected nanofluids (Chapter 5).

3. Study of the impact of the boiling process on nanoparticles suspended in a fresh nanofluid (Chapter 5).

4. Determination of how nanoparticles and surfactants influence the geyser boiling phenomenon (Chapter 6).

Thesis structure

This thesis is divided into 7 chapters, including this chapter covering the short overview of the topic. Literature review is presented in Chapters 2 and 3. It starts with a general introduction to nanofluids in Chapter 2, including synthesis and stabilization methods, and thermophysical properties of nanofluids. Then, the literature review expands to heat transfer processes in a thermosyphon working with nanofluids in Chapter 3. Starting from the assessment of effects that are possible to obtain by changing typical working fluid (e.g. water) by nanofluids, this chapter contains the comprehensive analysis of studies conducted so far, identification of boiling process as crucial for enhancements caused by nanofluids, and finally focuses on boiling regimes and possible effects caused by nanofluids and surfactant solution. Chapter 3 ends with the conclusions drawn from the literature review and shows how knowledge gaps are filled with the research study shown in presented dissertation. This partially covers the first objective of this thesis.

Chapters 4 through 6 address results and discussion. Chapter 4 starts with an introduction of investigated working fluids, including two types of graphene oxide nanofluids, two types of gold nanofluids, nanohorn and silica nanofluids, distilled water and solution of surfactant (sodium dodecyl sulfate) which was used as stabilizer for nanohorn and graphene oxide nanofluids. Results from the experimental characterization focus mostly on graphene oxide nanofluids, as their properties are still not well investigated.

Chapter 5 presents the performance of two-phase closed thermosyphon filled with earlier mentioned working fluids. It starts with the description of the test rig and measurement procedures, and then moves to time-averaged analysis of the collected experimental data. This part includes parameters describing work of the thermosyphon, such as thermal resistance or heat transfer capacity, and investigates boiling curves, temperature distributions, and internal pressure. Inner surface of the evaporator was checked with endoscopy camera to evaluate micro-sized changes of surface caused by deposition of nanoparticles. Finally, graphene materials that remained in the working fluid taken out from the device after experiments was analyzed under scanning electron microscope.

Chapter 6 discusses the geyser boiling phenomena. High-precision pressure transmitters located along the device allowed for detection of geyser events analyzed in this

chapter. The differences between working fluids operated in the wide temperature range are underlined and compared by using methodology of data reduction implemented in Python programming language. The code allowed for averaging the frequency and amplitude of detected geyser events over the whole experimental time and gave an answer how nanoparticles and surfactant solution influence boiling behavior.

Chapter 7 summarizes the presented research and looks into perspectives for further work in this scientific area.

Chapter 2

Nanofluids

The primary goal of creating suspensions with particles was to improve a thermal conductivity of a base fluid. Attempts with micro-sized particles did not succeed, mostly due to problems with stability and clogging [45]. The new way appeared with a development of nanotechnology. In 1984, Yang and Maa [224] published the study on boiling of suspensions with nano-sized particles. In 1993, Grimm [65] patented (in Germany) suspensions of aluminum particles with sizes between 80 nm and 1 μm and concentrations from 0.5 to 10 vol.% as a method of thermal conductivity enhancement [136]. The term *nanofluids* was officially introduced 11 years later by Choi and Eastman [38] from Argonne National Laboratory of USA. They published a theoretical discussion on thermal conductivity of copper nanofluid.

Nanofluids are defined as suspensions of nanoobjects with at least one dimension smaller than 100 nm [31]. Nanoparticles are characterized as nanoobjects with all spatial dimensions smaller than 100 nm [1]. The term *nanoparticle* is commonly used for both - nanoobject and nanoparticle [31, 100, 117] and is used in this thesis in a similar way.

Additional chemicals, such as surfactants or polymers, improve stability of nanofluids. They inhibit agglomeration and sedimentation, and often change thermophysical properties of nanofluid, affect its boiling behavior, etc. Their presence in a suspension should

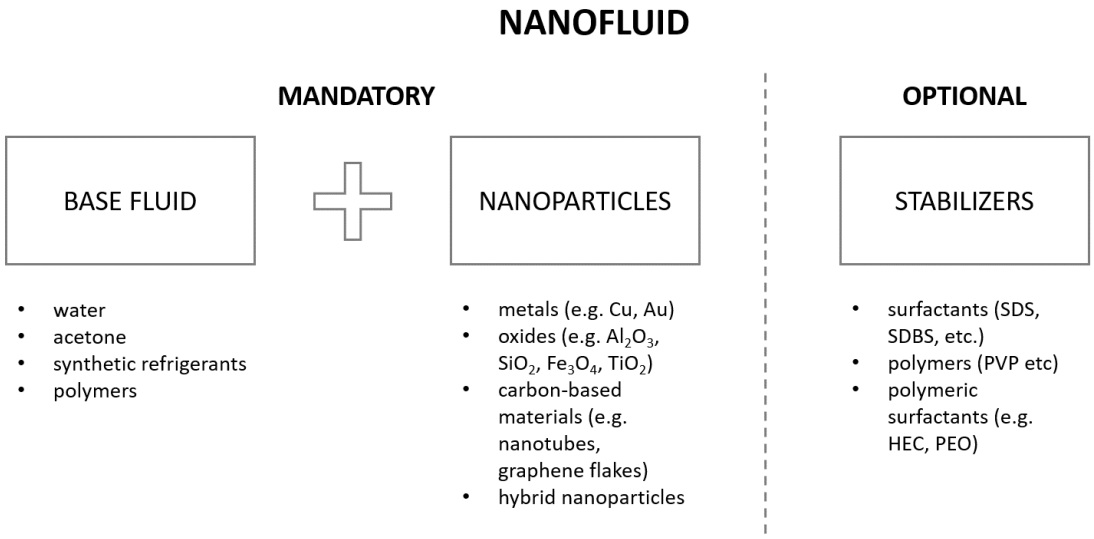

Figure 2.1: Components of nanofluids

be carefully analyzed, yet as the literature confirms it is often neglected. In this study all three components (Fig. 2.1) are taken under consideration. Details on synthesis of different types of nanofluids and the most common stabilizers - surfactants and polymers - are presented in the following sections.

2.1 Synthesis and stabilization

Nanofluid covers combinations with variety of nanoparticles, base fluids and stabilizers. Production processes of nanofluids are classified into:

- *one-step method* produces and disperses nanoparticles directly in base fluids. It allows for avoiding the oxidation of metal nanoparticles and leads to nanofluid production with well-controlled sizes of nanoparticles. It is often based on expensive vacuum techniques.
- *two-step method* disperses earlier synthesized nanoparticles in a base fluid. This technique is easily scalable and easier to conduct, but the final product is of lower quality, particles agglomerate and sediment more often [45, 67]. Stability is often improved by addition of chemical substances, such as surfactants or polymers.

Both methods (one- and two-step) lead to a stable product, but the approach to synthesis must be carefully chosen depending on used material and required application. These factors are the most important to consider: thermal stability, dispersability in diverse media, chemical compatibility, and ease of chemical manipulation [45].

Surfactants and polymers

The reason of adding surfactants into nanofluids is to improve their stability. Surfactants (or surface active substances) are amphiphilic, usually organic compounds. They consist of a lyophilic part (mostly hydrophilic polar group), a lyophobic part which is often hydrophobic hydrocarbon chain [2, 37, 108]. Taking into account the polar group character, surfactants are classified into two main groups [37]:

- nonionic surfactants,
- ionic surfactants which include:
  - anionic surfactants,
  - cationic surfactants, and
  - amphoteric or zwitterionic surfactants.

From them, anionic and nonionic surfactants are the most commonly used in the industry.

Small amount of surfactant added to water does not noticeably affect its physical properties, except surface tension and eventually viscosity (surfactant solution shows non-Newtonian behavior in some cases) [37]. Due to amphiphilic nature, surfactants show a tendency to aggregate in solutions into various structures like micelles and bilayers, and to concentrate at interfaces [37, 108]. In case of liquid-vapor interface of water-based solutions, surfactants adsorb with their hydrophilic head located toward the liquid and hydrophobic tail towards the vapor [108]. This relocation requires from several seconds

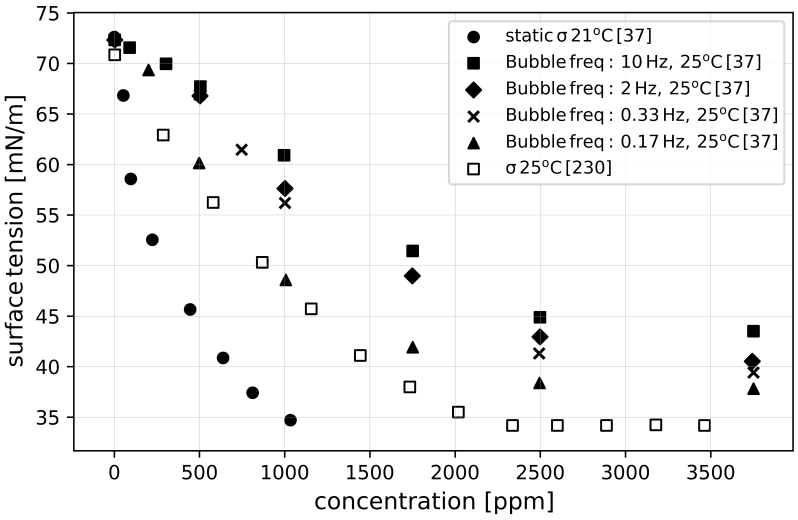

Figure 2.2: Dynamic and static surface tension of sodium dodecyl sulfate [37, 230]

to hours, depending on the type and concentration of surfactant, temperature of solution, and conditions at the interface. It reduces static surface tension, but before reaching the equilibrium, the surface tension changes with time what is defined as dynamic surface tension. At fixed concentration of surfactant, static surface tension is usually lower than the dynamic one and it should be taken into consideration during measurements (see Fig. 2.2). Increase in temperature causes a decrease in both static and dynamic surface tension [37, 108].

Increase in surfactant concentration reduces static surface tension, but only to the value of critical micelle concentration (CMC). From this point, aggregates or colloid-sized clusters called micelles are formed. Their structures and sizes change with time. CMC indicates efficiency of a surface tension reduction. Further increase in surfactant concentration does not affect the surface tension or changes it with a lower slope. High concentration may affect other physical properties of solution [2, 37, 138]. The most common methods for the determination of CMC are based on surface tension, self-diffusion, conductivity [37]. Values are plotted against the surfactant concentration and cmc is then determined as a breakpoint in an asymptotic function [37].

One of most commonly used surfactants is sodium dodecyl sulfate (SDS). It is an organic compound with the formula of $CH_3(CH_2)_{11}SO_4Na$ and structure shown in Figure 2.3 a). Figure 2.3 b) showcases molecular dynamic simulation of sodium bridging. Bruce et al. [25] simulated this phenomenon indicating that sodium ions located in the first shell of headgroups may interact with only one headgroup (72%), or bridge two (23%), or even three (5%) headgroups in SDS/water solutions (see green arrows in Figure 2.3b).

Polymers are an alternative for surfactants to enhance stability of nanofluids. As large molecules (or macromolecules), they are comprised of many repeatable units (monomers) created in polymerization process. Their addition to water increases the viscosity of solution and may cause shear-rate dependent rheology. The difference grows with the increase in polymer concentration or its molecular weight [108, 229]. Among the polymers, only a group of polymeric surfactants with surface-active characteristics, shows notable impact on surface tension (σ). The most common polymers from this group are hydroxyethyl

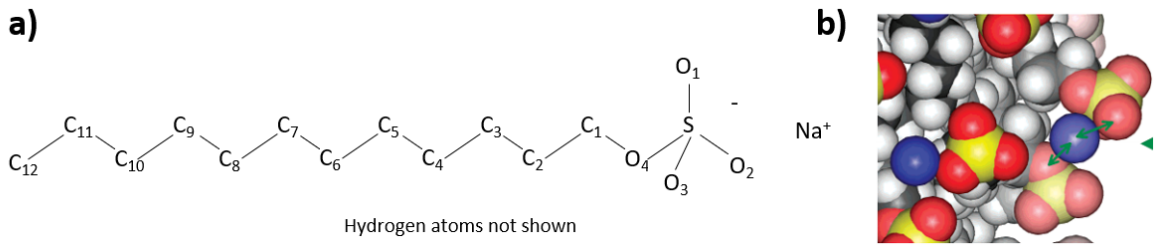

Figure 2.3: a) Structure of sodium dodecyl sulfate, b) Molecular dynamic simulation (blue - sodium, red - oxygen, yellow - sulfur, dark gray - carbon, light gray - hydrogen) [25].

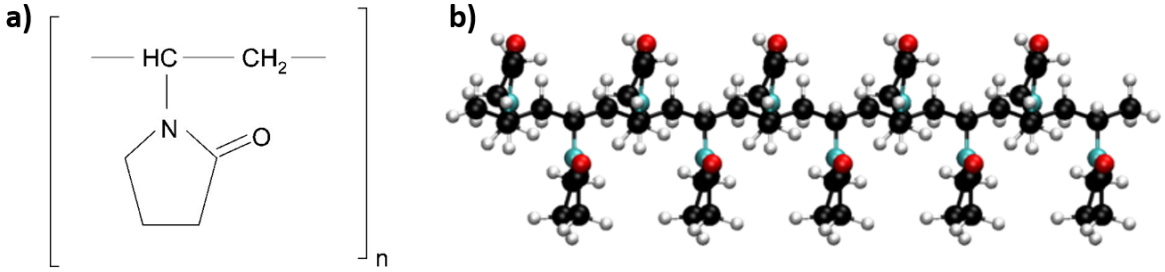

Figure 2.4: a) The repeating unit of polyvinylpyrrolidone (PVP) [115], b) PVP chain (red - oxygen, blue - nitrogen, black - carbon, and white - hydrogen) [112]

cellulose (HEC) and polyethylene oxide (PEO). Increased viscosity of aqueous polymeric additive solutions should be considered during the σ measurements, particularly at high bubble frequency [37, 108, 229].

One of polymers used to stabilize nanofluids is polyvinylpyrrolidone (PVP), called also polyvidone or povidone. It is a light hydroscopic powder soluble in both water and different organic solvents. The repeating unit of PVP is shown in Figure 2.4 a) and simulation of PVP chain in Figure 2.4 b). Its molecule contains a hydrophobic group (the alkyl group) and strongly hydrophilic group (the pyrrolidone moiety). PVP has excellent solubility in water [98] and its solution is characterized by good wetting properties and the ease of film forming. That is why it is used as an adhesive, emulsifier, surfactant, stabilizing addition or shape controlling agent.

2.2 Thermophysical properties of nanofluids

This section focuses on parameters relevant for heat transfer processes in the thermosyphon. Research community still debates whether nanofluids can be treated as a single-phase fluid or should be considered as a two-phase fluid. The answer seems to be dependent on particular property and nanofluid components. The property of a nanofluid treated as one-phase fluid is often called *effective*.

Most of available correlations that allow for calculation of thermophysical properties of nanofluids are based on volume concentration. It is not always possible to measure

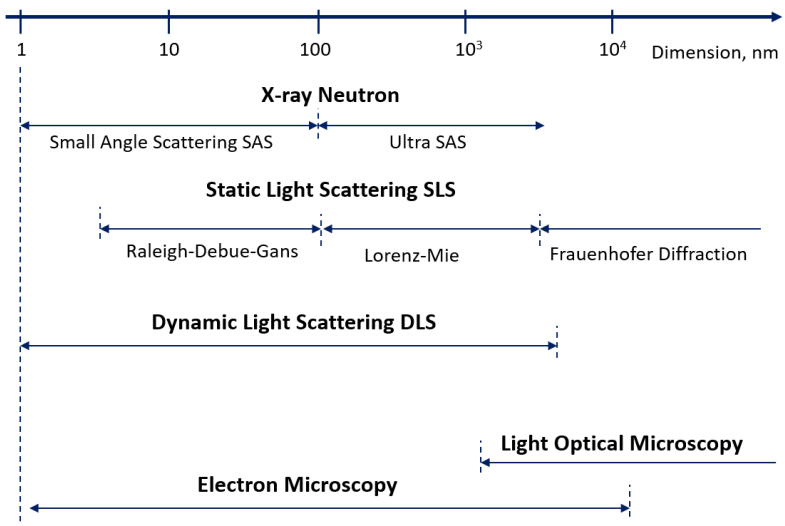

Figure 2.5: Techniques for size determination of colloidal systems [214]

this parameter, thus following relation with a mass concentration was proposed [19, 108]:

$$\phi_{vol} = \frac{1}{\left(\frac{1-\phi_{wt}}{\phi_{wt}}\right)\frac{\rho_{np}}{\rho_{bf}} + 1} \tag{2.1}$$

Where ϕ_{vol} is volume concentration, ϕ_{wt} mass concentrations; ρ_{np} and ρ_{bf} densities of nanoparticles (np) and base fluid (bf), respectively.

Size of nanoparticles

Size and shape of nanoparticles may influence thermophysical properties of final suspension. Currently, all available methods allowing for direct determination of size of naparticles suspended in base fluid enforce some compromises according to sample preparation. A review of techniques for size determination of particles in nanofluids are presented in Fig. 2.5.

The most common techniques are scanning electron microscope (SEM), transmission electron microscopy (TEM), atomic forces microscope (AFM), and dynamics light scattering (DLS). First three require small amount of diluted and dried samples. Particles are measured separately from the base fluid what can affect the results but this approach gives an overview on particles shape. In case of DLS, there is a critical concentration above which too much noise is detected and the quality of results is too low. Thus, samples are often diluted what can alter the final outcomes. DLS estimates diameter of a sphere that has the same diffusion coefficient (D) as the measured particle. This includes structures on the surface, ionic strength of medium or agglomerates, thus results are usually higher than the real size of particle core [214].

Dynamic Light Scattering (DLS) is used to characterize size or hydrodynamic radius of nanoparticles dispersed in a liquid. A typical DLS system consists of a coherent light source (laser) that illuminates the sample. Due to the thermal agitation, particles are bumped by fluid molecules surrounding them what causes their random motion, called Brownian motion. Resulting fluctuations of the scattered light are detected at a known

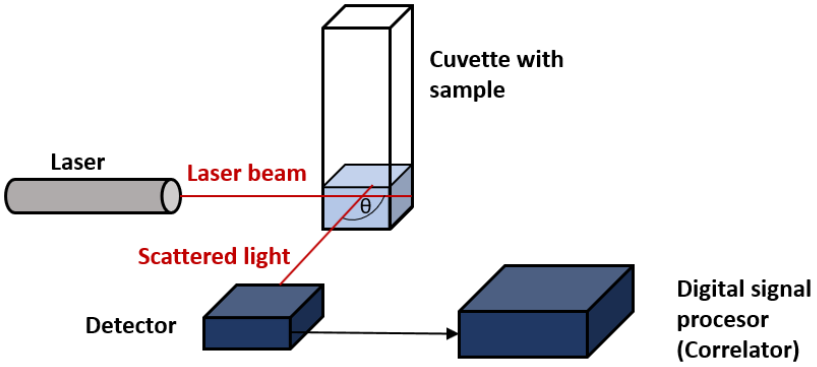

Figure 2.6: Dynamic Light Scattering method (DLS) [118]

scattering angle θ. The intensity of a laser beam depends on particles size - the smaller particle sizes the faster Brownian motion. The Stokes-Einstein equation allows to connect the diffusion coefficient measured by DLS and particle size [118, 201]. The general scheme of DLS measurement is presented in Fig. 2.6.

Thermal conductivity

Improved thermal conductivity of nanofluids was the main motivation for their development and is one of the most discussed topics in this area. As the thermal conductivity of solids is much higher than that of liquids, researchers attempted to develop suspensions with solid particles to enhance heat transfer properties of base fluids. Prior to the development of nanotechnology, micro-particle suspensions failed because of poor stability, significantly increased pumping power and clogging of flow channels [45]. Nanofluids seem to overcome these issues and they have been receiving increased attention worldwide since their first presentation by Choi and Eastman [38].

Thermal conductivity of nanofluids depends on a number of factors, such as type of the base material (of both base fluid and nanoparticles), size, shape and concentration of particles, pH value, pressure, and temperature. For this reason, studies on physical mechanisms responsible for enhancing the thermal properties of nanofluids present many divergences among themselves and one complete theory on heat conductivity in nanofluids does not currently exist.

Conventional thermal conductivity theory fails when predicting the degree of thermal conductivity improvement by nanofluids [24, 155]. Additional phenomena must be considered in the nanoscale, e.g. Brownian motions of particles, molecular-level layering on the liquid-particle interface, the ballistic nature of heat conduction in particles (increase of the phonon free path length due to liquid layering), or clustering of nanoparticles [18, 24, 155]. Difficulties arise from problems with understanding the multiscale of nanofluids, including the molecular scale, the microscale, the mesoscale and the macroscale [24]. Quality of results in the available literature are indecisive. Majority of them show raising trend in nanofluids thermal conductivity with the increase of temperature and concentration of nanoparticles [24]. Some researchers [17] argue that Maxwell equation allows for good estimation of thermal conductivity of nanofluid. Understanding mechanisms of nanofluids behavior requires wide range of results obtained from analysis of well characterized materials.

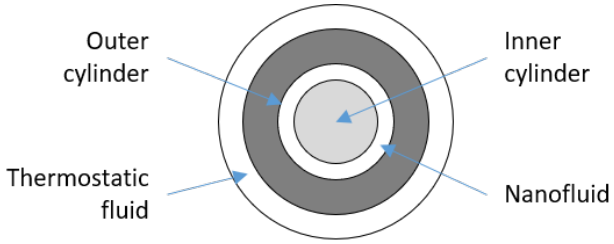

Figure 2.7: Cross-section of the cylindrical cell [217]

Multiple comprehensive reviews on thermal conductivity of nanofluids were published [4, 9, 12, 121, 120, 172, 192, 228], and thus will not be repeated here.

Thermal conductivity measurements are conducted using three groups of methods: steady-state methods (the temperature is maintained to be constant during the experiment), transient techniques (temperature varies during the experiment in a controlled way), and thermal comparator techniques. The latter are rarely used for nanofluids [152, 217].

Group of the devices with one of the highest measurement accuracy is based on cylindrical cell method. Cross section of measuring device is schematically shown in Fig. 2.7. Investigated fluid is placed between two concentric cylinders maintained at constant temperature. A constant heat load is provided to an inner cylinder and the temperature of the outer cylinder is constant and controlled by a thermostat. Heat flux needed to maintain the temperature difference between external and internal surface is measured.

Viscosity

Viscosity is an important parameter affecting heat transfer and fluid flows, in particular pumping power needs. In case of nanofluids, it has received increasing attention since 2006 [134]. Available literature presents studies on nanofluids showing both shear rate-dependent viscosity (Newtonian nature) and shear rate-independent viscosity (non-Newtonian nature). The most commonly used correlations for nanofluids viscosity is Einstein's model for an effective viscosity suspension (μ_{eff}) that assumes spherical shape of particles [134]:

$$\mu_{eff} = \mu_f(1 + 2.5\phi) \tag{2.2}$$

Where μ_f is the viscosity of base fluid, ϕ is the volume concentration of nanoparticles.

Extensive overview of existing models for viscosity calculations is described in recent review paper [134] that summarizes experimental studies. Authors observed rising nanofluids viscosity with an increase in nanoparticles concentration but there were big inconsistencies between different studies. Literature did not provide a final answer on how temperature influences nanofluid's viscosity and in many cases, available correlations failed to predict its value. Researchers proposed empirical correlations, but they were usually applicable in a very narrow range of parameters, and particles types. There is also a need to understand how others factors, such us nanoparticles size and shape, or pH value affect viscosity of nanofluids. Another challenge is to check a long-time stability and influence of nanofluids on heat transfer systems [134].

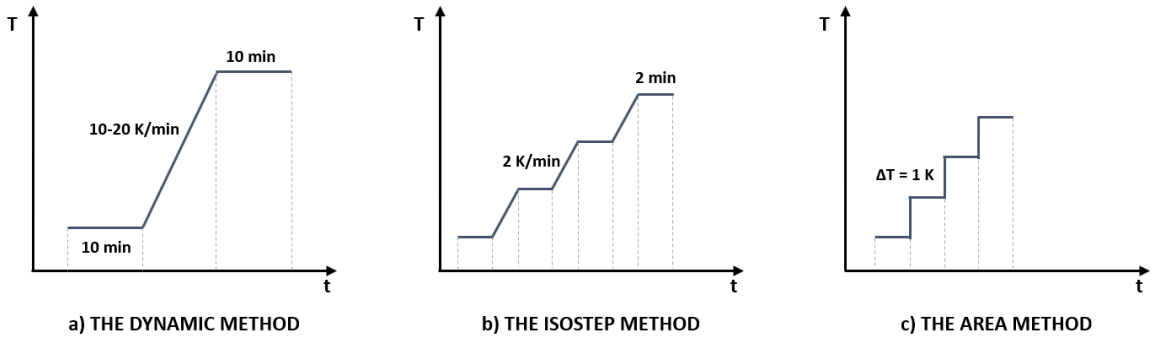

Figure 2.8: Measurement methods of differential scanning calorimetry (DSC): a) the dynamic method, b) the isostep method, and c) the areas method [55]

Specific heat capacity

The specific heat capacity, commonly called specific heat, is the amount of heat needed to change the temperature of one kilogram of a substance by 1 K [156]:

$$C_p(T) = \frac{\delta Q}{\delta T} \tag{2.3}$$

Where T is temperature [K].

Next to the thermal energy that can be accumulated within a given material, the specific heat determines the speed of cooling or heating of a body defined as a thermal time constant [156]:

$$\tau = R \cdot C_p \cdot V \tag{2.4}$$

Where R is the thermal resistance of heat dissipation and V is the body volume. This constant takes small values for nanoscale particles, such as 1.2 x 10^{-11} s for a single graphene sheet [156].

One of the most common techniques for determination of specific heat capacity is differential scanning calorimetry (DSC). A sample of a known mass is heated or cooled and the change in heat flux is measured. The heat flux obtained by DSC is given with the equation [55]:

$$\dot{Q} = \int_{T_i}^{T_f} \dot{m} \cdot C_p \cdot dT = m \cdot C_p \cdot \beta \tag{2.5}$$

Where m is the mass of the sample, C_p specific heat capacity, dT temperature differential, and β the heating rate depending on the method used.

The most popular DSC techniques shown in Fig. 2.8 are: the dynamic method, the isostep method, and the area method [55]. Dynamic method consists of three following stages: achieving the thermal equilibrium to homogenize material temperature, heating with a constant heating rate of 10-20 K/min and reaching the thermal equilibrium again. The isostep method includes many short stages along the whole temperature range. Heating rate is usually between 1-2 K/min and isothermal stages are much shorter than in the dynamic method. The areas method includes following isothermal segments without heating stages [55].

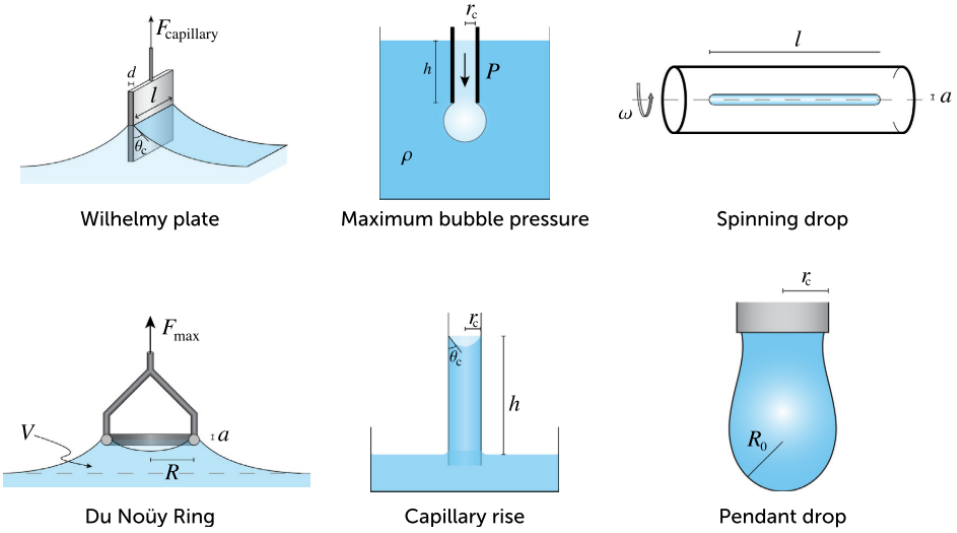

Figure 2.9: Methods of surface tension measurements [22]

The most common equation for calculating the specific heat capacity is the mixture rule [60]:

$$Cp_{nf} = \frac{\phi(\rho_{np} Cp_{np}) + (1-\phi)(\rho_{bf} Cp_{bf})}{\phi(\rho_{np}) + (1-\phi)(\rho_{bf})} \tag{2.6}$$

Where ϕ is volume fraction of nanoparticles ; ρ is density; nf, bf and np subscripts determines values for nanofluid, base fluid and nanoparticles.

Surface tension

Surface tension appears in many heat transfer correlations, such as Bond number, critical heat flux (CHF), or Kutateladze number. The most common methods of surface tension measurements are presented in Fig. 2.9 and includes [51]: pendant drop, Wilhelmy plate, maximum bubble pressure, Du Nouy Ring, capilary rise and spinning drop techniques. More information on these methods can be found in [22, 47].

Nanoparticles added to the base fluid change its surface property, but the current state of knowledge does explain this mechanism. A recent review [51] showed that surface tension of nanofluids is affected mostly by: type of nanoparticles and base fluid, (lack of) surfactant addition, temperature, particles size and shape, and nanoparticles concentration. Al_2O_3 is the most studied nanofluid with respect to the surface tension measurements. SiO_2 and various graphene-based nanofluids were described in only four papers each. For SiO_2 most research groups reported an increase in surface tension with increasing nanoparticles concentration and decreasing temperature. For graphene materials, half of presented analysis showed increase and half decrease in surface tension for higher concentrations. All papers showed surface tension reduction with an increase in temperature. Surface tension is strongly dependent on surfactant usage and most authors reported its decrease after surfactant addition. The review [51] highlighted the need for high-temperature measurements and development of more universal correlations and models, e.g. for different types of nanofluids and wide range of working conditions. They pointed out that some research groups did not measure nanofluid density, although it is required for surface tension interpretation.

Contact angle

Contact angle is the angle between the solid and liquid interface, as presented in Fig. 2.10. It is a parameter characterizing wettability of the solid surface by the liquid and is described by the Young's equation [37]:

$$\theta = \arccos\left(\frac{\sigma_{SV} - \sigma_{SL}}{\sigma_{LV}}\right) \tag{2.7}$$

Where σ_{SV} is the surface tension of the solid and vapor (called also surface free energy), σ_{SL} interfacial tension of solid and liquid, and σ_{LV}surface tension of liquid and vapor, respectively.

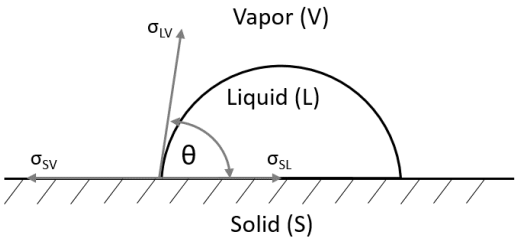

Figure 2.10: Graphical interpretation of the Young's equation [37]

Wettability strongly influences boiling heat transfer coefficient, thus understanding of how nanofluids affect contact angle is an important task. So far, the state of knowledge is just at the beginning and review of selected papers can be found in Hernaiz et al. [71]. Further research is required to explain the influence of nanoparticles on contact angle and determine correlations and models applicable for a wide range of materials.

Chapter 3

Heat transfer processes in a thermosyphon

3.1 Nanofluids in two-phase closed thermosyphons

The main goal of using nanofluids in thermosyphons is the reduction of their overall thermal resistance without changing other operating conditions. The working fluid properties that determine maximum heat transfer can be described with Figure Of Merit proposed by Reay and Kew [164] (and Rice [165]) for neglected loss of vapor pressure. For thermosyphons, it is defined as [164]:

$$M = \left(\frac{\Delta h k_l^3 \sigma_l}{\mu_l} \right)^{1/4} \tag{3.1}$$

Where Δh is latent heat of vaporization, k_l thermal conductivity of liquid, σ_l surface tension of liquid and μ_l viscosity.

Addition of nanoparticles affects all mentioned thermophysical properties, except latent heat of evaporation. To increase Figure Of Merit by nanofluids, the following relationship between the nanofluid and base fluid must be met [29, 100]:

$$\left(\frac{k_{nf}^3}{k_{bf}^3} \right) \left(\frac{\rho_{nf}^2}{\rho_{bf}^2} \right) \left(\frac{\mu_{nf}}{\mu_{bf}} \right) > 1 \tag{3.2}$$

Equation 3.2 can be applied only if nanofluid meets the assumptions of effective medium theory, so when it can be treated as a homogeneous liquid. It does not cover the interaction of nanoparticles with the evaporator wall which significantly changes properties of both working fluid and evaporator surface. Classical approaches to thermosyphon designs (such as Reay and Kew [164] or [232]) cannot be used in case of thermosyphons working with nanofluids. Experimental study is required to determine changes related to nanofluids. Big number of reliable experimental data is required for further development of mathematical tools.

Partial thermal resistances

To define expectations from using nanofluids as working fluids in the thermosyphon, determination and understanding of parameters describing capabilities of the device to

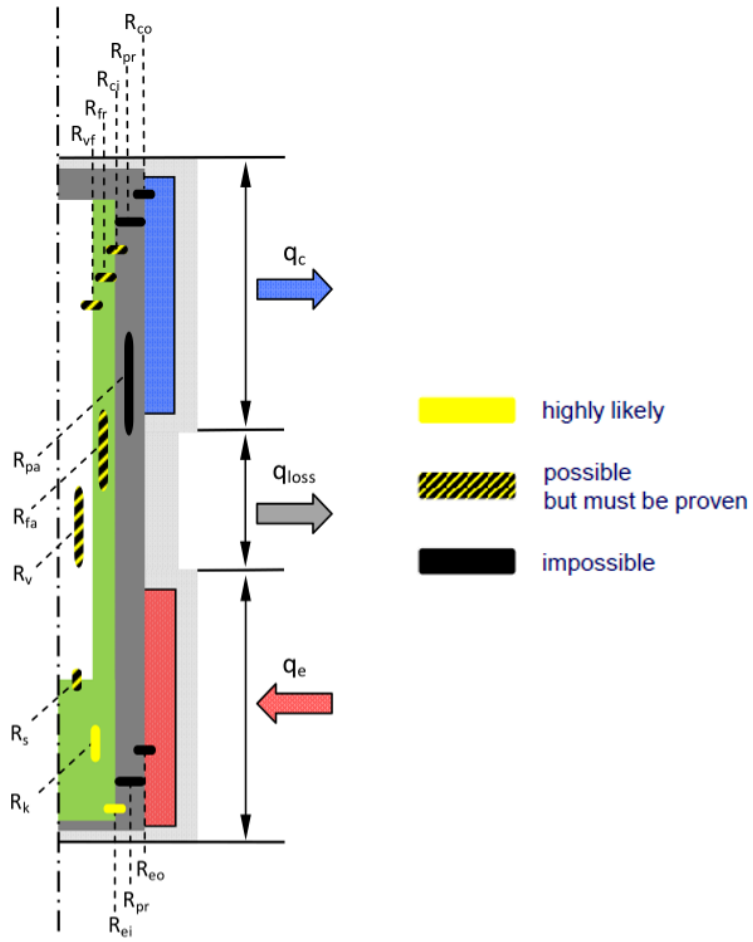

Figure 3.1: Color analysis of partial thermal resistances R_i possibly affected by nanofluids [30]

transport heat are required. An overall thermal resistance of the thermosyphon is expressed as [29, 218]:

$$R_{th} = \frac{\overline{t_e} - \overline{t_c}}{Q} \tag{3.3}$$

Where: $\overline{t_e}$ and $\overline{t_c}$ are the mean temperatures of the evaporator and condenser, respectively [°C], Q is the amount of energy transported by a device in the form of heat [W].

The overall thermal resistance is comprised of partial thermal resistances R_i, schematically analyzed in Figure 3.1. Each R_i refers to another physical mechanism responsible for heat transfer process [30]. Some of identified R_i cannot be influenced by working fluid, such as the thermal resistance between heat source (R_{eo}) or heat sink and internal surface of the thermosyphon wall (R_{co}). The next ones are thermal resistances of the pipe material itself in radial (R_{pr}) and axial (R_{pa}) directions. Other thermal resistances may be or may be not affected by nanofluids, thus their impact requires further investigation.

Thermal resistances in the condenser and adiabatic sections are influenced by nanofluid only if nanoparticles are somehow transported from the evaporator. Taking into account relatively low operating temperatures, particles cannot melt and evaporate. Thus, the question is whether they are carried by vapor.

Nanoparticles commonly used in nanofluids are usually from 4 nm to even more than 100 nm in diameter. Base fluid molecules with diameter of the order of 10^{-10} m (i.e. water molecule is about 0.28 nm) are not able to carry significantly larger nanoparticles from the free surface of the working fluid and transport them over long distances [30]. Further experiments [63] confirmed that particles are not transported by vapor, thus nanoparticles cannot affect partial thermal resistances in the upper parts of the device. As a result, changes in thermal resistance of condensate film in both axial (R_{fa}) and radial directions (R_{fr}), R_{vf} between the vapor and condensate, and R_{ci} between condensate film and inner wall of condenser can be neglected during normal operation conditions. The only known possibility of getting nanoparticles into upper parts of the device is operation under geyser boiling conditions. This regime is characterized by violent *eruption* of liquid gathered above the rising bubble, what may transport suspended nanoparticles to the condenser. However, conducted studies showed that negligible amount of particles was found in the condenser section [29, 63, 96, 218]. No mechanism allowing particles to attach to the inner surface of condenser wall was recognized.

Three of thirteen partial thermal resistances shown in Fig. 3.1 can be affected by nanofluids: thermal resistance of the fluid itself R_k, R_s of the phase interface between liquid and vapor, and R_{ei} between inner wall of the evaporator and heated fluid.

Thermal conductivity of nanofluid is higher than the one for water. Still, considering low concentrations of nanoparticles used in heat transfer applications, the possible enhancement is small. It is highly unlikely that this parameter has a decisive impact on the thermal performance of the thermosyphon, in particular during phase changes [30, 215].

Several thermophysical properties, including latent heat of vaporization and vapor pressure, determine the rate at which heat is transported through the vapor/liquid interface. As studies on these properties are rare [30] and the available results are inconsistent, the thermal resistance R_s is still in the group of *possible but must be proven* thermal resistances.

The last thermal resistance - R_{ei} between the evaporator wall and the heated working fluid (inner heat transfer coefficient of the evaporator) is undeniably influenced by nanofluid because particles interact with each other and the heater wall. Deposition into layers on the inner wall of the evaporator changes the properties of working fluid, but also the surface energy, roughness and chemistry. They affect the dynamics of bubble nucleation and create *thermal bridges*, what in turn enhances heat transfer capabilities. Due to deterioration, nanofluids cannot be described with an effective medium theory [30].

Deposition of nanoparticles

During boiling of nanofluids, particles deposit into a porous layer on the heater surface. Kim et al. [97] proposed microlayer evaporation as the main mechanism responsible for nanoparticles deposition (schematically shown in Fig. 3.2). Liquid gathered between the growing bubble and the heater surface evaporates fast what increases local concentration of nanoparticles, initially distributed uniformly in the microlayer. This decreases the distance between particles and leads to their deposition on the surface. Later, microlayer evaporator was experimentally confirmed by Kwark et al. [102].

Research on two types of silica nanoparticles (strongly and moderately hydrophilic) conducted by Quan et al. [159] showed that the distribution of deposited particles on the heater surface depends on nanoparticles wettability. Strong hydrophilicity translates

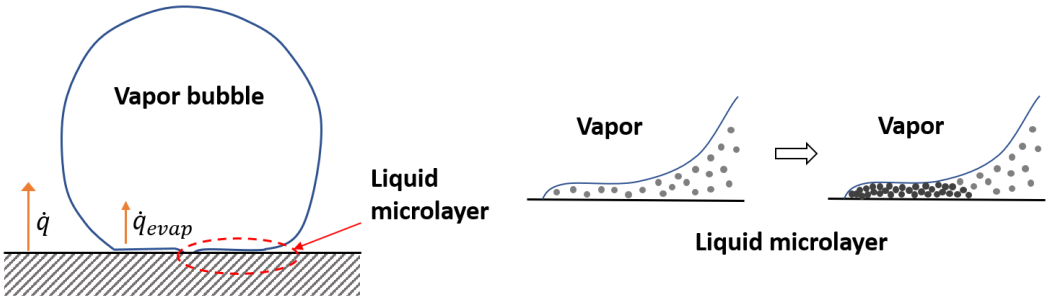

Figure 3.2: Mechanism of nanoparticle deposition during boiling (microlayer evaporation) [102]

into an uniform composition of particles in the droplet. The evaporation occurs mostly at the edges, thus fluid flows and transports suspended nanoparticles from the droplet center to the edges. Accumulated particles deposit into a layer along the original drop edge. This phenomenon is known as the coffee-ring effect [180]. Moderately hydrophilic particles are initially loosely distributed on the vapor-liquid interface and interparticle interactions prevent particles from attaining the drop edges and thus lead to irregular deposit. Created flat-like layer is much rougher than the coffee-ring pattern what will further affects boiling behavior, in particular bubble sizes and critical heat flux [159].

Deposition of nanoparticles influence surface roughness in three ways depending on the particle size and the initial surface roughness [200]:

- nanoparticle size is much smaller than the surface roughness: particles will fill the cavities and reduce the surface roughness.
- nanoparticle size is smaller than the surface roughness but the difference is not that significant (e.g. 47 nm and 0.524 μm, respectively): the number of active nucleation sites will be multiplied by splitting a single cavity into several nucleation sites, thus surface roughness in increased.
- size of nanoparticles or its agglomerates is greater than cavities: the surface roughness and number of nucleation sites may change diversely and the effect on surface roughness depends on how particles deposit.

In general, the increase in surface roughness improves phase change heat transfer due to enhanced nucleation site density [63, 218]. Enlargement of the heat transfer area as a result of increased roughness is rather small when compared to the uncoated surface. Thus, this effect can be neglected as a mechanisms for boiling heat transfer enhancement [30, 218].

Particle deposition influences the surface wettability [56, 200]. The interplay of wettability and porosity of porous layer is called wickability [195]. Deposition of nanoparticles affects chemistry and structure of the surface but also the surface energy. According to Young's equation, it modifies the force balance at the triple line [195, 200, 218]. All these mentioned factors affect heat transfer characteristics during boiling [56, 107, 127, 200, 218].

Different research groups tried to determine the effect of nanoparticle deposition on various parameters affecting boiling behavior. Kwark et al. [102] reported that deposited coating bonds well to the surface even after repetitive testing. Phan et al. [154] noticed

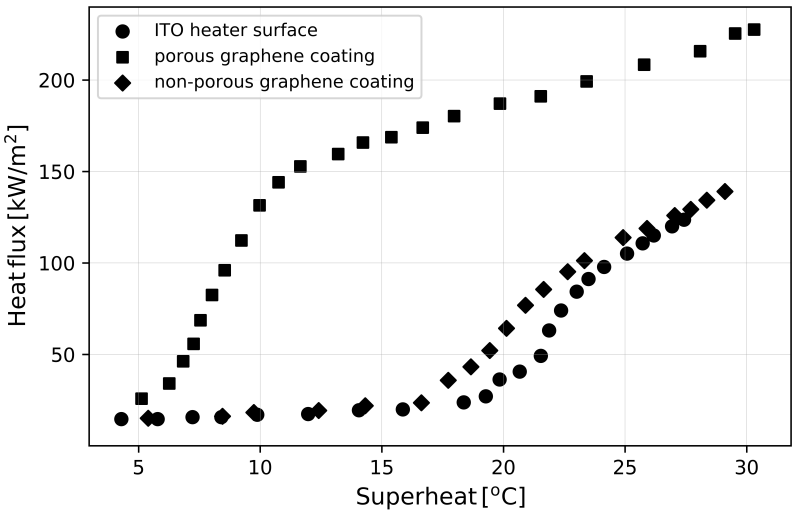

Figure 3.3: Boiling curves for heater ITO surface coated with porous and non-porous graphene [104] in [80]

existence of maximal thickness of deposited layer depending on duration of experiment and nanoparticle concentration. Park et al. [149] reported that CHF enhancement abated gradually due to reduction of layer porosity when boiling exceeds critical length. Lee et al. [104] in [80] also showed lowered heat transfer performance and CHF for non-porous graphene coating compared with porous graphene coating (see Figure 3.3).

As vapor cannot transport nanoparticles, none or very small number of particles is deposited in the condenser section [218, 63]. Qu and Wu [158] found that deposition of nanoparticles in the condenser may even cause the decrease of condensation heat transfer coefficient due to increased surface wettability.

Previous studies on thermosyphons with nanofluids

Tables 3.1, 3.2, and 3.3 provide a review of the available literature which considers water-based nanofluids operating as working fluid in two-phase closed thermosyphons. Publications are classified in a chronological order according to the type of nanofluid.

Table 3.1 includes studies on carbon-based nanofluids used as working fluid in a thermosyphon. Three publications analyzed the influence of multiwall carbon nanotubes and three of graphene-based nanofluids. These materials are characterized by big differences of dimensions in different directions - their length is orders of magnitudes larger than thickness or diameter. None of the papers investigated graphene oxide flakes or nanohorns what is the scope of this thesis.

Table 3.2 summarizes research on nanofluids based on oxides in thermosyphons. The most investigated nanofluids are Al_2O_3 and TiO_2. Only one paper [222] discussed the silica nanofluid and focused mostly on the functionalization effect on the fluid stability and basic coefficients describing thermal efficiency. More detailed analysis of the silica nanofluid effect on heat transfer in a thermosyphon is described in this dissertation.

Table 3.3 focuses on nanofluids based on silver. Part of articles considering gold nanofluids are included also in table 3.2 due to comparative analysis between TiO_2 and gold. Research on gold nanofluids used in a thermosyphon were conducted only by

one research team. Gold and silver are characterized by one of the highest thermal conductivity of known metals. For this reason, gold with different stabilization was also investigated in this work.

Tables 3.1 - 3.3 include following footnotes and acronyms:

Footnote	**Meaning**
a	outer diameter (d_o)
b	thickness/diameter
c	length
d	hydrodynamic diameter
e	GNP = graphene nanoplatelet
f	SDBS = sodium dodcylbenzenesulfonate
g	MWCNT = multiwall carbon nanotube; CNT = carbon nanotube
$\uparrow$	increase in a given parameter
$\downarrow$	decrease in a given parameter
$\rightarrow$	no effect of/on a given parameter
IA	inclination angle (the angle formed by the x-axis and thermosyphon symmetry line in the length direction)
FR	filling ratio (volume of working fluid to volume of the evaporator section)

Table 3.1: Analysis of available literature on thermosyphon working with carbon-based nanofluids.

Reference	**$d_i/L_{TS}/L_e/L_c$ (type of heater)**	**IA (α)**	**FR [%]**	**Water - based nanofluid**	**Concentration**	**Size [nm]**	**Comments and conclusions**
Graphene-based nanofluids							
Azizi et al. (2013) [16]	20[a]/450/160/200 (electric heater)	90	60	Graphene + Gum Arabic (GA)	4-20[b] 5-10 μm[c]	0.02 - 1wt.% + 0.5 wt.% GA	- ↑ in concentration and in heat flux → up to 10% enhancement in thermal efficiency compared to base fluid - ↑ in heat flux → ↓ in overall thermal resistance of the thermosyphon - addition of nanoparticles leads to the reduction of averaged temperature of the evaporator
Amiri et al. (2015) [10]	20/1000/350/400 (electric heater)	90	-	GNP-COOH; GNP-SDBS;	0.55-3.74[b] 0.5-3 μm[c]	0.025 - 0.1wt.% + SDBS/ pristine GNP ratio 0.5:1	- max enhancement of thermal efficiency up to 35% for SDBS and 68% for COOH compared with water - covalent functionalization (COOH) is more effective than non-covalent (SDBS) and shows lower decrease of pressure drop and viscosity
Soleymaniha et al. (2018) [187]	20/1000/350/400 (electric heater)	90	-	amine treated-GQD (graphene quantum dots)	5-20	0.001; 0.002wt.%	- nanofluids ↓ evaporator temperature and ↑ heat transfer coefficient compared to water - acid treatment → formation of abundant carboxyl and amine groups on GQDs surface → high stability os suspension - small concentration results in negligible increase in pressure drop and rheological properties
Multiwall carbon nanotubes (MWCNTs) nanofluids							
Liu et al. (2010) [113]	6/350/100/150 (electric heater)	90	50	MWCNTs	15[b] 5-15 μm[c]	1-2wt.%	- max heat transfer improvement for CNT nanofluid with concentration of 2 wt.% - thermosyphon wall has lower temperature and more uniform temperature distribution along the device while working with nanofluid - ↑ in pressure leads to ↓ in HTC in evaporator - nanofluid does not affect heat transfer in condenser - influence of nanofluids increases with ↑ in heat flux

Reference	$d_i/L_{TS}/L_e/L_c$ (type of heater)	IA (α)	FR [%]	Water - based nanofluid	Concentration	Size [nm]	Comments and conclusions
Multiwall carbon nanotubes (MWCNTs) nanofluids - continued							
Shanbedi et al. (2012) [181]	20[a]/450/160/200 (electric heater)	90	60	MWCNTs + EDA (enediamine)	10-20[b] 5-15 μm[c]	0.2-1.5 wt.%	- max heat transfer improvement for CNT nanofluid with concentration of 1 wt.% - ↓ in the overall thermal resistance of the thermosyphon with ↑ in heat flux
Heris et al. (2016) [227]	18/450/160/200 (electric heater)	90	60	MWCNTs	-	1 wt.%	- nanofluid ↓ the mean temperature of the evaporator - ↓ in overall thermal resistance of the device with an ↑ in suspension stability caused by carboxylic groups added to the main structure

Table 3.2: A literature review on thermosyphon working with nanofluids based on oxides nanoparticles.

Reference	**$d_i/L_{TS}/L_e/L_c$ (type of heater)**	**IA (α)**	**FR [%]**	**Water - based nanofluid**	**Concentration**	**Size [nm]**	**Comments and conclusions**
Oxides: Al_2O_3							
Khandekar et al. (2008) [91]	16/620/120/300 (electric heater)	90	100	Al_2O_3 CuO laponite JS clay	40-47 9-14 25[b]	1 wt.%	- ↓ in thermal performance of TS compared with water - Al_2O_3 showed the best thermal performance from tested fluids - ↓ wettability for Al_2O_3 and laponite than for water - nanofluids boiling characteristics are affected by particle interactions with cavities; ↑ in thermal conductivity of working fluid has negligible effect
Noie et al. (2009) [141]	20/1000/350/400 (electric heater)	90	-	Al_2O_3	20	1-3 % vol.	- up to 14.7% ↑ in thermal performance than for water - ↓ of temperature level along the device with nanofluid
Mousa et al. (2011) [132]	6.37/300/100/100 (electric heater)	30-90	12	Al_2O_3	40	0.25- 1.2 % vol.	- the lowest overall thermal resistance of the thermosyphon for FR = 40-60% -↑ in concentration → ↓ in thermosyphon thermal resistance
Kamayar et al. (2013) [85]	19/280/100/140 (electric heater)	90	-	Al_2O_3 $TiSiO_4$	13 <50	0.01- 0.075 % vol.	- ↓ overall thermal resistance of the TS up to 65% for Al_2O_3 (0.05%vol.) and 57% for $TiSiO_4$ (0.0075%vol.) - nanofluids decrease evaporator wall temperature - ↓ thermal improvement for increasing heat flux - deposited nanoparticles layer affect boiling mechanism as a result of changed roughness and wettability
Oxides: SiO_2							
Yang and Liu (2011) [222]	8/550/100/350 (rectangular TS electric heater)	90	87.5	SiO_2 functionalized with silane CAS 2530-83-8	30	0.5-2.5 % wt.	- ↑ in nanofluid stability by covalent bonding Si-O-Si - functionalization inhibits particle deposition in the evaporator - functionalization enhances HTC but does not affect CHT - traditional nanofluid SiO_2 reduced HTC and increased CHF due to ↓ in contact angle - no effect on condenser

Reference	**$d_i/L_{TS}/L_e/L_c$ (type of heater)**	**IA (α)**	**FR [%]**	**Water - based nanofluid**	**Concentration**	**Size [nm]**	**Comments and conclusions**
Oxides: TiO_2							
Grab et al. (2014) [63]	108/1440/-/400 (electric heater at the bottom)	90	150ml	TiO_2 Au	85 16/66	0.2 and 1.1 vol.% 5.2e-4 vol.%	- ↑ or ↓ in overall thermal resistance of TS for TiO_2 nanofluid depending on working conditions - up to 20% ↓ in overall thermal resistance of TS at low heat flux for gold nanofluid - vapor may transport only tiny amount of particles, thus nanofluids have negligible effect on condenser - nanofluids undergo aging process during thermosyphon operation - Type, size and shape of nanoparticles affect the characteristics of deposition layer in evaporator - dimensions of thermosyphon in this study were significantly larger than in other publications
Buschmann and Franzke (2014) [32]	25/500/22/100 (electric heater at the bottom)	90	-	TiO_2 Au	42/85[d] 13[d]	0.1-0.4 vol.% 2.88e-4 vol.%	- up to 24% ↓ in overall thermal resistance for TiO_2 (0.2-0.3%) - the increase in thermal conductivity of the nanofluid compared to water is up to 1.03% (TiO_2, 0.4 vol.%) what is roughly within experimental error - up to 2.93% ↑ in viscosity (measurement error: 3%) - no significant changes in surface tension for concentrations below 5 vol.% - TS thermal performance is due to nanoparticles deposition altering bubble release behavior - aging process may lead to ↓ of positive effect, in particular for high concentrations. Thus, complex interplay between evaporator surface, aging process, nanofluids concentration must be considered.
Fe_2O_3							
Huminic and Huminic (2011) [74]	13.6/2000/850/850 (circulating water)	30-90	12	Fe_2O_3	4-5	2, 5.3 vol.%	- nanoparticles affect the solid-fluid interface → changes in thermal performance of the thermosyphon - ↑ in inclination angle leads to ↑ in heat transfer - ↑ in concentration → ↑ in heat transfer coefficient

Table 3.3: A literature rerview on thermosyphon working with nanofluids based on metals.

Reference	**$d_i/L_{TS}/L_e/L_c$ (type of heater)**	**IA (α)**	**FR [%]**	**Water - based nanofluid**	**Concentration**	**Size [nm]**	**Comments and conclusions**
Ag-based nanofluids							
Tong et al. (2015) [197]	16/110/45/65 (electric heater)	90	16.67	Ag_2O	30	1 vol.%	- uncoated (hydrophilic) and coated (hydrophobic) glass tube was used - coating reduces overall thermal performance up to 16.9% due to ↑ in rate of falling condensed droplets and formation of dropwise condensation - nanofluids ↓ in overall thermal resistance up to 35.2% (uncoated thermosyphon) and 47.7% (coated thermosyphon) - up to 6% ↓ in overall thermal resistance by high-acceleration vibration - the circulation of working fluid may be interrupted by droplets entrained from the liquid-vapor interface and elongated liquid jets
Parametthanuwat et al. (2010) [146]	7.5;11.1;25.4/ Le/di = 5;10;20 (circulating water)	90	30/50/80	Ag	< 100	0.5 wt.%	- no effect of FR on heat transfer; working fluid properties affect heat transfer - they proposed correlation for predicting heat flux in vertical position
Sarafraz et al. (2014) [178]	10.7/280/100/100 (electrical heater)	0-70	25-80	Ag	40-60	0.1-0.4 vol%	- nanofluids reduce temperature along the thermosyphon - ↓ in overall thermal resistance with ↑ in nanofluid concentration - ↓ in overall thermal resistance with ↑ in heat flux - device working with nanofluids faster gain steady-state conditions

Majority of research reported in tables 3.1 - 3.3 showed the increase in thermosyphon thermal capacity when base fluid (water) was replaced by nanofluids. Results suggest that the main improvement comes not from the enhanced thermal conductivity of the nanofluid itself, but mostly from the interplay between nanoparticles, evaporator surface, and bubble release. Understanding of the deposition layer buildup mechanism exceeds the current state of thermodynamics and fluid mechanics knowledge and requires further investigations. This explain the lack of proper theoretical and numerical models and why available experimental results are incoherent. Further research and higher amount of data is required for fully understanding the mechanisms behind the use of nanofluids in thermosyphons.

Few studies confirmed no effect of nanofluids on condenser [29, 63, 113, 222] and none of reviewed research showed that nanoparticles affect the heat transfer in condenser section. The overall thermal resistance of the thermosyphon (see eq. 3.3) in most cases decreased with the addition of nanoparticles, increase in heat load, or increment in operating pressure. The positive effect of using nanofluids seems to be reduced for high heat flux. Some authors found an optimum concentration of tested nanofluids. Nanofluids decreased the temperature level of the device (or evaporator) in comparison with pure base fluid. Some research group reported that thermosyphon filled with nanofluid may operate at higher heat loads without a dry-out than in case of water.

The presented literature survey indicates that there is a lack of studies comparing working fluid behavior under comparable operating conditions and in similar device geometry. Not every nanofluid used in available literature was well characterized and described. It applies also to the usage of surfactant/chemical additives with the aim of improving stability.

In addition to mentioned papers, there are various studies on the effect of applying magnetic or electrical field on the thermal capabilities of the device [62, 69, 70, 122]. Next to the heat exchanger prototypes [40, 161], thermosyphons are also investigated in solar systems [59, 79]. Another trend considers nanofluids based on various base fluids, e.g. glycols [176], methanol [124, 126] or acetone [13].

3.2 Boiling process

Fundamentals of boiling process

For a given working fluid, the leading mechanism of heat transfer depends on the heat load and surface overheating (the difference between the inner wall of the heater and saturation temperature of the working fluid). Figure 3.4 shows well-known boiling curve for water at atmospheric pressure. A small heat input is transported only through natural convection. Then, the first bubble is formed (point A) what starts nucleate boiling regime. Here, bubble nucleates and grows up to level enough for its detachment from the surface. At the initial stage of this process, bubbles collapse in the liquid. With a further increase in overheating, increased number of bubbles move to the free surface where they release their vapor content. This regime is supposed to be the most effective region of heat transfer. Critical heat flux (CHF) is reached when the heat flux exceeds its maximum value, and leads to the transition boiling called also unstable film boiling regime. The surface is alternately covered by a vapor phase and liquid. The vapor acts as an insulation what significantly lowers the heat transfer efficiency and causes a rapid increase in the surface temperature [93]. Heat flux decreases and overheating rises to the

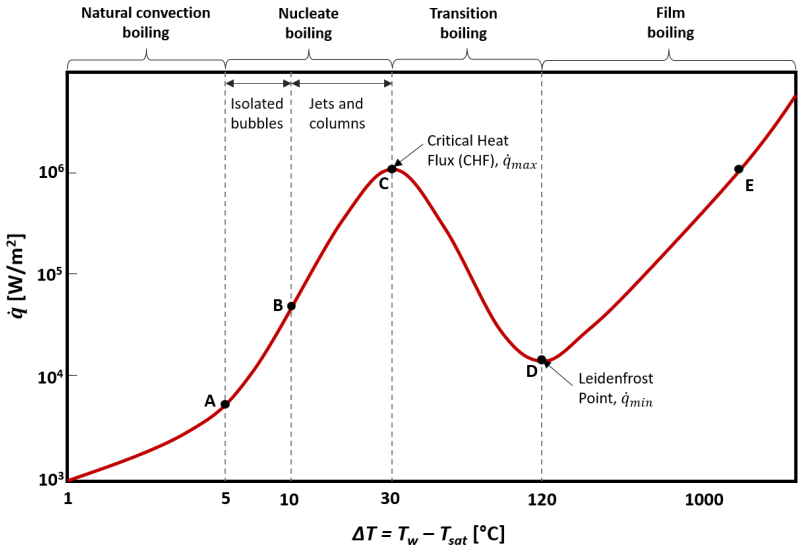

Figure 3.4: Pool boiling curve for water at atmospheric pressure [77, 130]

Leidenfrost point. From this point, film boiling begins. Vapor blankets over the heating surface with a continuous layer and no liquid is in contact with the wall [93, 108, 130].

Process of nucleate boiling consists of transitory sequences of nucleation, growth of bubble and its detachment. It takes place in natural pits and cavities on the surfaces, called nucleation sites. There are three stages attainable for cavities [15]:

- cavity is active when nucleation occurs.
- dormant cavity - nucleation is not currently developed but cavity contains the vapor that may nucleate.
- extinct or flooded when cavity does not include the vapor. Nucleation is possible only when overheating extends the value required for heterogeneous nucleation.

Activation of cavity depends on its size and shape, thermal boundary, temperature of the heater surface, surface energy, liquid surface tension and bulk pressure [107]. At the superheat enough for a quasi-steady regime of nucleate boiling, transportation of heat and mass ensues from the convection promoted by buoyancy, moving bubbles, evaporation and motion of the wetting line [15].

To improve process of heat transfer during boiling researchers attempt to [108]:

1. decrease of wall superheat and wall heat flux for the boiling onset (the point where boiling is initiated),
2. reduce or avoid the sharp temperature increment followed by sudden decrease, which sometimes occurs just before and after the boiling incipience,
3. reduce the wall superheat for boiling regime, mostly accomplished by activating a bigger number of nucleation sites and increasing bubble detachment frequency, decreasing diameter of departure bubbles, or increasing effective surface area,
4. shift critical heat flux (CHF) to higher heat flux values.

The above strategies extend the regime of effective boiling conditions (1, 2 and 4) or allow to transport more heat under the same working conditions (3).

Fundamental effectiveness indicators of boiling heat transfer are critical heat flux (CHF) and heat transfer coefficient (HTC) used interchangeably with the thermal resistance (R).

One of most common correlations for predicting boiling heat transfer of liquid was proposed by Rohsenow [167]:

$$\frac{C_p(T_w - T_{sat})}{\Delta h} = C_{sf}\left[\frac{q''}{\mu\Delta h}\sqrt{\frac{\sigma}{g(\rho_l - \rho_v)}}\right]^r \left(\frac{C_p\mu}{k}\right)^s \tag{3.4}$$

Where: C_p is specific heat of liquid, Δh the latent heat of vaporization, T_{sat} saturation temperature, T_w temperature of heater wall, q'' hest flux, μ viscosity of saturated liquid, σ surface tension, ρ_l and ρ_v density of saturated liquid and vapor, respectively, g acceleration of gravity, k liquid thermal conductivity. C_{sf}, r and s are empirical values. They are determined in the literature for well investigated fluids, such as for pure water on a relatively smooth surface: $s = 1.7$, $r = 0.33$ and C_{sf} in the range of $0.0065 - 0.05$ [136, 193].

Parameter C_{sf} in Rohsenow correlation covers many important phenomena [193]. It includes thermophysical properties of liquid but also interaction between liquid, vapor and solid at the heating surface. For nanofluids additional solid nanoparticles are present at the surface and interactions become even more complex. Roughness and condition of heating surface also play important role in heat transfer process. Stil, it needs to be determined which value of surface roughness (averaged, spacing, extreme or some combinations) is the most demonstrative. Contact angle and wettability are also connected with the geometry. All this translates into lack of simple equation to describe C_{sf}. With the current state of knowledge, it can be determined only empirically. Thus, it is understood as a constant describing all the interaction behind the heat transfer at the heating surface [193]. For nanofluids that tend to make layers on the heating surface this constant become even more complex.

Another universal correlations for calculation of heat transfer coefficient during boiling include [79]:

- Imura et al. [76]:

$$h_e = 0.32\left(\frac{\rho_l^{0.65}k_l^{0.3}C_{pl}^{0.7}g^{0.2}}{\rho_v^{0.25}\Delta h^{0.4}\mu_l^{0.1}}\right)\left(\frac{p_v}{p_{atm}}\right)^{0.3} q^{0.4} \tag{3.5}$$

- Kutateladze [168] in [79]:

$$h_e = 0.44Pr^{0.35}\left(\frac{k_l}{L_b}\right)\left(\frac{\rho_l}{\rho_l - \rho_v}\frac{qp\cdot 10^{-4}}{\rho_v g\Delta h\mu_l}\right)^{0.7} \tag{3.6}$$

- Shiraishi [182]:

$$h_e = 0.32\left(\frac{\rho_l^{0.65}k_l^{0.3}C_{pl}^{0.7}g^{0.2}}{\rho_v^{0.25}\Delta h^{0.4}\mu_l^{0.1}}\right)\left(\frac{p_v}{p_{atm}}\right)^{0.23} q^{0.4} \tag{3.7}$$

- El-Genk and Saber [49]:

$$h_e = \Psi(1+4.95)0.44\left(\frac{k_l}{L_b}\right)\left(\frac{10^{-4}qP}{g\rho_v\Delta h\mu_l}\frac{\rho_l}{\rho_l-\rho_v}\right)^{0.7} Pr_l^{0.35} \tag{3.8}$$

Where:

$$\Psi = \left(\frac{\rho_v}{\rho_l}\right)^{0.4}\left[\frac{p_v\nu_l}{\sigma}\left(\frac{\rho_l^2}{\sigma g(\rho_l-\rho_v)}\right)^{0.25}\right]^{0.25} \tag{3.9}$$

The second important parameter - critical heat flux (CHF) describes the thermal limit of the boiling phenomenon. The available studies confirm that nanofluids enhance CHF values, even up to 200% [20, 56, 97, 195, 200]. One of the most common explanation for the enhanced CHF [195] of nanofluids is so-called capillary wicking. Deposition of nanoparticles into porous layers on the heater surface affects heat transfer processes. As a result, liquid is transported through the hydrophilic pores and re-wets the surface underneath the growing bubble preventing growth of dry spots.

Group of Tetreault-Friend et al. [195] hypothesized that two heat transfer regions are formed in the porous layer during the bubble growth: the wicking-dominated and the conduction-dominated areas (see Fig. 3.5). Conduction dominates near the heater surface, while advection owing to the capillary wicking influences heat transfer close to the top layer-liquid interface. If temperature of the fluid being in contact with wall exceeds the local saturation temperature resulting from the capillary pressure in the pores, the vapor is generated at the bottom of layers. This inhibits wicking and leads to CHF. Thus, CHF value is determined by rivaling outcomes of liquid viscous pressure drop, capillary pressure and change of momentum by cause of evaporation [195].

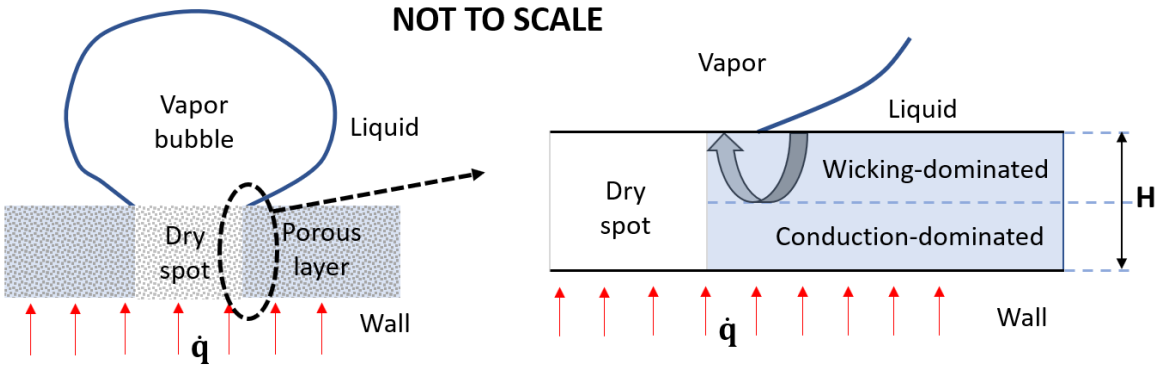

Figure 3.5: Heat transfer during bubble growth on the porous layer [195].

Jothi Prakash and Prasanth [80] concluded that both - surface characteristics (including roughness, micro-cavities, contact angle, nucleation site density, surface energy), and working fluid properties (density, viscosity, thermal conductivity, surface tension, and specific heat) improve boiling heat transfer process and CHF. Kamel et al. [84] discussed the latest studies on CHF enhancement by nanofluids. They extracted followinf factors as crucial for the CHF: thermophysical properties of base fluids and nanofluids, nanoparticles morphology (type, size, etc.), concentration of nanoparticles, heating surface characteristics (type, roughness, etc.), the capillary wicking forces, re-wetting phenomena, and operation conditions (pressure, mass flux, sub-cooling temperature).

Pool boiling of nanofluids

Experimental studies on boiling of nanofluid are summarized in Table 3.4. Acronyms used in Table 3.4 are summarized below.

Acronym	Meaning
BA	boric acid
CMC	carboxy methyl cellulose
CNT	carbon nanotubes
fCNT	functionalized carbon nanotubes
GO	graphene oxide
ITO	indium tin oxide
PVA	polyvinyl alcohol
PVP	polyvinylpyrrolidone
rGO	reduced graphene oxide
SDBS	sodium dodecylbenzenesulfonate
SDS	sodium dodecyl sulfate
SLS	sodium lauryl sulfate

Table 3.4: A literature review on pool boiling of water-based nanofluids

Reference (Publication year)	**Nanoparticles**	**Concentration**	**Size [nm]**	**Type of heater**	**Surface analysis**	**Effect on heat transfer coefficient (HTC)**	**Effect on critical heat flux (CHF)**
Yang and Maa [224] (1994)	Al_2O_3	0.1-0.5 wt.%	50, 300, 1000	Horizontal tube	-	Enhancement	-
Das et al. [46] (2003)	Al_2O_3	0.1, 1, 2, 4 wt.%	38	Cylindrical cartridge	SEM	Deterioration	-
You et al. [225] (2003)	Al_2O_3	0.001 - 0.05 g/L	-	Cylindrical cartridge	-	No effect	200% enhancement
Vassalo et al. [202] (2004)	SiO_2	0.5 vol.%	15,50,3000	NiCr wire	Eyes	No effect	50 nm: 200% enhancement
Bang and Chang [19] (2005)	Al_2O_3	0.5 - 4 vol.%	10 - 100 (average: 47)	Square flat heater	Roughness	Deterioration	up to 32% enhancement
Wen and Ding [213] (2005)	Al_2O_3	0.32 - 1.25 wt.%	10 - 50 (measured in suspension: 90-450)	Flat disc heater	-	Up to 40% enhancement for 1.25%	-
Kim et al. [94] (2006)	Al_2O_3 TiO_2	10^{-5} - 0.1 vol.%	47 85	NiCr wire NiCr/Ti wire	SEM	-	Up to 200% enhancement
Kim et al. [97] (2007)	Al_2O_3 SiO_2 ZrO_2	0.001 - 0.1 vol.%	110 - 210 20 - 40 110 - 250	Stainless steel wire and flat plate heater	SEM	Deterioration	Enhancement
Liu et al. [111] (2007)	CuO	0.1 - 2 wt.%	30	Flat horizontal pipe with micro-grooved heating surface	AFM	Enhancement: 25% at 100 kPa and 150% at 7.4 kPa	Enhancement: 50% at 100 kPa and 200% at 7.4 kPa
Chopkar et al. [39] (2008)	ZrO_2	0.005 - 0.15 vol.% (+ optional 1.0 vol.% tetramethyl ammonium hydroxide)	20-25	Flat surface	Roughness profile	Enhancement for low concentration; additional increase with surfactant	-
Liu and Liao [110] (2008)	SiO_2 CuO	0.2 - 2 wt.% (+ 0.5 wt.% SDBS surfactant)	35 50	Flat horizontal copper surface	SEM and AFM	No effect/ slightly reduced	Enhancement
Soltani et al. [188] (2009)	Al_2O_3 SnO_2	0.3 - 2 wt.% 0.5 - 2 wt.%	20 - 30 55	Vertical cylindrical glass vessel	-	Enhancement with increase in concentration, except for small concentrations	-

Reference (Publication year)	**Nanoparticles**	**Concentration**	**Size [nm]**	**Type of heater**	**Surface analysis**	**Effect on heat transfer coefficient (HTC)**	**Effect on critical heat flux (CHF)**
Golubovic et al. [61] (2009)	Al_2O_3 BiO_2	0.001 - 0.1 g/l	23, 46 38	NiCr wire Vertical cartridge heater	SEM	-	Enhancement up to 50% (Al_2O_3) and 33% (BiO_2)
Park et al. [147] (2009)	CNT	0.0001 - 0.5 vol.% + PVP polymer (3:1 wt. ratio to CNT)	⌀10 - 20; length of 10000 - 50000	Flat surface	SEM	Deterioration up to 38.2%	Enhancement up to 200% for 0.001 vol.%
Liu et al. [114] (2010)	CNT	0.5 - 4 wt.%	⌀15; length of 5000 - 15000	Vertical cartridge	TEM	Enhancement up to 38.2%	Enhancement up to 60% at atmospheric pressure and 200% at 7.4 kPa
Kathiravan et al. [88] (2010)	Cu	0.25 - 1 wt.% with/without 9 wt.% SLS	10	Plate heater	AFM	Deterioration	Enhancement up to 48% for 1 wt.%. 80% deterioration for SLS solution
Kwark et al. [102] (2010)	Al_2O_3 CuO Diamond	0.025 - 1 g/l	139±100 143±80 86±50	Cartridge heater	SEM	No effect/ deterioration	Enhancement up to 80%
Truong et al. [198] (2010)	Al_2O_3 ZnO Diamond	0.1 vol.% 0.1 vol.% 0.01 vol.%	42 75 143	Bare and sandblasted horizontal plate	SEM, EDS spectra, confocal microscopy, contact angle	-	Enhancement up to 35% for ZnO and Al_2O_3, 11% for diamond compared to bare heater
Soltani et al. [189] (2010)	Al_2O_3	0.8 - 1.4 wt.% + 0.2 - 1.0 wt.% CMC	20 - 30	Vertical cylindrical glass vessel	-	Enhancement up to 25% for 1.4 wt.%	-
Stutz et al. [190] (2011)	Fe_2O_3	1 g/l	10	Platinum wire	SEM, AFM	Enhancement for boiling time shorter than 30 minutes, then deterioration	Enhancement up to 40% depending on boiling duration
Wen et al. [212] (2011)	Al_2O_3	0.001 - 0.1 vol.%	20 - 150 (SEM) 50 - 900 (DLS)	Plate surface	SEM, AFM	Enhancement up to 200% for smooth surface, no effect for rough one	-
Yang and Liu [223] (2011)	SiO_2 functionalized	0.5 - 2.5 wt.%	30	Vertical cartridge	SEM	Enhancement up to 27% for 7.4 kPa	No effect

Reference (Publication year)	**Nanoparticles**	**Concentration**	**Size [nm]**	**Type of heater**	**Surface analysis**	**Effect on heat transfer coefficient (HTC)**	**Effect on critical heat flux (CHF)**
Kathiravan et al. [90] (2011)	CNT	0.25 - 1 vol.% with/without 9 vol.% SLS	⊘ 10 - 15	Plate heater	-	Enhancement up to 200% for 1 vol.% nanofluid without surfactant	Enhancement up to 70% for 0.5 vol.% nanofluid with SLS
Cieslinski and Kaczmarczyk [41] (2011)	Al_2O_3 Cu	0.01 - 1 wt.%	5-250 (47 mean) 57-257 (48 mean)	Copper and stainless steel tube	-	Enhancement for stainless steel tube and deterioration for copper tube	-
Hedge et al. [68] (2012)	CuO	0.01 - 0.5 vol.%	10 - 100	NiCr wire	SEM, TEM	-	Enhancement up to 130%
Pham et al. [153] (2012)	Al_2O_3 Al_2O_3 + CNT CNT	0.05 vol.% 0.05 vol.% + 0.05 vol.% 0.05 vol.%+ 10 vol.% BA	-	Plate heater	SEM, roughness, CA, EDS	-	33% enhancement 122% enhancement 108% enhancement
Sakashita [173] (2012)	TiO_2	0.0011 wt.% + 0.010 wt.% SDS	25	Copper block and auxiliary heaters	SEM	-	Enhancement up to 140%
Lee et al. [105] (2012)	Al_2O_3 Fe_3O_4 TiO_2	10^{-4} - 0.01 vol.%	40 - 80 25 15	NiCr wire	SEM	Enhancement	Enhancement up to 80%
Jung et al. [82] (2012)	Al_2O_3	10^{-5} - 0.1 vol.% ± 10^{-5} - 0.1 vol.% PVA	45 (DLS: 300)	Plate heater	AFM	Deterioration	Enhancement up to 220%
Mourgues et al. [131] (2013)	ZnO	0.01 vol.%	-	Cartridge (sample in vertical/horizontal position)	Photos	Enhancement/ deterioration	Enhancement up to 73%
Shoghl and Bahrami [183] (2013)	CuO ZnO	0.01 - 0.02 wt.% +0.01 - 0.02 wt.% SDS	-	Rod heater	AFM, SEM	Deterioration / enhancement by adding SDS	-
Vazquez and Kumar [203] (2013)	SiO_2	0.2 - 2 vol.%	10	NiCr wire	SEM	-	Enhancement up to 270%
Amiri et al. [11] (2014)	CNT CNT-Cysteine CNT-Ag	0.01 - 0.1 wt.%	⊘ max 60; max length 15000	Plate heater	SEM	Enhancement for covalent nanofluid, deterioration for non-covalent (CNT)	Enhancement up to 300%

Reference (Publication year)	**Nanoparticles**	**Concentration**	**Size [nm]**	**Type of heater**	**Surface analysis**	**Effect on heat transfer coefficient (HTC)**	**Effect on critical heat flux (CHF)**
Vafaei [200] (2014)	Al_2O_3	0.001 - 0.1 vol.%	20-150	Cartridge heater	SEM, AFM	Enhancement/ deterioration depending on cavity size, wettability and heat flux	-
Sarafraz and Hormozi [?] (2015)	CuO	0.1 - 0.4 wt.% + 0.1 wt.% SDS/ SDBS/ Triton X-100	45-50	Cylindrical plate with bolt heater	SEM	Enhancement with surfactant; deterioration without surfactant	-
Cieslinski et al. [42] (2015)	Al_2O_3 Cu	0.01 - 1 wt.%	5-250 (47 mean) 7-257 (48 mean)	Stainless-steel tube	SEM	Enhancement for smooth tubes, deterioration for porous-coated tubes	-
Kamatchi et al. [83] (2015)	rGO	0.1 - 0.3 g/l	322 (mean hydrodynamical size)	NiCr wire	SEM	-	Enhancement up to 245%
Sakashita [174] (2016)	TiO_2	0.002 wt.%	25	Cartridge heater	Photos	-	Enhancement up to 200% at 0.1 MPa
Sarafraz et al. [179] (2016)	CNT fCNT	00.1 - 0.3 wt.%	⌀15-20; length 1500-2000	Cartridge heater with disc surface	SEM	Enhancement up to 35% (fCNT), deterioration up to 13% (CNT)	Enhancement up to 31%
Ali et al. [8] (2017)	TiO_2	12 wt.%, 15 wt.%	5-30	Cartridge heaters	-	Enhancement up to 138%	-
Karimzadehkhouei et al. [86] (2017)	TiO_2 CuO	0.001 - 0.2 wt.%	340±40 (one particle: 20-50) 350±50 (one particle: 10-20)	Cartridge heater	-	Enhancement up to 15% Enhancement up to 35%	-
Salari et al. [175] (2017)	Fe_2O_3	0.1 - 0.3 wt.% + 0.15 vol.% nanolphenol ethoxylate	20	Cartridge heater with disc surface	Microscopy images	Enhancement up to 29%	Enhancement up to 30%
Ciloglu [43] (2017)	SiO_2	0.01 - 0.1 vol.%	50-934 (414 mean, dry particle: 20)	Hemispherical copper block with a ring heater	AFM	Deterioration	Enhancement up to 45%
Dadjoo et al. [44] (2017)	SiO_2	0.001 - 0.01 vol.%	7-14	Cartridge heaters in cylindrical copper block	AFM	Enhancement up to 125%	Enhancement up to 111%

Reference (Publication year)	**Nanoparticles**	**Concentration**	**Size [nm]**	**Type of heater**	**Surface analysis**	**Effect on heat transfer coefficient (HTC)**	**Effect on critical heat flux (CHF)**
Manetti et al. [119] (2017)	Al_2O_3	0.0007 - 0.007 vol.%	10	Cartridge heater in copper block	SEM	Enhancement up to 75% and 15% for smooth and rough surface, respectively	-
Karthikeyan et al. [87] (2018)	fCNT	80 ppm + 500/800 ppm of SDS	-	Cartridge heater in brass-copper block	SEM	Enhancement/ deterioration depending on nanofluid stability	-
Watanabe et al. [210] (2018)	TiO_2 Al_2O_3 SiO_2	1.5 g/l	21 13 20 (DLS: 800)	Cartridge heater in copper block	Images	Enhancement/ deterioration depending on boiling time	Enhancement up to 58%
Rostamian and Etesami [169] (2018)	SiO_2	0.005 - 0.1 vol.%	7-14	Cartridge heater in copper block	Roughness	Enhancement for concentrations below 0.01 vol.%	Enhancement
Kouloulias et al. [99] (2018)	Al_2O_3	0.0012- 0.0024 vol.%	-	NiCr wire	SEM	Visualization only	-
Mori et al. [129] (2018)	TiO_2	0.1 vol.%	21 (DLS: 200)	ITO heater in copper block	-	-	Enhancement up to 100%
Wang et al. [204] (2018)	SiO_2	0.05 - 0.15 wt.%	20	ITO heater on glass surface	SEM	Increased bubble departure frequency by moderately hydrophilic nanoparticles	-
Kim et al. [95] (2018)	rGO	0.0005 vol.%	Thickness: 0.7 length 1000	Micro-pillar arrays covered by graphene	SEM	Enhanced for low-level graphene coating	No effect for low-level graphene coating; deteriorated for thick graphene coating

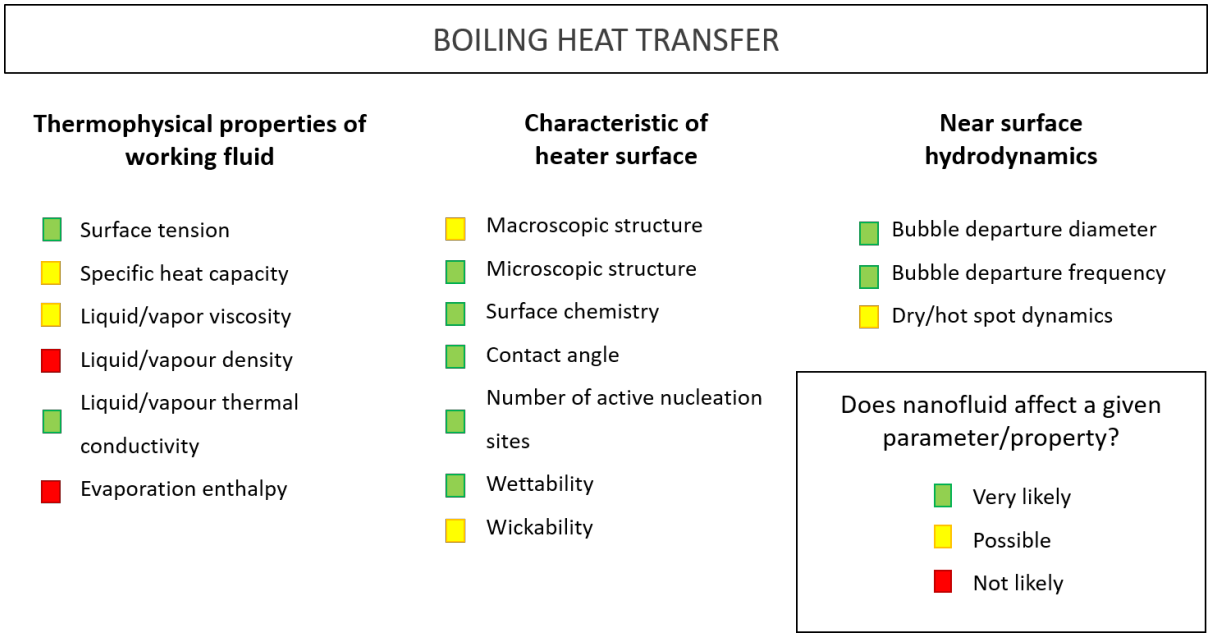

Figure 3.6: Various ways in which nanofluids affect parameters influencing boiling heat transfer

The boiling process, and thus boiling heat transfer coefficient, depends on a multitude of parameters summarized in Fig. 3.6. Together with a diversity of used nanoparticles and their poor characterization, they causes a strong inconsistency of the results published in the literature. Most of reported papers hold the view that nanofluids increase the heat transfer coefficient (e.g. [114, 148, 213, 214]). Enhancement is explained by: reduction of thermal resistance caused by particles deposition or modification of cavities sizes [53]. Decreased number of active nucleation sites and reduced capillary wicking due to fouling formation of nanoparticles are reported to deteriorate HTC [53, 179].

Nanoporous layer deposited on the heater surface affects not only the surface roughness but also the density of active nucleation sites, wettability, liquid spreadability, surface chemistry, and structure [56, 107, 127, 195, 200]. The surface roughness influences surface wettability and the other way around. With decrease in wettability, the possibility of cavity flooding decreases. Probability of nucleation sites activation is higher when both fluid and vapor are in contact with the heating surface, thus it improves heterogeneous nucleation process [15]. Nucleation site density, porosity, wettability and roughness interact strongly and depend on each other. Nano-deposition alters also surface chemistry and structure that leads to modifications in the force balance at the triple line. All mentioned factors have a crucial impact on characteristics of boiling heat transfer process [56, 200].

The following conclusions can be drawn from the presented analysis:

- The most commonly investigated nanofluids in boiling experiments are metal oxides, in particular Al_2O_3. Recently, carbon-based nanofluids (e.g. carbon nanotubes or graphene) and hybrid particles gained increasing attention.

- Addition of nanoparticles enhances (even up to 200%), decreases or does not affect boiling heat transfer coefficient. 61% of the reviewed papers reported increase in HTC, 30% decrease, and 9% no effect. Results depended on working conditions, used nanofluid, stabilization, and experimental procedures. However, there is no

clear conclusion which parameters are directly responsible for such a big difference in results.

- Despite of conflicting results on boiling heat transfer coefficient, critical heat flux (CHF) is enhanced by replacing water with water-based nanofluids. Only 6% of studies showed no effect of nanoparticles on CHF. The highest increase was 270% for CNT nanofluid [11]. The CHF improvement is associated to the nanoparticles deposition on the heater wall, rather than changed nanofluid properties itself.

- There is still a need for more systematic and comprehensive studies on pool boiling of nanofluids and mechanisms responsible for noticed effects. It should include proper sample preparation and characterization of key properties, investigation of the stabilizer effect and well-planned long-term experiments that gives repeatable results and allows for further drawing conclusions.

- Only few studies analyze the effect of surfactant addition. Many research groups do not mention whether they use or not any stabilizers. Available research shows (e.g. [136, 218]) that addition of surfactant to nanofluid may significantly alter the results.

- Researchers should consider additional concerns, such as possibility of clustering and sedimentation of nanoparticles, erosion of heating surfaces, time-dependent performance, costs analysis, possibility of large-scale production and influence on human beings and the ecology. After solving these problems, nanofluids have a chance to become reliable and high-effective working fluids.

Boiling regimes in thermosyphons

Two-phase flow regimes occurring in a thermosyphon and heat transfer capabilities of the device are complementary and depend on each other. This section analyzes possible co-current flow patterns inside a thermosyphon. It will help to understand and explain the trends observed in experimental results.

Flow of liquid and vapor in the thermosyphon interact continuously. Even small changes in working conditions may lead to flow disruptions due to lack of external pumping forces. Visualization conducted using a reflux transparent thermosyphon of 8 mm in diameter and 500 mm in length showed analogy of flow patterns inside the thermosyphon with a flow boiling in vertical channels. Observed flow patterns were divided into four regimes:

- slug/plug flow,

- bubble flow,

- churn flow, and

- geyser flow.

For low pressure and heat loads water operated in geyser boiling regime [186, 185].

Geyser boiling (or geysering) is a boiling regime of thermosyphon and its scheme is presented in Fig. 3.7. During this phenomenon four main phases may be highlighted:

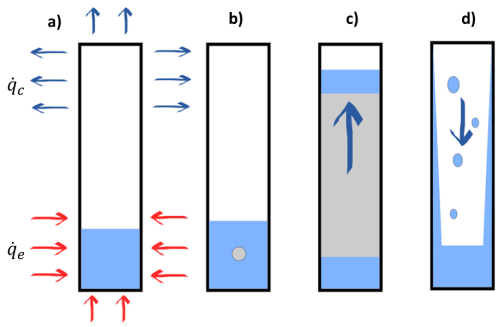

Figure 3.7: Consecutive phases of geyser boiling

- heat is supplied to the evaporator and stored within the working fluid, the superheat between the evaporator wall and liquid pool increases (a),
- bubble nucleation and its rapid growth to the size of pipe diameter due to evaporation from the surrounding liquid film. It may enhance heat transfer due to movement of bulk liquid what translates into a decrease in the pool temperature (b),
- *geyser event*: bubble expansion that pushes the fluid trapped above into the condenser (c). The large difference between the vapor pressures inside the bubble and in the condenser section forces the high speed of the liquid,
- return of the propelled liquid (d).

Afterwards, there is a quiet period again until the fluid pool temperature reaches the superheat required to nucleate another bubble. The phenomenon occurs mostly at low pressures due to rapid increase of vapor density and specific volume resulting from decreasing pressure, for large filling ratios, or during start-ups [35, 92, 109, 186, 215].

Visualization of this phenomenon captured in a transparent thermosyphon for water is presented in Fig. 3.8. Smith et al. [186, 185] confirmed that the working fluid gathered above the growing bubble can be pushed even up to the top of thermosyphon with a high speed. At the same time, significant pressure peak was noticed in measured signal. Then, the system came back to the initial conditions and the cycle started again. For a given heat load, intensified vapor production resulted in large bubbles that grew faster. Once the Taylor-type bubble was formed, strong evaporation of surrounding fluid occurred. Vapor was produced with a high rate as a result of significant difference between the liquid and vapor density. The boiling conditions become more unsteady and explosive what resulted in a geysering regime.

At higher pressure and for low heat fluxes, observed geyser boiling regime turned into slug/plug flow. Bubbles could still grow and coalesce to Taylor-like shapes at superheated liquid pool. Occasionally, small amounts of liquid in form of *liquid bridges* was pushed upwards but did not reach the condenser. The expelled liquid was so thin that returned to the evaporator pool together with a condensate film on the thermosyphon wall. It translated into much steadier operating thus no pressure peaks were noticed for this regime [186].

Changing water to the working fluids characterized by lower surface tension inhibited geysering and led to different boiling regimes[186]. It highlights the significance of

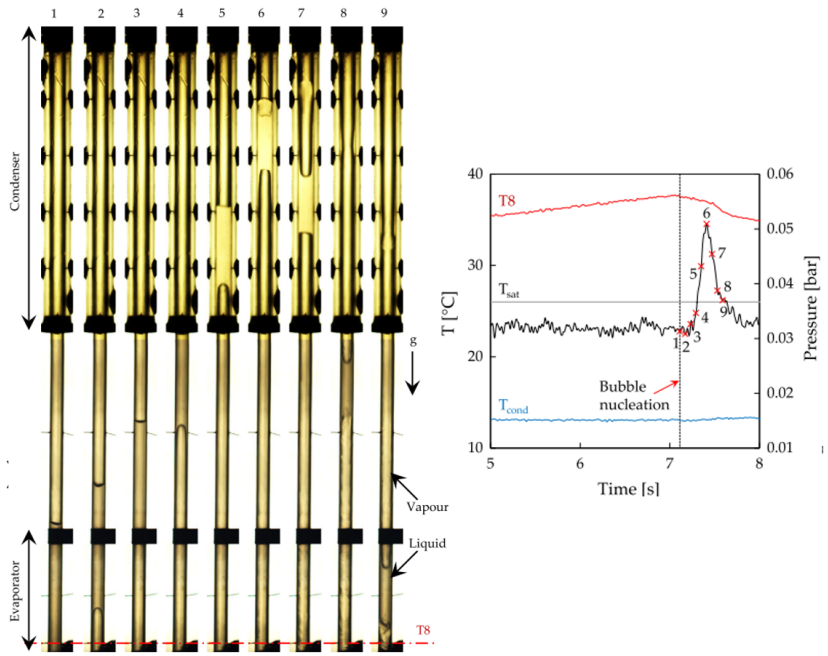

Figure 3.8: Visualization of geyser boiling in a transparent thermosyphon with water: high speed images (left), temperature and pressure signals (right) [186]

proper selection of working fluid. To the best author's knowledge, there is no analogous visualization available for nanofluids used as working fluids in the thermosyphon. It was only possible to look for similarities based on working fluid properties, pressure, and temperature measurements.

Geyser boiling

Detection of geyser boiling requires high resolution and continuous pressure measurements, thus the phenomenon often remains unrecognized. There is limited number of studies on that topic and their summary are shown in Table 3.5. It compares details of tested devices, including information of characteristic parameters, such as filling ratio (volume of working fluid to the volume of evaporator section), inclination angle (the angle formed by the x-axis and thermosyphon symmetry line in the length direction), and tested parameters.

Table 3.5: A summary of previous research on geyser boiling

Reference	**Type of device**	**Dimensions [mm]**	**Length/ diameter ratio**	**Heat flux Q[W]**	**Working fluid**	**Filling ratio [%]**	**Inclination angle [°]**	**Changing parameters**
Morgan and Brandy, 1962 [128]	missiles (two feed lines attached to the bottom of the tank)	d = 178 L = 60200	34	N/A	Liquid oxygen	N/A	90	- inert gas (helium) injection; - subcooled topping; - external recirculation lines.
Murphy, 1964 [133]	Aluminum/pyrex vertical tubes (missile suction line)	d = 102,152,203,330 L = 610-8534	1.5-30	30.8-53000	water, R113, nitrogen, hydrogen	N/A	90	- system geometry - working fluids - heating rate
Burkhalter et al., 1968 [27]	transparent (missile suction line)	d = 30,64 L = 378,756,1216	12.5-25	28-1870	water	N/A	90	- system geometry - heating rate - temperature of fluid in reservoir
Ozawa et al., 1979 [144]	forced flow boiling vertical system (heating: electrical)	di = 18.3; do = 21.5; L = 914.4; Le = 1000-3000; La = 600-2600	197	70 - 690	water, methanol	7-83	90	- heat load; - pipe diameter; - filling ratio; - pressure
Fukano et al., 1983 [57]	Copper thermosyphon (cooling: water, heating: electrical)	di = 9.53;20.9 do = 13.7; 26.7 L = 914.4; Le = 457.2; Lc = 152.4	44,96	340 - 2270	water, methanol	7-83	90	- heat load; - pipe diameter; - filling ratio; - pressure
Negishi, 1983 [140]	copper and glass thermosyphon (cooling: water, heating: water)	do = 15; di = 13 L = 330; Le = 150 Lc = 150	25	15 - 75	water, ethanol	5 - 100	10 - 90	- inclination angle - filling ratio - working fluid - material of thermosyphon
Casarosa, 1983 [35]	brass and glass thermosyphons (cooling: water, heating: electrical)	di = 42; L = 870 Le = 73; Lc = 305	21	19 - 144	water	above 112	90	- heat flux; - pressure
Negishi, 1984 [139]	glass thermosyphon (cooling: water, heating: electrical)	do = 24.8; di = 22 L = 1010; Le = 500 Lc = 500	46	25	water	30	90	- observation of temperatures for geyser boiling conditions

Reference	**Type of device**	**Dimensions [mm]**	**Length/ diameter ratio**	**Heat flux Q[W]**	**Working fluid**	**Filling ratio [%]**	**Inclination angle [°]**	**Changing parameters**
Lin, 1994 [109]	transparent thermosyphon (cooling: water, heating: electrical)	do = 32; di = 29.6 L = 550; Lc = 310 Le = 140/190	19	6 - 66	water, ethanol	30 - 140	90	- cooling medium temperature - filling ratio - heat load
Kuncoro, 1995 [101]	glass thermosyphon (cooling: water, heating: electrical)	Evap: Le = 1507 do = 22; di = 18 Cond: Lc = 600 do = 58; di = 50 Adiab: La = 150 di = 18-50	125	19 - 165	water, R113	100	90	- heat flux - working fluid - pressure
Noie, 2007 [142]	copper thermosyphon (cooling: water, heating: electrical)	do = 16; di = 14.5 L = 1000; Le = 410 Lc = 430	69	50	water	15, 22, 30	5 - 90	- filling ratio; - inclination angle
Emami, 2009 [50]	copper thermosyphon (cooling: water, heating: electrical)	do = 16/22/26 di = 14/20/24 L = 1000; Le = 410 Lc = 430	45 - 83	50 - 312	water	15 - 45	5 - 90	- filling ratio - inclination angle - pipe diameters - heat input - coolant mass flow rate
Khazaee, 2010 [92]	copper thermosyphon (cooling: water, heating: electrical)	do = 17/27 di = 15/25 L = 1000; Le = 430 Lc = 410	40 - 67	100 - 200	water	30 - 100	90	- filling ratio - pipe diameters - heat input - coolant mass flow rate
Chen et al. [36]	stainless 304SS, heated vertical channel (heating: electrical)	do = 38; di = 32 L = 1750/2650 4heaters: Le = 400 de = 100	55,83	1000 - 4000	water	12.5 - 87.5	90	- heat flux - geometry - temp of working fluid - coolant inventory
Agunlejika et al., 2016 [3]	horizontal thermosyphon reboiler (heating: steam flow)	Riser: do = 51 L = 1619 Reboiler: do = 30.5 16 steam-heaters: Ao = 0.6094m^2	N/A	3.7 - 12.2	water	N/A	0	- steam pressure - heat flux - valve position - static liquid head

Reference	**Type of device**	**Dimensions [mm]**	**Length/ diameter ratio**	**Heat flux Q[W]**	**Working fluid**	**Filling ratio [%]**	**Inclination angle [°]**	**Changing parameters**
Xia, 2017 [221]	flat thermosyphon (cooling: water, heating: copper rod)	flat evap and con: do = 100; di = 90 Le = 40 La = 60	N/A	830 - 5900	water, ethanol, acetone	10 - 90	0	- filling ratio - heat flux - temperature of cooling water - working fluid
Tecchio, 2017 [194]	Loop thermosyphon: two parallel condensers and a shared evaporator (heating: electrical)	Lc = 320 and 650 Le = 550 (horizontal); de = 68 (partially filled evaporator)	N/A	100 - 850	water	50 - 90	90	- filling ratio - heat load - working fluid
Jafari, 2017 [78]	Copper thermosyphon (cooling: water, heating: thermofoil heater)	do = 35; di = 33 L = 500; Le = 75 Lc = 150	15	30 - 700	water	16, 35, 135	90	- experimental and numerical work - heat load - filling ratio
Alammar et al., 2018 [7, 6]	Copper thermosyphon without adiabatic section (cooling: water, heating: electrical)	do = 22; di = 20.2 L = 400; Le = 200	20	20 - 400	water	25,65,100	90	- heat load - filling ratio - inclination angle; - coolant inlet temperature - coolant mass flow rate
Wang, 2018 [208]	Glass thermosyphon (cooling: water, heating: water)	do = 18; di = 15 L = 500; Le = 160 Lc = 180	33	10 - 120	water	75	90	- CFD simulations - visual observations
Smith, 2018 [186, 185]	Sapphire thermosyphon (cooling: water, heating: electrical)	do = 8; di = 10 L = 500; Le = 100 Lc = 200	62.5	17 - 160	water, ethanol, HFE - 700	50 - 100	90	- working fluid - filling ratio - heat load - visualization

Morgan and Brandy (1962) [128] published one of the first papers on the geysering effect in vertical pipes, defining it as an ejection of liquid by the release of vapor. They found that the phenomenon depends on the reduced pressure boiling and the ability of the system to release vapor, thus processes of liquid heating, bubble formation and its further behavior must be considered. They recognized three regimes of boiling. The first one is characterized by relatively low bubble population and little mutual interference. Then, these interferences between bubbles start and lead to liquid circulation. Lower and smaller bubble tends to flow faster in the wake of the above bubble (the wake effect) and joins it. It creates a vapor 'slow-moving mass' or the large cylindrical (Taylor) bubbles. Merged bubble acts as a barrier for normal escape of vapor what translates into the geyser boiling. Morgan and Brandy [128] proposed and analyzed several possibilities to avoid the geysering, among others inert gas helium injection and external or internal recirculation lines.

Murphy (1964) [133] proposed a correlation allowing for the determination of geyser and non-geyser conditions. It was later shown [27, 101] that this approach works for a very small number of applications because it does not include dependency of the heat input.

Burkhalter et al. (1968) [27] experimentally investigated geysering in transparent vertical tubes. They draw a conclusion that there is a certain total energy that may be released in a geysering regime. Thus, for high heat loads, the energy is transferred by both boiling and geysering. For smallest heat flux, they found only Taylor bubbles without geysering.

Ozawa et al. (1979) [144] tested vertical forced flow boiling system. They found out that the period and amplitude of geysering increases with heat flux density and decreases with inlet velocity. Higher amplitudes are also related to the greater heated length.

Negishi and Sawada (1983) [140] studied the inclination and the filling ratio effects of two working fluids (water and ethanol) on the heat transfer performance in thermosyphon. Heating and cooling of the evaporator and the condenser were carried out by water cycles what allows for a self-adjustment of the system. They found that for filling ratios below 5% there was no liquid pool and the main mechanism was liquid droplets evaporation. Geyser boiling described as 'the turbulent motion of the liquid caused by the explosive expansion of a boiling bubble' appeared when filling ratio exceeded 60%. The optimal filling ratio to obtain stable operation and relatively high heat transfer performance was 40% for water and 50% for ethanol. The highest performance was obtained for an inclination angles between 20° and 40° but the differences up to 90° were not significant. Dry-out phenomenon occurred for inclination angle of 15°. Maximum overall heat transfer coefficient was higher for water (2400 – 3000 W/m^2K) than for ethanol (900 – 1100 W/m^2K).

Fukano et al. (1983) [57] experimentally investigated various operation limits of the thermosyphon filled with methanol and water, among others oscillation, dry-out and boiling limits. They occurrence depended mostly on heat load and filling ratio. Boiling limit took place for high filling ratio, dry-out for low filling ratio and oscillation for the moderate filling ratio and in relative large tube diameter (authors tested two inner diameters: 9.53 and 20.9 mm). Wall temperature varied by about 100°C during these fluctuations.

Casarosa et al. (1983) [35] observed geyser effect during the operation of thermosyphon filled with water at low pressure conditions (between 0.03 and 1 bar). They found that the geyser frequency increased and intensity remained constant for an increase

in heat flux at the constant pressure inside the device, measured in the condenser section. Increasing pressure caused decrease in the intensity of the geysers for the same heat flux applied to the device. They argued that the frequency of geysers depends on thermal capacity of the whole system (or its parts). At conditions of low pressure (below 0.15 bar) they found no influence of thermo-physical properties of materials on the superheat between evaporator wall and working fluid. A Nusselt correlation based on the experimental data using the least squares method was proposed.

In 1986, Fukano et al. [58] continued to study on oscillations in a thermosyphon, dividing them into three types. Geyser boiling was described as periodic oscillation and was registered only for filling ratio of 33%. The authors found that oscillations were triggered by flooding which causes dry-out of the evaporator wall and then re-wetting occurred. They proposed a correlation for the heat input at which oscillations begin.

Lin et al. (1995) [109] performed an experimental work on geyser boiling in a vertical, transparent thermosyphon filled with water and ethanol. They determined that the period of geyser events decreases with an increase in heat load (in the range of 6 – 66 W), decrease in filling ratio (in the range of 30 – 140%), shorter evaporator section (compared length: 140 and 190 mm) and a drop of temperatures in the condenser (cooling medium temperature: 5 - 30°C). They determined the parametric range of geysering region for water depending on filling ratio, heat flux, and pressure.

Kuncoro et al. (1995) [101] compared operation of a thermosyphon when filled with water and freon R113. A glass thermosyphon was electrically heated and had 2.8 times larger diameter of the condenser compared to the evaporator section. The authors showed that the geysering frequency depends on the heat load, geometry of the device and thermophysical properties of the working fluid. No superheat was observed for water employed as working fluid, thus they proposed that an internal-energy storage pattern is responsible for geyser boiling. The situation changed for R113 that was characterized with a good wettability and a near-zero contact angle. Superheat was always reached before bubble initiation and its degree was reduced with an increase in heat load and pressure.

Noie et al. (2007) [142] conducted experiments to check the influence of filling ratio and inclination angle on the thermal performance of the copper thermosyphon heated electrically. The tested filling ratios were 15%, 22% and 30%. The values were considered due to a dry-out phenomenon for the values lower than 15% and possibility of geyser boiling for filling ratios larger than 30%. Maximum condensation heat transfer coefficients were obtained for the inclination angle in the range of 15 and 60°. They found that the geyser boiling did not limit the heat transfer performance, but can be dangerous for the mechanical resistance of the device.

Later (2009), the same research group [50] studied the geyser boiling in more detail. They showed experimentally that the phenomenon occurred only under specific conditions, such as filling ratios larger than 30% and the smallest tested diameter of the device (inner diameter of 14 mm). They showed that there was no effect of coolant mass flow on the geyser boiling behavior. Period and amplitude of events decreased with a decrease in inclination and amount of working fluid. The increase in the diameter of the pipe was related to the lower frequency and amplitude of geysers. A bigger device diameter allowed the working fluid to form larger bubbles, thus the driving forces needed to move the bubble were lowered and the bubble vanished.

Khazaee et al. (2010) [92] investigated the effect of filling ratio, heat input, coolant mass flow rate and aspect ratio (ratio of the evaporator length to the inside diameter of the pipe) on the geyser boiling in thermosyphon. They recognized period and amplitude

of surface temperature oscillations as a measure of boiling regime. Rise in heat input decreased the period of events and the intensity of temperature changes what was the opposite effect to the increase in filling ratio. When the coolant mass flow rate increased, the frequency of geysers, as well as the surface temperatures of the evaporator and condenser increased. For constant filling ratio (35%) and heat load (100 W), increase in aspect ratio from 17.2 to 28.6 shortened the geyser period by 16%. The authors proposed a correlation for period of temperature oscillation τ_{to} including the impact of filling ratio, inclination angle, aspect ratio, heat flux, mass flow and specific heat.

Chen et al. (2015) [36] studied experimentally geysering performance in a vertical heated system with a heat source at the bottom and no cooling circulation. The main motivation was to check possibilities of geyser boiling as a heat sink under nuclear accident conditions when cooling system is damaged. They recognized three main phases of geysering: thermal storage, vapor eruption and liquid refilling with occasionally subcooled or superheated boiling. Instead of single bubble responsible for geysering they found out sudden and rapid vaporization of the bubble population. Superheated liquid surrounding bubbles caused violent expansion of the vapor content. It induced decrease in the pressure below the vapor what in turn led to more vapor generation, even to the level of the whole cross-section of the channel occupation. Authors linked this behavior with a geometry of the device, in particular long and non-heated channel what is not the point when considering thermosyphon. They also investigated the influence of heat flux, sub-cooled temperature, coolant inventory and geometry on the working fluid performance. With increase in heat load, the geysers frequency and amplitude increased.

Agunlejika et al. (2016) [3] conducted an experimental study on horizontal thermosyphon reboiler. They showed that system instabilities can be determined in terms of flow rate, temperatures and pressure fluctuations. They propose the mechanisms for geysering in such a systems. During geysering transition between churn and slug flows were detected as a result of variations in vapor velocity and quality. They recognized three regimes of stability depending on the heat flux which are from the lower values: low flow or no circulation, sustained oscillations and stable system.

Xia et al. (2017) [221] conducted a visualization study on the phase-change instabilities in flat thermosyphon employing water, acetone or ethanol as working fluids and operating under sub-atmospheric pressure. They noted that the geyser boiling (or intermittent boiling) may harm the steady and safe operation of the device and determined the influence of different parameters, such as heat load, filling ratio and coolant temperature. They recognized three boiling regimes for the heat input between 13.1 and 93 W/cm^2: natural convection, geyser boiling and nucleate boiling. Heat load significantly affected the geyser events up to the value of 69.6 W/cm^2. For higher heat loads, it had almost no effect. Temperature of cooling water reduced the intensity of geysers only for the medium range of the thermal loads (between 23.6 and 69.6 W/cm^2). The maximum amplitude for temperature of the evaporator wall and pressure were 3.1°C and 0.8 kPa for water filling ratio of 50% and the lowest cooling water temperature. No geysering was found for ethanol and acetone. Moreover, the visualization showed that the droplet of condensate falling into the evaporator pool may act as a nucleate site, even when no other nucleation site is active.

Smith et al. (2018) [186, 185] studied the geyser boiling in a transparent sapphire thermosyphon. They determined a confinement number as a quantity measure of growing bubble confinement for a given pipe diameter. They proposed the flow maps for each working fluid as a dependency between confinement number and rate of vapor production.

The maps indicate regimes of slug/plug flow, bubble flow, churn flow and geyser flow. Geyser boiling occurs for high confinement numbers and high vapor production rate, in particular during working at low pressure conditions. They highlighted that heat is transported through the device as both latent and sensible heat during geyser boiling. However, such instabilities may cause shock damages to the thermosyphon constituents.

Alammar et al. (2018) [7] published a study on the influence of different parameters (filling ratio, inclination angle and heat load) on the performance of the thermosyphon without adiabatic section. They found that after geysering occurrence, the temperature distribution of the evaporator wall becomes more uniform what leads to the lower thermal resistances of the device.

A month later, authors [6] added effects of coolant flow rate and inlet temperature to the previous results. They found that the temperature oscillation is not affected by increasing coolant mass flow rate for filling ratio of 100%, while for lower filling ratios it causes a decrease in geysers frequency. Oscillation period decreases additionally with an increase in inlet of cooling temperature (tei) for filling ratios of 25 and 100%, or a decrease in tei for 65% fill of the evaporator.

Jouhara et al. (2015) [81] presented the first three-dimensional CFD simulation that included prediction of geyser boiling. Jafari et al. (2017) [78] studied numerically and experimentally the effect of filling ratio on thermosyphon operation. They found that the optimal filling ratio is below 35% for the heat transfer, however the risk of dry-out phenomena can occur in this range. Wang et al. (2018) [208] combined CFD analysis (improved and original Lee model based on volume fraction equation method) with a visualization of geyser boiling in thermosyphon. They recognized geyser events with a period of approx. 90-100 seconds. Improved Lee model that included a superheat for activation of nucleation allowed to reproduce the geyser boiling in reasonable agreement with experiments.

To sum up, the effects of key parameters on the geyser boiling behavior reported by different research groups are presented in Table 3.6. The table focuses on water data as it is the most commonly investigated working fluid in reference to the geyser boiling phenomenon.

Filling ratio and heat load are the most investigated parameters influencing the geyser boiling and the results are rather unequivocal. Increase in heat load leads to more frequent geysers (up to certain value of heat flux [50]) and their intensity is reduced or not affected. When considering the increase in the working fluid mass, the geysers showed significantly higher intensity (again at least up to some heat flux [221]) and period of the phenomena decreased. Increase in inclination angle and length of the evaporator caused less frequent events with higher amplitude. The intensity of the geysers is not affected by coolant mass flow rate and increased by elongation of the evaporator section or heating the temperature of cooling water.

The above analysis indicates that geyser boiling in thermosyphons is still not well understood. Experiments require high-resolution sensors, which make investigations challenging. The effect of geysering on the averaged heat transfer performance of thermosyphon operated with classical single-phase liquids seems to be negligible small. However, geysering causes high mechanical load and may even lead to shock damage of the device components. As thermosyphons are used in systems usually intended to work for long periods of time, these features provoked rising awareness of geyser boiling in the last years. The literature survey shows that there is nearly no research on the effect of nanofluids, influence of surfactants etc. what motivates my study.

Table 3.6: Summary of key parameters affecting geyser boiling for water

WATER DATA		The effect of increase ↑ in							
Reference		Heat load	Filling ratio	Inclination angle	Pressure	Coolant mass flow rate	Temp of coolant	Inner diameter	Evaporator length
Amplitude	Increase ↑		[140, 109, 142, 50, 78] [92][3] [221][4]	[50]			[221][6]		[109]
	Decrease ↓	[92]	[221][5]		[35]			[50]	
	No effect	[35]				[50, 92] [7][9]			
Frequency	Increase ↑	[92, 35, 109, 196] [50][1]				[92]	[7] [7,9]		
	Decrease ↓	[50][2]	[50, 109, 92]	[50]		[7][7,8]	[109][7][8]	[50, 92]	[109]
	No effect					[50] [7][9]			

[1] Up to 150 W; [2] Small or no geysers for heat flux higher than 150 W; [3] No geysers for filling ratios below 30%; [4] Heat fluxes smaller than 69.6 W/cm^2; [5] Heat fluxes higher than 69.6 W/cm^2; [6] Heat fluxes in the range of 23.6 – 69.6 W/cm^2; [7] Filling ratio of 25%; [8] Filling ratio of 65%; [9] Filling ratio of 100%

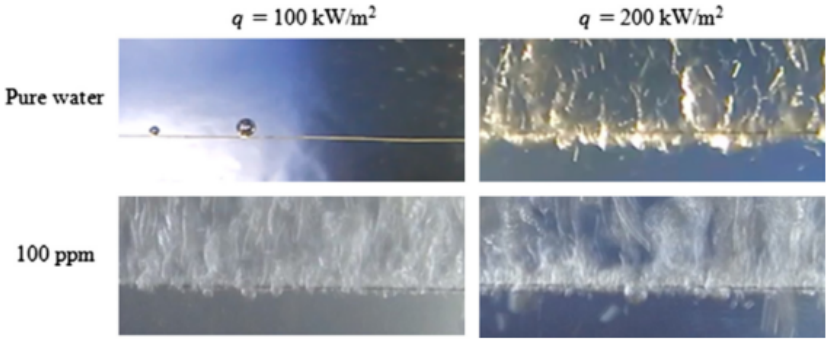

Figure 3.9: Comparison of boiling behavior of pure water and surfactant solution (aqueous Nicotine) [138]

Boiling of stabilizers

Nanofluids are often stabilized with surfactants or polymers what can influence the boiling process. The literature review on that issue is presented in following sections.

Surfactant boiling

Most of the experimental papers report that the surfactant addition causes an increase in boiling heat transfer of water, mixtures and organic fluids [2, 37, 108, 138]. Decrease in surface tension, which usually occurs in surfactant solutions, influences a pool boiling process by affecting the dynamics of bubble nucleation and size of detaching bubble [108]. The visual comparison of pure water and surfactant solution (aqueous Nicotine) [138] is shown in Figure 3.9.

The temperature difference between the wall temperature T_i and liquid's saturation temperature T_{sat}, commonly called overheating or superheat, during nucleation boiling is given by the equation 3.10 [108]:

$$T_i - T_{sat} = \frac{T_{sat} \cdot \upsilon_{lv}}{\Delta h} \frac{2\sigma}{r} \tag{3.10}$$

Where υ_{fg} is the specific volume difference between liquid and vapor, Δh is the latent heat of vaporization, σ surface tension, and r radius of a surface cavity.

This equation indicates that reduced surface tension translates into lower superheat of the wall required to form a bubble. At given temperature difference more bubbles are formed according to the relationship $N \propto e^{-\sigma^3}$, where N is number of nuclei in liquid boiling [37]. Bubble growth period is slightly extend, while the waiting period and time between two successive bubbles is significantly decreased [37].

The second parameter - bubble departure diameter - also depends on the surface tension and its decrease is even higher with increasing surfactant concentration. More bubble with more regular shapes are formed on the surface as a consequence of reduced inter-bubble coalescence. Both trends result in enhancement of boiling heat transfer. Surfactant solution shifts boiling curve and boiling onset to the lower wall superheat in comparison to water [37, 108]. Reduced surface tension means lower amount of energy required to create a bubble. It promotes cluster mode of detaching bubbles and facilitates activation of nucleation sites. This induces higher bubbles departure frequency (affected also by cavity-cavity interaction, microlayer evaporation, and coalescence of bubbles), a more vigorous boiling process, smaller bubble diameters, and shorter life-time of bubbles in cluster mode [2, 218, 205].

Depending on the boiling regime, addition of surfactant changes ratios of convection and latent heat to the total heat flux. In partially developed boiling regime, reduced surface tension facilitates activation of dormant nucleation sites and enhances contribution of latent heat component. For fully developed nucleation, bubbles departure at higher frequency preventing vapor agglomeration on the heating surface. It moves the balance to the convection part [37, 108].

Wang et al. [205, 206] argued that enhancement of heat transfer capabilities is not an effect of surface tension reduction but rather two mechanisms occurring during surfactant boiling: bubble bursting/explosion and bubble jet phenomena. The first one occurs when bubbles appearing in a short distance from each other merge. Surfactant molecules move to the coalescence point, what significantly decreases the surface tension compared to other locations at the gas-liquid interface. As a result, the merged bubble expands rapidly and explodes at the point with the lowest surface tension. The bubble explosion was seen in conducted visualization for all tested surfactant solutions (anionic surfactant of sodium dodecylbenzenesulfonate SDBS, catonic surfactant of cetyltrimethylammonium chloride CTAC and nonionic surfactant of alkyl polyglycoside 1214) but did not occur for deionized water, ethanol and silicone oil.

The second mechanism - bubble jet phenomena leads to the ejection of small bubbles from the main bubble. The jetted bubbles flow into the pool volume and do not return in case of surfactants. It allows for effective latent heat release. After splitting, the main bubble decreases reducing dry-out spot, and fresh liquid wets heater again. Mentioned behavior was found in all surfactant solutions and ethanol. However, in ethanol jetted bubble resulting from nucleation process may return to the heated wire. Both described mechanisms lead to smaller dry-out spots, more intense disturbance, and, as a result, improved heat transfer. Although silicone oil has lower surface tension than ethanol, it does not indicate bubble jet and bubble explosion phenomena. Small bubbles appearing

on the heater moves along the wire until they coalesce and grow enough to detach. [205, 206, 218].

Next to mentioned effects, changed behavior is also attributed to the Marangoni effect causing the surface tension gradient. It affects bubble growth behavior, leads to more stable bubbles and prevents jetted bubbles from returning to the heater surface. On the other hand, Marangoni effect is found to decrease bubble rise velocity what reduces internal circulation [37, 108, 205, 206]. To sum up, addition of surfactant modifies properties at the vapor-liquid interface what translates into changes in nucleation process, and dynamics of bubbles forming and detachment. Heat transfer enhancement up to critical micelle concentration (cmc) of surfactant is attributed to the reduced surface tension of the solution. For higher concentrations, slope of heat transfer increase may remain constant or decrease according to viscous characteristics. Moreover, most of researchers agreed that surfactant addition enhances boiling heat transfer but it cannot shift the critical heat flux (CHF) to higher values [37, 108].

Research on surfactant boiling still requires further investigations. One of the main concerns is solution stability in the long-term use. Witharana [214] reported that surfactant may fail at high temperatures what translates into deposition on the surface that changes properties of the heater surface [214]. The problem was also highlighted by Hetsroni et al. [72]. Although fresh surfactant solution (Habon G) shifted sub-cooled boiling curve to the smaller wall superheat in comparison to water, after some time they observed degradation of Habon G. This resulted in about five-fold increase in wall temperature at the boiling onset point when experiments run with increasing heat flux. From this point, superheat was sharply reduced. Phenomena was not observed for series with decreasing heat flux. Authors linked this behavior with a large vapor coating resulting of degraded surfactant [72].

Another issue is the impact of surfactants on the environment. The challenge is to find a surfactant that is environmentally-friendly, and at the same time, the addition of its small amount enhances heat transfer capabilities.

Polymer boiling

As the boiling behavior of surfactant solutions is mostly related to the reduction of surface tension, mechanisms standing behind polymer boiling must differ significantly. Except the group of polymeric surfactants (see section 2.1), polymers do not noticeably affect the surface tension. Simultaneously, they increase the solution viscosity and often show non-Newtonian behavior, especially for high concentrations, high molecular weight, and high degree of polymerization.

Most of the studies on polymer boiling available in the literature concern polymers with surface-active characteristics [37, 108]. However, comparable to boiling of surfactant solutions, dynamic surface tension should also be considered in case of polymer boiling. Diffusion transport of molecules to the liquid-vapor interface and their succeeding positioning is rather slow. It takes from seconds to minutes depending on polymer chemistry, molecular weight and concentration. The time of boiling bubble detachment in water is estimated at 10-100 ms. The difference in time scale leads to intricate interfacial behavior affecting the nucleate boiling dynamics [37, 108, 229].

As already mentioned, polymer solutions are often characterized by the shear-thinning non-Newtonian behavior. Increased viscous resistance against the bubble growth may lead to even higher dynamic surface tension compared to water. This parameter depends

on the solution viscosity, capillary radius and surface characteristic [37]. Nevertheless, some authors report the heat transfer enhancement compared to water when optimal concentration of polymer is selected [37, 108]. Visualizations ([151, 170, 229] in [37]) showed that for a few low molecular weight additives bubbles are again smaller (as a result of high viscosity preventing bubble growth), detach in a more ordered trend and with higher velocity what reduces their coalescence. Mechanisms responsible for this behavior is still not well understood as a consequence of limited number of available studies on boiling phenomena with polymers solutions that are not surfactants [37, 108].

Increased viscosity, shear thinning rheology, process of diffusion transport and reorientation, and affected microconvection near the surface translates into various effects of aqueous polymeric solutions on nucleate boiling heat transfer. Some of polymers enhanced, some reduced, and some did not affect the efficiency of thermal energy transport [37, 108].

To sum up, the majority of the literature reported enhanced boiling heat transfer and not affected critical heat flux values by addition of surfactant to solution. Surfactants reduce surface tension of solutions and modify vapor-liquid interfaces. This influences dynamics of bubble nucleation and size of detaching bubble. Due to reduced inter-bubble coalescence more bubbles with more regular shapes are formed on the heating surface. Additional mechanisms, such as bubble bursting, bubble jet phenomena, or Marangoni effect are associated with improved heat transfer capabilities.

In case of polymers, there is no agreement how they influence boiling heat transfer and different effects on heat transfer capabilities are published. It seems to be dependent on type of polymer additive, its concentration, molecular weight and chemistry. Exception is the group of polymeric surfactants which reduce surface tension and always enhance boiling heat transfer coefficient. Other types of polymers do not noticeably affect surface tension. Their addition increases solution viscosity and promotes the shear-thinning non-fluidic behavior. Limited number of available studies on polymer boiling inhibits understanding of mechanisms behind this phenomena.

To the best author knowledge, there is no research on properties and boiling behavior of surfactants and polymers under different working condition, including reduced pressure. Among the properties measurements, there is a need for determination of the surface-liquid-vapor surface tension under temperature and pressure conditions used for boiling in real applications. Additionally, only a few studies on the contact angle are available. Correlation between this parameter and boiling behavior should also be verified. Further research using different methods, including visualization, experiments, and analytical approach in wide range of parameters, and types of additives are necessary to determine heat transfer mechanisms related to boiling patterns of surfactants and polymers solutions.

Impact of stabilizers on boiling of nanofluids

Murshed et al. [135] investigated the effect of NaDBS surfactant with concentration ratio to carbon nanotubes (CNT) varying from 1:20 to 1:1. They determined the critical concentration of surfactant (here 1:5) to obtain maximum CHF and burnout heat flux (BHF) values. SEM analysis of wire after boiling showed that increasing concentration of surfactant intensifies the process of particles deposition on the wire what is presented in Figure 3.10. Surfactant strongly influenced the deterioration process.

The opposite effect was found by Chopkar et al. [39]. They found that addition

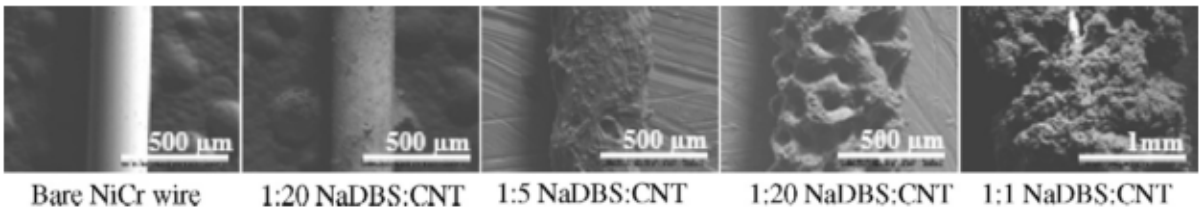

Figure 3.10: SEM images of NiCr wire after pool boiling experiments of CNT nanofluid with different concentrations of surfactant (NaDBS) [135] in [136]

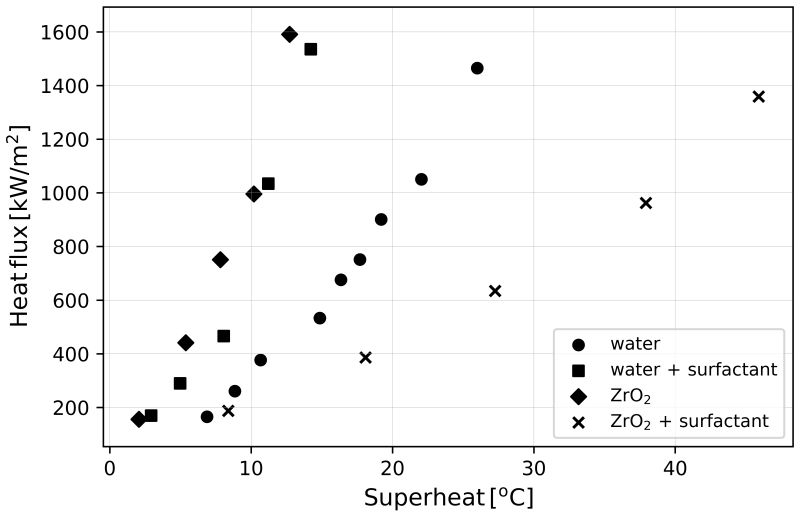

Figure 3.11: Boiling curves of 0.005% ZrO_2 nanofluids with and without surfactant (1.0% vol.) [39]

of 1.0% vol. surfactant (tetramethyl ammonium hydroxide) to ZrO_2 nanofluids worsen boiling heat transfer and shifted the boiling curve to the right what can be seen in Figure 3.11. They noticed that repeating the experiments shifted the boiling curve to even higher overheating. Authors ascribed this behavior to decreasing roughness due to trapping nanoparticles in the surface cavities.

Kathiravan et al. [88, 89] studied nucleate pool boiling with silver and copper water-based nanofluids. They found that CHF of nanofluids was higher than that of base fluid and increased with nanoparticles concentration. 9% vol. surfactant solution (sodium lauryl sulfate SLS) reduced CHF to about one forth of the water value. CHF of nanofluids with surfactant addition were also lower than that of pure water but higher than the one of a base fluid (here: water plus SLS surfactant). Boiling heat transfer coefficient was lower for nanofluids compared to base fluid and decreased with increase in concentration. This shifted boiling curves to the right what is shown in Figure 3.12.

The same research group [90] tested carbon nanotubes (CNT) nanofluids which showed opposite behavior. Nanofluids reduced superheat for a given heat flux and CHF compared to water. Nanoparticles lowered CHF also when 9% SLS solution was used as a base fluid. In this case, only 0.5% vol. CNT nanofluid enhanced heat transfer compared to water for the whole range of heat fluxes. 0.025% vol. and 1.0% vol. CNT/SLS nanofluids showed worse heat transfer capacity than water for low heat fluxes due to delay in the boiling

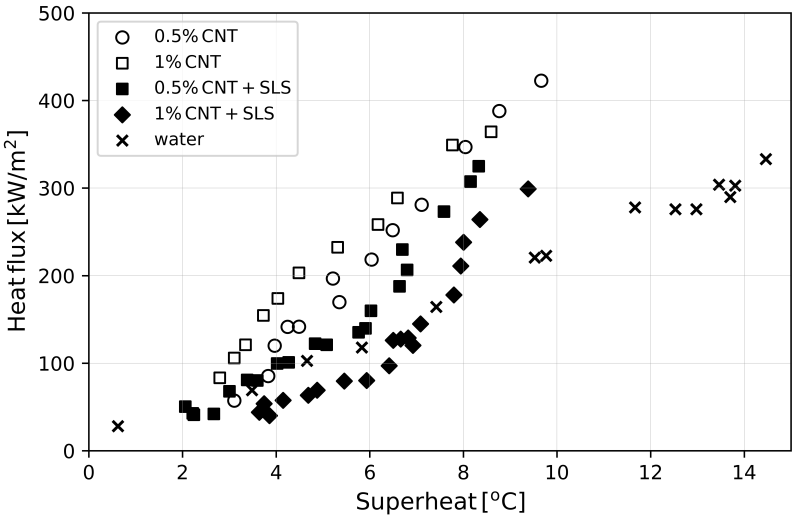

Figure 3.12: Boiling curves of CNT water-based nanofluids with and without SLS surfactant [90]

onset. However, the results were compared with pure water, not aqueous solution of SLS which was a base fluid for these samples. Authors [88] showed previously that surfactant itself reduces CHF and boiling heat transfer coefficient so comparing with pure water may be misleading.

Soltani et al. [189] investigated the influence of CMC (carboxy methyl cellulose) with concentrations between 0.2 - 1.0 wt.% on Al_2O_3 nanofluid boiling. They found that increase in CMC concentration lead to increase in boiling surface temperature, and thus reduction in heat transfer coefficient. However, for a small concentration of CMC (0.2%) the trend was opposite and solution showed higher heat transfer capabilities than water.

Shoghl and Bahrami [183] reported that addition of 0.01/0.02wt.% sodium dodecyl sulfate (SDS) to ZnO and CuO nanofluids (0.01/0.02wt.%) enhanced heat transfer coefficient to the values up to 74% higher than for water. For comparison, ZnO nanofluid without SDS slightly decreased and CuO showed 7% increase of HTC. Further study conducted by the same research group [137] demonstrated that ZnO and Al_2O_3 nanofluids reduced heat transfer during boiling while CNT addition caused the enhancement. Possible decreases authors linked to the increase in viscosity.

3.3 Summary of the literature review

The following summary may be delivered from the foregoing literature review:

1. Nanofluids consist of a base fluid, nanoparticles and optional stabilizer. Each component influences the final properties of nanofluid. Impact of surfactant or polymer is often neglected in the literature, although **chemical stabilizer can affect thermophysical properties of nanofluid and their boiling behavior**. Therefore there is a gap of knowledge, which should be filled with careful experimental studies.

2. Based on obtained experimental data researchers proposed empirical correlations for thermophysical properties of nanofluids and heat transfer coefficients. They are

usually applicable in a very narrow range of parameters and types of nanofluids, and are not verified in various conditions. This show a **need for higher amount of comparable data with proper characterization of used nanofluids**.

3. Nanofluids influence three of partial thermal resistances of the thermosyphon: thermal resistance of the fluid itself, of the phase interface between liquid and vapor, and between inner wall of the evaporator and heated fluid. The next few ones are in the group of 'influence is possible but must be proven', and seem not to have decisive impact on the overall thermal resistance of the device. **The thermal resistance between the evaporator inner wall and the heated working fluid is crucial for the final effect of using nanofluids.**

4. During boiling of nanofluids particles may deposit into layers on the heater wall (inner wall of evaporator in case of a thermosyphon). It changes the surface chemistry, structure, and energy, what in turn affects the force balance at the triple line, bubble nucleation, and wetting dynamics. **Deposition processes exceed the current state of thermodynamics and fluid mechanics knowledge and require further investigation.**

5. A boiling regime characterized by a sudden and violent expansion of a bubble that pushes the fluid trapped above in the direction of condenser (geyser event) may occur in thermosyphon for some working conditions. This periodical behavior is called geyser boiling (or geysering) and is still not well-understood. Reported literature survey indicates that **there is nearly no research on how nanofluids or surfactants affect geyser boiling regime**.

6. Working fluid properties affect boiling regime in a thermosyphon. Visualization of nanofluid behavior operating in the thermosyphon is not currently available to the best author knowledge. **The interplay between nanoparticles, base fluid and evaporator surface play a crucial role in the thermal capacity of the thermosyphon working with nanofluids.** It makes visualization of processes inside a device challenging. Changing tube material from copper to sapphire or glass alters the surface characteristics and properties, thus is not reliable for comparison. The only possibility is to compare with a base fluid and to search for similarities based on working fluid properties, pressure, and temperature measurements.

7. Multiplicity of parameters influencing nanofluid behavior explains why experimental results available so far are incoherent. It results in the lack of proper theoretical and numerical models. **Reliable and comparable data is required for fully understanding the mechanisms behind the nanofluid usage in thermosyphons.**

8. **Classical approaches to design of thermosyphon are not applicable to thermosyphons working with nanofluids** due to interactions of nanoparticles with the evaporator wall changing surface conditions and working fluid properties over time. Reliable experimental database is required to determine issues related to nanofluids what allows for further development of mathematical tools.

9. Overview of the literature indicates that **only a few papers tried to compare different working fluid under comparable operating conditions and the thermosyphon geometry.** Among the carbon-based materials, no studies on

graphene-oxide or nanohorn nanofluids in thermosyphon are available. Only one paper discussed the silica nanofluid and focused mostly on the functionalization effect on the fluid stability and basic coefficients describing thermal efficiency. Two papers analyzes the impact of gold nanofluids on thermosyphon operation. In these studies heat was supplied to the evaporator via electric heater at the bottom of the device, thus thermosyphon cannot control the amount of transferred heat.

Heat transfer in thermosyphon working with nanofluids is complex process including parallel phase change transitions. Phenomena depend on many parameters which cannot be controlled and analyzed at the same time. Reported inconsistencies show the need of more systematic investigations on nanofluids in different applications, including pure boiling systems and thermosyphons. Usage of wide range of nanoparticles materials, concentration and sizes, as well as different types of surfactants, and surface conditions are highly recommended. Focus should be put on repeatable experiments with time-dependent analysis based on highly precise equipment. This will help to detect mechanisms responsible for nanofluids behavior and will allow to determine divergences resulting from process of nanoparticles deposition on the heater surface.

To address some of concerns reported in previous paragraphs, the following methodologies are proposed:

- **Series of systematic experimental studies** on thermosyphons filled with various nanofluids. Proper selection of tested fluids allows for filling the knowledge gaps underlined in the literature review. Chosen nanoparticles includes graphene oxide flakes, gold, single wall carbon nanohorns, and silica nanoparticles. They show various properties, concentrations, shapes and sizes.

- **Examination of the inner wall of evaporator section** using endoscopy camera to check macro-scale changes caused by nanoparticles deposition during the thermosyphon operation.

- **Investigation of the surfactant effect** by testing aqueous solution of surfactant with the same concentration as in tested nanofluids to differentiate changes caused by nanoparticles and surfactant. It addresses the gap of knowledge caused by a common omission of the surfactant impact on results.

- **Characterization of tested nanofluids**. The focus is put on graphene oxide flakes as the most innovative material with high theoretical thermal conductivity and large specific surface area reported in the literature. Results of some properties determination available in the literature differ significantly and depend on the production route.

- **Analysis of the particles remained in the fluid after all experimental series** to check how they change under boiling conditions.

- **Data reduction methodology based on statistics to investigate geyser boiling** in more details. This allows for comparison of geyser boiling parameters (frequency and intensity of averaged geyser event) regardless of the working fluid or operation conditions.

Chapter 4

Experimental characterization of investigated nanofluids

Thermophysical properties of working fluid influence boiling heat transfer coefficient, and in consequence efficiency of heat transfer in thermosyphon. Nanofluids affect some of base fluid properties (Fig. 3.6). Thus, characterization of investigated working fluids was performed with focus on graphene oxide nanofluids. These materials are relatively new and with high potential, but still poorly characterized. No research on graphene oxide nanofluids used as working fluid in thermosyphon is currently available in the literature. Knowing the properties of these working fluid (among others size and shape of graphene oxide flakes, thermal conductivity, contact angle, density, viscosity, and surface tension) will allow for better understanding of obtained experimental results.

Due to multiplicity of experimental cases and nanofluids types, most of the results are divided into two groups which consider: 1) graphene oxide (GO) nanofluids and 2) nanofluids based on silica, nanohorn, and gold nanoparticles. Nomenclature for all tested working fluids is summarized in the Table 4.1 for GO-related working fluids and Table 4.2 for other investigated working fluids.

Table 4.1: Nomenclature for water-based nanofluids with graphene oxide flakes and related working fluids

Working fluid	**Type of particles**	**Particles concentration**	**Surfactant**	**Surfactant concentration**
Water	-	-	-	-
SDS solution	-	-	Sodium dodecyl sulfate	0.01 g/L
GO (fresh)	Graphene oxide flakes	0.1 g/L	-	-
GO + SDS	Graphene oxide flakes	0.1 g/L	Sodium dodecyl sulfate	0.01 g/L

Table 4.2: Nomenclature for water-based nanofluids with gold, silica, and nanohorns nanoparticles, and related working fluids

Working fluid	**Type of particles**	**Particles concentration**	**Stabilizer**	**Stabilizer concentration**
Water	-	-	-	-
SDS solution	-	-	Sodium dodecyl sulfate	0.01 g/L
Silica	Silica	2%vol.	-	-
Nanohorns	Nanohorns	0.1 g/L	Sodium dodecyl sulfate	0.01 g/L
Au1 / gold + PVP	Gold	0.1 g/L	Polyvinylpyrrolidone (PVP)	1%
Au2 / gold + KOH	Gold	0.1 g/L	Potassium hydroxide (KOH)	100 μM

Figure 4.1: Investigated working fluids: a) gold nanofluid, nanohorn nanofluid, water solution of SDS, silica nanofluid, b) graphene oxide nanofluid

Figure 4.1 presents investigated working fluids before the experiments. Details on preparation process and characterization with focus on graphene materials are presented in the following sections.

4.1 Graphene oxide nanofluids

Graphene is a two-dimensional sheet of sp^2-hybridized carbon [143]. For the first time, it was isolated by Andre Geim and Konstantin Novoselov (2010 Prize Nobel in Physics winners) in 2004. Graphene gained interest due to its unique properties, such as ambipolar field effect, high carrier mobility, good thermal and electrical conductivity [143, 163].

Nomenclature for materials based on graphene may be misleading. In the literature, term 'graphene' is currently used to refer various materials, such as two-dimensional sheet-like carbon forms, multilayer materials made by graphite exfoliation, or graphene oxides. The differences according to the recommended nomenclature presented by Editorial Team for Carbon [23] are underlined in following paragraph.

Graphite is a 3D material, the most stable allotrope form of carbon existing in the nature. Its oxidation leads to a bulk solid called *graphite oxide*. Further exfoliation of graphite oxide results in a graphene oxide (GO) or a few-layer graphene oxide in case of partial exfoliation. *Graphene oxide* (GO) is a mono-layer material with a honeycomb structure reach in oxygen content (C/O atomic ratio is typically between 2.0 and 3.0). It is modified chemically by oxidation and exfoliation 'that is accompanied by extensive oxidative modification of the basal plane' [23]. The exfoliation is the process of graphene oxide sheets separation from oxidized graphite stacks. It occurs under action of external forces, such as ultrasonication or mechanical treatment. Term graphene oxide is used to emphasize the process which the material has undergone. If GO is then treated in chemical, thermal, photo-chemical etc. way to reduce its oxygen content, the resulting material is called *reduced graphene oxide* (rGO) (see Fig. 4.2). The reduction may change properties, i.e. from hydrophilic GO to hydrophobic rGO. Finally, *graphene* is 'a single-atom-thick sheet of hexagonally arranged, sp^2-bonded carbon atoms that is not an integral part of a carbon material, but is freely suspended or adhered on a foreign substrate' [23]. Other two dimensional graphene-based materials should be called by special names what differentiate them from the isolated mono-layer. The individual structures of graphite

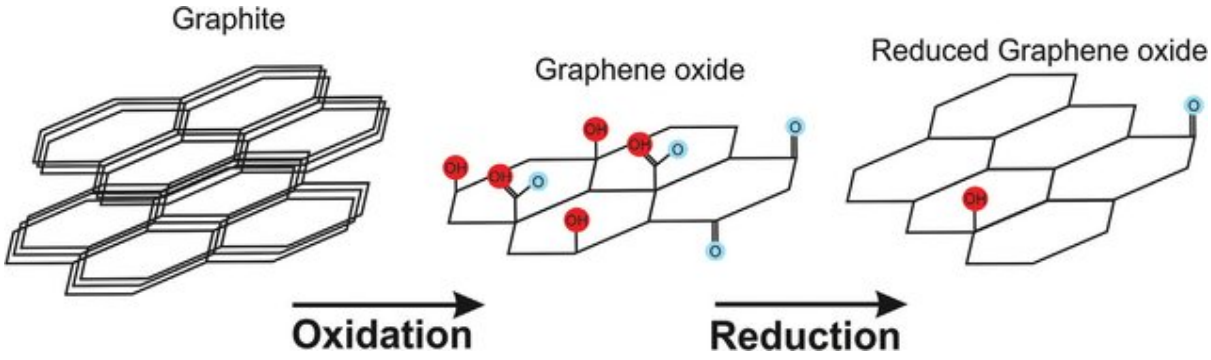

Figure 4.2: Difference between graphite, graphene oxide (GO) and reduced graphene oxide (rGO) [233]

and other 3D carbon materials are called *graphene layers* to distinguish the old and new nomenclatures.

Synthesis methods of graphene materials can be divided into two major groups: bottom-up and top-down [143]. The first category includes epitaxial methods and chemical vapor deposition. Both lead to good quality material but the production is expensive and gives only minuscule amount of product [106, 143]. Thus, this form of graphene is not suitable for heat transfer applications. The second type of techniques starts with macroscopic objects and reduce their sizes through a special treatment. It includes direct exfoliation, oxidizing-reduction method, electrochemical and chemical exfoliation [143, 148]. This approach allows to obtain relatively cheap product on a mass scale with potential to apply into industry.

Method of synthesis

Graphene oxide (GO) nanofluids were prepared in cooperation with Institute of Electronic Materials Technology (ITME) in Warsaw through a modified Hummers method (top-down technique) [171]. Process is schematically presented in Fig 4.3.

Source graphite material was oxidized chemically at 50°C by a treatment with a solution of 95% sulfuric acid (10 g graphite per 1 l of acid), sodium nitrate with a 2:3 mass ratio to graphite and potassium permanganate (6:1 mass ratio). Obtained slurry was first diluted in deionized water, and then H_2O_2 was added. In the next step, the solution was washed using a micro-filtration device. First sample was diluted with deionized water to ensure concentration of 0.1 g/l. Additionally, 0.01 g/l of sodium dodecyl sulfate was added to the second one. Both nanofluids were then mixed for 4 hours using magnetic stirrer. The samples were stable at the room temperature for over 6 months.

Size and shape of particles

Scanning electron microscope (SEM)

Samples of graphene oxide flakes under SEM microscope are presented in Fig. 4.4. Nanofluids underwent a special treatment before SEM analysis, including diluting and drying. Investigated flakes showed irregularity in dimensions, both between various flakes and in a single flake (thickness vs length). Some flakes were folded or creased. This feature could come from production or sample preparation for SEM.

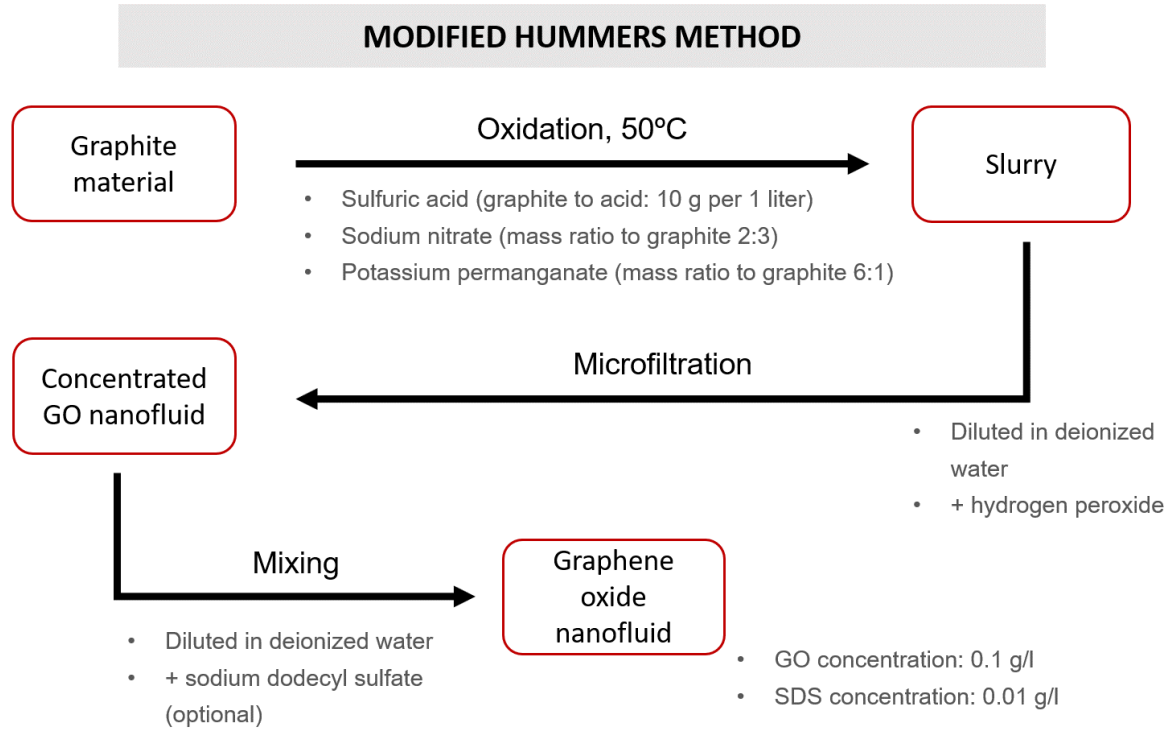

Figure 4.3: Synthesis of investigated graphene oxide nanofluid

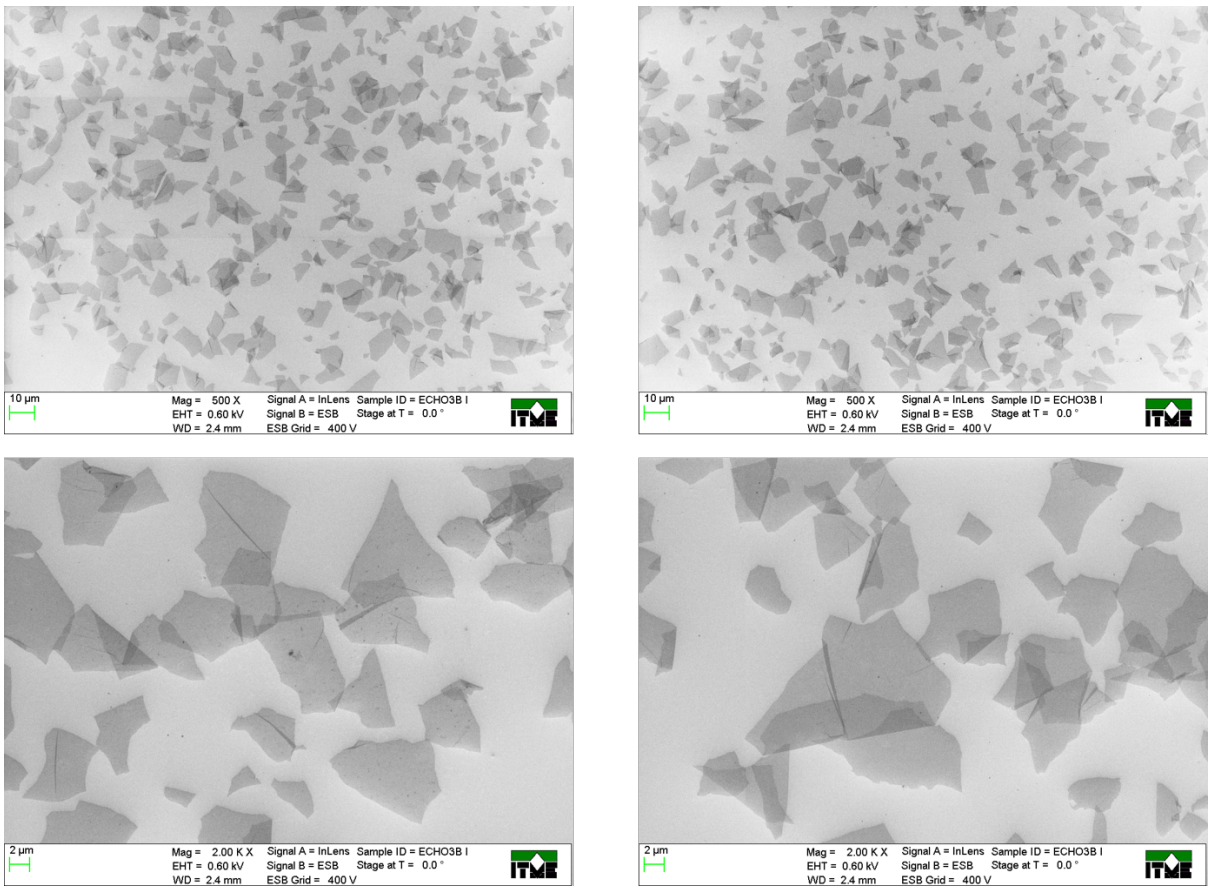

Figure 4.4: Fresh sample of graphene oxide flakes under scanning electron microscope (SEM)

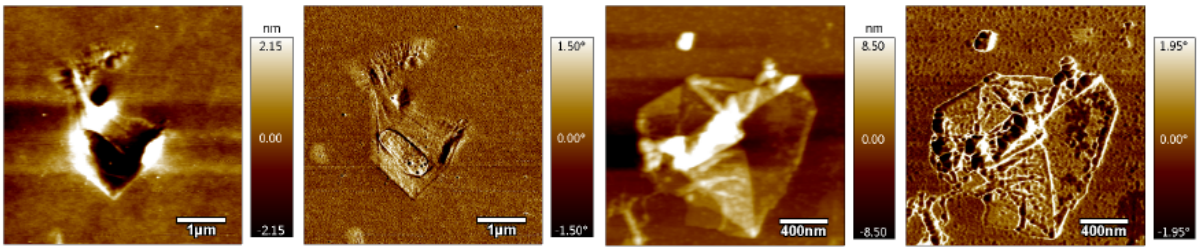

Figure 4.5: Graphene oxide flakes under atomic force microscope (AFM)

Atomic force microscope (AFM)

Thickness of graphene oxide flake shown in Fig. 4.5 was determined using atomic force microscope (MFP 3D BIO, Asylum Research/ Oxford Instruments). Due to sample specification and the nanometric size of flakes, the microscope was equipped with an AC160TS-R3 scanning probe (Olympus). The measurement was conducted using a Semi-Contact mode with a tip radius of approx. 7 nm. The experiments were performed at the ambient air with a temperature of about 23°C and an averaged air humidity of about 19%. Graphene oxide flakes had thickness of approx. 1 - 10 nm.

Dynamic Light Scattering (DLS)

Dynamic Light Scattering (DLS) equipments are well widespread. Measurements are simple, quick, and possible over the wide temperature range what is uncommon for other techniques. DLS technique is highly reliable method for spherical objects but the relationship between dimensions and diffusion coefficient for non-spherical particles is relatively complex [116]. Thus, DLS may provide only a rough approximation of the hydrodynamic diameter of graphene flakes dispersed in water and general trends following changes in conditions.

Typical results of DLS measurements give values based on intensity, relative particle numbers, and volume. The relative particle numbers are usually calculated from Mie Theory which is based on the Maxwell equation and describes electro-magnetic wave scattering. It assumes spherical shape of particles and determines the particle diameter based on backscattering angular profile. To avoid this theory for measurements of graphene flakes which are characterized by significant differences in thickness and length, results shown in this section are based on the intensity of scattered light. To prevent using the Mie theory, the values based on number and volume particle fraction are excluded from calculations. Results obtained from intensity distribution have usually higher values than the ones from volume fraction, which in turn are higher than the ones estimated from particle number [118, 201].

Experiments with nanofluids based on graphene oxide flakes were carried out at Jaume I University in Castellon de la Plana (Spain) using two devices based on DLS methodology: commercial Malvern Zetasizer Nano-ZS and customer-adapted Vasco Flex Particle Size Analyzer. Both are presented in Fig. 4.6. Each data point is the average of three sample measurements. The refractive index (n), called also a real part indicates the phase velocity was set to 2.6988 [211]. Imaginary part or extinction coefficient (k) refers to mass attenuation during propagation through the material. The k values are not precisely known for nanofluids [116] due to their variety. As this value was needed for the equipment software, 1.2955 was used according to the literature [211]. Later, in data

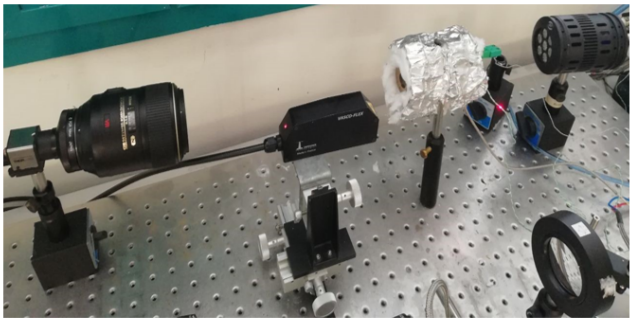

Vasco-Flex Particle Size Analyzer

Malvern Zetasizer Nano-ZS

Figure 4.6: DLS equipments used for determination of size distribution in graphene oxide nanofluid

analysis this extinction coefficient was avoided to use - results were based on intensity distribution, as described in previous paragraph.

Examples of particle size distributions determined with a Malvern Zetasizer NANO-ZS are shown in Fig. 4.7. All measurements with a Malvern Zetasizer NANO-ZS were carried out with 15 runs and a scattering angle of 173° in a glass cuvette PSC115. The cuvette had inner dimensions of 10x10x450 mm and was filled 3.5 ml of measured fluid.

Fig. 4.7 (left) presents the intensity size distribution of GO (0.33 g/l) with SDS (0.033 g/l) in the dependence of temperature measured using Malvern Zetasizer. The strong trends of increasing intensity and decreasing particle size occurred with temperature increment. The distribution curve was also more narrow for higher temperatures. Fig. 4.7 (right) presents the size distribution of GO nanofluid (0.1 g/l) in the temperature range from 45°C to 60°C where the reduction of graphene oxide may happen. This process depends on many conditions, such as temperature and time. For the case shown in the Fig. 4.7 (right), decreasing intensity of peak for the approx. 700-800 nm was seen with increasing temperature. At the same time, peak intensity for 5560 nm was slightly increasing. This may suggest that agglomerates started to being formed at this temperature.

Figure 4.8 shows the Vasco-Flex device with focus on measurement unit. Tested samples had an order of magnitude higher volume than in Nano-ZS Zetasizer. Due to dark color of tested nanofluid, visualization of heating processes inside the unit (Figure 4.8 b) was not possible.

After a long period of contact between nanofluid and measurement cell (14 hours), unexpected deterioration of graphene oxide nanofluid occurred. It led to agglomeration and sedimentation of flakes presented in Fig. 4.9. The same sample left outside the device kept its stability. Figure 4.9 c) shows that sedimented graphene material played as nucleation sites, although temperature in this case was only 50°C.

Figure 4.10 presents SEM analysis of two samples:

- row a: nanofluid underwent the whole experimental series and were left in the device for about 14 hours.

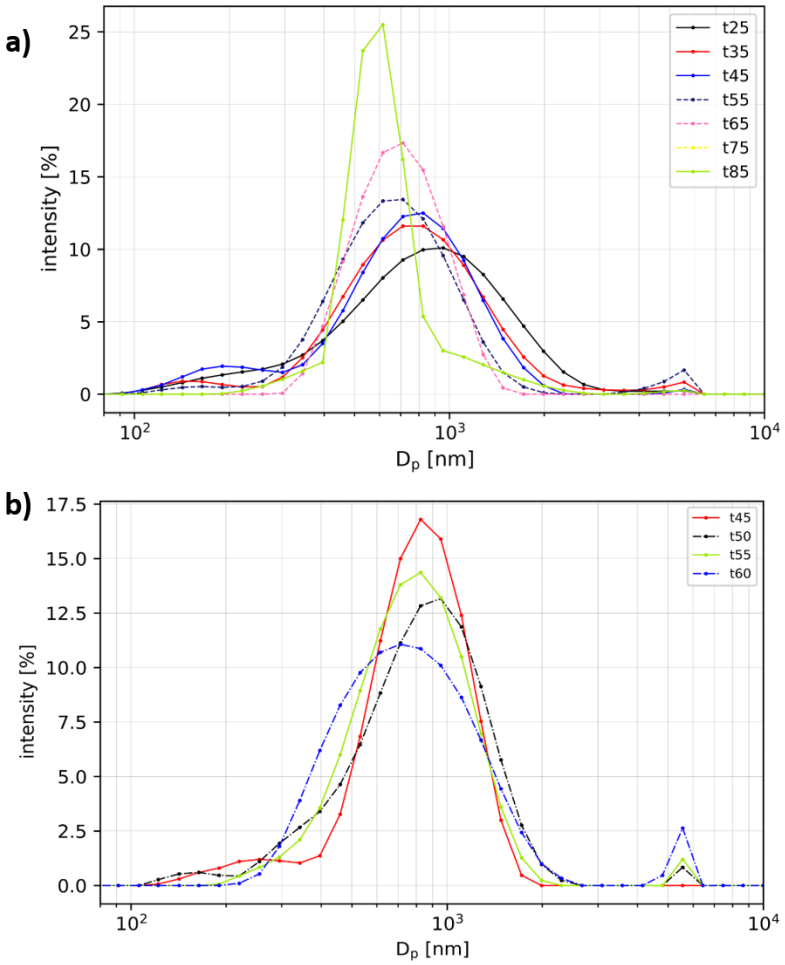

Figure 4.7: a) Size distribution of graphene oxide nanofluid (0.33 g/L) with SDS in the dependence of temperature. b) Size distribution of GO (0.1 g/l) in dependence of the temperature range from 45°C to 60°C

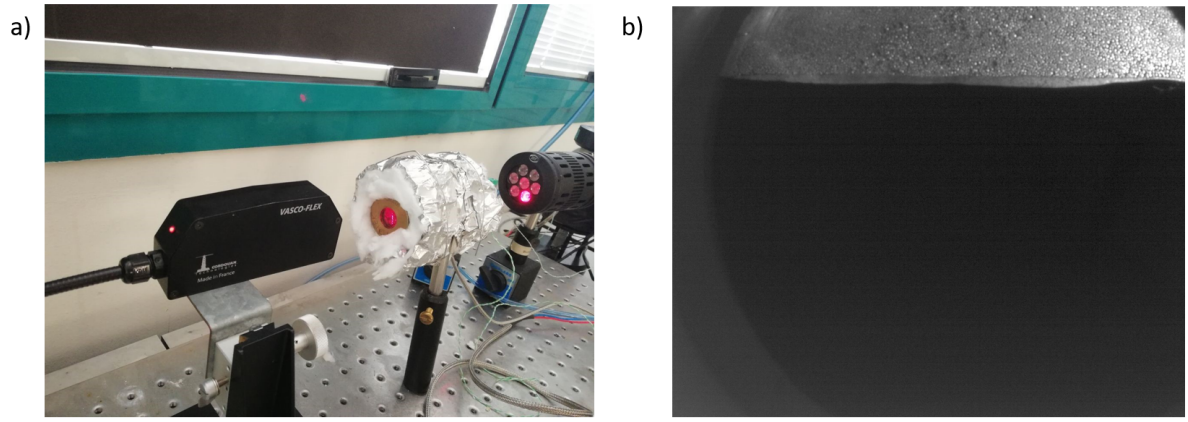

Figure 4.8: Vasco-Flex device (DLS technique) with a view on the measurement unit

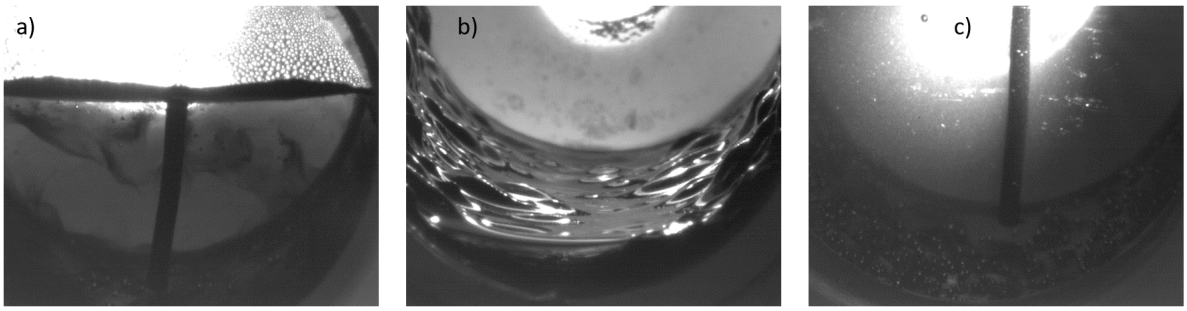

Figure 4.9: Deterioration of graphene oxide nanofluid after long-interaction with Vasco Flex measurement cell

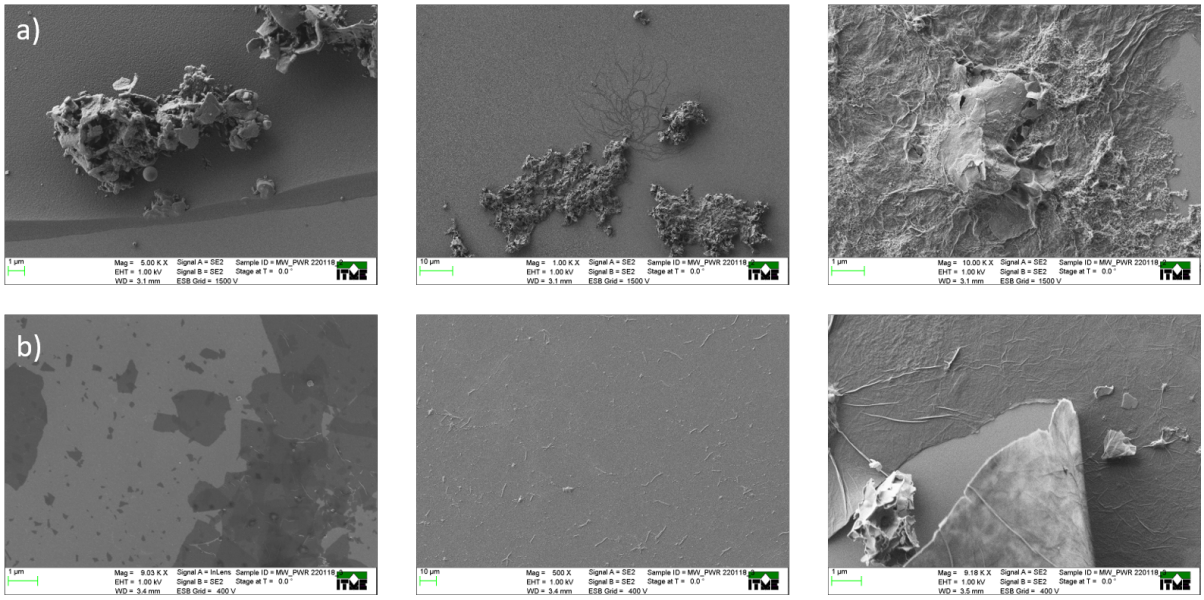

Figure 4.10: Graphene oxide material after measurements: row a) nanofluid left in the device for approx. 14 hours, b) nanofluid taken out from the device directly after completed experimental series

- row b: nanofluid was taken out from the device directly after finishing the last experimental point (85°C).

Fluid which was in the experimental unit over a night (row a) deteriorated completely. For the case *b* (nanofluid taken out from the measurement cell directly after finishing experiments), such a strong interaction between nanofluid and measuring unit was not noticed. However, heating up to temperatures higher than 50-60°C may lead to the reduction of graphene oxide. As a result, some flakes were partly destroyed (see the last figure of row b).

The comparison of the results for GO nanofluid (0.38 g/l) obtained at two kinds of equipment is shown in Fig. 4.11. In the temperature range of 30°C - 70°C, the differences were always smaller than 10%, except the lowest point. DLS can only give a rough estimation of sizes for flake-shape particles as explained in the introduction. These differences were considered as acceptable, even though the deterioration of graphene oxide nanofluid in Vasco-Flex device was reported. Due to fact that the measured samples

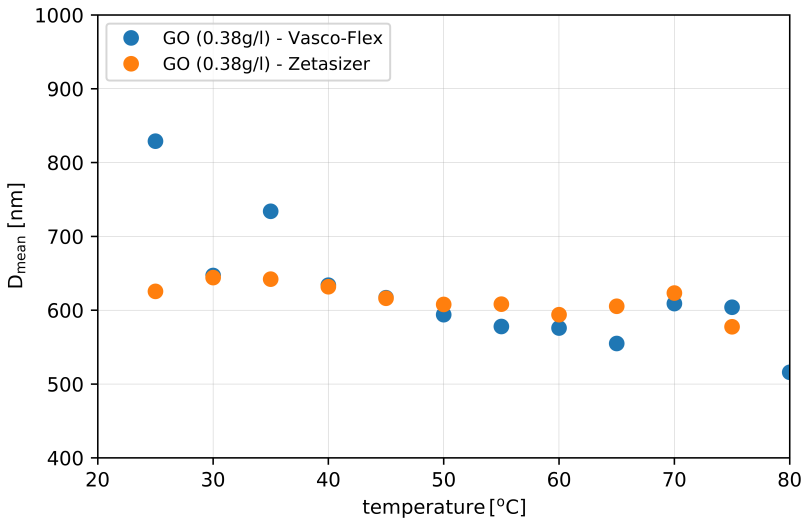

Figure 4.11: Comparison of mean hydrodynamic diameter of graphene oxide flakes (GO nanofluid, 0.38 g/L) measured with two devices

were water-based, bubbles could appear at temperatures higher than 75°C. It resulted in scattered data at this region and bad data quality reported by the equipments. These values were excluded from further analysis.

The hydrodynamic diameter of graphene oxide flakes averaged over the temperature range from 25°C to 75°C were:

- graphene oxide nanofluid (0.1 g/l) without surfactant: 901 nm,
- graphene oxide nanofluid (0.1 g/l) with sodium dodecyl sulfate (0.01 g/l): 769 nm.

Please note that typical thickness of graphene oxide flakes was of approx. 1-10 nm (Fig. 4.5), thus these hydrodynamic diameters should be treated as a rough estimation.

Thermal conductivity

Thermal conductivity of graphene sheets shows a strong anisotropy and its value along the flake length is one of the highest of known materials [156]. At the room temperature graphene can reach up to 4000 W/mK in the length direction [156] while diamond $\sim$ 2200 W/mK. The values obtained experimentally differ significantly and some of them are much lower (e.g. 600 W/mK for graphene [231]).

Effective thermal conductivity (called simply thermal conductivity) of tested graphene oxide nanofluid (0.1 g/l) was measured using ring-gap apparatus [48]. All surfaces in contact with measured fluid were silver-plated (20 μm) to prevent thermal radiation and corrosion. Convection was almost obviated, thus heat was transported through the fluid only by conduction [48]. Any temperature disturbances were treated as a part of systematic error, thus were included in calibration with water and toluene [162].

Thermal conductivity was calculated as [48]:

$$k_{nf} = \frac{q}{2\pi\Delta T\left[\frac{l}{ln(r_o/r_i)} + \frac{2r_i r_o}{r_o - r_i}\right]} \tag{4.1}$$

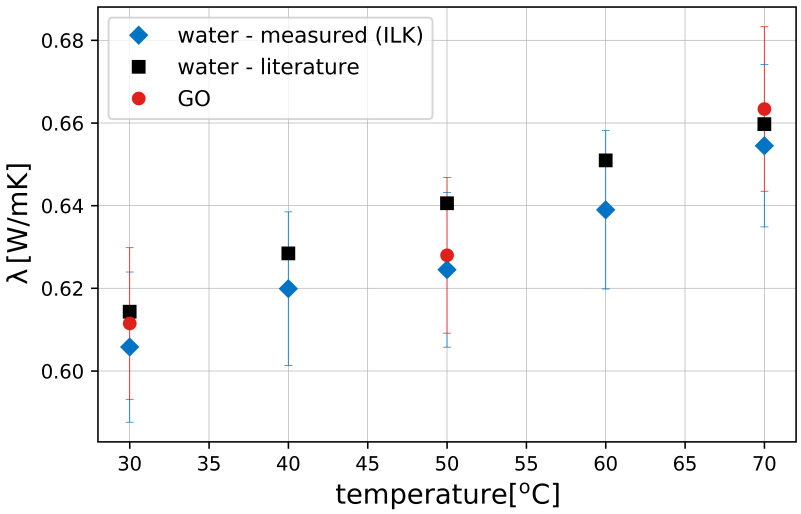

Figure 4.12: Thermal conductivity of graphene oxide nanofluid compared to water

Where q was heat flux imposed on the sample from the inner to the external cylinder, ΔT - difference between the temperatures of internal and external surfaces of cylinders, r_i and r_o - inner radius of the inner and outer cylinders, respectively (8 mm and 9 mm), l is the length of the cylindrical part (61 mm).

The relative changes in thermal conductivity were compared to the measured values of a base fluid instead of literature data. This approach includes systematic errors of the measurement device. Due to very low concentration of graphene oxide flakes in tested nanofluids, the enhancement varied between 0.5% and 1.5% in comparison with measured values of water (Fig 4.12). The trend was visible but the improvement was smaller than an experimental error (±3%).

Similar results were obtained using KD2 Pro analyzer [73]. This is a commercial device with an accuracy reported by manufacturer of ± 5%. Maximum enhancement for GO thermal conductivity compared to water was 5% at 50°C. Again, trend was visible but reported improvement was smaller than the measurement error. Reliability of KD2 Pro analyzer for measurements of nanofluids are commonly discussed in the research society but results seem to show proper trends [26] when the measurements are conducted precisely with high accuracy and caution. Device must be first calibrated with well-known fluids and all the parameters (among others temperature, sensor position and vibrations) must be controlled very carefully.

Viscosity

Figure 4.13 shows viscosity of graphene oxide nanofluid in dependence on shear rate. Measurements were performed using a Malvern Kinexus Pro stress-controlled rheometer with a cone-and-plate geometry (cone angle: 1° and diameter of 60 mm) [71]. Experiments were conducted at 21°C ± 0.1°C ensured by Peltier temperature control system. Steady-state conditions were obtained by waiting a holding time of 300 s. A logarithmic shear stress ramp included a shear rate range of 10 - 1000 1/s. The uncertainty of viscosity measurements were reported to be lower than 4%. GO nanofluid was shear thinning and showed moderately non-Newtonian behavior [71].

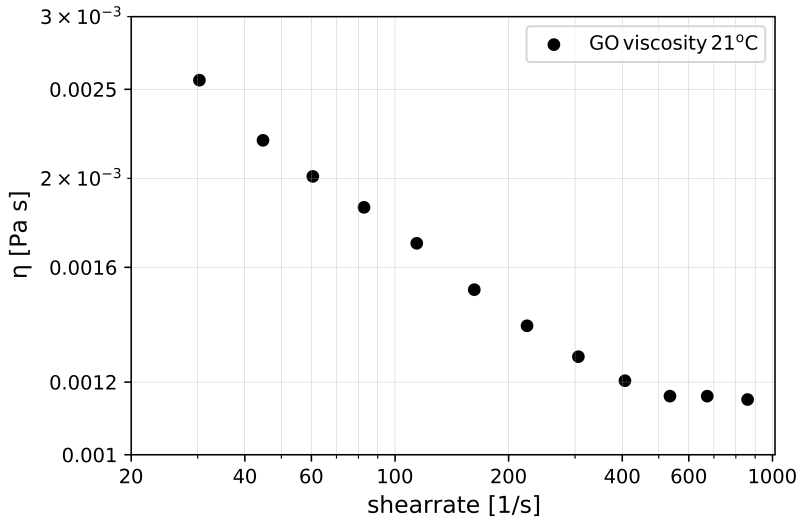

Figure 4.13: Viscosity of graphene oxide nanofluid [71]

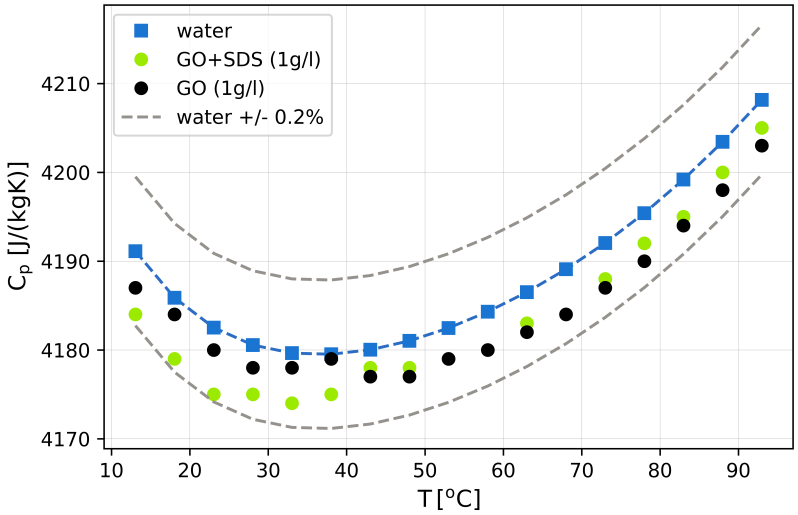

Figure 4.14: Heat capacity of graphene oxide nanofluids and water [216]

Specific heat capacity

Graphene oxide nanofluid was prepared in a similar way as described previously but concentration of graphene flakes was 1 g/l. Optional stabilization was 0.1 g/l of sodium dodecyl sulfate (SDS) what gave the same ratio of surfactant to GO flakes as in the sample of 0.1 g/l GO nanofluid.

The measurements were conducted using DSC device Q200 by TA Instruments at ILK Dresden [216]. Obtained results in comparison with water are presented in Fig. 4.14. Nanofluids reduced heat capacity but only up to 0.2% compared to water values. Thus, changes in specific heat capacity of used nanofluid may be neglected.

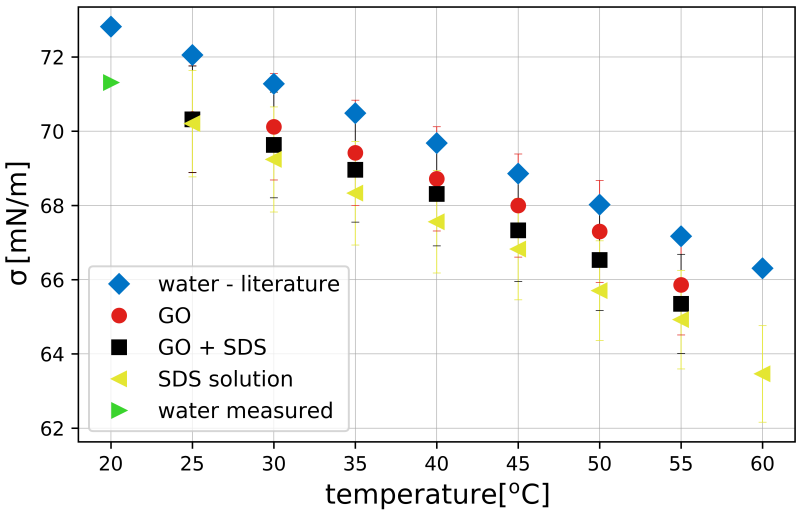

Figure 4.15: Surface tension of graphene oxide nanofluids and reference fluids [234]

Density

Measurements [71] confirmed that density (parameter needed for calculations of surface tension) of graphene oxide nanofluids was similar to that of water due to small concentration of particles. Differences were lower than 0.1‰which is below a measurement uncertainty.

Surface tension

Surface tension measurements were performed using tension meter PI-MT1A.KOM (Polon-Izot, Warsaw, Poland). The device was based on Noüy Ring methodology and operates with Zuidema and Waters coefficient [234]. A platinum ring had a diameter of 9.6914 mm with a wire diameter of 0.2030 mm. A 20 mL sample was maintained in the constant temperature controlled by Peltier system with an accuracy of 0.1 K. The device was calibrated with one hundred measurements of distilled water at 20°C. The mean value was 71.31 mN m^{-1} with a standard deviation of 0.18 mN m^{-1} which is approx. 2% lower that literature values from NIST database [234].

Figure 4.15 presents surface tension of graphene oxide nanofluids (with and without SDS), water, and water solution of sodium dodecyl sulfate (SDS). Presented results are an averaged values of ten measurements at a given temperature and include calibration error. It applies to all cases except water for which literature data is used.

Results in the temperature range of 25°C - 55°C show that addition of both - graphene oxide flakes and sodium dodecyl sulfate slightly reduced surface tension in comparison to water. Solution of surfactant (sodium dodecyl sulfate) had the biggest impact on the σ decrease - up to 3.3% difference compared to water. Addition of SDS to graphene oxide nanofluid caused a slight reduction of σ compared to nanofluid without surfactant. Although the amount of SDS in nanofluid was the same as in SDS solution, interaction between surfactant and graphene oxide flakes impeded surface tension reduction to the level possible with pure surfactant solution.

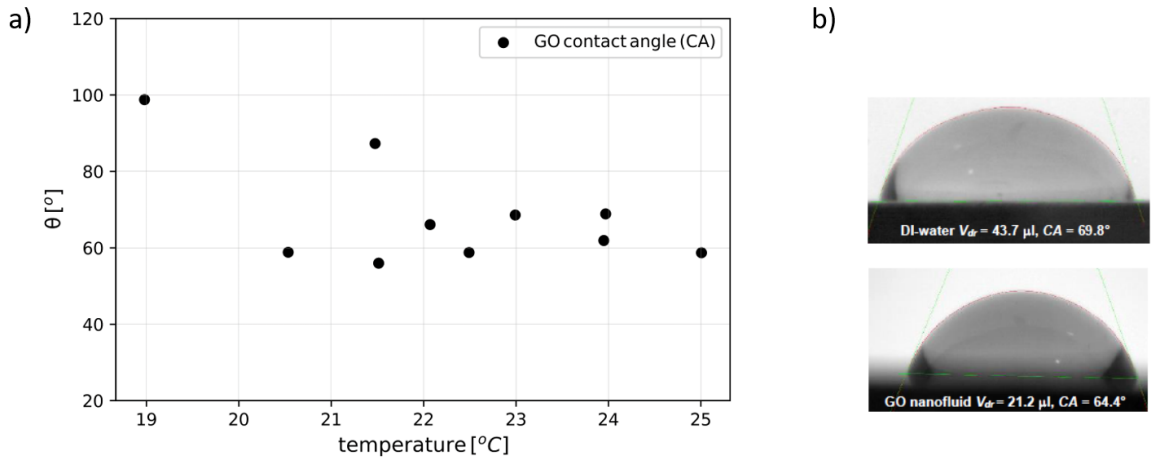

Figure 4.16: a) Raw data of contact angle measurements. Each point represents result from one of research teams, b) Examples of droplets of water (above) and GO nanofluid (below) from UJI [71]

Contact angle

Contact angle can be understood as a quantitative parameter describing wettability of a solid by a given liquid. Usage of nanofluids adds at least one additional phase (solid particles). For flow applications nanofluids are often considered as single-phase fluid with changed effective thermophysical properties. Devices used for contact angle measurements uses only small volume of fluid being immobile or in slow movement. Thus, particles may move independently from the base fluid creating e.g. coffee-ring following from capillarity flow or structural disjointing pressure [71], and treating them as single-phase fluid is questionable.

Traditional equipments available nowadays cannot recognize such effects. Literature provides a small amount of data which differs significantly and cannot be compared. For this reason, a benchmark study on contact angle of investigated graphene oxide and two more nanofluids was performed within NANOTENSION project of the COST Action CA15119 [71]. It includes results from nine research teams using various measurement devices (both commercial and customer-adapted) but the same nanofluids and stainless steel solid surface [71]. The summary of raw data for GO nanofluid (prepared in a way schematically presented in Fig. 4.3) in dependency of the temperature is presented in Fig. 4.16 with example of droplets for water and GO nanofluid. Results exclude Wilhelmy method focusing on dynamic contact angle what is later shown in Fig. 4.18. Different values at the same temperature comes from the same team but using different volumes of droplets.

Contact angle depends on the temperature, thus mass should be used instead of volume. For the experimental conditions, ambient temperature varied in the range of 19 - 25°C for different teams. The water density, and in consequence GO nanofluid, was between 998.55 kg/m^3 and 997.25 kg/m^3 what gave 1.3‰ of difference. It allowed for using volume instead of mass for contact angle calculations.

Based on the obtained data, a following equation for estimation of contact angle of nanofluid was proposed [71]:

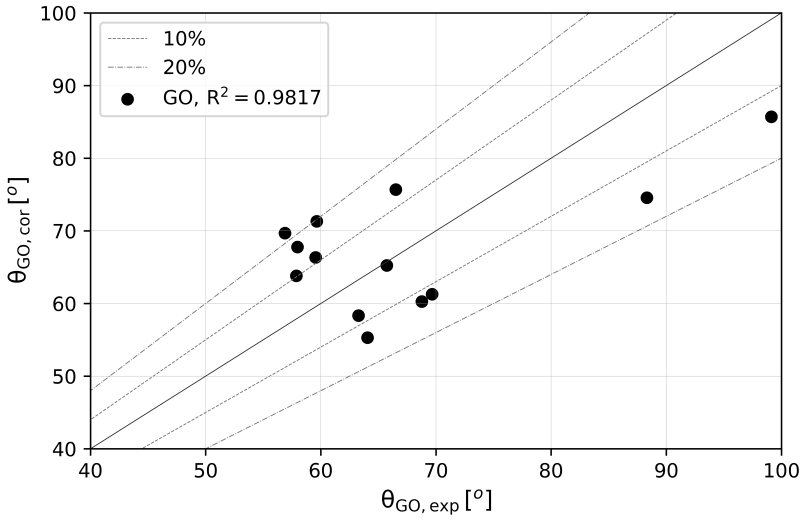

Figure 4.17: Comparison of experimental and fitted contact angles according to eq. 4.2 [71]

$$\theta_{fl}(t, V_{dr}) = a_{0,fl} + a_{t,fl}t + a_{V,fl}V_{dr}^{1/3} \tag{4.2}$$

Where: $\theta_{fl}(t, V_{dr})$ indicates the contact angle of a certain fluid at a given temperature t for a certain droplet volume V_{dr}.

For graphene oxide nanofluid coefficients $a_{0,fl}$, $a_{t,fl}$, $a_{V,fl}$ obtained by fitting data using Lavenberg-Marquardt algorithm and described in more details in [71] are:

- $a_{0,fl} = 183.079 \pm 44.077, [^\circ]$
- $a_{t,fl} = -4.388 \pm 1.881, [^\circ/^\circ C]$
- $a_{V,fl} = -797.574 \pm 504.529, [^\circ/\mathrm{m}]$

The quality check of this equation (4.2) - comparison of experimental and calculated contact values are presented in Fig. 4.17. This is the first equation available for estimation of contact angle of nanofluid and a coefficients are still characterized by high uncertainty. Even though, the same procedure applied to water values including independent data from literature showed compliance less that 10% in most cases [71].

Authors [71] performed a theoretical discussion that the contact-angle under zero-volume conditions depends on temperature and pressure what is also true for other thermophysical properties. It is impossible to conduct experiments with zero-volume droplets and decreasing droplet volume may lead to increase in experimental errors. Thus, the calculation were done using eq. 4.2 with assumption that the droplet volume is equal to 0. Resulting $\theta_{fl,0}(t, 0)$ is called limiting contact angle. As the water shows weak variation of pressure under ambient temperature, calculation of $\theta_{fl,0}$ allows for analyzing the temperature dependency. Comparison of limiting contact angles for nanofluid and according base fluid gave an information about the differences between each other.

This round robin test showed that contact angle of nanofluids may be measured by variety of techniques and equipments only if the experimental conditions and procedures (including preparation of nanofluids, cleaning of surface, volume of droplet, etc.) are taken

into consideration. Base fluid should always be measured for comparison. In opposite to other contact angle studies, the limiting contact angle (contact angle for zero-volume) can be treated as an effective thermophysical property characterizing the nanofluid. It is a function of the temperature, solid surface energy, solid-liquid interfacial interaction and the characteristics of nanofluid [71].

Dynamic contact angle

Movement of the liquid over the surface leads to changes in contact angle. This characterizes dynamic contact angle, including an advancing θ_{ad} and receding θ_{re} contact angle (see Fig. 4.18a). Advancing contact angle indicates maximum possible static contact angle for a given pair of fluid-surface, while receding gives the minimum value. Contact angle hysteresis is the difference between θ_{ad} and θ_{re}. It depends on the surface heterogeneity, solution impurities absorbing on the surface, or swelling, rearrangement or changes of the surface by the solvent [14].

Figure 4.18 presents the dynamic contact angle of graphene oxide nanofluid. Values depended on the state of surface - when it was dry (the first cycle) advancing contact angle showed its highest values. For wet surface (cycles no. 2-5 and the first one for θ_{re}), dynamic contact angle decreased but the difference was significantly higher for the θ_{ad}. This behavior is known as the initial formation of wetting lamella [71]. It means that nanofluid showed enhanced capability to wet stainless steel surface once it became wet.

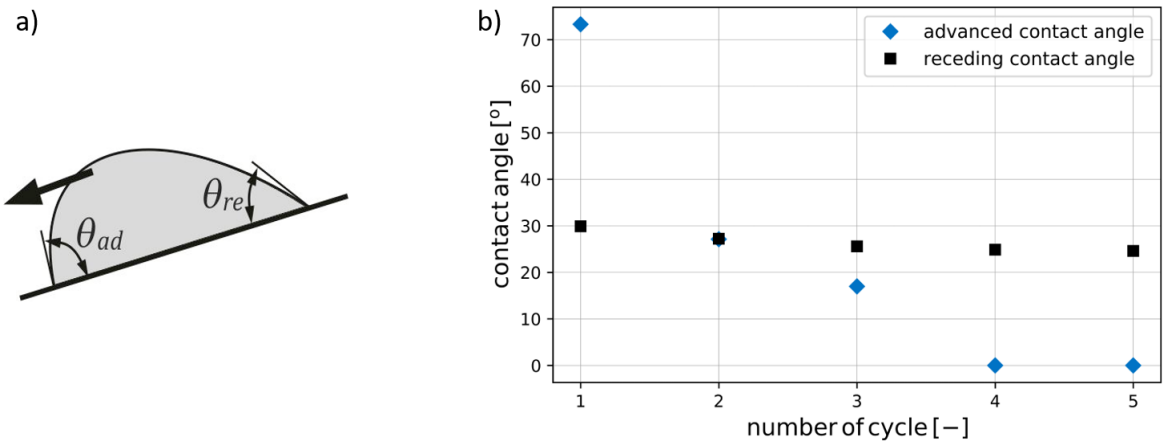

Figure 4.18: a) Advancing (θ_{ad}) and receding (θ_{re}) dynamic contact angle in the case of a liquid drop sliding on a tilting surface, b) Dynamic contact angle of graphene oxide nanofluid [73]

4.2 Other investigated nanofluids

Gold nanofluid

Gold nanofluids were chosen due to the highest thermal conductivity of gold among the metals (418 W/mK [207]). Both gold nanofluids with concentration of 100 mg/l were prepared directly in water by pulsed laser ablation technique by Particular GmbH (Germany). A 99.99% pure gold with thickness of 0.5 mm was placed in an ablation

chamber filled with 100 ml Mili-Q water. Laser (Nd:YAG ns-Laser Rofin Powerline E20) worked with a wavelength of 1064 nm, pulse duration of 7 ns, 15 kHz repetition rate, and pulse energy of 0.35 mJ. Laser beam was focused onto the gold sample by a F-Theta lens with a focal length of 100 mm. The resulting reddish-brown suspension shown in Fig. 4.1 (left) is gold nanofluid Au1 stabilized with 1% of polyvinylpyrrolidone (PVP). PVP is a soluble polymer and more details on this stabilizer can be found in Section 2.1. A photo of Au2 stabilized with 100μM of potassium hydroxide (KOH) does not exists but its appearance was practically the same as Au+PVP. Diameters of nanoparticles were determined at 20°C using a Nicomp 380 DLS-ZLS (Particle Sizing Systems, Inc., USA). Measured sizes were in the range of 50 and 70 mm with the mean value of 64.12 mm (Au+PVP) and 66.85 mm (Au+KOH). Due to low nanoparticles concentration, changes in thermal conductivity, density, and heat capacity were negligible [54, 100]. Viscosity measurements confirmed that nanofluid did not show a non-Newtonian behavior [100].

PVP prevents aggregation of nanoparticles via the repulsive forces and stabilizes the suspension due to hydrophobic components oriented into solvent and interacting with other carbon chains (steric hindrance effect) [98]. Kyrychenko et al. [103] conducted molecular dynamic simulations for silver nanoparticles of 4.5 nm diameter and PVP oligomers and the result is presented in Figure 4.19.

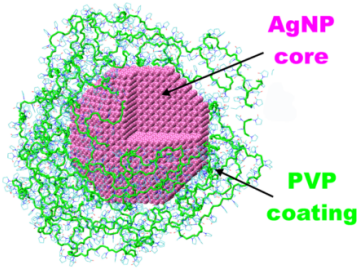

Figure 4.19: Molecular dynamic simulation of a silver nanoparticle coated with PVP [103]

In case of gold nanoparticles, density functional theory studies showed that hydrophilic components bind to gold surfaces through the oxygen atom mainly by Van der Waals interactions [98, 112]. PVP adsorption onto gold modify the surface free energy of different facets and too high polymer concentration may promote aggregation of the smaller nanoparticles [98], thus PVP concentration in investigated nanofluid was 1%.

Nanohorn nanofluid

Single wall carbon nanohorns, commonly called nanohorns are currently not available commercially. They are aggregates of graphene sheets and thousands of them tend to associate with each other to form structures like dhalia flower or buds [145]. Their overall diameters vary from tens to hundreds of nanometers. Due to numerous graphene flakes assembled in one nanohorn, the specific surface area reaches even up to several hundredths of square meter per gram [145]. Thus, this material is promising for heat transfer applications.

The nanohorn nanofluid was synthesized through two-step method by a high-pressure homogenization (Carbonium Srl, Italy) at CNR-ICMATE (Padua, Italy). Prepared nanofluid had a concentration of 0.1 g/L and was stabilized with 0.01 g/l of SDS. The average hydrodynamic sizes of nanoparticles determined with Dynamic Light Scattering

(DLS) varied between 100 nm and 150 nm. The suspension was stable against sedimentation for months.

The stabilization of nanohorn nanofluids was made with sodium dodecyl sulfate (SDS) with a relatively high concentration (10% of particles concentration). Thus, its influence on the results was determined by using water solution of SDS with the same concentration as in nanohorn nanofluid (0.01 g/l) as the next working fluid.

Silica nanofluid

A water-based silica (silicon dioxide) nanofluid was prepared by Fraunhofer- Institut für Keramische Technologien und Systeme IKTS from SIPERNAT® 22 S (Evonik Industries AG, Germany). The raw material was dispersed unfractionated with higher concentration and then diluted to concentration of 2 % vol. Addition of KOH ensured the pH-value of 10.5 required for working with copper pipe. The mean size of agglomerates were measured by manufacturer using DLS method (Zetasizer Nano ZS, Malvern Instruments GmbH, Germany). DLS gives two most common options to calculate the size of particles: xDLS called also Z-average or quantile calculation from size distribution. The most popular 50% method (x50) of the later one determines the size for which 50% of the total distribution are smaller than this size. Results obtained within these two methodologies may differ. In the case of used silica nanofluids, the values were 110 nm (xDLS) and 77 nm (x50).

A thermal conductivity of 2% silica nanofluid were determined under the temperature range of 20°C - 60°C using a static device – ring-gap apparatus [28] based on coaxial-cylindrical cell method. For the temperature of 20°C - 30°C the thermal conductivity of silica nanofluids was about 2% higher than that of water and decreased to about 1% at 60°C.

Chapter 5

Two-phase closed thermosyphon

5.1 Test rig and measurement procedure

Experiments were carried out using a two phase closed thermosyphon located in the Institut für Luft- und Kältetechnik (ILK) in Dresden, Germany. Figure 5.1 a) presents a photo of the complete set-up. 1800 mm long device made of copper (CW024A) pipe had an inner diameter of 20 mm and a wall thickness of 1 mm. Evaporator and condenser sections had a length of 400 mm and both were wrapped with copper pipes working as coiled heat exchangers. Water inside the coils heated and cooled evaporator and condenser sections, respectively. Two thermostats LAUDA Eco RE 1050 GW (LAUDA, Germany) with a temperature constancy of ± 0.02K controlled temperatures of circulating mediums. Inlet and outlet temperatures of water were measured directly near the thermosyphon using Pt 100 elements (TMG Temperaturmesstechnik Geraberg GmbH, Germany) with a working range of -20°C to +150°C. An accuracy of sensors were ± 1/3 (0.3 K + 0.005 ϑ) where ϑ was the value of currently determined temperature. Thus, maximum uncertainty of ± 0.24 K was imputed to the highest applied temperature (85°C). Volume fluxes of ± 12 l/h with a maximum error of ± 0.76 l/h were measured using two Krohne Optiflux 5000 (KROHNE, Germany). The whole device and water connections were fully insulated with an Armaflex insulation.

A custom-made sensor (TMG Temperaturmesstechnik Geraberg GmbH, Germany) shown in Fig. 5.1 c measured temperature of working fluid inside the evaporator. The probe was connected to the lowest part of the thermosyphon and consisted of six Pt 100 elements positioned at different heights of the section (80, 125, 170, 215, 260, and 305 from the bottom of the device) what is shown in Fig. 5.1 c. Operating range of these sensors was from -20°C to +150°C. The accuracy was determined as ± (0.15 K + 0.002 ϑ). Thus, maximum uncertainty of measurement was ± 0.32 K for the highest applied temperature (85°C).

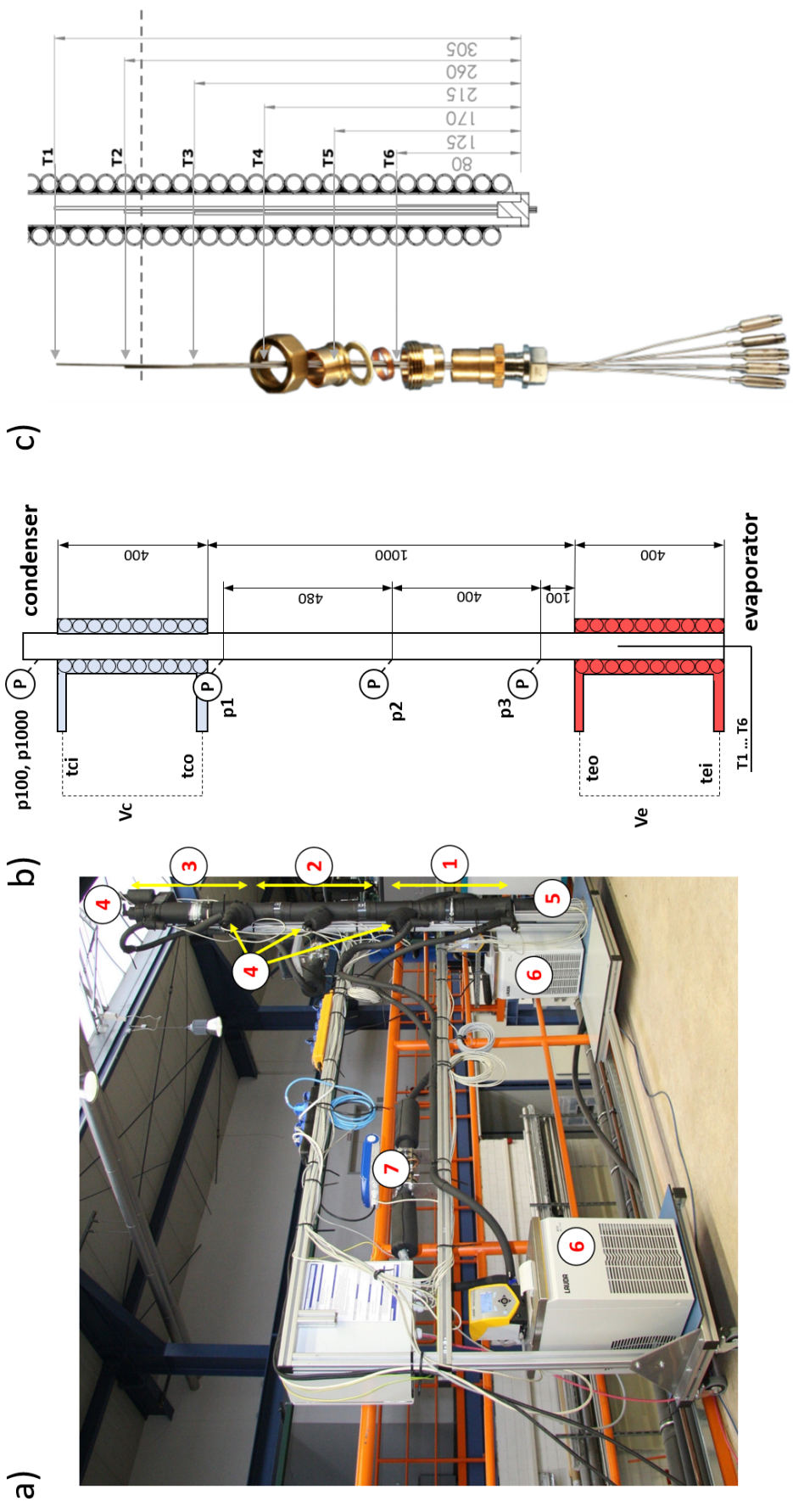

Figure 5.1: a) Photo of the test rig: 1 - evaporator, 2 - adiabatic section, 3 - condenser, 4 - pressure transmitters, 5 - temperature sensor, 6 - thermostats, 7 - flow meter. b) Scheme of thermosyphon including dimensions. c) Custom-made temperature sensor (no. 5)

Internal pressure was measured at four different positions what marked in Fig. 5.1 b. Three transmitters with a measurement range of $0 - 400$ Pa were placed along the adiabatic section and two more just below the end cap of the device. At the highest point two pressure gauges with various measurement ranges ($0-10^4 \pm 2.5$ Pa and $0-10^5 \pm 250$ Pa) worked simultaneously to ensure high quality of data. All sensors (TRAFAG GmbH, Germany) had a response time of 1 ms. Filling nozzle were located at the top of thermosyphon using the same connection as pressure transmitters. 85 ml of working fluid in a liquid phase was supplied to the device what filled almost 68% of the evaporation section (so-called filling ratio of 0.68).

Data acquisition was provided by a message-device consisting of a high-resolution analogue digital converter transforming the signal from measurements. Its connection with ProfiSignal software (Delphin Technology AG, Germany) allowed to supervise results on-line at PC.

All the experiments followed a standardized procedure. In both cooling and heating cycles volume fluxes of water were kept constant at the value of 12 $\pm$ 0.76 l/h. Each working fluid was tested within two measurement series: inlet temperature of cooling water equal to 15°C (mean measured value was 14.59 $\pm$ 0.12°C) and 25°C (25.06 $\pm$ 0.14°C). In plots presented in this thesis c25 indicates experimental series of $t_{ci} = 25$°C and c15 of $t_{ci} = 15$°C. Temperature of heating medium varied in the range of 30°C and 85°C at 5 K steps. Losses between heat source (thermostat) and device caused that real maximum inlet temperature of heating water was 80.56 $\pm$ 0.23°C.

When volume fluxes and inlet temperatures of heating and cooling water in coils stabilized, the measurement took an hour for each combination of parameters. After finishing the experiments with a given working fluid, the inner surface of the device was analyzed with a SOMIKON HD endoscopy camera. Images were shot to evaluate if nanoparticles deposited into macro-scale porous layers. Then, the surface was very carefully cleaned mechanically with brushes and lint-free cleaning rags, and rinsed with acetone. After drying, the surface was checked again with the endoscopy camera. If no particles or other surface pollution were found, the device was closed and evacuated. Then, filling procedure was repeated with the next working fluid. For graphene oxide nanofluids, agglomerates remaining in working fluid taken out from the thermosyphon after experiments were additionally characterized under the scanning electron microscope (SEM) to check their structure.

The following sections analyze data averaged over the time of experiment (an hour for each combination of parameters). Color and symbol code is unified with reference to the working fluid and experimental series (understand as inlet temperature of cooling water (15°C or 25°C) and changing temperature of heating water).

5.2 Error analysis

The error analysis presented in the following figures is based on Gaussian law of error propagation.

Heat fluxes in the evaporator and condenser sections were calculated as:

$$Q = \dot{V} \cdot \rho \cdot C_p \cdot (t_{out} - t_{in}) \tag{5.1}$$

Where $\dot{V}$ is volume flow rate, ρ density of water at operating conditions, C_p specific heat capacity at a constant pressure, t_{out} and t_{in} inlet and outlet temperatures of water,

respectively. Thus, uncertainty was determined as:

$$\Delta Q = \sqrt{\left(\frac{\delta Q}{\delta \dot{V}} \cdot \sigma_{\dot{V}}\right)^2 + \left(\frac{\delta Q}{\delta \rho} \cdot \sigma_{\rho}\right)^2 + \left(\frac{\delta Q}{\delta C_p} \cdot \sigma_{C_p}\right)^2 + \left(\frac{\delta Q}{\delta t_i} \cdot \sigma_{t_i}\right)^2 + \left(\frac{\delta Q}{\delta t_o} \cdot \sigma_{t_o}\right)^2} \tag{5.2}$$

And following:

$$\Delta Q = \sqrt{\left[\rho \cdot C_p \cdot (t_i - t_o) \cdot \sigma_{\dot{V}}\right]^2 + \left[\dot{V} \cdot \rho \cdot C_p \cdot \sigma_{t_i}\right]^2 + \left[-\dot{V} \cdot \rho \cdot C_p \cdot \sigma_{t_o}\right]^2} \tag{5.3}$$

Overall thermal resistance of the thermosyphon was calculated using eq. 3.3 with an experimental uncertainty:

$$\Delta R_{th} = \sqrt{\left[\frac{1}{Q_c} \cdot \sigma_{T_e}\right]^2 + \left[-\frac{1}{Q_c} \cdot \sigma_{T_c}\right]^2 + \left[\frac{T_c - T_e}{Q_c^2} \cdot \sigma_{Q_c}\right]^2} \tag{5.4}$$

5.3 Calibration of the thermosyphon

Insulation covered the whole test-rig but neither the device or water hoses could be ideally protected from heat losses. For this reason, analysis of the difference between heat supplied to the evaporator and heat released in the condenser was carried out.

Graphene oxide nanofluids

Figure 5.2 presents thermal losses along the thermosyphon expressed as a difference between heat released in condenser and heat provided to the evaporator (left), and percentage difference (right). For an inlet temperature of cooling water of 25°C, these losses were in the range of -2.9% and -9.4% with a mean value of -6.56% (Fig. 5.2). In case of t_{ci} = 15°C, the losses range was between -5.4% and 10.5% with a mean value of 0.8% (Fig. 5.3). The values above 0% were a result of higher ambient temperature than the temperature of condenser section. This acted as an external source of heat to the cooling water. Losses on water cycles between thermostats and the thermosyphon were excluded from these calculations. Inlet and outlet temperatures were measured directly before and after the coil heat exchangers at evaporator and condenser sections.

Nanofluids based on silica, nanohorn and gold nanoparticles

Thermal losses along the thermosyphon filled with nanofluids based on silica, nanohorn and gold nanoparticles are presented in Fig. 5.4 for t_{ci} = 25°C and Fig. 5.5 for t_{ci} = 15°C. These losses were between -4.5% and -14.9% with a mean value of -7.1% for t_{ci} = 25°C. Experimental series with t_{ci} = 15°C noticed thermal losses in the range from -5.3% to 8.4% with a mean value of -2.5%. Again, values above 0% came from higher ambient temperature than the temperature in cold part of the thermosyphon (condenser). The lowest values were a result of lower ambient temperature than usual. Except few points, thermal losses were lower than 10%.

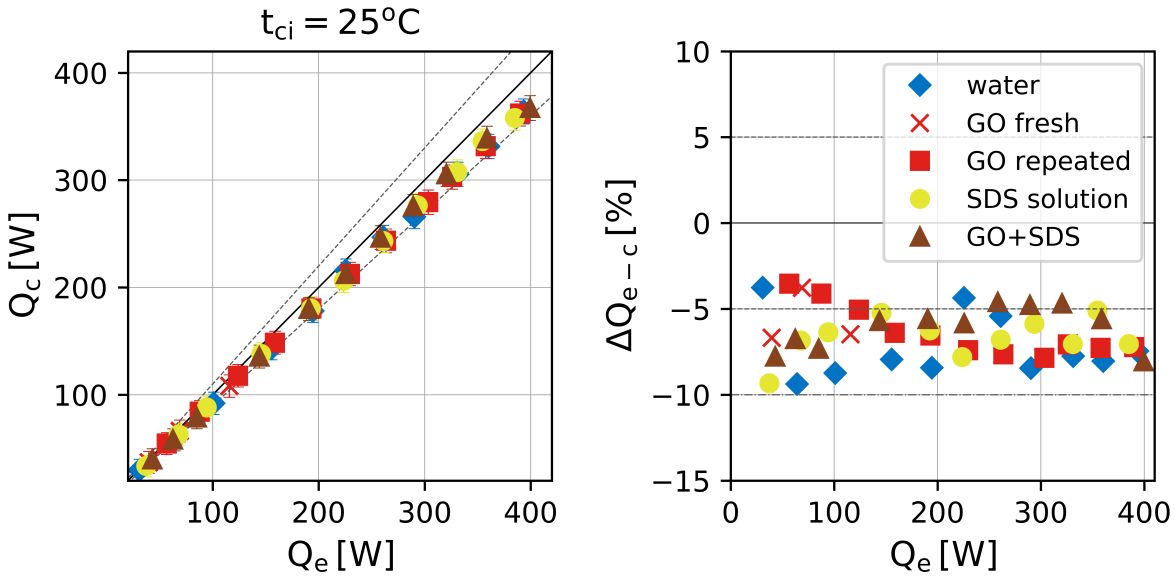

Figure 5.2: Thermal losses along the thermosyphon for GO-related working fluids (inlet temperature of cooling water: 25°C): (left) difference between heat supplied to the evaporator vs heat released in condenser, (right) percentage loss of heat

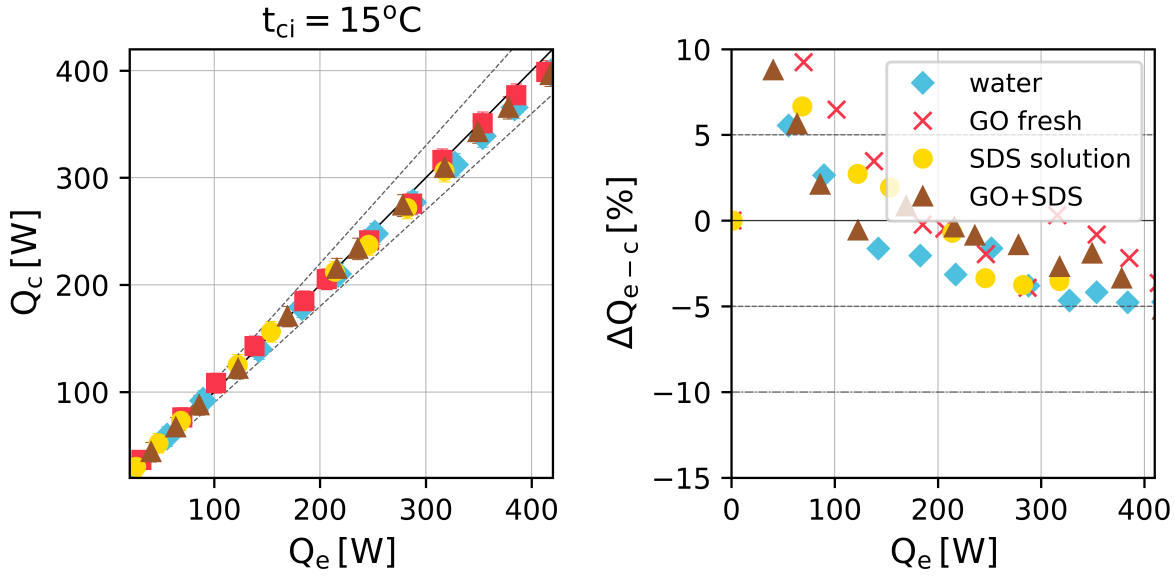

Figure 5.3: Thermal losses along the thermosyphon for GO-related working fluids (inlet temperature of cooling water: 15°C): (left) difference between heat supplied to the evaporator vs heat released in condenser, (right) percentage loss of heat

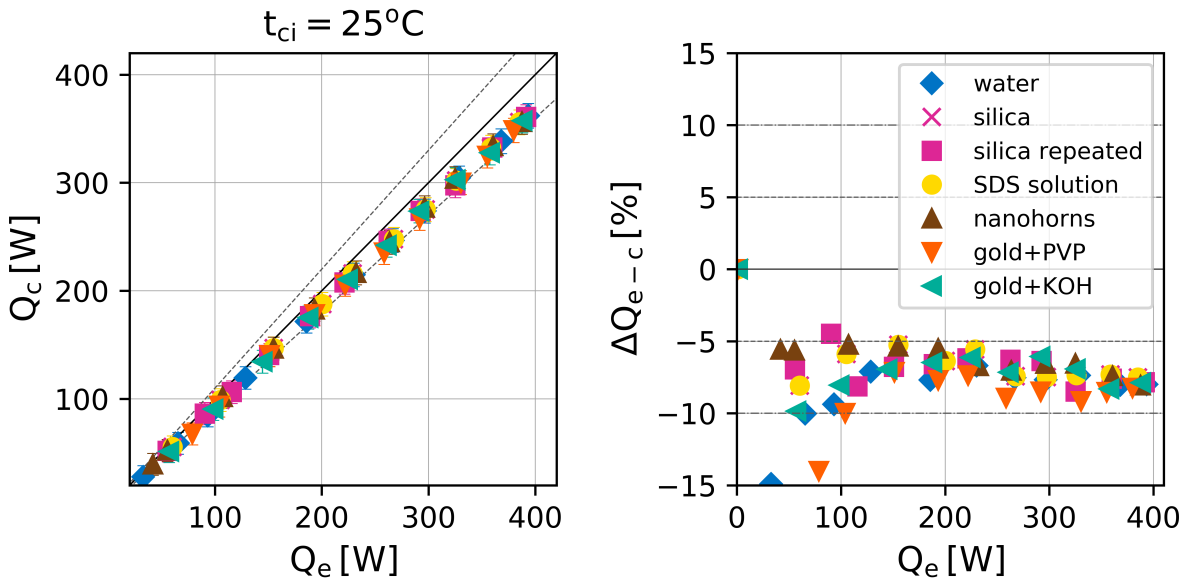

Figure 5.4: Thermal losses along the thermosyphon for nanofluids based on silica, nanohorn and gold nanoparticles and related base fluids (inlet temperature of cooling water: 25°C): (left) difference between heat supplied to the evaporator vs heat released in condenser, (right) percentage loss of heat.

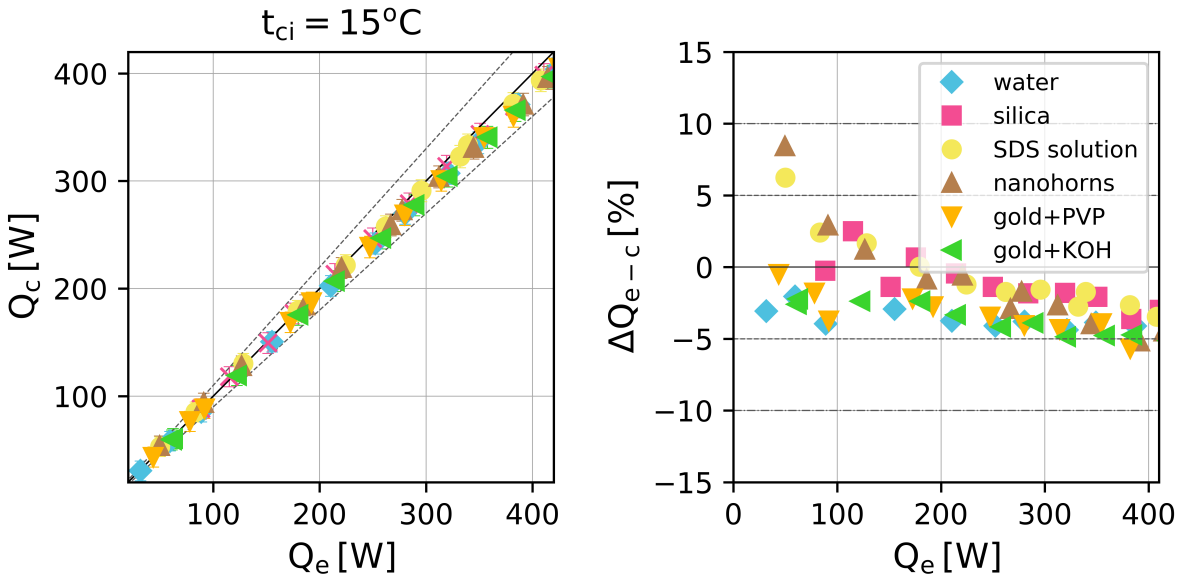

Figure 5.5: Thermal losses along the thermosyphon for nanofluids based on silica, nanohorn and gold nanoparticles and related base fluids (inlet temperature of cooling water: 15°C): (left) difference between heat supplied to the evaporator vs heat released in condenser, (right) percentage loss of heat.

5.4 Thermal resistance of a thermosyphon

One of fundamental indicators determining efficiency of heat transfer through a thermosyphon is its overall thermal resistance defined according to eq. 3.3. In this case, mean temperatures of evaporator and condenser (T_e and T_c) were calculated as an arithmetic mean from inlet and outlet temperatures of heating and cooling water.

Graphene oxide nanofluids

Figures 5.6 and 5.8 present an overall thermal resistance of a thermosyphon correlated with a heat flux released in the condenser for GO-related working fluids. Circles highlight the same operating conditions (inlet temperatures and volume fluxes of heating and cooling medium). The dependence between the thermal resistance and inlet temperature of heating water is shown in Fig. 5.7 for $t_{ci} = 25°C$ and Fig. 5.9 for $t_{ci} = 15°C$. Data shown in these plots highlights additionally that differences in inlet temperatures caused by changes in ambient temperature varied in a very narrow range and their impact on the results was negligible.

Increase of the evaporator temperature (and consequently heat flux) reduced thermal resistance of the device. It reached almost a constant value of 0.078 ± 0.003 W/K for all tested working fluid when heat flux released in the condenser section exceeded the value of approx. 170 W. It corresponded to the temperature of heating water of about 55°C. For this regime, maximal thermal capacity of the thermosyphon was determined by partial thermal resistances not depending on working fluid.

Significant decrease in thermal resistance of the thermosyphon was visible at low temperatures of the evaporator, and in consequence low temperature differences between two ends of the device (evaporator and condenser). For these conditions, usage of nanofluids caused both lower thermal resistance and increased amount of heat transferred through a thermosyphon when compared to the base fluid for the same operating parameters.

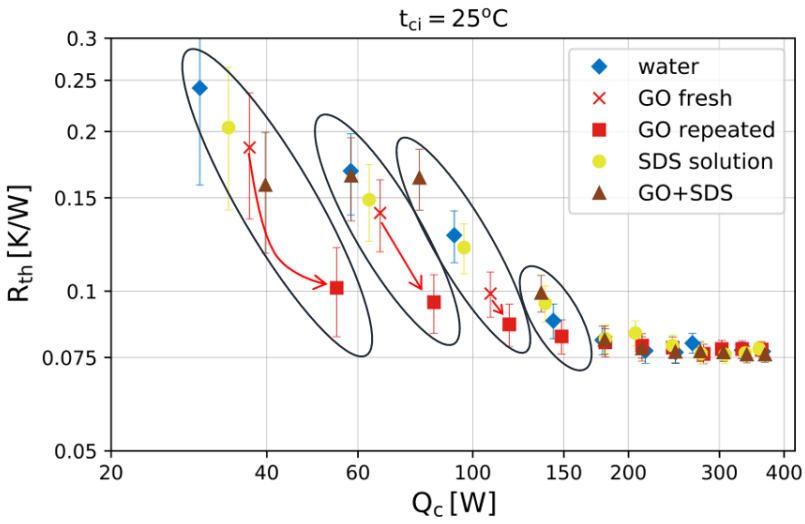

Figure 5.6: Thermal resistance of thermosyphon with GO-related working fluids in dependence on heat released in the condenser (inlet temperature of cooling water: 25°C)

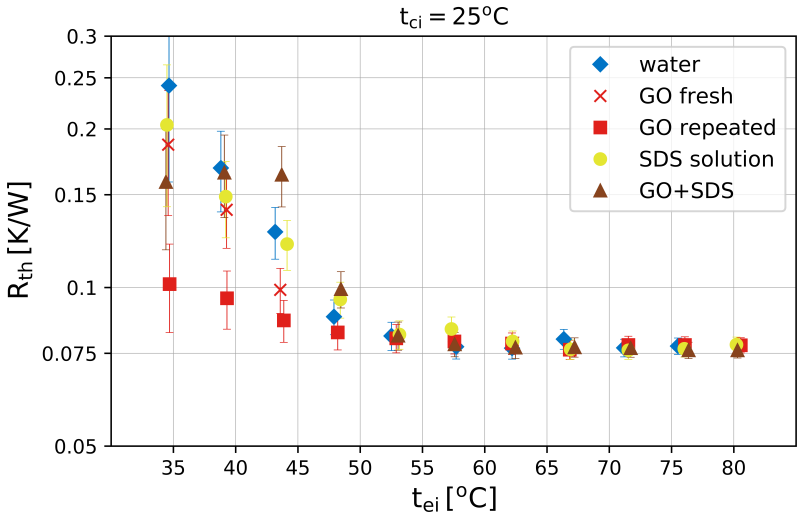

Figure 5.7: Thermal resistance of GO-related working fluids in dependence on inlet temperature of heating water (inlet temperature of cooling water: 25°C)

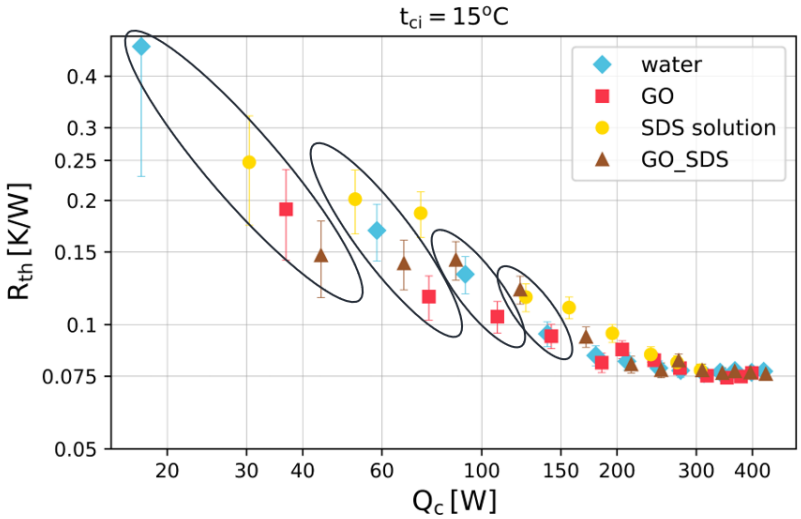

Figure 5.8: Thermal resistance of GO-related working fluids in dependence on heat released in the condenser (inlet temperature of cooling water: 15°C)

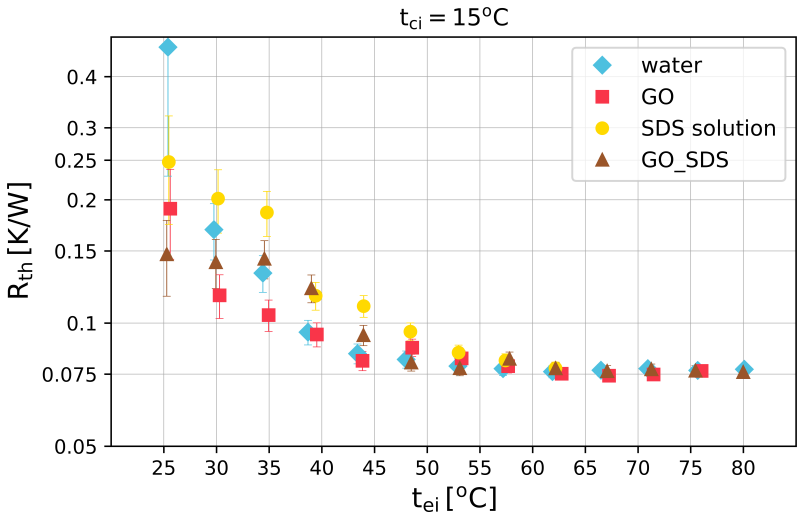

Figure 5.9: Thermal resistance of GO-related working fluids in dependence on inlet temperature of heating water (inlet temperature of cooling water: 15°C)

Red symbols (crosses and squares) indicates the same working fluid: GO nanofluid without surfactant at a cooling temperature of 25°C. The differences marked with red arrows in Fig. 5.6 came from the time of experiments. Points marked with crosses were obtained directly after filling procedure, while squares show results of experiments repeated after finishing the first measurement series ($t_{ei} = 35 - 80$°C at 5 K steps). Fresh GO nanofluid (red cross) reduced overall thermal resistance of the thermosyphon for low heat load by about 20% compared to water. After approx. 20 hours of the device operation, R_{th} decreased to about 42% of value for base fluid. It suggests transient-like characteristics of the results, at least at the beginning of thermosyphon operation. This agrees with previously published literature [29, 102]. At the beginning of series with fresh nanofluid, nanoparticles were equally dispersed in the volume of working fluid. During boiling *backing process* occurred - nanoparticles deposited into layers on the inner surface of the evaporator. Photo of this surface taken with endoscopy camera is presented in Fig. 5.35 b. This process took certain amount of time (here: approx. 12 hours of thermosyphon operating) and caused an improvement in heat transfer efficiency.

Deposition of nanoparticles affects surface characteristics, including chemistry, wettability, and roughness what alters surface energy and force balance at the triple line. This lead to increase in density of nucleation sites, and consequently improved boiling process. Another possible changes are in wickability - interplay between wettability and porosity. If deposited layer was porous, the fresh portion of fluid could wet the surface below growing bubbles decreasing the overheating. Increase in heat transfer area due to deposition of particles should not play an important role because the changes are small compared to whole available and uncovered surface. Unfortunately, detailed characteristic of this layer was not possible with available design of the test-rig and mechanisms described above could not be experimentally proven. Current state of knowledge on deposition of nanoparticles is described in section 3.1.

Reduction of graphene oxide starts at the temperatures of about 50 - 60°C. This process may affect wettability of particles. Reduced graphene oxide (rGO) is hydrophobic but it can absorb water into its structure after being sufficient time in contact with water

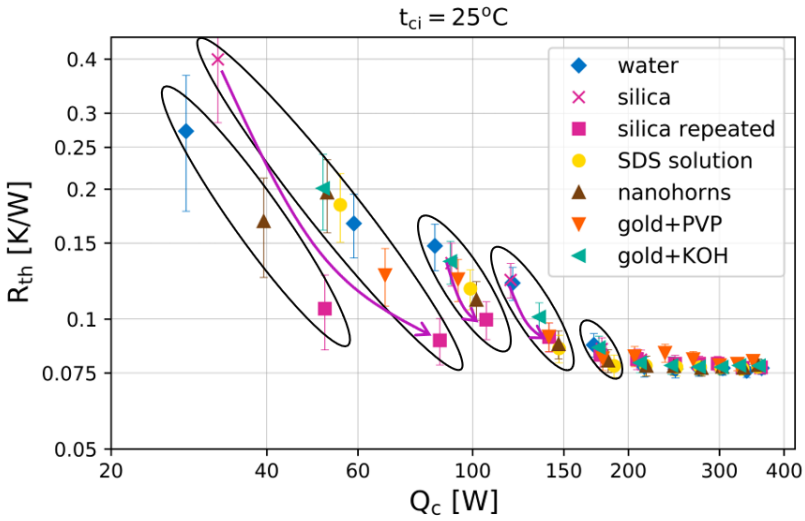

Figure 5.10: Thermal resistance of the thermosyphon with various working fluids in dependence on heat released in the condenser (inlet temperature of cooling water: 25°C)

[5]. Kamatchi et al. [83] reported dual wettability of rGO caused by activation of the carboxyl groups on the flake surface. Contact angle on both rough and smooth surfaces decreased after boiling experiments conducted with graphene oxide nanofluids [83]. It could lead to capillary wicking. Additionally, deposition process increased permeability improving conditions for capillary wicking [5].

Literature reports exceptionally high values of thermal conductivity (even up to 3500 - 5300 W/mK in the length direction [150, 231]) and surface area (from 736 m^2/g [125] to 2630 m^2/g [231]) of graphene materials. Thus, particles deposited on the inner surface of the evaporator could act as a thermal bridge between wall and working fluid. It had bigger impact at low heat loads where this thermal resistance is more important in reference to the overall thermal resistance than in case of high heat loads and developed boiling.

Attachment of SDS surfactant to graphene material (Fig. 5.37 f) could inhibit interaction between particles and inner surface of the evaporator section. Addition of surfactant (SDS) decreased thermal capacity of the thermosyphon in comparison to graphene oxide nanofluid.

Nanofluids based on silica, nanohorn and gold nanoparticles

Thermal resistance of the thermosyphon with various working fluids (including nanofluids based on silica, nanohorn and gold nanoparticles) in dependence on heat released in the condenser for inlet temperature of cooling water equal to 25°C is shown in Fig. 5.10. Nearly no effect of working fluid was found for heat loads higher than approx. 200 W what corresponded to the inlet temperature of heating water higher than 50°C for t_{ci} = 25°C (Fig. 5.11). Overall thermal resistance of the device in this case was 0.078 K/W ($\sigma = 2.1 \times 10^3$ K/W). For experimental series with t_{ci} = 15°C (Fig. 5.12 and 5.13), the limiting values were 260 W and 60°C, respectively.

Circles in Fig. 5.10 and 5.12 indicate the same operating conditions (inlet temperature of heating and cooling medium). For 30°C $\leq t_{ei} \leq$ 45°C and t_{ci} = 15°C water caused the highest overall thermal resistance of the thermosyphon. Nanohorn and gold nanoflu-

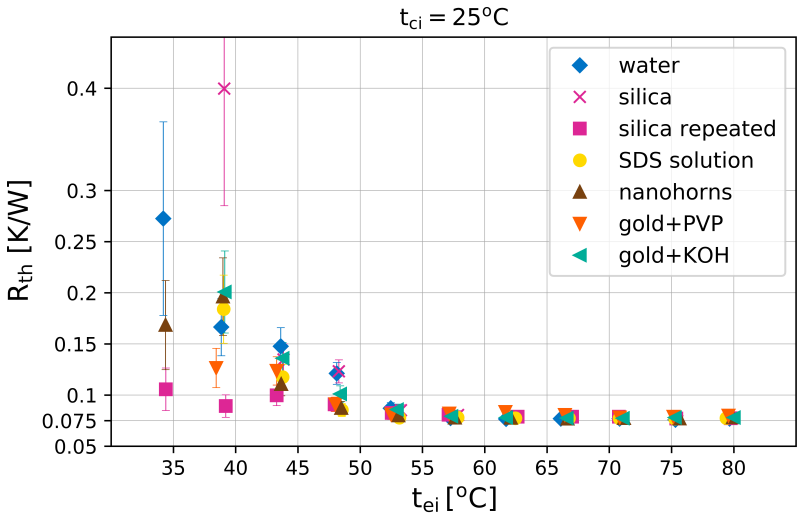

Figure 5.11: Thermal resistance of the thermosyphon with various working fluids in dependence on inlet temperature of heating water (inlet temperature of cooling water: 25°C)

ids enhanced heat transfer efficiency for most combinations of the operating conditions but especially for t_{ci} = 15°C. SDS solution showed very similar behavior to nanohorn nanofluid. In general, the lower the inlet temperature of heating water, the higher R_{th} reduction caused by nanofluids in comparison to water.

Application of silica nanofluid (pink squares, *silica repeated*) resulted in the lowest thermal resistance with almost a constant value of 0.077 K/W ($\sigma = 2.1 \times 10^3$ K/W) for t_{ei} higher than 50°C (35°C for t_{ci} = 15°C). For experimental series with condenser temperature of t_{ci} = 25°C and heating water temperature lower than 50°C, the thermal resistance was 0.093 K/W ($\sigma = 5.6 \times 10^3$ K/W). Pink crosses (*silica*) represents results from the first experimental series conducted shortly after filling procedure with silica nanofluid. These first points showed higher thermal resistance than water but values decreased with each next point. Repeating these test cases led to significant reduction in the overall thermal resistance of the device (see arrows in Fig. 5.10). It was time needed for *backing process* - forming the strong deposition layer on the evaporator wall which affected heat transfer in a way similar to that described for GO nanofluids. It highlighted time-dependent character of the nanofluid effect, at least at the beginning of thermosyphon operation. But after some period of time the thermal efficiency was increased for the low heat loads and small temperature differences between the both ends of the thermosyphon. These are often problematic conditions for heat transfer so nanofluids may become a promising alternative for such applications.

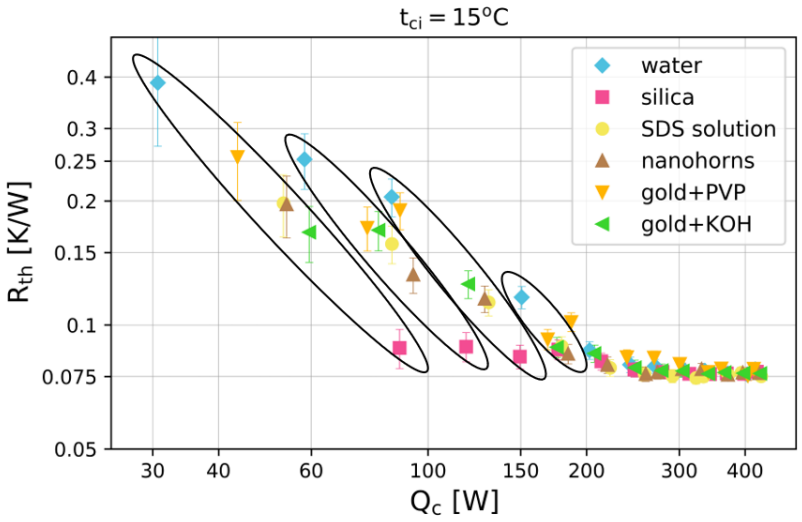

Figure 5.12: Thermal resistance of the thermosyphon working with various working fluids in dependence on heat released in the condenser (inlet temperature of cooling water: 15°C)

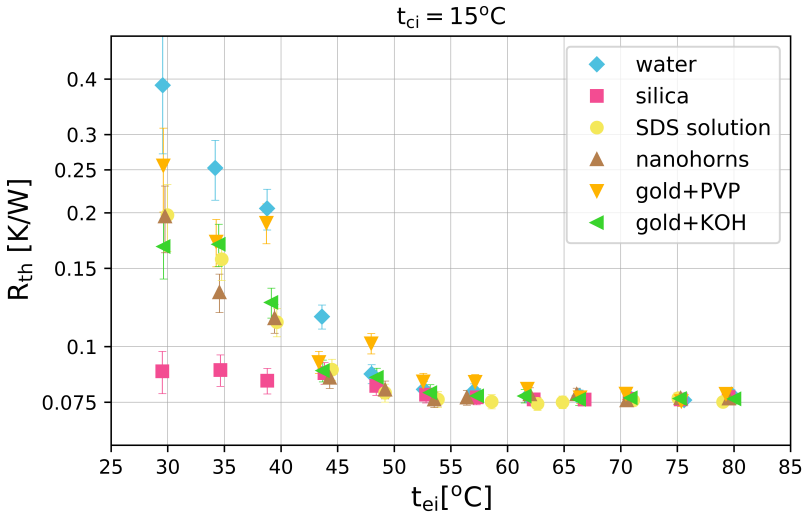

Figure 5.13: Thermal resistance of the thermosyphon with various working fluids in dependence on inlet temperature of heating water (inlet temperature of cooling water: 15°C)

5.5 Boiling curves

Boiling curves are expressed as dependence between heat supplied to the evaporator and overheating at the evaporator wall. Overheating was calculated as:

$$\Delta T = t_e - t_{sat} \tag{5.5}$$

Where: t_e is mean temperature of heating water and t_{sat} is a saturation temperature following the measured pressure at given conditions.

Graphene oxide nanofluids

Fig. 5.14 shows boiling curves for inlet temperature of cooling water of 25°C and Fig. 5.15 for 15°C case. GO nanofluid without surfactant significantly affected heat transfer processes in the thermosyphon for small heat loads. Boiling curve was shifted to the left compared with the one corresponding to water. It means that more heat was removed from the surface at the same temperature or/ and that temperature conditions changed and surface was less overheated. Analogous to overall thermal resistance, differences between working fluids disappeared for the overheating higher than 10 K for t_{ci} = 25°C (13 K for t_{ci} = 15°C). It refers to heat supplied to the evaporator of approx. 260 W for t_{ci} = 25°C (280 W for t_{ci} = 15°C).

GO+SDS nanofluid showed behavior similar to water. Exceptions were heating temperatures of 50°C and 55°C at t_{ci} = 15°C series. At these operating conditions, two parallel states of boiling occurred and randomly switched between each other. Each regime gave different results what is marked with black circles in Fig. 5.15. At these temperatures reduction of graphene oxide may occur. It could have an impact on the boiling process but detailed mechanisms behind this behavior were not found out. This phenomena was not seen in any other test case.

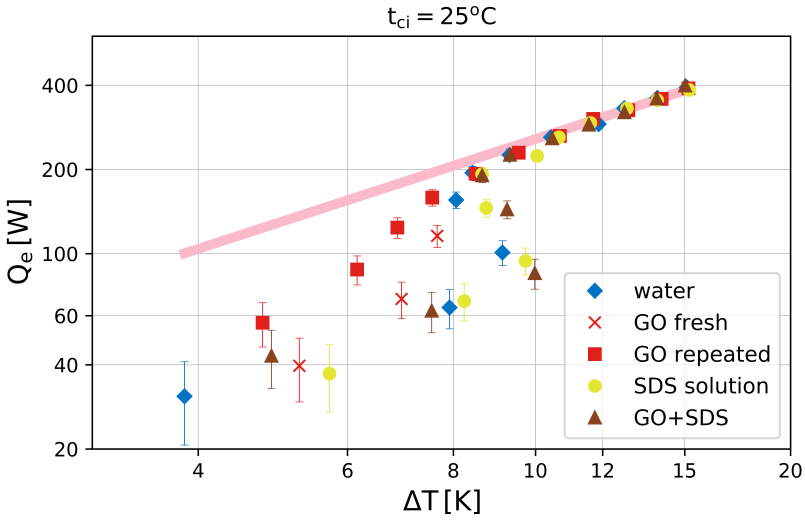

Figure 5.14: Boiling curves for experimental series with GO-related working fluids (inlet temperature of cooling water of 25°C)

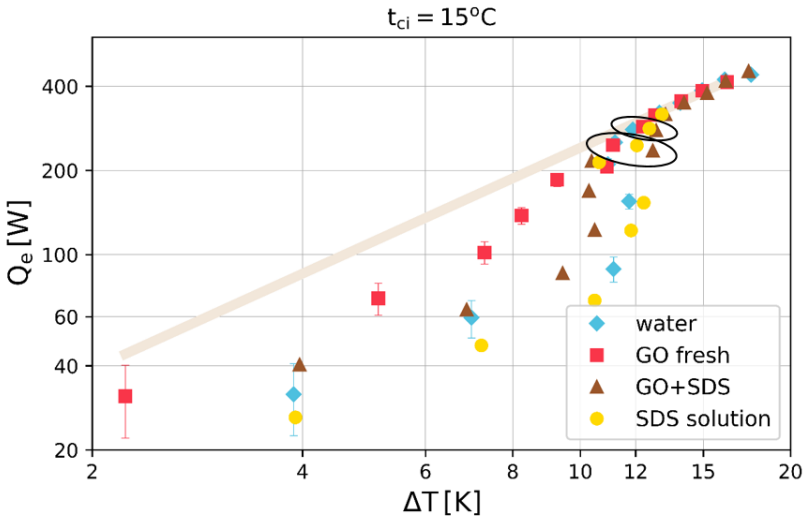

Figure 5.15: Boiling curves for experimental series with GO-related working fluids (inlet temperature of cooling water of 15°C)

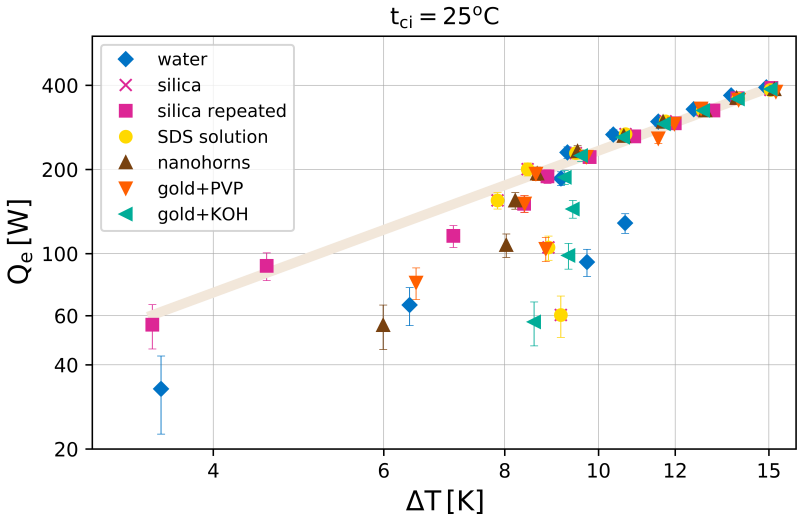

Figure 5.16: Boiling curves for experimental series with nanofluids based on silica, nanohorns, and gold nanoparticles and related base fluids (inlet temperature of cooling water of 25°C)

Nanofluids based on silica, nanohorn and gold nanoparticles

Boiling curves for nanofluids based on silica, nanohorn and gold nanoparticles are presented in Fig. 5.16 for $t_{ci} = 25°C$ and Fig. 5.17 for $t_{ci} = 15°C$.

Investigated nanofluids changed boiling regimes, especially for low heat loads, analogical to GO nanofluids. For both inlet temperatures of cooling water, values obtained for silica nanofluid formed almost nearly straight lines in a plot with log-log axis. Results for different working fluids reached similar values and joined this line at about 200 W. Silica reduced wall overheating and increased the amount of heat transferred at the same operating conditions. Mean temperature of the thermosyphon was shifted in this case,

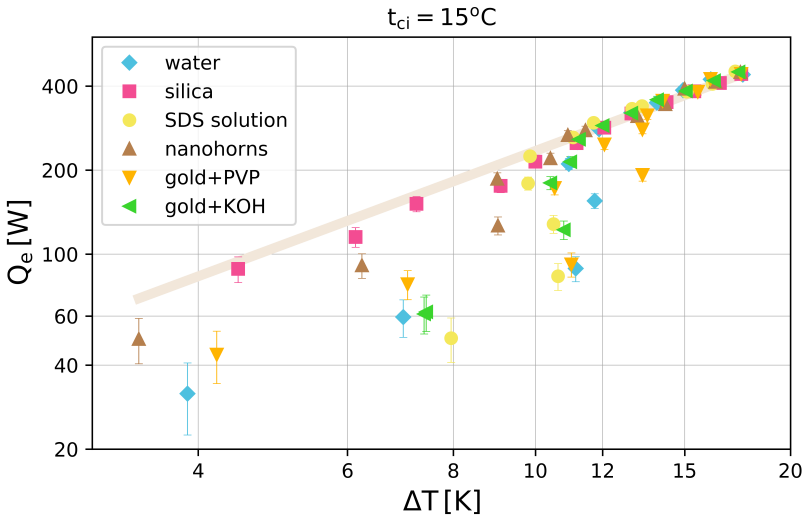

Figure 5.17: Boiling curves for experimental series with nanofluids based on silica, nanohorns, and gold nanoparticles and related base fluids (inlet temperature of cooling water of 15°C)

although heating and cooling temperatures were the same for all tested working fluids. Nanofluids changed the working point of the thermosyphon for low evaporator temperatures, and thus low heat fluxes.

5.6 Heat transfer capacity

Thermosyphons are used in various applications. The amount of heat transported through thermosyphon from hot to cold side is an important factor in cost analysis and designing process. The percentage increase of the amount of thermal energy transferred by a thermosyphon for a given fluid $Q_{c,NF}$ compared to the reference working fluid (base fluid) $Q_{c,ref}$ at the same working conditions was calculated as:

$$\Delta Q_c = 100\% \left(\frac{Q_{c,NF}}{Q_{c,ref}} - 1 \right) \tag{5.6}$$

Graphene oxide nanofluids

The impact of working fluid on the amount of energy transfered through a thermosyphon in form of heat is presented in Fig. 5.18 for t_{ci} = 25°C and Fig. 5.19 for t_{ci} = 15°C. Inlet temperature of heating water used in x-axis was the one measured directly before enter of medium to the evaporator coil. Positive effect was noticed for experiments with temperature of heating water below 50°C.

Pure GO nanofluid transported the highest amount of heat in both experimental series (t_{ci} = 15°C and 25°C). GO+SDS nanofluid operated with similar performance to SDS solution and a trend which fluid was more effective was not formed for the whole range of tested parameters. These working fluids transported lower amount of heat than water in some cases, among others for t_{ci} = 15°C series.

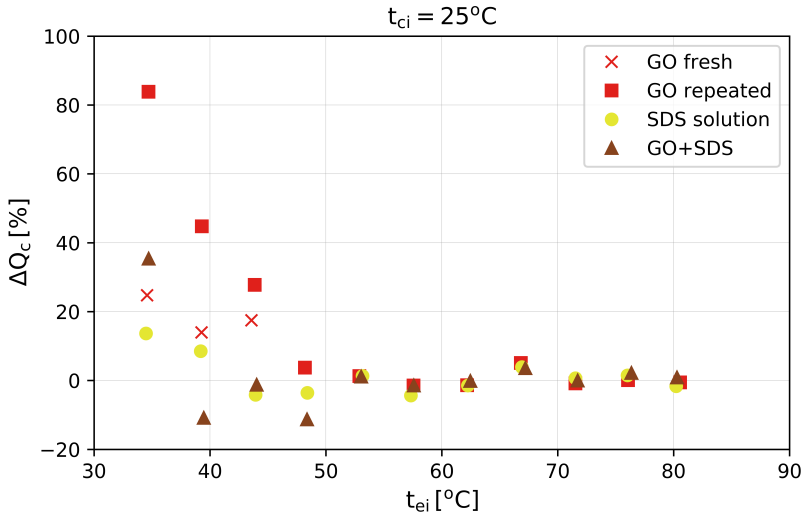

Figure 5.18: Percentage changes in the amount of heat transferred by different working fluids compared to the base fluid for experimental series with inlet temperature of cooling water of 25°C

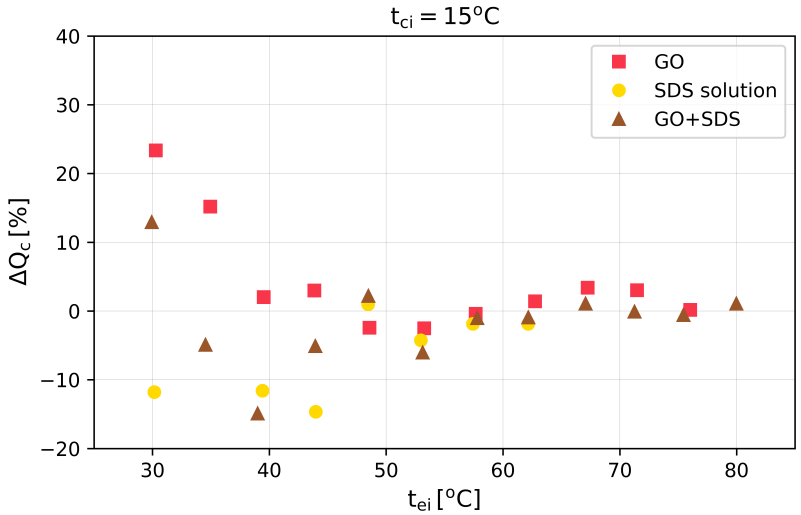

Figure 5.19: Increase in the amount of heat transferred by different working fluids compared to the base fluid for experimental series with inlet temperature of cooling water of 15°C

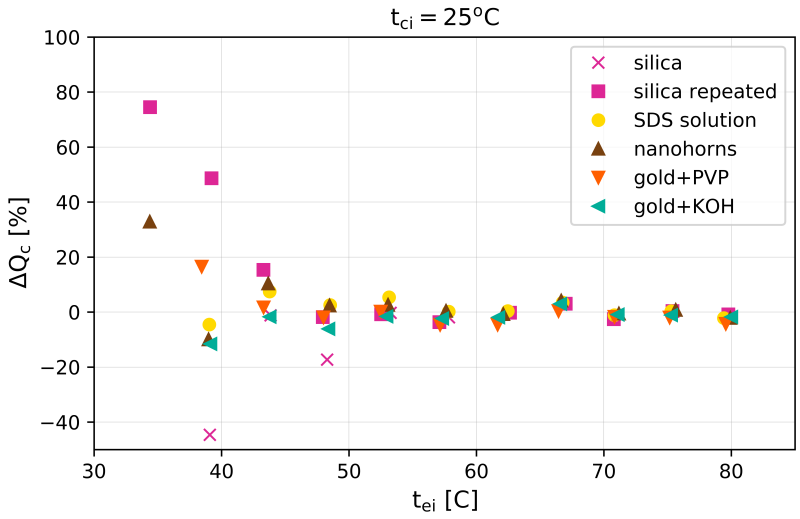

Figure 5.20: Percentage changes in the amount of heat transferred by various working fluids compared to the base fluid for experimental series with inlet temperature of cooling water of 25°C

Nanofluids based on silica, nanohorn and gold nanoparticles

Figure 5.20 shows percentage changes in the amount of transferred energy in form of heat in a dependence on working fluid with focus on nanofluids based on silica, nanohorns and gold nanoparticles. Differences were seen for inlet temperatures of heating medium below 50°C, similar to all previous analysis. The highest improvement (even up to 80%) was noticed for silica nanofluid. Results for nanohorn nanofluid and SDS solution were very close to each other. It suggests that observed effects came mostly from the presence of surfactant in nanofluid, not the nanoparticles itself. SDS which is an anionic surfactant reduced surface tension affecting the boiling process.

An increase in the amount of transferred heat is in high demand for many industrial applications. This is especially true at places with a confined space for cooling/heating equipment or with small temperature differences, exactly where nanofluids show the highest enhancement.

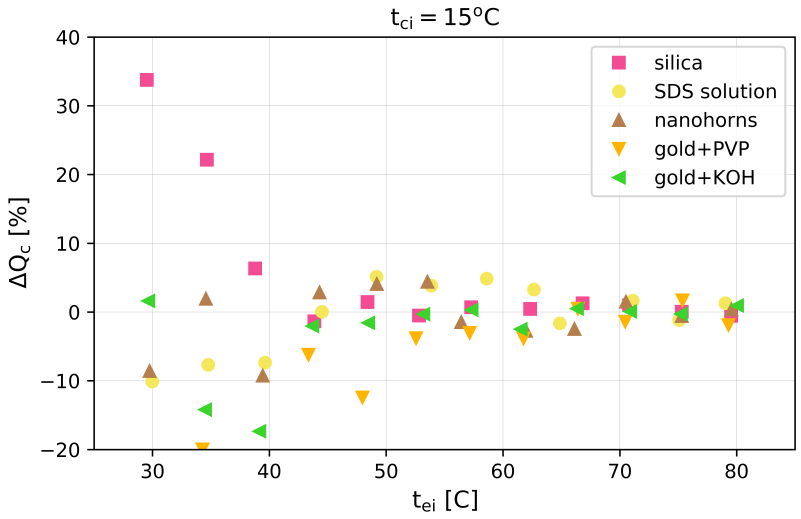

Figure 5.21: Percentage changes in the amount of heat transferred by different working fluids compared to the base fluid for experimental series with inlet temperature of cooling water of 15°C

5.7 Time-averaged internal pressure

Graphene oxide nanofluids

Pressure inside a thermosyphon was measured at four different locations what was described in details in section 5.1. Figure 5.22 shows pressure from the lowermost pressure transmitter (100 mm above the upper end of the evaporator, 500 mm from the bottom of the device) averaged over measurement time (one hour) for both experimental series (t_{ci} = 15°C and 25°C). Grey lines indicate the parabolic fit to the data (light gray for t_{ci} = 15°C and dark gray for t_{ci} = 25°C). Except the lowest heat loads, all investigated working fluids matched the same parabolic curve at a given temperature of cooling water, even if amount of transferred heat was different. Working fluid did not affect internal pressure of a thermosyphon within an experimental error. Increment in the inlet temperature of cooling water t_{ci} by 10 K (from 15°C to 25°C) significantly increased the time-averaged pressure. The slope of pressure parabolic curve is steeper in a case of t_{ci} = 25°C than for t_{ci} = 15°C, in particular for high heat loads.

Figure 5.23 shows analogous parabolic curves fitted to the pressure data gathered at four locations along the thermosyphon: p1 (1300 mm from the bottom), p2 (900 mm from the bottom), p3 (500 mm from the bottom), p1000 (at the top). In general, pressure minimally decreased from the bottom to the top. Differences resulting from the location of transmitters were significantly lower than variations following changes in operating conditions. Pressure p1000 was slightly higher than other values due to higher measurement uncertainty. For all test cases with a pressure not exceeding 100 mbar, calculations were based on the pressure transmitter with a range of 0 - 100 mbar located parallel to p1000 at the top of the device. Data for p100 pressure has not been added to this plot for a greater clarity.

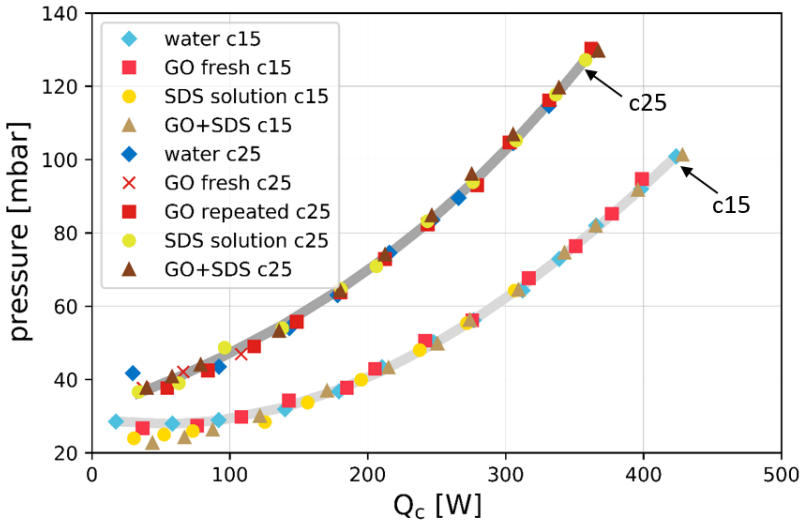

Figure 5.22: Time-averaged pressure inside a thermosyphon based on a lowermost pressure transmitter p3. c25 indicates experimental series of $t_{ci} = 25°C$ and c15: $t_{ci} = 15°C$

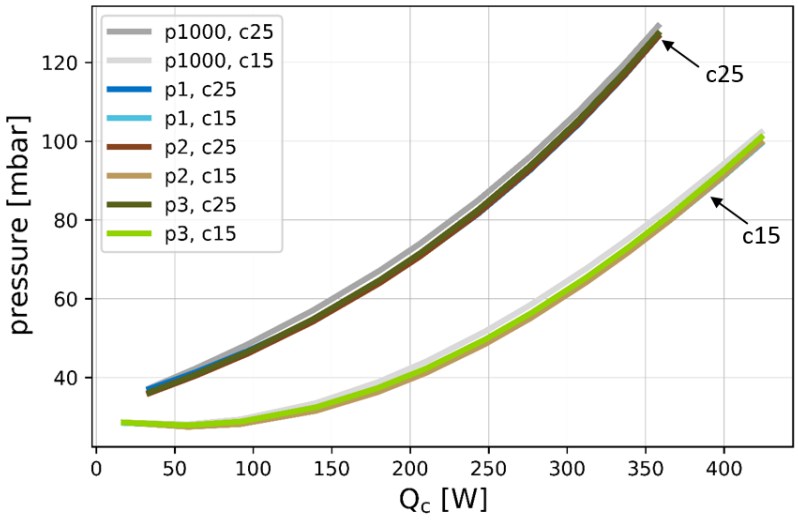

Figure 5.23: Time-averaged pressure inside a thermosyphon working with water based on a pressure transmitters located along the thermosyphon (order starting from the top: p1000, p1, p2, p3)

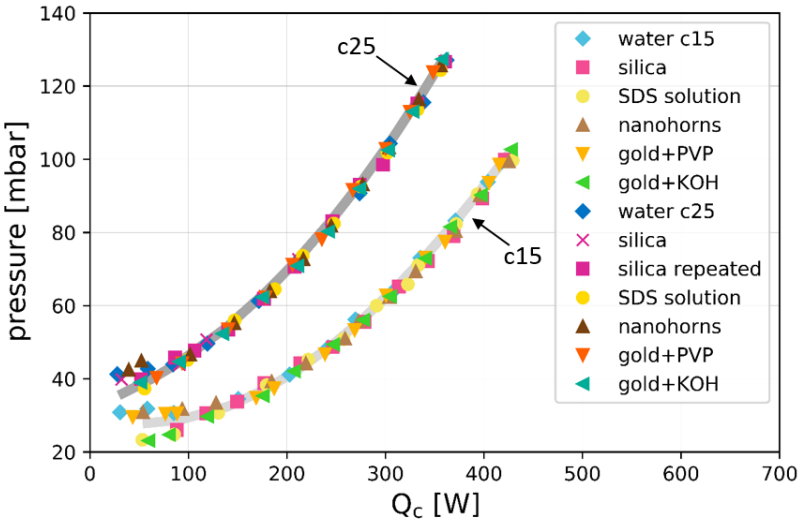

Figure 5.24: Time-averaged pressure inside a thermosyphon based on a lowermost pressure transmitter p3

Nanofluids based on silica, nanohorn and gold nanoparticles

The internal pressure p3 of a thermosyphon filled with nanofluids based on silica, nanohorn and gold nanoparticles is shown in Fig. 5.24. Comparison between pressure transmitters located along the device is shown in Fig. 5.25.

All symbols below 'water c25' indicate experimental series of $t_{ci} = 25°C$ and between 'water c15' and 'water c25' characterize experimental series of $t_{ci} = 15°C$. No differences were noticed in time of backing process for silica (between first test cases after filling the device and repeated ones). General trends are similar to that observed for GO nanofluids - increase in evaporator temperature led to higher internal pressure. Differences are bigger for higher heat loads. 10°C increment in the condenser temperature had even higher impact on the internal pressure.

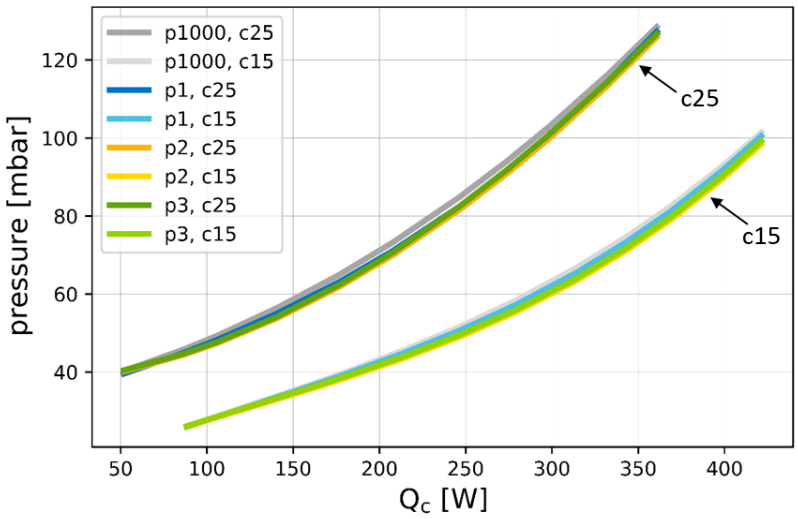

Figure 5.25: Time-averaged pressure inside a thermosyphon working with silica nanofluid, based on a pressure transmitters located along the thermosyphon (order starting from the top: p1000, p1, p2, p3)

5.8 Temperatures of heating and cooling medium

Graphene oxide nanofluids

Time-averaged inlet and outlet temperatures of heating water are shown in Fig. 5.26 for t_{ci} = 25°C and Fig. 5.27 for t_{ci} = 15°C. For heat fluxes higher than approx. 180 - 220 W, all temperatures joined an almost straight line. The differences between working fluids for low heat loads came from variances in thermosyphon capabilities to transfer thermal energy. Boiling regimes (pure convection for the lowest evaporator temperatures and boiling for higher heat loads) may additionally determine the amount of heat transferred.

Inlet and outlet temperatures of cooling water for both experimental series are compared in Fig. 5.28. Outlet temperatures for t_{ci} = 15°C and t_{ci} = 25°C formed straight lines with the same inclination angles. No deviations were found for any of tested working fluids, even for the time of backing effect. It agreed with the results published by Grab et al. [63] that nanoparticles cannot be transported by vapor, and thus no effect on condenser was noticed.

Nanofluids based on silica, nanohorn and gold nanoparticles

Results obtained for nanofluids based on silica, nanohorn and gold nanoparticles were very close to those of GO nanofluids (Fig. 5.29 and 5.30). All temperatures followed a straight line for inlet temperature of heating water higher than 50-55°C, while some differences occurred for lower heat fluxes. Outlet temperatures for silica nanofluid (*repeated*), which performed the highest heat transfer efficiency, followed this straight line even for low evaporator temperatures. Outcomes for fresh silica nanofluid (shortly after filling procedure) in most cases coincided with water values.

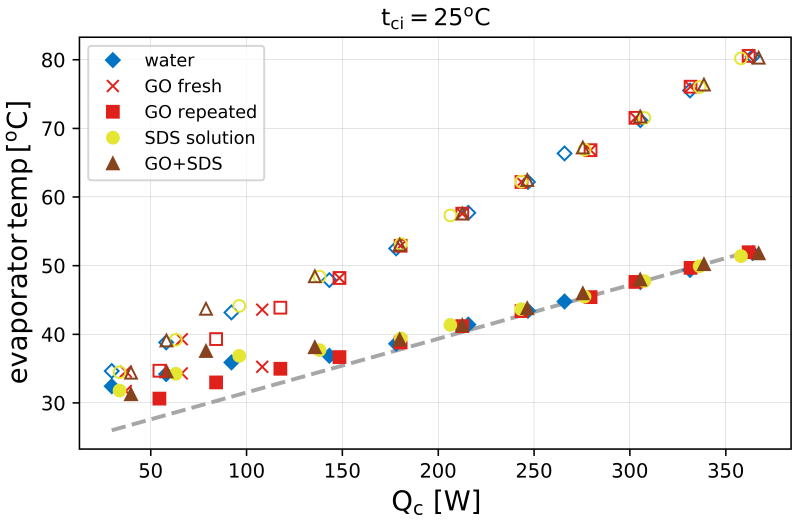

Figure 5.26: Inlet (empty symbols) and outlet temperatures (filled symbols) of water heating the thermosyphon filled with GO-related working fluids ($t_{ci} = 25°C$)

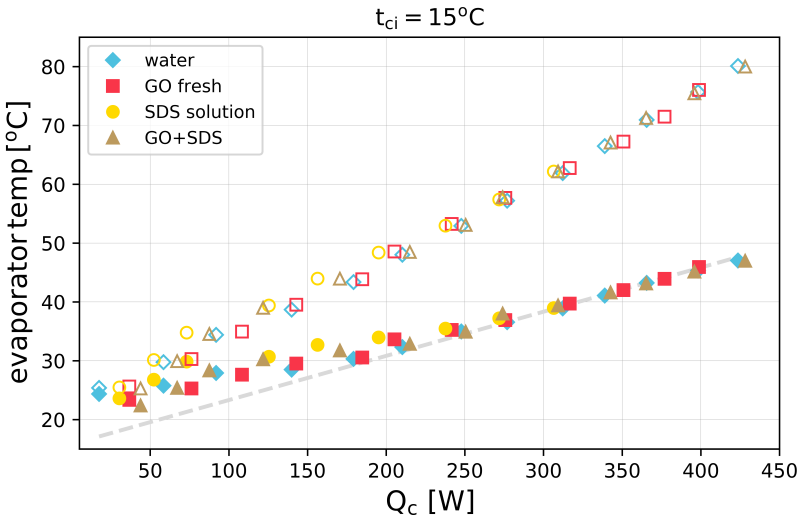

Figure 5.27: Inlet (empty symbols) and outlet temperatures (filled symbols) of water heating the thermosyphon filled with GO-related working fluids ($t_{ci} = 15°C$)

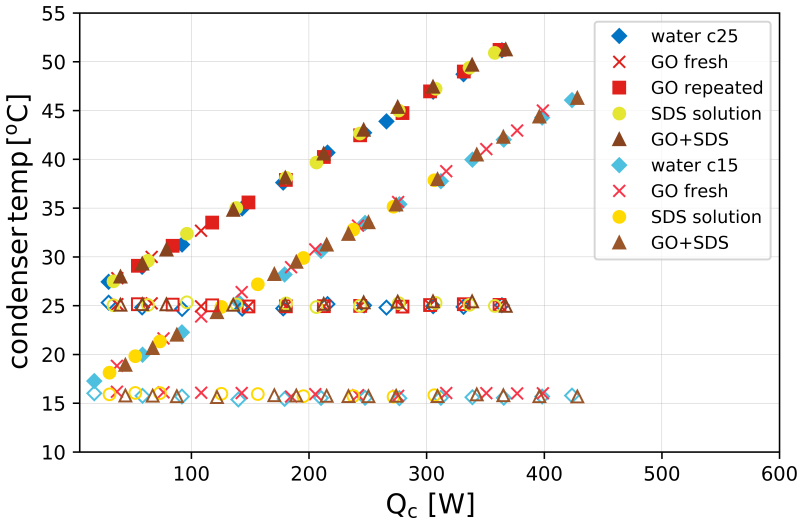

Figure 5.28: Inlet (empty symbols) and outlet temperatures (filled symbols) of water cooling the condenser of thermosyphon filled with GO-related working fluids. All symbols below water c15 correspond to $t_{ci} = 15°C$, above to $t_{ci} = 25°C$

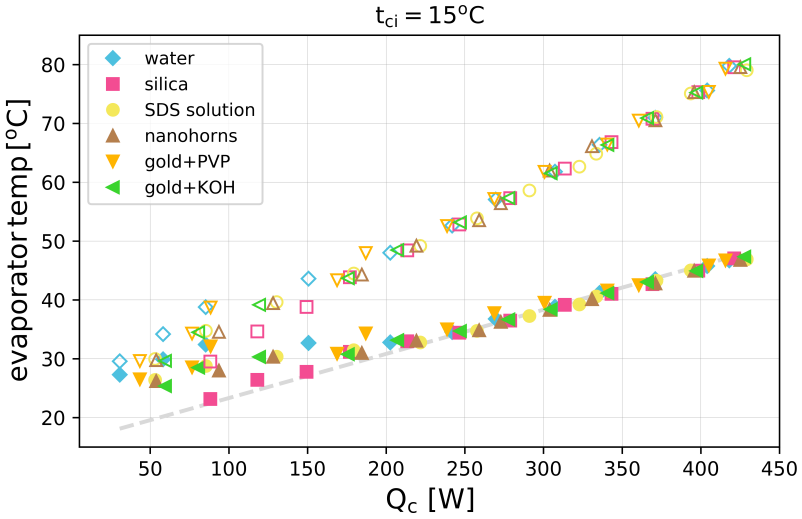

Figure 5.29: Inlet (empty symbols) and outlet temperatures (filled symbols) of water heating the thermosyphon filled with nanofluids based on silica, nanohorn and gold nanoparticles and related base fluids ($t_{ci} = 15°C$)

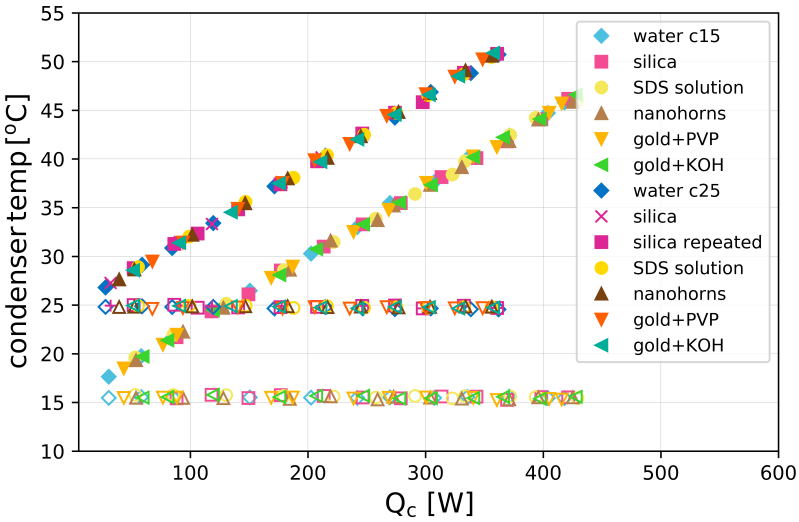

Figure 5.30: Inlet (empty symbols) and outlet (filled symbols) temperatures of cooling water

5.9 Temperature distribution in the evaporator

Nanofluids based on silica, nanohorn and gold nanoparticles

Figures 5.31 and 5.32 present the time-averaged temperature distribution in the evaporator for high and low temperatures of heating water. Temperatures in the working fluid sump were measured using a sensor consisting of six Pt100 elements described in details in section 5.1. Y-axis showcases normalized distance $\overline{h_T}$ of these temperature sensors t_1 to t_6 what is additionally marked in the upper left plot in Fig. 5.31. The lowermost Pt100 (t_6) is positioned at $\overline{h_T} = 0$ and the value of $\overline{h_T} = 1$ is reached at the outlet of the evaporator coil. The normalized distance was calculated as:

$$\overline{h_T} = \frac{h_{ti} - h_{t6}}{h_{eo} - h_{t6}} \tag{5.7}$$

Where $t_i = t_1 - t_6$, and t_{eo}, h_{ti} references to the position of a given Pt100 element.

The time-averaged temperature in a x-axis was calculated as:

$$\overline{t_T} = \frac{t_{co} - t_{ti}}{t_{co} - t_{t6}} \tag{5.8}$$

Where $t_i = t_1 - t_6$, and t_{eo}.

Eq. 5.8 includes the condenser outlet temperature as a reference temperature, instead of evaporator outlet temperature. The averaged pressure did not vary along the thermosyphon within an experimental error (see Fig. 5.25). If temperature t_{co} followed the condensation in the condenser, it could be also a reference evaporation temperature at the upper part of the evaporator, above the working fluid sump which was overheated).

Thermosyphon was always filled with 85 ml of working fluid. At rest, working fluid reached the level of 270 mm from the bottom of the device, 35 mm below t_1 and 10 mm above t_2. This corresponded to the normalized distance of approx. $\overline{h_T} = 0.6$. Pt100 element t_1 was always above the working fluid, while t_2 and following sensors were in the

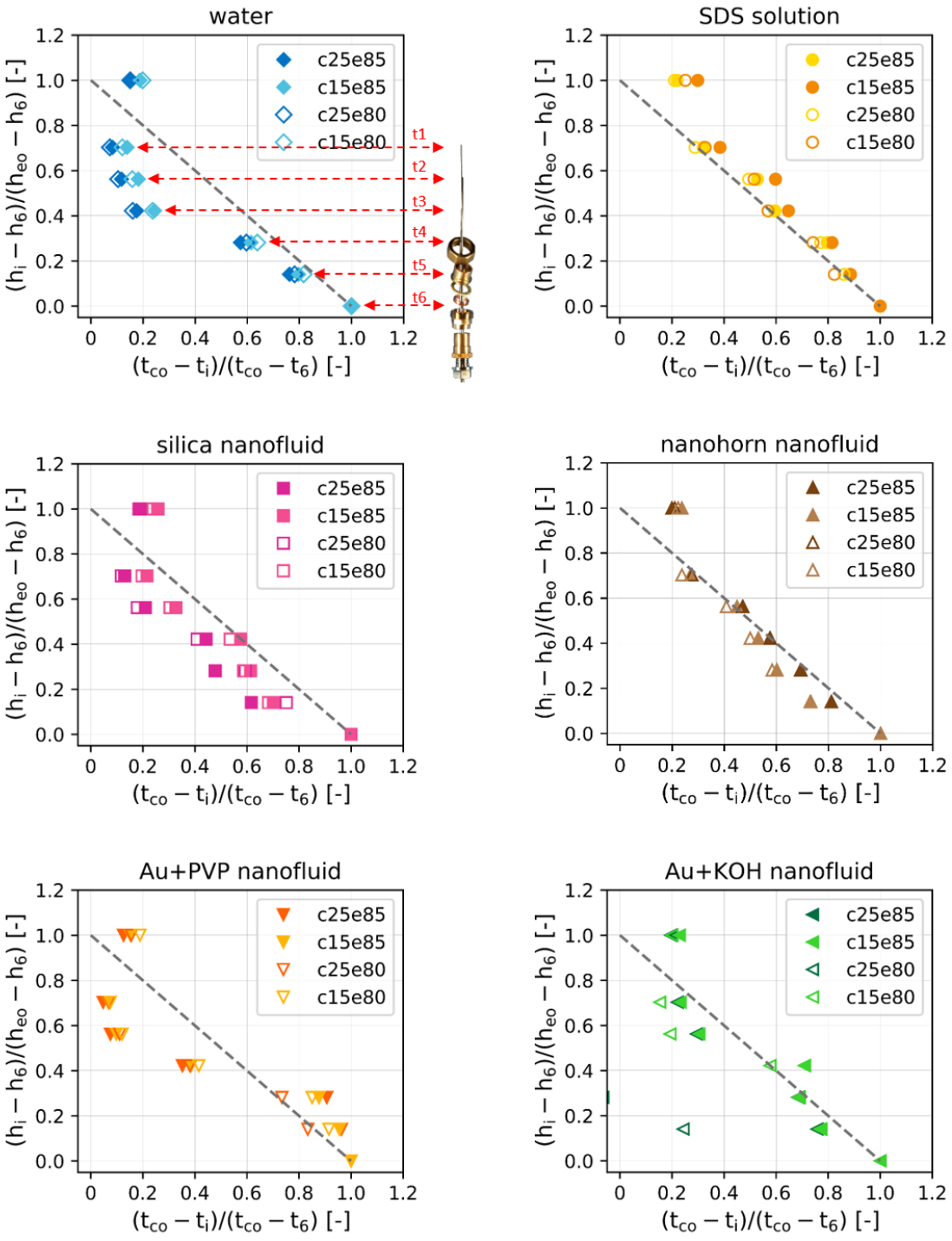

Figure 5.31: Normalized time-averaged temperature distribution in the working fluid for nanofluids based on silica, nanohorns and gold particles. c25 indicates temperature of cooling water of 25°C, e80 and e85 inlet temperature of heating water of 80°C and 85°C, respectively

liquid at rest. When thermal load was provided to the evaporator, part of working fluid circulated in a closed cycle or was expelled in geyser event. Thus, Pt100 elements t_2 and following could measure the temperature of liquid, vapor, or their mixture in *splish-splash*

region.

Condensate returning to the evaporator were heated from the uppermost part of the evaporator. This thin film could evaporate even before reaching the working fluid sump if overheating was enough. This also explains why t_{co} was chosen as a reference temperature in eq. 5.8. For high temperatures of heating water, temperatures of water in the lowest part of the evaporator (t_4, t_5, and t_6) followed a straight line, slightly below the dashed line that represents a linear temperature decrease from t_6 to t_{co}. Temperatures t_1 - t_3 located in the upper part of the evaporator were significantly lower than t_4 - t_6. Heating water was provided from the bottom of the device, thus it had higher temperature at the bottom. Second, the upper part of the evaporator was temporarily emptied by geyser events and evaporation of the condensate film could occur at that time. It kept overheating at lower temperatures. Then previously expelled liquid returned from the condenser and cooled the upper part of the evaporator. This area was constantly heated by a heating water, thus the temperatures measured in the working fluid sump were always higher than t_{co}.

Temperature distribution of sodium dodecyl sulfate solution differed when compared with water. In case of SDS, all temperatures t_1 - t_6 followed more or less on the dashed line. The main regime was nucleate boiling and geysering did not add temperature disturbances in the upper part of the evaporator. Temperature t_2 was probably influenced by bubbles that detached and broke through a liquid-vapor interface of the working fluid. Nanohorn nanofluid behaved in a similar way to SDS solution what was also seen in time-dependent patterns described in the next section.

All the other working fluids - silica, gold, graphene oxide nanofluids showed temperature distributions between water and SDS solution (see fig. 5.31 and 5.33). When the working fluid behavior was closer to the nucleate boiling regime, the temperature distribution better followed the dashed line. Temperatures t_2 and t_3 were entirely or partly in liquid. When geysering occurred or the big amount of working fluid circulated in the device, these Pt100 elements were outside of the liquid, in a vapor phase.

Figures 5.32 and 5.34 show analogous normalization of temperature distribution in the working fluid sump but for low evaporator temperatures (inlet temperature of heating water of $t_{ei} = 40 - 45°\mathrm{C}$). Here, none of working fluids followed a dashed line indicating the linear temperature reduction. At these conditions (low evaporator temperatures), almost no geysering occurred and the amount of heat transferred achieved low values. The quantity of returning condensate small and temperatures measured outside of the liquid were affected by a radiation from the evaporator wall and were excluded from further analysis.

For low heat loads, temperature was almost entirely distributed along the working fluid sump and was close to that of the lowest Pt100 element (t_6) what gave $\overline{t_T} = 1.0$. Temperatures t_4 and partly t_3 were scattered for analyzed cases and sometimes reached even higher values than t_6. However, these temperatures were still lower than inlet temperature of heating water. Mechanisms behind this behavior are not understood. It could be affected by nanoparticles which changed the evaporator surface or by activation of nucleation sites that led to nucleating and growing of single bubbles.

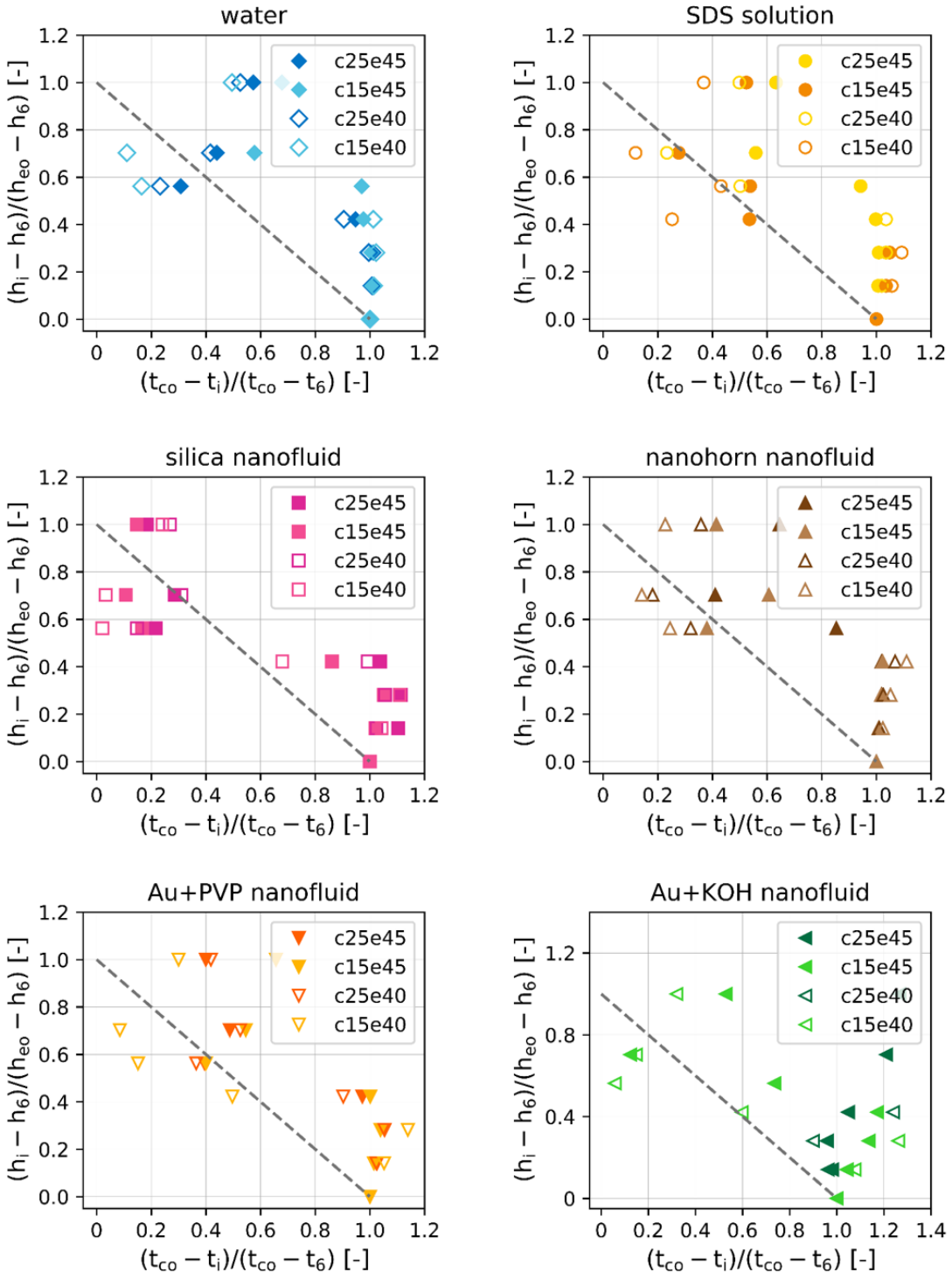

Figure 5.32: Normalized time-averaged temperature distribution in the evaporator with nanofluids based on silica, nanohorns and gold particles for low temperatures of heating water. c25 indicates temperature of cooling water of 25°C, e40 and e45 inlet temperature of heating water of 40°C and 45°C, respectively

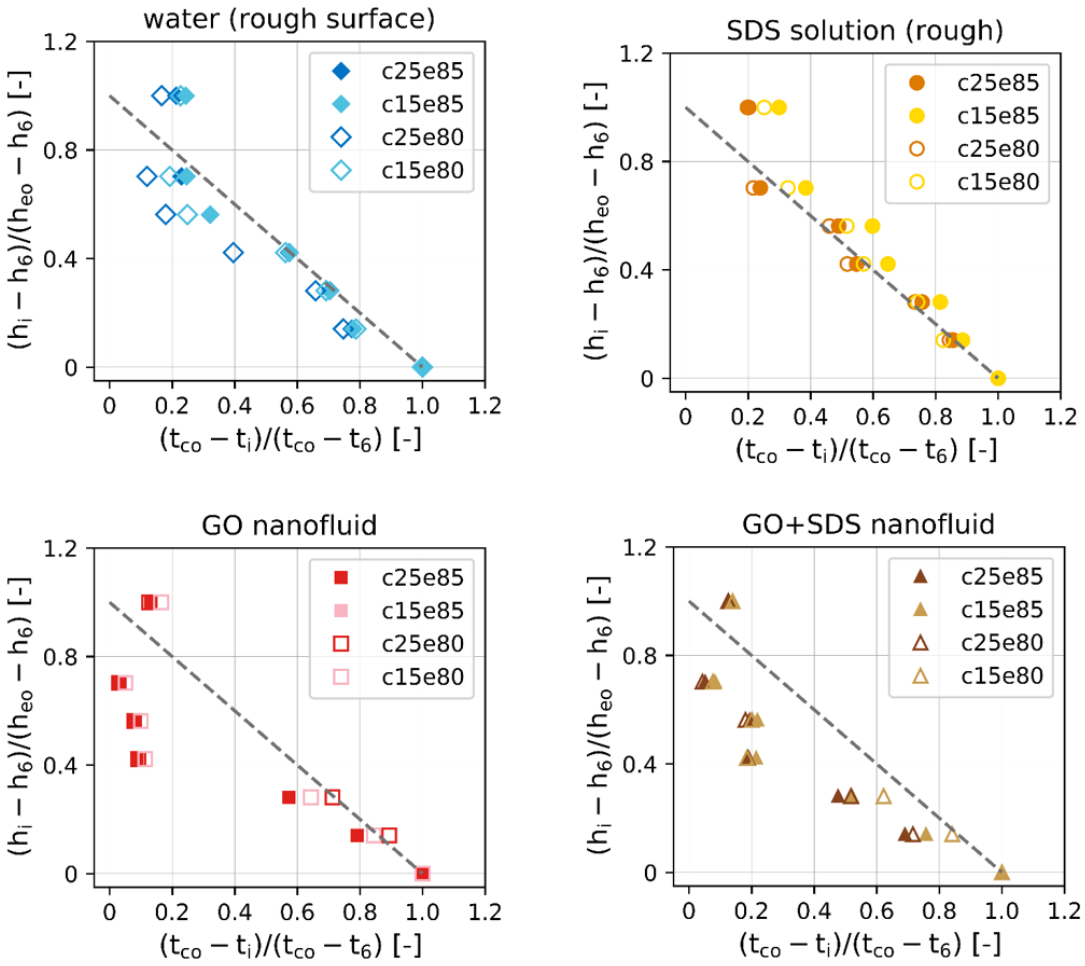

Figure 5.33: Normalized time-averaged temperature distribution in the working fluid for graphene oxide nanofluids. c25 indicates temperature of cooling water of 25°C, e80 and e85 inlet temperature of heating water of 80°C and 85°C, respectively

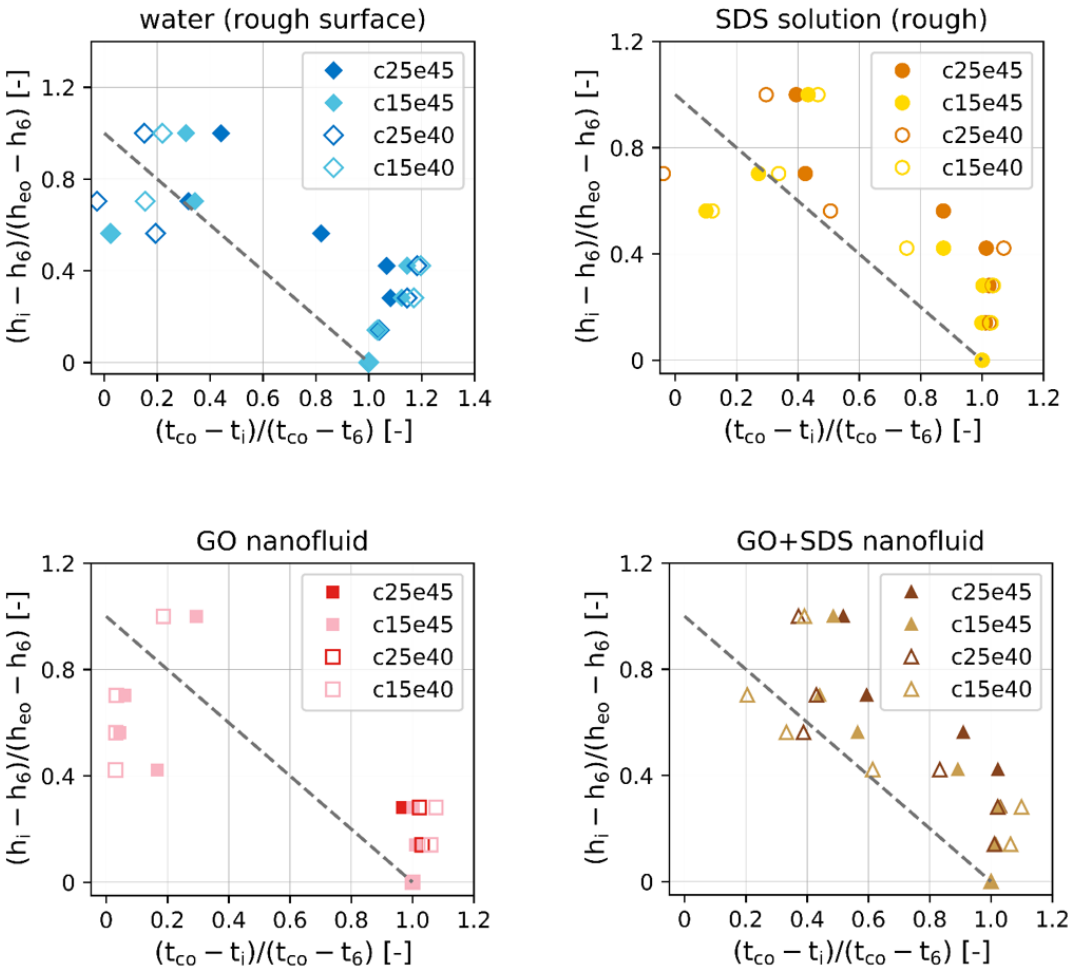

Figure 5.34: Normalized time-averaged temperature distribution in the evaporator with graphene oxide nanofluids. c25 indicates temperature of cooling water of 25°C, e40 and e45 inlet temperature of heating water of 40°C and 45°C, respectively

5.10 Evaporator surface and SEM analysis of particles

Graphene oxide nanofluids

Deposition process took place for all tested nanofluids what completely changed the characteristics of nanofluid itself and the heater surface. Most of previously dispersed particles deposited on the inner wall of the evaporator. Fig. 5.35 b shows the layer found with an endoscopy camera at approx. 20 cm from the bottom of the thermosyphon. Due to light conditions inside the pipe, the resolution of the picture could not be improved. Kim et al. [97] confirmed by using EDS (energy-dispersive spectrometer) spectroscopy that analogous layers on the heater surface after boiling of Al_2O_3, ZrO_2, and SiO_2 nanofluids were made of nanoparticles material.

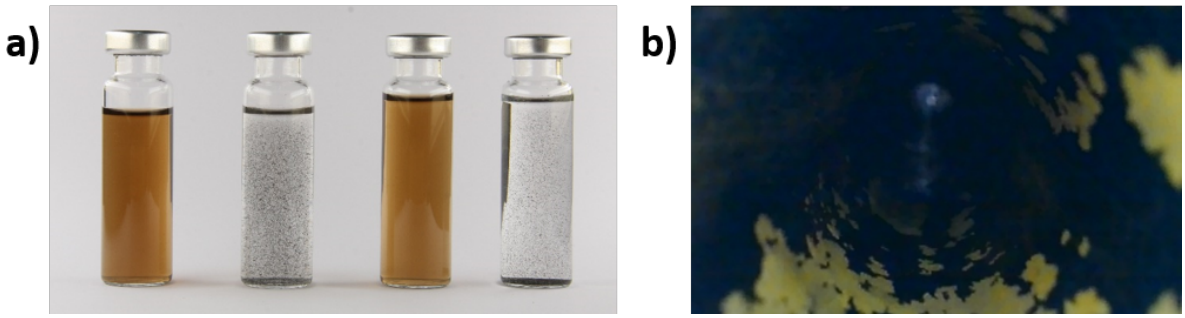

Figure 5.35: a) Samples of GO nanofluids before and after experimental series in a thermosyphon. First two from left were GO (0.1 g/1) nanofluid without surfactant; the right ones contained additionally 0.01 g/l of SDS. b) Deposition layer (black areas) formed on the inner surface of the evaporator after GO nanofluid boiling

Comparison of fresh nanofluids and samples after finishing all experimental series with a given working fluid is presented in Fig. 5.35 a. Fluids completely changed their appearance and color. Part of nanoparticles that were not deposited on the wall agglomerated and remained in the fluid taken out from the device what is noticeable in Fig. 5.35 a). These agglomerates were later dried and prepared as samples for SEM microscopy. Results of this analysis are presented in Fig. 5.36 and Fig. 5.37.

Fresh material of graphene oxide was described in details in section 4.1 and flakes under SEM microscopy are shown again in Fig. 5.36 a) for a comparison. Although some flakes were folded, material showed strong sheet-like shape. Overlap of flakes occurred during drying process due to difficulties in choosing the proper concentration of diluted nanofluid in sample prepared for SEM analysis. Other cases in Figure 5.36 show agglomerates that remained in working fluid after all experimental series with pure GO nanofluid. They lost their flake-shape characteristics (e.g. Fig. 5.36 c) and became very irregular with respect to structure. Some of them looked like a sponge (e.g. Fig. 5.36 d), or few connected sheets like graphene paper (e.g. Fig. 5.36 b), and other chaotic structure.

Figure 5.37 presents SEM analysis of particles which were present in the working fluid after experimental series conducted with GO+SDS nanofluid. Again, graphene material lost its flake characteristics. Agglomerates gained variable shapes and structures - from sponge-like sheets (e.g. Fig. 5.37 d), through rolled tubes or balls (e.g. Fig. 5.37 a) or c) to other irregular forms. Figure 5.37 f) shows that crystals of sodium dodecyl sulfate

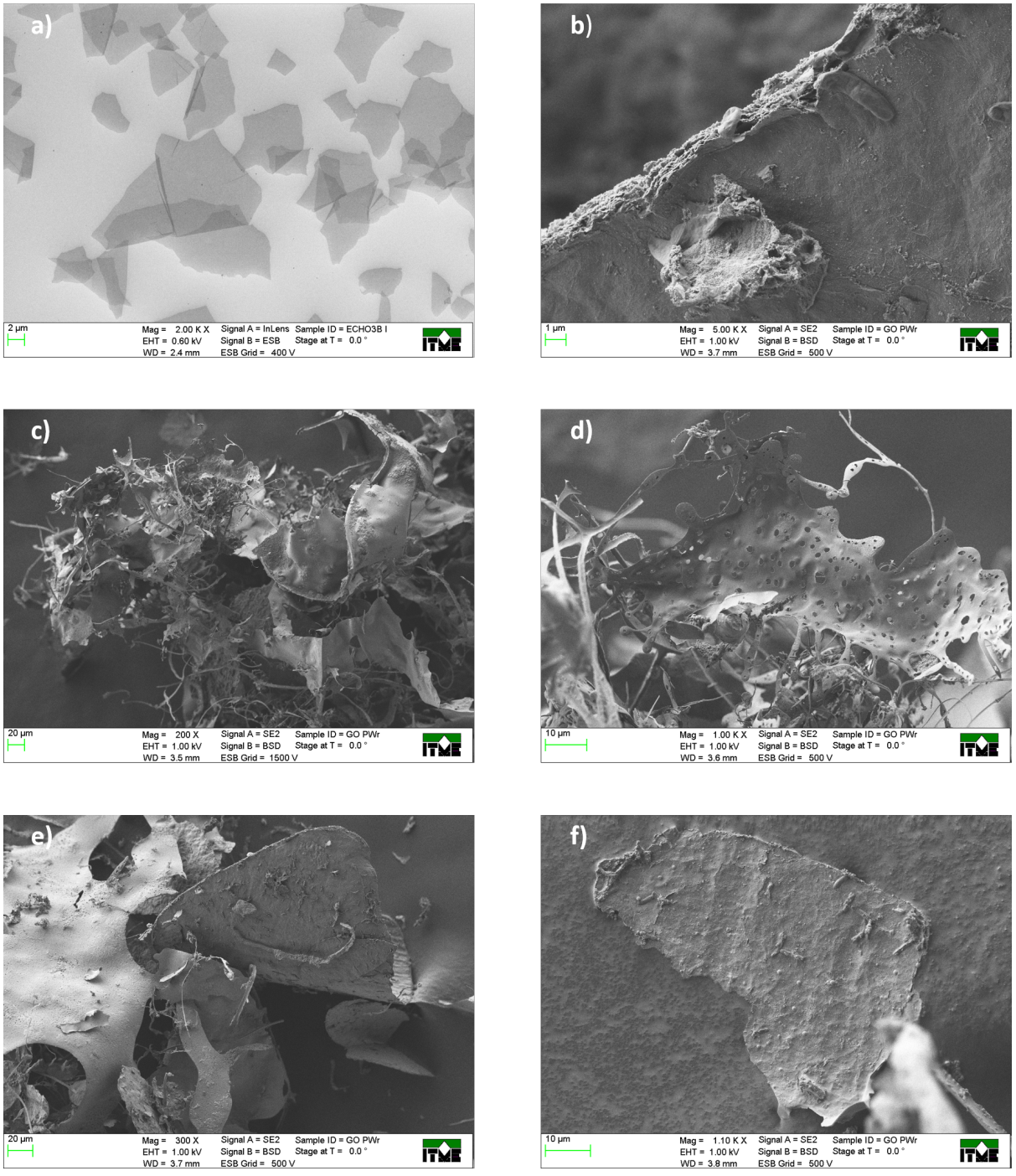

Figure 5.36: SEM analysis of: a) prepared material, b-f) agglomerates that remained in working fluid after experiments with GO nanofluid.

may attach to graphene oxide flakes. This finding is very important in terms of further understanding of GO-based nanofluids behavior.

Construction of the test-rig did not allow for determining the structure of deposition layer under SEM microscope. Special ring that could be taken out with a purpose of a surface analysis under microscope was placed in a tailor-made temperature probe located at the bottom of the thermosyphon (see: Fig. 5.1 c). Particles deposited into layer on the evaporator surface at approx. 20 cm from the bottom of the device (see: Fig. 5.35 b).

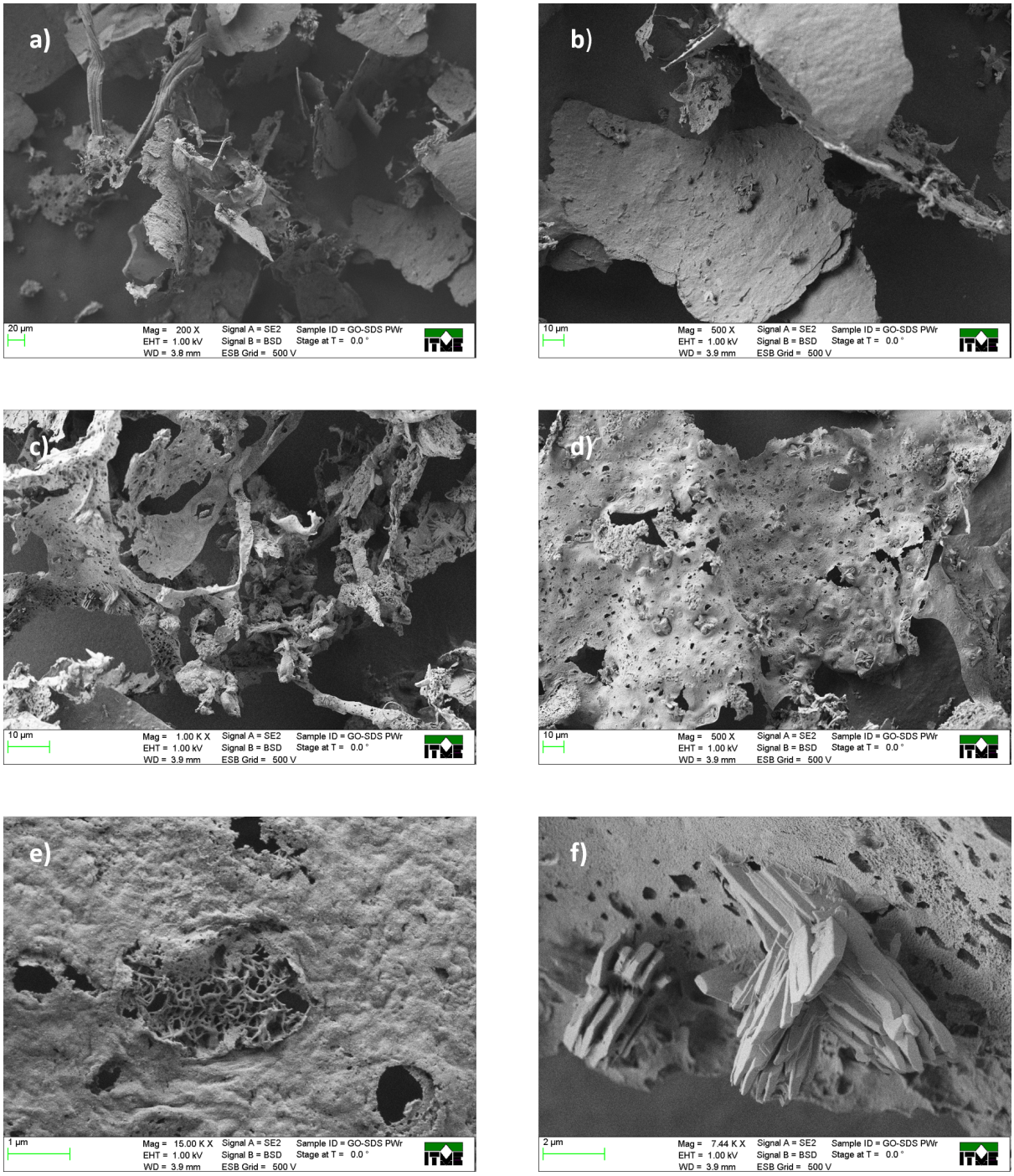

Figure 5.37: SEM analysis of agglomerates that remained in working fluid after experiments with GO+SDS nanofluid

Working fluid at rest reached a level of about 27 cm from the bottom. Considering that part of working fluid circulates between condenser and evaporator during thermosyphon operation, this layer was in a *splish-splash* region. It suggests that some part of deposition took place during nucleation and detachment process due to microlayer evaporation. Additionally, evaporation of a thin film falling back from the condenser could cause additional deposition of particles at evaporator part above the fluid level. There were no literature available at the time of experiment designing which acknowledged this behavior.

This resulted in the lack of possibility for detailed characterization of a layer deposited on the evaporator wall.

Nanofluids based on gold, silica, and nanohorns nanoparticles

Figure 5.38 presents prepared nanofluids and their appearance after all experimental series with a given working fluid conducted in a thermosyphon.

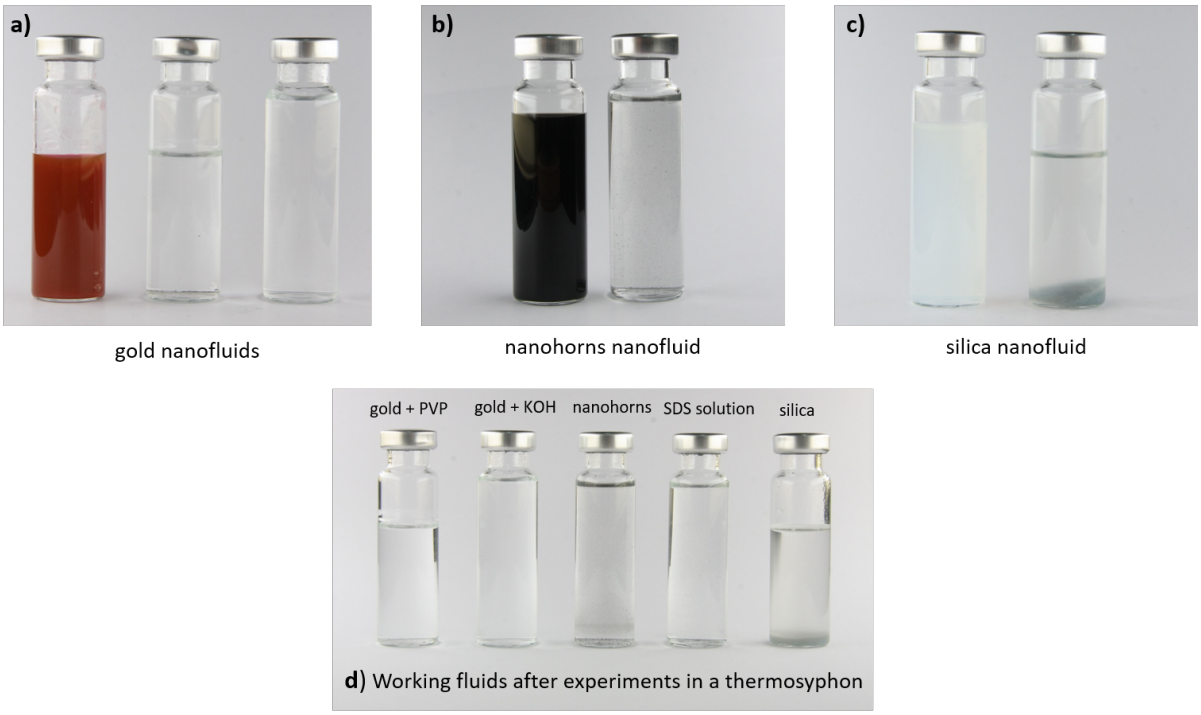

Figure 5.38: Samples of nanofluids before and after experimental series in a thermosyphon: a) gold nanofluids (from left: fresh Au+PVP nanofluid, Au+PVP and Au+KOH after experiments), b) nanohorns nanofluid, c) silica nanofluid, d) working fluids after experiments

Results were similar to that described for GO nanofluids - tested nanofluids became almost pure base fluids with some agglomerated particles. Majority of previously dispersed nanoparticles deposited on the inner surfaces during experiments. Figure 5.39 presents different elements of a thermosyphon that were in contact with working fluid during operation. Particles were mainly found on the upper part of the inner evaporator surface. Silica agglomerates found on a ring located in the bottom of the thermosyphon and at temperature probe (Fig. 5.39 e), g) did not strongly attach to the surface. This effect was opposite for layer found in the evaporator section (Fig. 5.39 f), approx. 20 cm from the bottom. This massive layer was firmly attached to the walls. Boiling experiments with silica conducted by Watanabe et al. [210] showed that deposited silica layer was characterized by the greatest adhesion force to the heated surface in comparison with TiO_2 and Al_2O_3. Unfortunately, more detailed analysis of the silica deposit was impossible due to construction of the test rig as explained before. Therefore, the structure of the silica layer left open questions, such as presence of crystallization fouling [179] or whether polymerization took place.

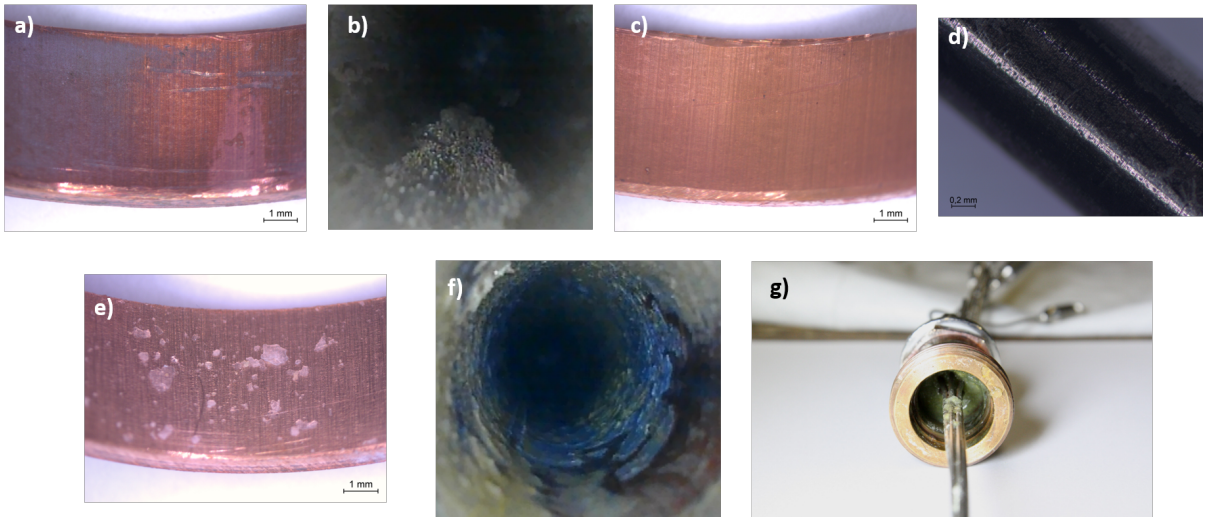

Figure 5.39: Different elements of thermosyphon after experimental series with different working fluids: a) and b) presents ring from temperature sensor and part of evaporator seen with an endoscopic camera after boiling of gold+PVP nanofluid, c) ring after gold+KOH nanofluid operation, d) temperature sensor after operation with nanohorn nanofluid, e-g) ring, inner surface of the evaporator and temperature probe after experiments with silica nanofluid.

Manually cleaning (used for other cases) was not enough to remove this silica layer. It required drill with sandpaper to remove it what resulted in changed roughness of inner surface. That is why thermosyphon was tested again with water and SDS solution. These repeated values were treated as reference baselines for all later test cases (among others GO nanofluids) to ensure that no other parameters except changes of working fluid was taken into account.

5.11 Chapter summary

Thermosyphons working with nanofluids offer promising solutions for low heat load applications with small temperature differences between hot and cold part of the device. For these conditions, working fluids affected capacity of heat transfer and changed the mean temperature level without changing operation conditions. This may reduce costs that would be otherwise spend for e.g. increasing the low rate by using a bigger pump or enlarging a surface area which is often strictly limited by application requirements.

From the analysis presented in the previous sections following conclusions can be drawn:

- Changes in thermal behavior of thermosyphon following from usage of nanofluids were limited to the evaporator section. No effect on condenser were noticed.
- Influence of both nanoparticles and chemical stabilizers should be always investigated. Each of these components had an impact on the working fluid behavior during operation of thermosyphon.
- Nanofluids caused similar effect to increase in temperature of cooling water - increment in the mean temperature level of the condenser.

- The possible mechanisms behind the improvement of heat transfer efficiency during boiling of nanofluids depended on nanofluid type and may include:
  - changed conditions of the evaporator surface as a result of nanoparticles deposition,
  - interaction of nanoparticles both at the evaporator wall and freely moving in the fluid,
  - interactions between nanoparticles and chemical stabilizers (e.g. surfactant),
  - changed thermophysical properties of working fluid, among others surface tension and viscosity.

Chapter 6

Geyser boiling

Although time-averaged overall thermal resistance of a thermosyphon was not affected by working fluid for high heat loads within an experimental error, corresponding time-dependent behavior differed. Major of tested working fluids operated under geyser boiling regime for high evaporator temperatures. Such phenomena often remains unrecognized and is still not well investigated. It may initiate disturbances to the heat transfer continuity and cause additional mechanical load, and engender shock damage of the components. Thermosyphons are used in systems often expected to operate for long periods of time. Thus, more and more effort is put to improve understanding of this boiling regime.

This section focuses on geyser boiling and determines parameters that characterize this phenomena regardless different working fluids and operating conditions. The analysis is based on pressure from the lowermost transmitter p3 located 100 mm above the upper end of the evaporator section, and 500 mm from the bottom of the device. It was chosen as a representative pressure due to being located nearest to the boiling area.

6.1 Characteristic patterns of detected geyser events

Geyser boiling consists of irregular but repetitious pressure increments resulting from an ejection of working fluid towards the condenser without its previous evaporation. A single pressure peak with following decrease in pressure signal is called a *geyser event*.

Figure 6.1 shows example of pressure distributions inside the thermosyphon filled with water at two different temperatures of heating water: 55°C and 85°C. Dots at Fig. 6.1b) and d) represent the experimental points.

Geyser events depended on the operating conditions, including evaporator temperature and following internal pressure. Their frequency and intensity (understood as an amplitude of a pressure peak) varied for presented cases. The waiting period between first and second event lasted 73.4 sec in case of $t_{ci} = 55$°C and only 7.4 sec for $t_{ci} = 85$°C. Amplitudes of shown events were: 40.22 and 37.72 mbar for $t_{ci} = 85$°C, and 52.49, 50.36 for $t_{ci} = 55$°C. The differences in minimum pressure values reached before the first and second peak was 0.3 mbar for $t_{ci} = 85$°C and 1.04 mbar for $t_{ci} = 55$°C. Speed of pushed working fluid calculated from a delay in a pressure increase between p3 and p2 transmitters were in the range of 6.5 - 10 m/s for presented cases. This estimation includes error resulting from the frequency of saving data and possibility that maximal pressure value occurred in the time lapse between consecutive measurement points. Values are

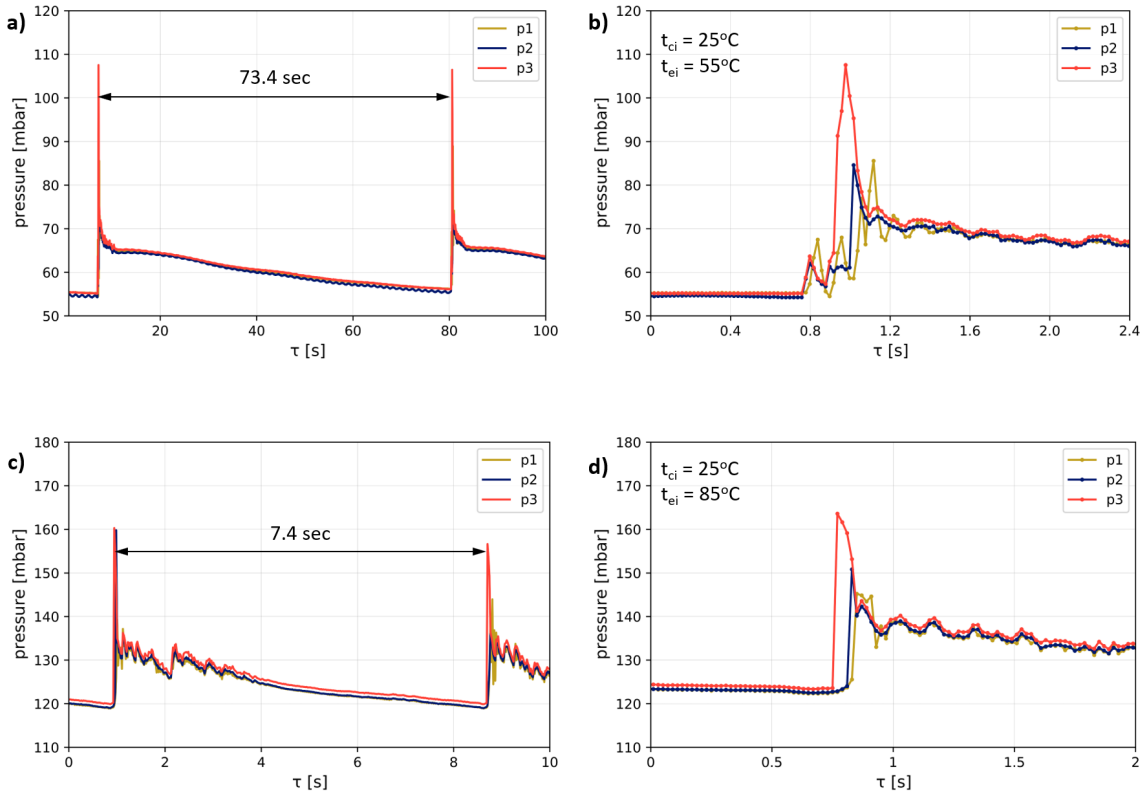

Figure 6.1: Example of pressure patterns of geyser events for distilled water at two different temperatures of heating water: a-b) 85°C and c-d) 55°C (inlet temperature of cooling water: $t_{ci} = 25°C$)

significantly lower than the sound speed that is operation limit of the thermosyphon due to risk of blocking condensate to the evaporator.

Temperature probe located at the bottom of the device with six temperature sensors also gave a response to the geyser boiling. Temperature signals from the most upper ones (*t1* and *t2*) and the most lower ones (*t5* and *t6*) are presented in Fig. 6.2 and Fig. 6.3. Temperatures from the middle sensors followed patterns from the presented ones and are omitted to increase clarity of the plots. Temperatures measured in vapor and liquid gave opposite rising/decreasing trend, thus it was possible to observe changing level of liquid in the evaporator during the thermosyphon operation.

Figure 6.4 show 20 seconds of pressure distributions inside a thermosyphon filled with different working fluids under the same operating conditions (inlet temperature of heating water $t_{ei} = 85°C$ and inlet temperature of cooling water $t_{ei} = 25°C$). Variations in time-dependent behavior are easily noticeable, although the time-averaged efficiencies were similar for all presented cases. Distilled water and GO-based nanofluids showed strong geysering regime. In case of silica, and even more for nanohorns and SDS solution geyser boiling was significantly suppressed or almost entirely prevented. Detailed analysis of each working fluid behavior is presented in the following sections.

Some of detected geyser events showed additional variations in pressure distributions. One example is a small peak before the main geyser event, as seen in Fig. 6.1 b). Understanding of this behavior requires further research. It could be caused by e.g. forming of

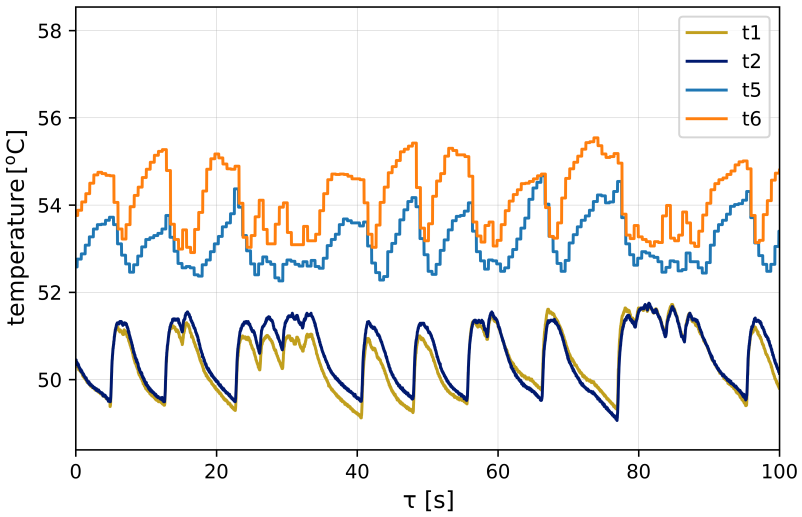

Figure 6.2: Response of temperature sensors located inside the evaporator section on geyser boiling for distilled water (t_{ci} = 25°C, t_{ei} = 85°C)

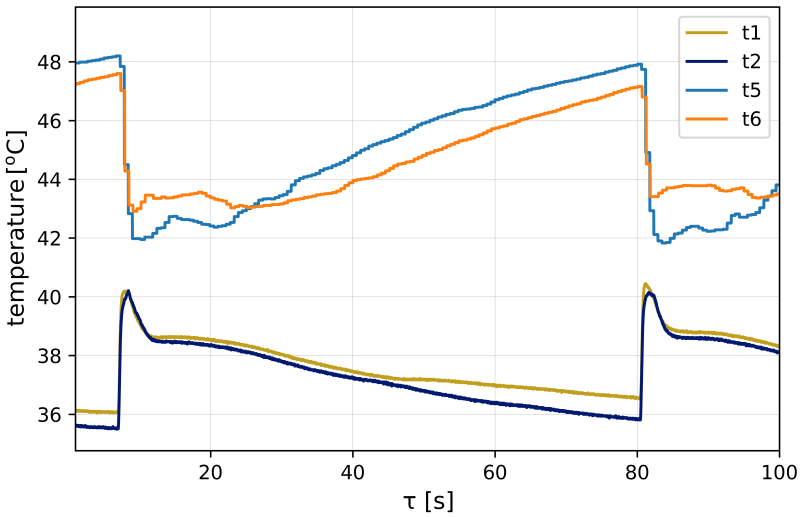

Figure 6.3: Response of temperature sensors located inside the evaporator section on geyser boiling for distilled water (t_{ci} = 25°C, t_{ei} = 55°C)

big bubble that was finally able to release part of stored thermal energy without pushing the fluid above it towards the condenser. Another example was a double peak structure, as presented in Fig. 6.4 (water). In these cases, geyser events were followed by pressure fluctuations with another smaller pressure peak. Not every peak was followed by a second one fast enough to form a double-peak characteristics. A second peak reached always lower value than a first one. It suggests that peak intensity was a measure of the thermal energy stored during bubble formation. Time of bubble development for the second peak was shorter, thus it could contain less thermal energy. Also internal pressure did not decrease to such a low value as before the first peak and pressure difference between condenser and rising bubble could be lower. As a result, the second event was less intense

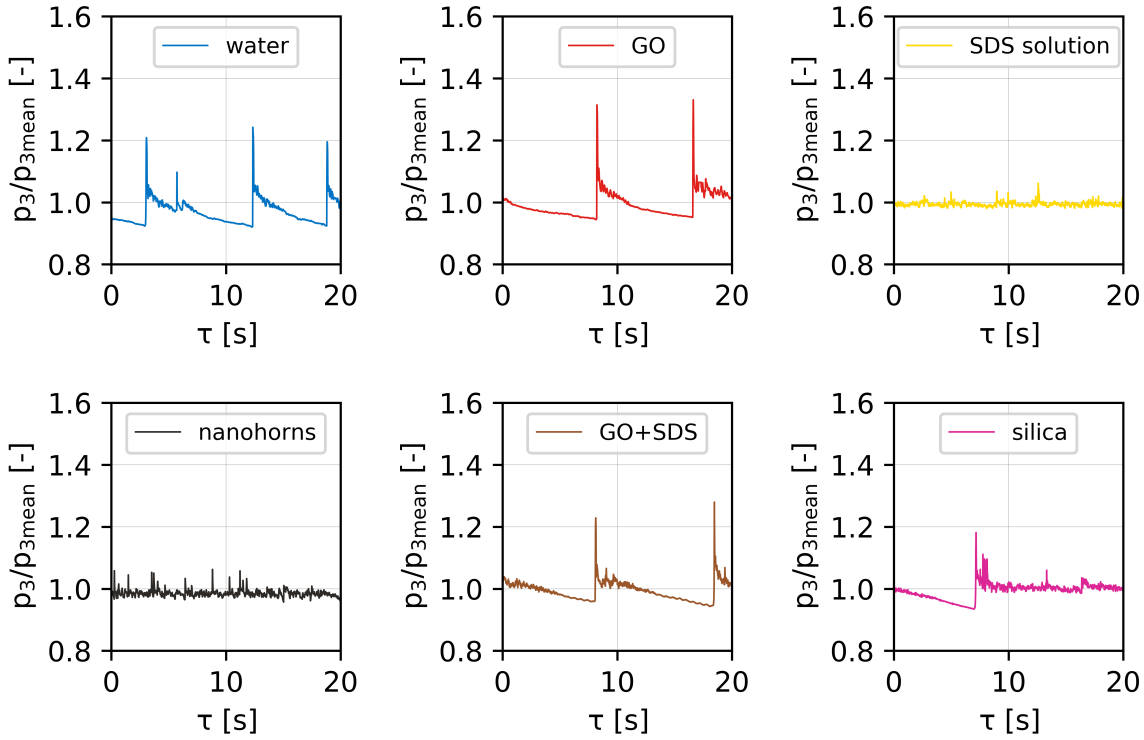

Figure 6.4: Pressure patterns for different working fluids at the same operating conditions ($t_{ei} = 85°C$ and $t_{ci} = 25°C$)

and violent compared to the first one. One physical explanation of such behavior could be that the second bubble grew faster and achieved an instable state earlier due to still overheated fluid and circulation occurring in the surrounding fluid when the first bubble release part of a stored thermal energy. First bubble could also activate a nucleation site so the second bubble could be developed more easily. To the best author knowledge, there are no studies on physical mechanisms behind this behavior. To sum up, multi-geysers seem to result from an insufficient release of thermal energy by the first bubble causing geyser event.

Even for a given working fluid and operating conditions, the characteristics of geyser events (including their frequency and amplitude) varied from one event to another over the experimental time. Analysis of each geyser event independently would be very time-consuming or even impossible what shows a need for proposing a methodology of data reduction.

6.2 Statistical approach to determination of geyser boiling

The phenomenon of geyser boiling is repetitious but waiting periods between consecutive events and their intensity vary. Detection of geysering requests continuous pressure measurements with a high accuracy. Gathered data still needed to be carefully analyzed to determine occurrence of the geyser events. Strict definition of geyser event does not exist and distinction between real geyser peak and pressure fluctuations following nucleate

boiling or a transmitter response following a previous event is a challenging task. Pressure increase took few milliseconds but decline lasted longer. For these reasons, problems with identification of the phenomenon occurs and results from research on that topic are limited.

Geysering depends on operating conditions and working fluid. Considering a big amount of data collected during experiments, methodology for data reduction that can be implemented regardless of operating conditions and working fluid was required to compare the results.

Detection of geyser events based on time-dependent pressure signal saved each 0.02 seconds was proposed. It required determination of two fundamental parameters: the lowest pressure difference between the current and time-averaged values (amplitude of pressure increase), and the shortest time break between two consecutive geyser events (a waiting time). The first one (minimal pressure increment) should protect against calculation of noises following e.g. violent nucleate boiling. Tested working fluids operated at different regimes and thus pressure fluctuations varied depending on the test case. It was impossible to set one threshold value for all conditions. Therefore, the probability density was used. All pressure values related to geysering were assumed to be outside the range of -$2\sigma_{SD}$ to +$2\sigma_{SD}$ what represents 95.5% of values in case of Gaussian distribution. σ_{SD} denoted a standard deviation which is a measure of the spread of a distribution computed as:

$$\sigma_{SD} = \sqrt{\frac{\sum_{i=1}^{N}(p_i - \bar{p}_{mean})^2}{N-1}} \tag{6.1}$$

Where N is a number of time steps for a given test case.
Each peak that exceeded threshold line given by the σ_{SD} rule with an increasing trend was then considered as a potential geyser event. The values of the threshold lines were marked as *mph* in plot labels.

The second parameter was a waiting period which indicated a minimum time break between two successive geyser events (*mpd*). It allowed for avoiding the signal noise resulting from a previous liquid push without its previous evaporation and its return due to gravity forces. Here again, geyser boiling characteristics depended on working fluid used and operating conditions. Thus, finding this parameter for a given test case started with results determination for a wide range of waiting period values. Obtained results for water at inlet temperature of heating water between 65°C and 85°C are presented in Fig. 6.5.

The value on the constant line after curve bending was taken for further calculations. The example of influence of this parameter on detected events is presented in Fig. 6.6 for water. The double or even triple counting of the same event is seen among others for low values of waiting period (e.g. $mpd = 5$, thus 0.1 second). In case of high *mpds*, some evident geyser events could be omitted.

The last step was to check if detected peaks overlap the ones determined with the naked eyes. This half-manual procedure gave a relatively fast method of geysering analysis that allowed for comparison of big databases. This methodology was applied for all test cases with different working fluids and operating conditions.

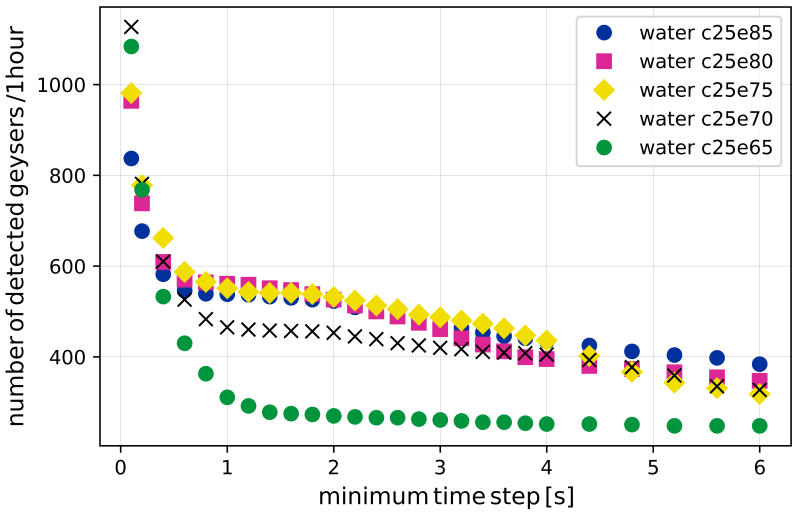

Figure 6.5: Analysis of waiting period effect on the number of detected geyser events depending on operating conditions. c25 means inlet temperature of cooling water equal to 25°C, e65-85 indicates inlet temperatures of heating water between 65°C and 85°C, respectively

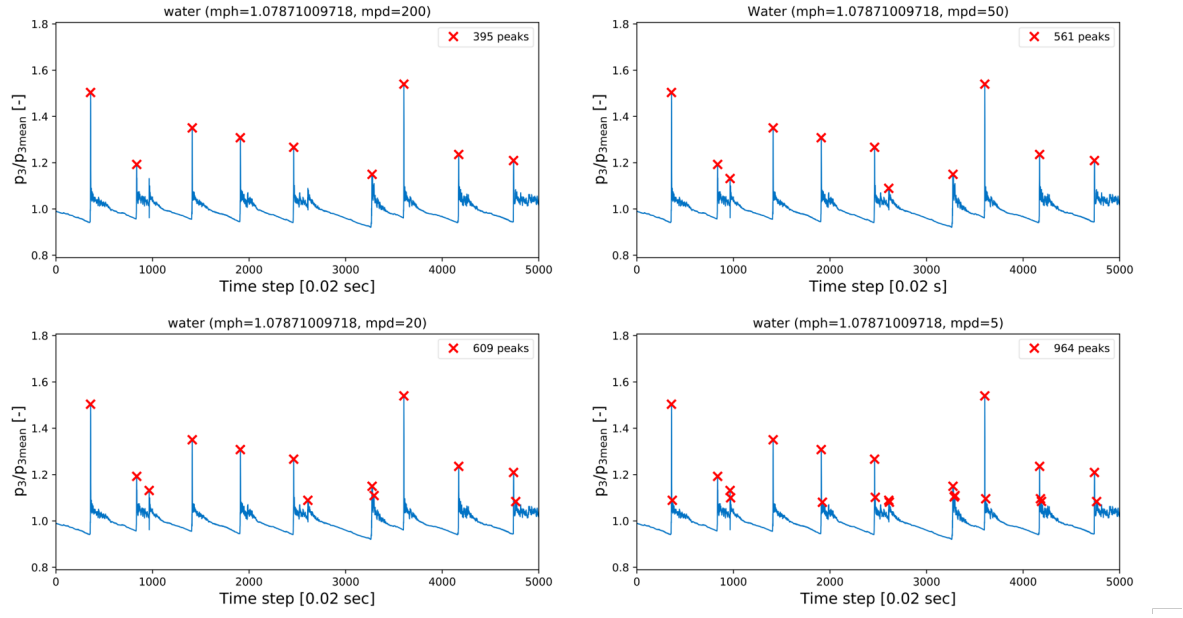

Figure 6.6: Detected pressure peaks in dependence of waiting period (*mpd*) and influence on the number of detected geyser events for water

6.3 Instantaneous pressure distributions

Analysis of geyser boiling characteristics shown in this section were provided by implementation of methodology described in the previous section into a Python script. Sample of detected geyser events marked with crosses is presented in Fig. 6.7 for water used as a working fluid. Plots show geyser events during the first 100 seconds of experiments, while the number of detected peaks in the right upper corner refers to one hour which

was the whole time of experiment. Y-axis represents the ratio of the actual pressure signal from the lowermost transmitter p3 to the pressure averaged over the measurement time. In case of water, geyser event was preceded by a strong pressure decline. A real pressure amplitude following the fluid ejection was slightly higher than that calculated from the averaged pressure, thus the threshold value was reduced to $\pm 1.5\sigma_{SD}$ for two highest evaporator temperatures.

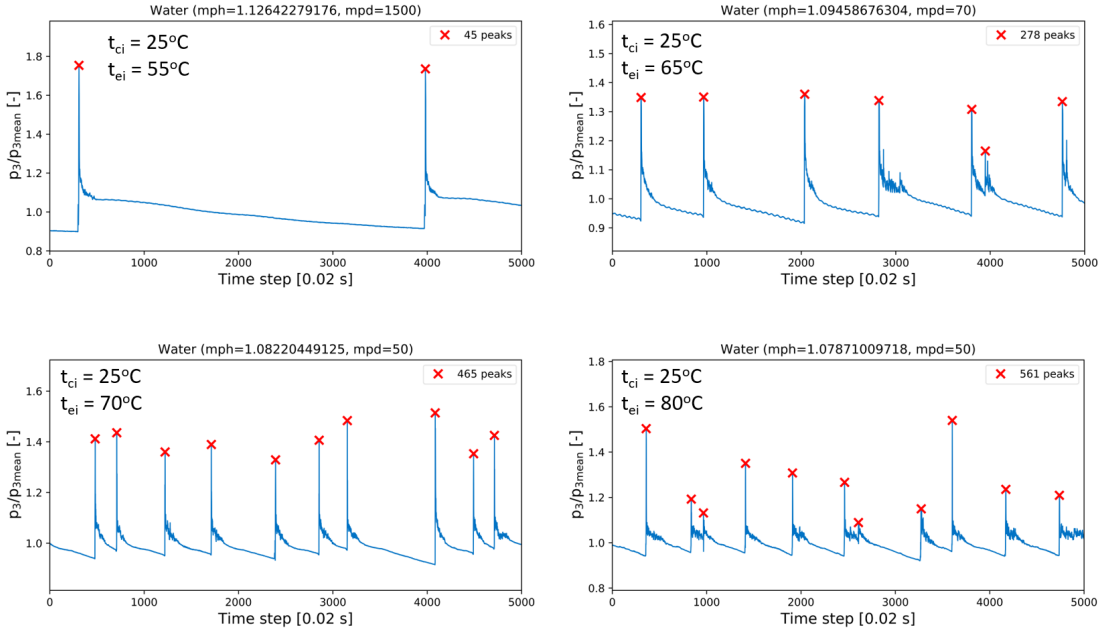

Figure 6.7: Detected geyser events for chosen working conditions in thermosyphon operating with distilled water

Thermosyphon with water operated under a quite regular geysering regime for inlet temperature of heating medium t_{ei} higher than about 55°C. Geyser event started with a sudden and sharp pressure increment, often preceded by significant pressure decrease. Peak was then followed by a rather short time of decreasing pressure fluctuations. For high heat loads, liquid returning to the evaporator could initiate nucleate boiling but for most cases these fluctuations were probably an echo of previous geyser event. Sometimes, the second (or third) smaller pressure peak occurred during these fluctuations. After that period, pressure decreased again (up to about σ_{SD} lower than the time-averaged value) until new bubble grew enough to push liquid towards the condenser.

Set of plots with detected geyser events for all other tested working fluids under various operating conditions are presented in Fig. 6.8 - 6.14. First issue to notice is that the boiling behavior strongly depended not only on operating conditions but also on working fluid. Presented patterns for various fluids differed significantly between each other.

Instantaneous pressure distributions inside a thermosyphon filled with silica nanofluid showed higher number of geyser events compared to water. With increasing heat load, the periods of pressure fluctuations after a peak became longer. For $t_{ei} = 85$°C, pressure fluctuations lasted even for about 20 seconds. Pressure minimum before the geyser event reached lower values than one σ_{SD} from the averaged pressure. Reasons behind these changes seem to connect with a nanoparticles deposition on the inner wall of the

evaporator. Formed layer changed the roughness, surface energy and nucleation site density what affected the boiling process. Silica deposition was very massive what could inhibit wickability described by Kim et al. [97] as one of mechanism influencing boiling of nanofluids.

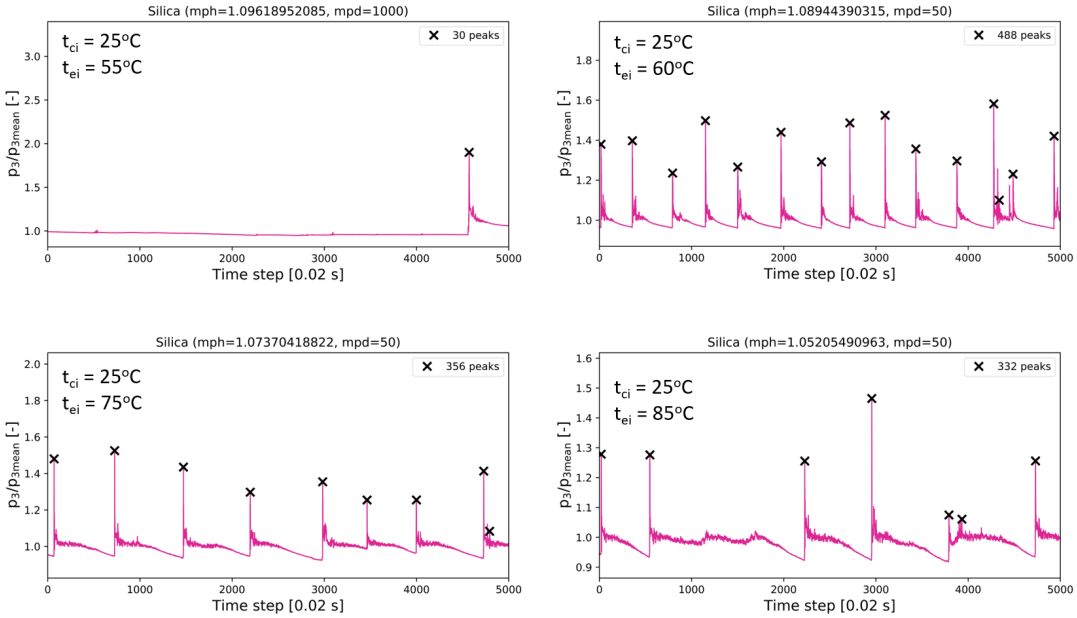

Figure 6.8: Detected geyser events for chosen working conditions in thermosyphon operating with silica nanofluid

Pressure distributions for two gold nanofluids were different from water and varied also between each other. Nanoparticles used in both nanofluids were the same, thus the differences came from the stabilization used - polymer PVP (Au1 nanofluid, Fig. 6.9) and KOH (Au2 nanofluid, Fig. 6.10). Au+PVP underwent typical geyser boiling but with various regularity and intensity. Standard deviation for pressure signal p3 was characterized by the highest value from all tested working fluids (7.66 mbar). Au+KOH showed more structured behavior with long periods of pressure fluctuations, especially for t_{ei} of 80°C and 85°C. For the latter, this pattern seems to indicate a nucleate boiling regime with occasional pressure increments, e.g. low intensity geyser events or kind of slug-plug structures. In this case, standard deviation was only 1.72 mbar, significantly lower than for water (5.15 mbar). In general, both gold nanofluids caused more pressure peaks than water in comparable operating conditions, while Au+KOH reached lower amplitudes than Au+PVP. KOH is supposed to associate in water and should not noticeably change the surface tension and contact angle. Fluid taken out from thermosyphon after all experiment was transparent with only single agglomerates. This suggests that changes in Au+KOH behavior compared to water resulted from particles deposition. Here, wickability effect could play a role. On the other hand, PVP has film-forming properties. Its addition could influence thermophysical properties of fluid, such as viscosity or wettability. Although most polymers (except polymeric surfactants) do not change surface tension of solution, adsorption of molecules on the vapor-liquid interface may affect forces acting during bubble nucleation, growth and detachment. Further research is required to explain mechanisms behind boiling of polymer solutions. To the best author knowledge, there

is no study on nanofluids stabilized with polymers under changing pressure conditions. Differences between both gold nanofluid clearly showed that apart from nanoparticles, used stabilization may significantly influence the results. Next to changes on the evaporator surface, interaction on vapor-liquid interface (bubble surface) may be affected due to addition of chemicals.

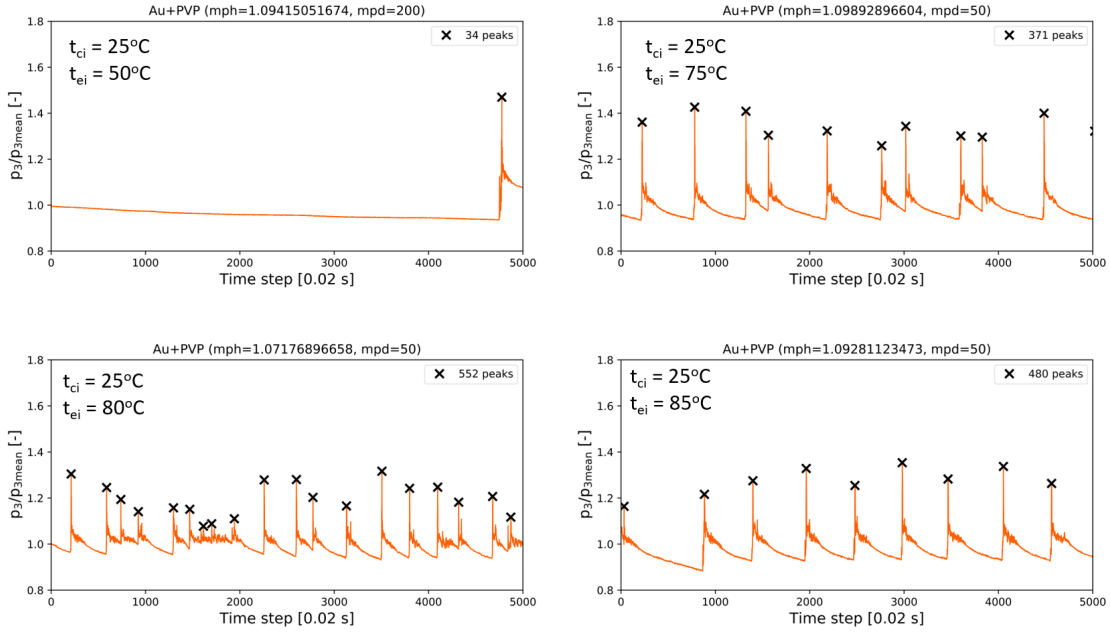

Figure 6.9: Detected geyser events for chosen working conditions in thermosyphon operating with Au+PVP nanofluid

Time-dependent behavior of nanohorn nanofluid differed significantly from water. Long periods of fluctuating pressure occurred even for $t_{ei} = 65°C$. For higher evaporator temperatures, regime turned into pressure fluctuations assumed to be a nucleation boiling with randomly distributed peaks. The standard deviation of pressure signal p3 was decreased to 40% of the water value. Peaks with lower amplitude than in case of water were detected but they were clearly outside the values of stochastic fluctuations.

Solution of sodium dodecyl sulfate (SDS) prevented geyser boiling almost entirely. SDS as an ionic surfactant is characterized by reduced surface tension, what translates into smaller sizes of bubbles. Visualization reported by Wang et al. [206] showed that two other mechanisms during boiling of surfactant solutions occurred: bubble bursting and a jet-flow phenomena. Both mechanisms led to smaller dry-out spots and more intense disturbances. Surfactants could inhibit geyser boiling by preventing formation of big bubbles as a result of reduced surface tension. Moreover, lower surface tension translated into less energy required to create a bubble and to activate nucleation site what promoted clustered mode of bubbles detachment. Bubbles detached at smaller sizes with higher frequency, influenced also by cavity-cavity interactions, microlayer evaporation, and bubbles coalescence [2, 206, 218]. For these reasons, bubbles could not achieve sizes big enough to push fluid gathered above towards the condenser and main regime for high heat loads were a nucleate boiling.

SDS suppressed geysering but also reduced the whole pressure fluctuations. Standard deviation was the lowest from all tested working fluid and for pressure p3 and

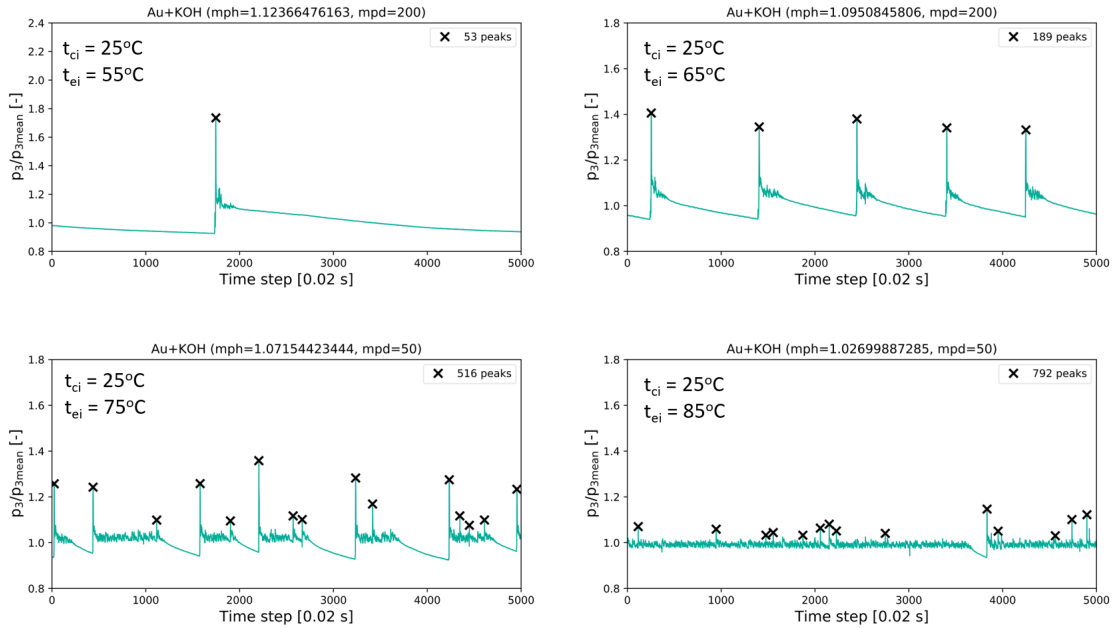

Figure 6.10: Detected geyser events for chosen working conditions in thermosyphon operating with Au+KOH nanofluid

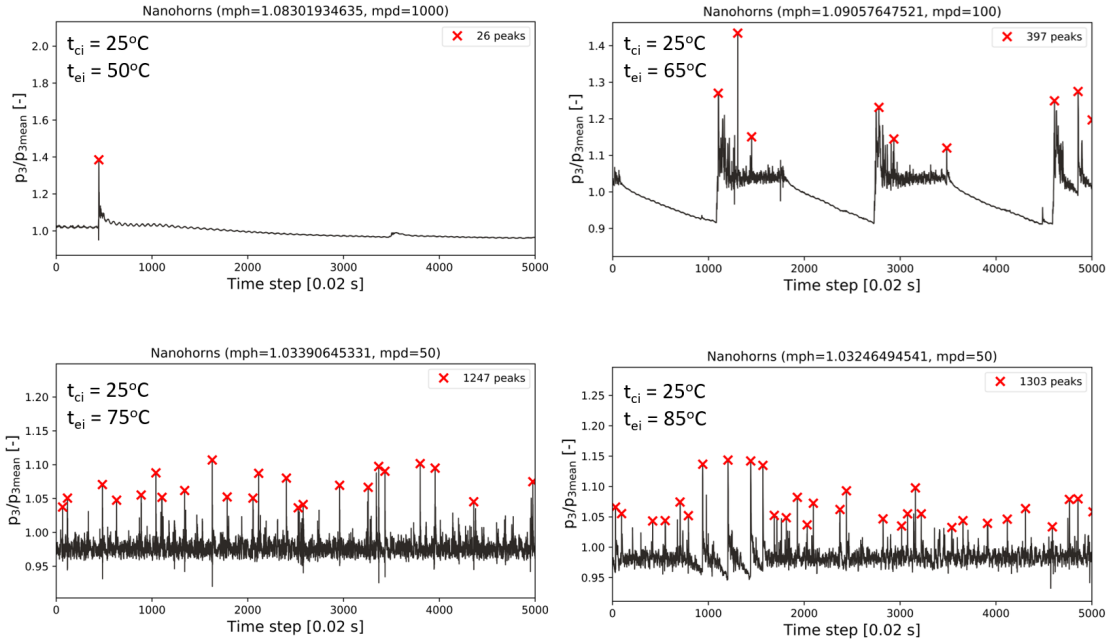

Figure 6.11: Detected geyser events for chosen working conditions in thermosyphon operating with nanohorns nanofluid

highest evaporator temperature it was equal to approx. 1 mbar. It suggests that pressure distribution for surfactant solution showed practically Gaussian distribution which is characteristic for a pure nucleate boiling. As the mean pressure was almost the same, the differences in amount of heat transported through the device came mainly from boil-

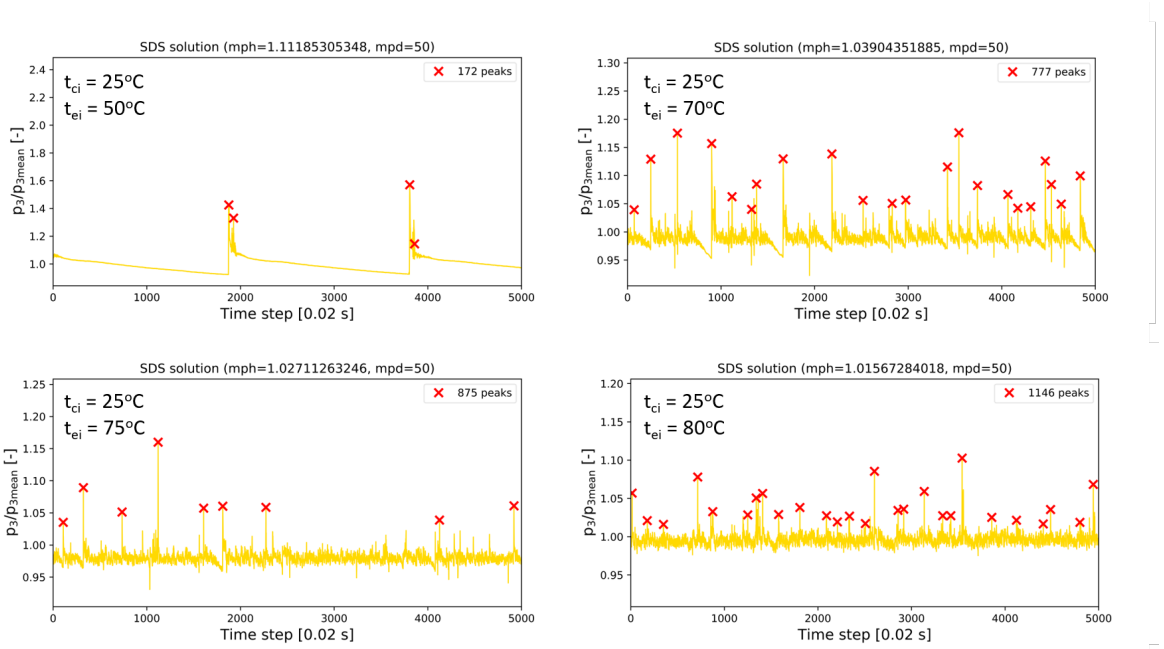

Figure 6.12: Detected geyser events for chosen working conditions in thermosyphon operating with SDS solution (0.01 g/L)

ing regime (geyser boiling for water and nucleate boiling for SDS). For t_{ei} = 80°C, heat released in condenser by water was 1.8% higher than in case of SDS. Thus, geysering gave negligible influence on the overall amount of heat transferred what is in agreement with Noie et al. [142] and Emami et al. [50].

Taking into account the effect caused by SDS solution, it seems that changes in nanohorn boiling behavior resulted mostly from the presence of surfactant. This observation is similar to conclusions from gold nanofluids behavior which showed significant differences in results depending on stabilization used. In case of nanohorn nanofluid, particles caused higher fluctuations and more frequent but irregularly distributed pressure peaks than for pure surfactant solution.

Similar results were expected for graphene oxide nanofluid stabilized with the same concentration of SDS as in case of SDS solution and nanohorn nanofluid (fig. 6.13). However, GO+SDS did not follow their behavior. Observed regime was again geyser boiling with slightly lower frequency and similar amplitudes to that of water, often with double-peak structures. This behavior was strongly correlated with interactions between graphene oxide flakes and SDS. Surfactant attached to the flake surface (SEM analysis, Fig. 5.37 f), thus its concentration in a base fluid decreased what in turn reduced effect on surface tension of working fluid. This explains the differences in surface tension measured for pure GO nanofluid and GO+SDS showed in Fig. 4.15. Higher surface tension of this working fluid compared to pure surfactant solution inhibited the positive effects on bubble nucleation process mentioned in previous paragraphs. It was reported that GO nanoparticles themselves may lower the surface tension of nanofluids [33, 51]. Thus, question whether SDS was attached to the graphene oxide entirely or partly remains open.

Pressure signal for pure GO nanofluid (fig. 6.14) was characterized by irregular and quite randomly distributed geyser events. Periods of pressure fluctuations following the

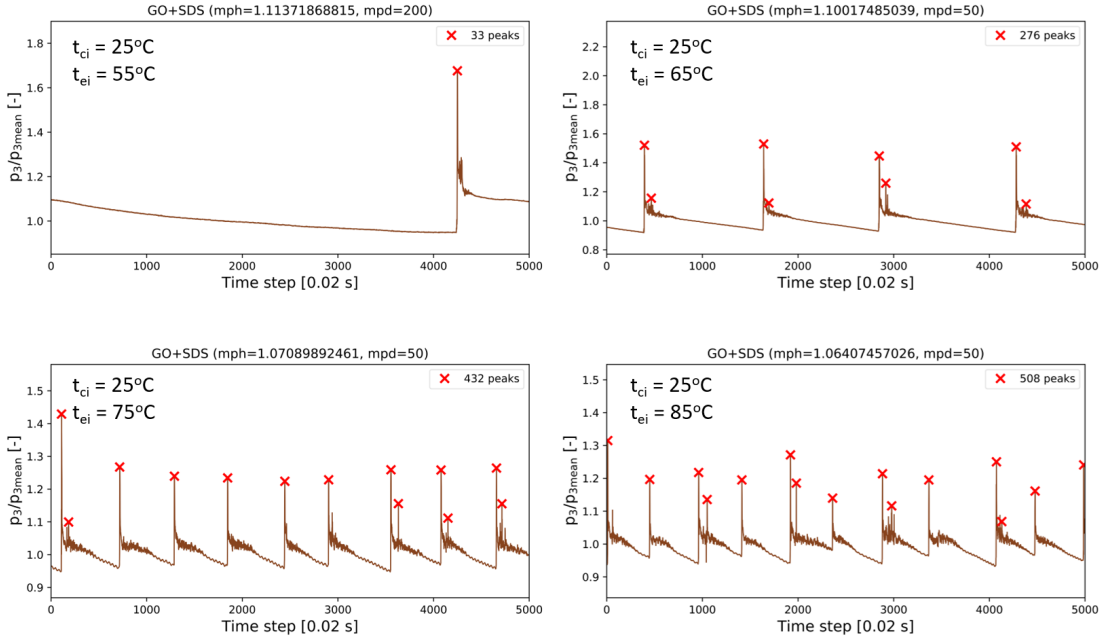

Figure 6.13: Detected geyser events for chosen working conditions in thermosyphon operating with GO+SDS nanofluid

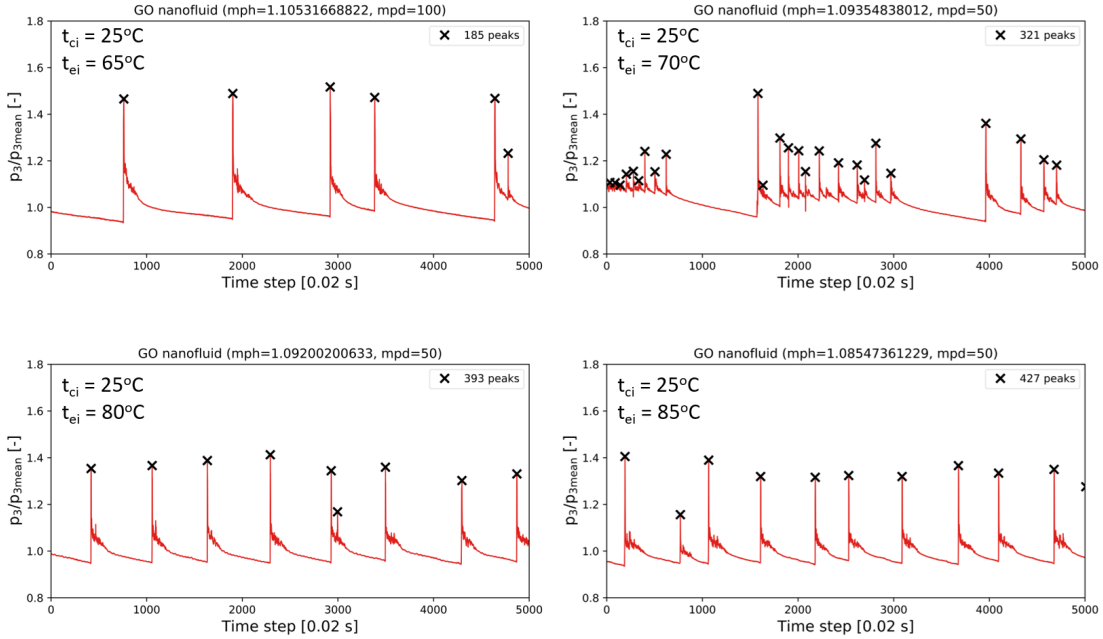

Figure 6.14: Detected geyser events for chosen working conditions in thermosyphon operating with GO nanofluid

peak were shorter and the minimum pressure values before the liquid ejection were higher than for GO+SDS nanofluid.

The matrix presented in Fig. 6.15 summarizes boiling regimes for different operating conditions proposed by observations of instantaneous pressure distributions. Additional

analysis of averaged frequency and amplitude of detected events is proposed to compare the differences between behavior of tested working fluids.

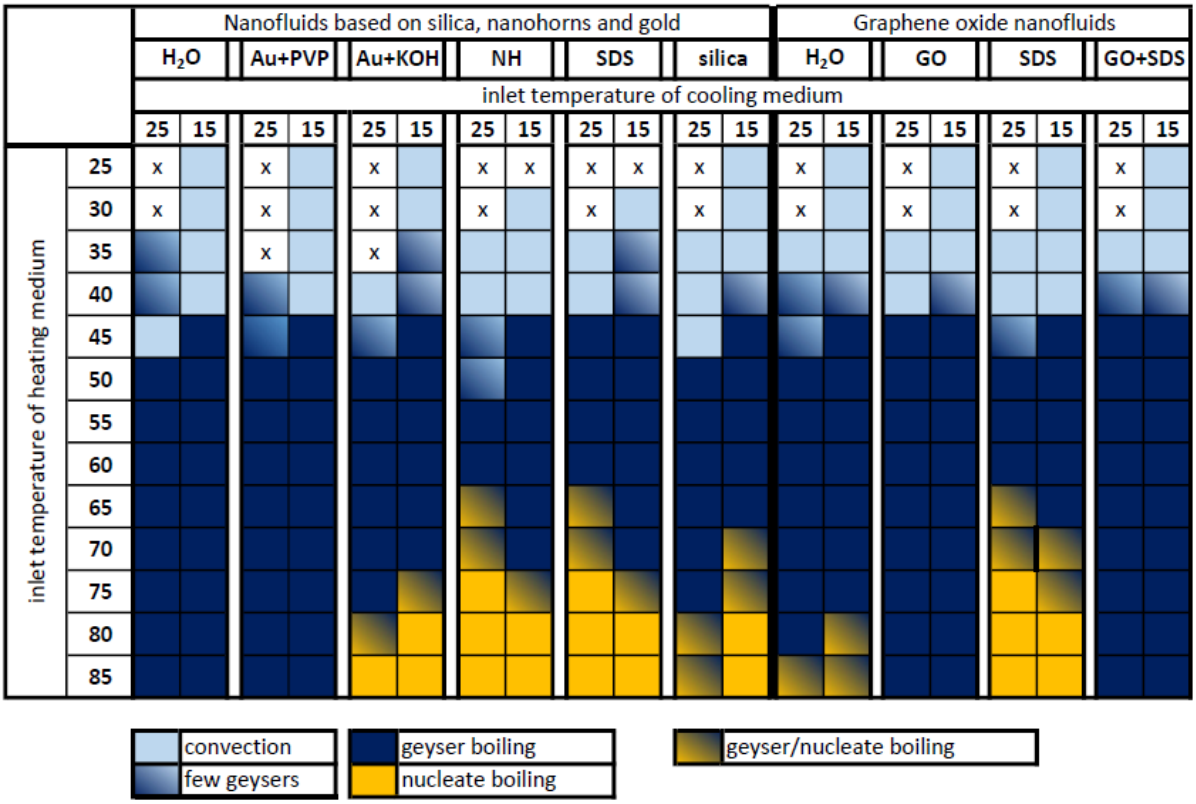

Figure 6.15: Boiling regimes for different operating conditions proposed by manual observations of instantaneous pressure distributions

This map provides an useful information allowing for selection of best-performing working fluid for a given application and operating conditions. For example, when it is expected to avoid geyser boiling (e.g. to reduce mechanical load) in thermosyphon heated at the temperature level of 75-85°C, nanohorn nanofluid, SDS solution, silica nanofluid or gold nanofluid stabilized with KOH should be considered. Taking into account other parameters of thermosyphon, such as its overall thermal resistance or the amount of transported heat, it is possible to choose the advisable working fluid during process of thermosyphon designing.

6.4 Frequency and amplitude of detected geyser events

Figure 6.16 shows the frequency of detected geysers for nanofluids based on gold, nanohorn, and silica particles, and related base fluids. In general, geysering frequency increased with the evaporator temperature. This agrees with studies published by Casarosa et al. [35], Lin et al. [109] and Khazaee et al. [92] who reported increment in geyser events frequency for higher heat loads. At low evaporator temperatures, nearly none geyser events were detected zero. Up to $t_{ei} = 60°C$, all working fluids except SDS solution and silica nanofluid showed similar averaged frequency.

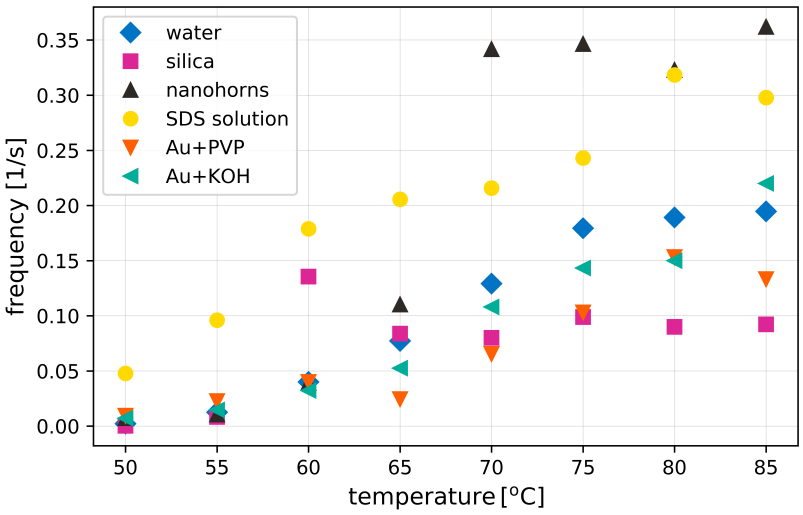

Figure 6.16: Frequency of detected geysers in dependency on inlet temperature of heating water for condenser inlet temperature of 25°C

Figure 6.17 showcases a relative amplitude ($p_3/p_{3_{mean}}$) of detected geyser events. General trends show that geysering intensity decreases with an increase in evaporator temperature. This is with an agreement with Khazaee et al. [92] who reported decrease in geysering amplitude with an increase in heat load. Casarosa et al. [35] reported no effect of heat load on the geysering intensity. No other results were available in the literature on this issue to the best author knowledge.

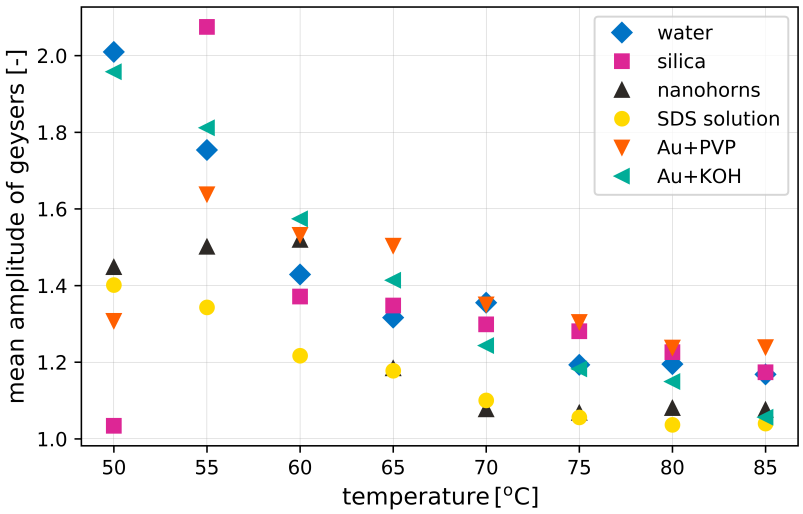

Figure 6.17: Relative amplitude of detected geysers in dependency on inlet temperature of heating water for condenser inlet temperature of 25°C

Replacing water with silica nanofluid caused unusual characteristics of geysering frequency. With increasing inlet temperature of heating water higher than $t_{ei} = 60$°C, the frequency of geysers were almost constant but their amplitude decreased. Compared to water, silica nanofluid significantly reduced or even entirely suppressed geyser boiling for

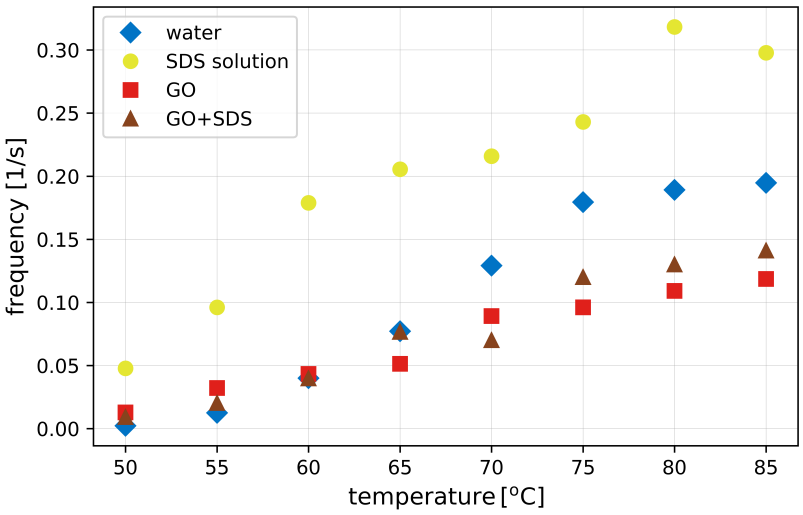

Figure 6.18: Frequency of detected geysers in dependency on inlet temperature of heating water for GO-related working fluids (condenser inlet temperature of 25°C)

some operating conditions. Very few geysers with high amplitude for $t_{ei} = 55$°C suggests that thermal energy could not be easily released, e.g. due to lack of active nucleation sites. Elongated periods of pressure fluctuations with increasing evaporator temperature decreased the amplitude of geyser events. If pressure fluctuations indicated a nucleate boiling regime, thermal energy was released more regularly and thus geyser events had lower intensity. These boiling characteristics of silica were affected by nanoparticles deposition layer formed on the inner wall of the evaporator section.

Both gold nanofluids showed similar frequency of geyser events up to $t_{ei} = 60$°C but different intensity. For low evaporator temperatures, Au+KOH caused more intense geyser events, while for high temperatures Au+KOH reduced mean amplitude of geysers compared to Au+PVP. Again, with evaporator temperature increment, frequency of detected geyser events increased but their intensity decreased.

SDS solution indicated significantly more geyser events with relatively smaller intensity than any other working fluid for low evaporator temperatures. For high heat loads ($t_{ei} > 70$°C), nanohorns nanofluid showed higher frequency of geysering with similar or slightly higher intensity than solution of sodium dodecyl sulfate. Both working fluid had significantly higher geysering frequency and lower amplitude than water and their behavior could be classified more as a nucleate boiling with randomly distributed pressure peaks than characteristic geyser boiling.

Figures 6.18 and 6.19 present parameters of detected geyser events for GO-related nanofluid. General trends show similar tendencies as described above - frequency of geyser events increased but their intensity decreased with increasing evaporator temperature (and thus heat load).

Both graphene oxide nanofluids reduced geysering frequency compared to base fluids (water and SDS solution) for high evaporator temperatures. However, normalized pressure amplitude of geyser events were higher than in case of base fluids. As previously described, similar behavior of GO+SDS to nanohorns nanofluid and SDS solution was expected. Due to attachment of SDS crystals to surfaces of graphene flakes, the surface tension of this fluid was higher than in case of pure SDS solution. It inhibited influence

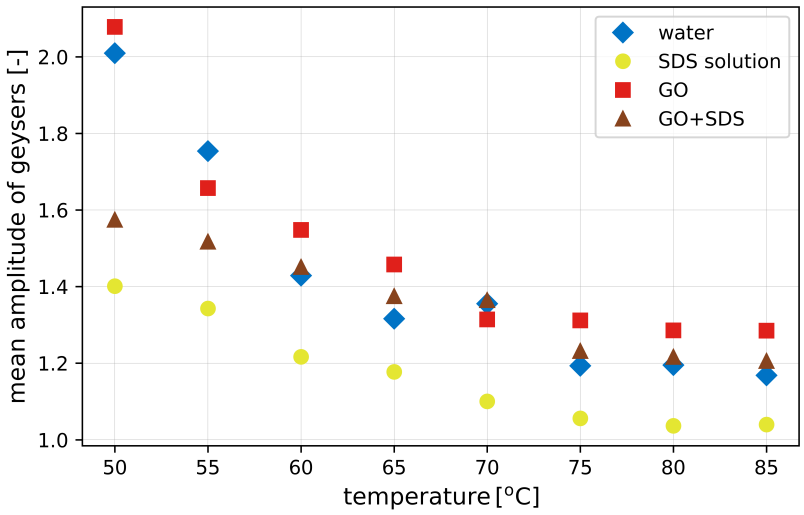

Figure 6.19: Relative amplitude of detected geysers in dependency on inlet temperature of heating water for GO-related working fluids (condenser inlet temperature of 25°C)

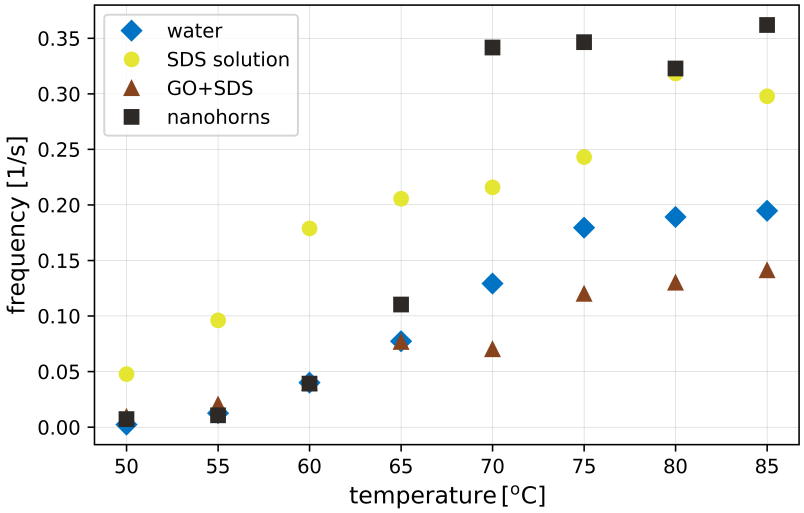

Figure 6.20: Analysis of SDS surfactant (sodium dodecyl sulfate) effect on frequency of detected geysers in dependency on inlet temperature of heating water (condenser inlet temperature of 25°C)

on boiling behavior in a similar way to pure SDS solution or nanohorns nanofluid. Differences between water, SDS solution, nanohorn nanofluid and GO+SDS nanofluid are additionally compared in Fig. 6.20 and Fig. 6.21.

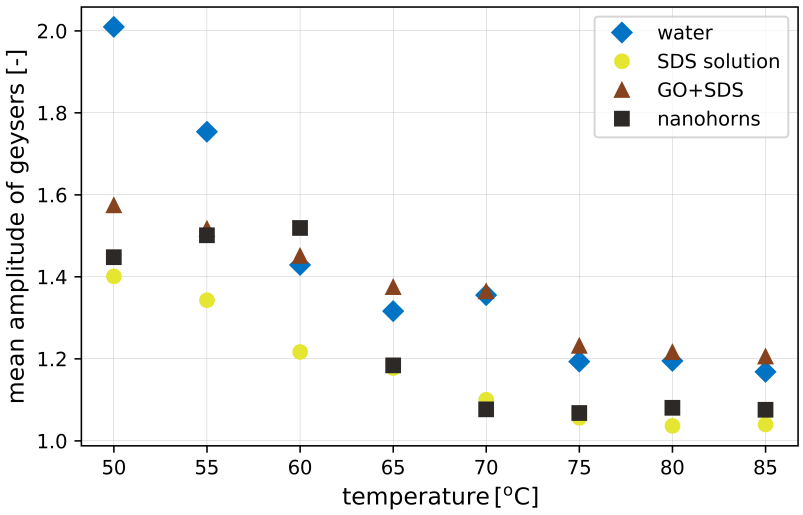

Figure 6.21: SDS influence on relative amplitude of detected geysers in dependency on inlet temperature of heating water for GO-related working fluids (condenser inlet temperature of 25°C)

6.5 Chapter summary

Working fluid affected boiling behavior, even if time-averaged data did not show any differences within an experimental error for high thermal loads (above approx. 200 W). Understanding of mechanisms behind geyser boiling is still in its initial stage and further research is required to develop and prove possible theories. The task is even more complex for nanofluids, where interactions between base fluid, nanoparticles, chemical stabilizers and evaporator surfaces must be considered.

The following conclusions may be drawn from the above analysis of time-dependent data.

- The characteristic parameters of geyser events - their amplitude and frequency - depended on temperatures in the evaporator and condenser section, and used working fluid. Thermal energy were stored and released in a different way depending on working fluid and operating conditions.

- Nanofluids may or may not lower the geyser events amplitude and frequency depending on their type, components, and operating conditions.

- In general, rising the evaporator temperature (and thus heat load and temperature difference between two ends of a thermosyphon), caused an increase in the frequency of detected geyser events, and a decrease in their amplitudes.

- Reduction in geysering intensity (understood as pressure amplitude) was mostly the result of surfactant addition. Stabilizer affected thermophysical properties of working fluids, such as reduced surface tension following the usage of sodium dodecyl sulfate. This may prevent formation of bubbles big enough to push working fluid gathered above towards the condenser without its previous evaporation.

- Effect related to nanoparticles were restricted to the solid-vapor interphase at the evaporator wall (deposition layer). Chemical stabilizers, among others surfactants are expected to change the vapor-liquid interface (bubble surface) what affected boiling behavior.
- Even if nanofluids were stabilized with the same amount of SDS surfactant, their boiling behavior differed due to interactions between surfactant and surface of nanoparticles. If the surface chemistry and energy allow for attachment of surfactant to the surface of particle, concentration of stabilizer in a base fluid decreases. This in turn reduces the effect caused by stabilizer (e.g. lower surface tension). The surface chemistry of nanoparticles is another factor that should be considered with respect to boiling behavior of nanofluids.

Chapter 7

Conclusions and perspectives

This thesis addresses the research questions of nanofluids usage as working fluids in a thermosyphon with special emphasis on boiling behavior. Introduction chapter highlighted the importance of nanofluids in context of heat transfer applications. Comprehensive literature review suggested that each of nanofluid components (nanoparticles, base fluid and optional stabilizer) may alter final properties of nanofluids. Proper characterization of nanofluids is still a problem due to need of using highly-specialized and often customer-adapted equipment traditionally used in various fields of science, including chemistry, physics, material science, thermodynamics and thermal energy transfer. Nanometric scale is a barrier to overcome that needs unified cognitive efforts. Available techniques does not allow for e.g. thermophysical properties determination under conditions used in real applications, such as low pressure boiling. All this caused incoherent data in the literature and shows a need for bigger experimental databases of comparable data.

Thermosyphons has relatively simple construction and does not require mechanical power to operate but thermodynamics responsible for heat transfer is complex. Classical approaches to thermosyphon design are not applicable for nanofluids. Mathematical tools cannot be developed without understanding of mechanisms behind nanofluids behavior. Results available so far are incoherent and determination of issues related to nanofluids is possible only by systematic experimental work. Influence of stabilizers addition that are often excluded from results analysis should be common consideration.

During boiling of nanofluids, nanoparticles tend to deposit on the heater surface. Deep understanding of this mechanism still requires further research together with analysis of agglomerates that remain in the working fluid.

Literature address little attention to geyser boiling phenomena. This common regime in thermosyphons includes repetitive ejections of liquid gathered above the growing bubble in the direction of condenser without its previous evaporation. It cause additional mechanical loads and may decrease time period of operation of thermosyphon often used in applications respected to work for a long time. Nearly no research cope with influence of nanofluids or surfactants and polymers on geyser boiling phenomena.

From the investigations presented in this thesis, following conclusions may be drawn.

- All nanofluid components (base fluid, nanoparticles, and stabilizer) interact and may change working fluid behavior in the thermosyphon, including boiling process. Nanoparticles changes the interactions on the evaporator wall (solid-liquid interface), while chemical stabilizers affect interaction on vapor-liquid interface (bubble surface). Thus, they should be considered integrally.

- The positive effect of nanofluids on heat transfer capabilities in thermosyphon is restricted to the evaporator section. Nanofluids did not influence heat transfer in the condenser.

- Nanofluids in a thermosyphon showed time-dependent characteristics after filling the device with fresh fluid, at least at the beginning of thermosyphon operation. Heat transfer capabilities of the device were significantly increased after the first experimental series. Some period of time was needed for a *backing process* - deposition of nanoparticles on the evaporator wall. Theses layers affect the roughness, surface energy, wettability, surface tension, and density of active nucleation sites.

- Deposited nanoparticles did not cover the entire heater surface uniformly. In case of tested thermosyphon, the layer was found in the upper part of the inner wall of the evaporator.

- Particle deposition may create thermal bridges between inner wall and surface reducing thermal resistance of this contact. Its impact is higher for low heat loads where this thermal resistance shows a higher impact on the overall thermal resistance of a thermosyphon compared to high heat loads with developed boiling.

- The lower the inlet temperature of heating water, the higher overall thermal resistance reduction caused by nanofluids in comparison to water. Low heat loads and small temperature differences between two ends of a thermosyphon (hot and cold) where nanofluids show the biggest impact are often problematic conditions in heat transfer applications. Thus, nanofluids may become an interesting alternatives for such applications.

- The highest improvements in heat transfer capabilities of a thermosyphon for low heat loads was gained by usage of silica nanofluid, followed by graphene oxide nanofluid.

- The possible mechanisms affecting heat transfer efficiency during nanofluid boiling in a thermosyphon include:

  - nanoparticles deposition into a (porous) layer on the evaporator wall that influences boiling conditions at surface, examples: silica nanofluid, graphene oxide nanofluid,
  - interaction of nanoparticles both at wall and freely moving in fluid volume, e.g. gold nanofluids,
  - affecting thermophysical properties of a working fluid, among others surface tension and viscosity. The best examples here are nanohorn nanofluid, SDS solution and GO+SDS nanofluid. Nanohorns and SDS solution showed similar behavior. The effect was different for GO+SDS, despite the same amount of SDS was added. Additional interaction between surfaces of graphene oxide flakes and surfactant occurred resulting in changed working fluid properties.

- Investigated working fluids shifted the working point of a thermosyphon what includes differences in the amount of heat transferred though a device and the temperature levels compared to water at analogous operating conditions (inlet temperatures and heat fluxes of heating and cooling water).

- For high heat loads, the differences between time-averaged thermal performance of a thermosyphon for various working fluids were negligible. However, corresponding time-dependent characteristics differed significantly. In this region, geyser boiling occurred for water, gold nanofluids and graphene oxide nanofluids.

- Sodium dodecyl sulfate surfactant added to the base fluid lowered its surface tension. As a result, bubbles could not reach sizes big enough to push fluid gathered above them towards the condenser. This changed boiling regime from geyser boiling to nucleate boiling.

- Attachment of SDS to the graphene oxide flake reduced concentration of surfactant in a base fluid what in turn increased the surface tension. In consequence, geysering could not be suppressed what was the case for SDS solution or nanohorns nanofluid.

- Averaged frequencies and amplitudes of geyser events described the geyser boiling characteristics regardless the working fluid and operating conditions and allows for comparison of wide range of test cases. General trends showed that frequency of geyser events increased but their amplitude decreased with increasing heat loads but the exact values depended on working fluid and operating conditions.

- Peak intensity (pressure amplitude) seems to be a measure of a thermal energy stored during bubble formation.

Properly chosen nanofluids used as working fluid in a thermosyphon keep a great promise for heat transfer improvements. This is especially true for applications with low level of heating temperature, small differences between two ends of a device, and low heat fluxes provided to the evaporator. As a result of the work done for this thesis, the following have emerged as work for the future.

- More detailed analysis of evaporator surface after particle deposition and checking the layer properties, such as porosity, wettability, and wickability. Here, collaboration between material and thermodynamics engineers, chemists and surface physicists would be a great help.

- Development of mathematical tools describing thermosyphon operating with nanofluids are in a high need. The first step consider deep understanding of the nanofluids behavior.

- To address better understanding of nanofluids behavior in a thermosyphon, systematic experimental study considering a wide range of working fluids and operating conditions are suggested. Focus should be put on good characterization of nanofluids used in heat transfer applications. This includes contact angle and surface tension measurements. These properties have significant impact on boiling behavior but are poorly investigated with regards to nanofluids. Nanofluids are often characterized under conditions that differ significantly from that met in real applications. It is especially true for low pressure devices and requires further research and development of measurement techniques.

- To help draw firm conclusions, research should differentiate effects caused by nanoparticles themselves and by chemical stabilizers. This includes research on boiling of polymer/surfactant solutions and nanofluids with their addition, physical interplay

between nanoparticles, base fluid and chemical stabilizers. In a high need is understanding their behavior under changing conditions, in particular under low pressure.

- Another task is to explain how nanoparticles reduction (such as reduction of graphene oxide in the temperatures ranges of 50-60°C) affect boiling behavior and deposition process.
- Boiling of non-Newtonian fluids (which is often a case for nanofluids) received very little attention in the literature. This could give some insight into understanding boiling behavior of nanofluids.
- Long-term behavior of nanofluids with respect to their properties and behavior in heat transfer systems should be thoroughly investigated. Thermosyphons are often supposed to work in long-life applications, thus their long-term stability seems to be crucial issue for their commercialization.
- Relatively cheap and mass production of nanofluids with precisely characterized properties and possibilities are another challenge to overcome barriers in front of nanofluids to be commercialized.

List of publications

1. **A. Kujawska**, B. Zajaczkowski, L.M. Wilde, M.H. Buschmann. Geyser boiling in a thermosyphon with nanofluids and surfactant solution. *International Journal of Thermal Sciences*, 139 (2019) 195-216.
doi: https://doi.org/10.1016/j.ijthermalsci.2019.02.001

2. M. Hernaiz, V. Alonso, P. Estellé, Z. Wu, B. Sundén, L. Doretti, S. Mancin, N. Çobanoğlu, Z.H. Karadeniz, N. Garmendia, M. Lasheras-Zubiate, L.L. Hernández López, R. Mondragón, R. Martínez-Cuenca, S. Barison, **A. Kujawska**, A. Turgut, A. Amigo, G. Huminic, A. Huminic, M.R. Kalus, K.G. Schroth, M.H. Buschmann. The contact angle of nanofluids as thermophysical property. *Journal of Colloid and Interface Science*, 547 (2019) 393-406.
doi: https://doi.org/10.1016/j.jcis.2019.04.007

3. **A. Wlazlak**, B. Zajaczkowski, M. Woluntarski, M.H. Buschmann. Influence of graphene oxide nanofluids and surfactant on thermal behaviour of the thermosyphon. *Journal of Thermal Analysis and Calorimetry*, 136 (2019), 843-855.
doi: https://doi.org/10.1007/s10973-018-7632-x

4. **A. Kujawska**, B. Zajaczkowski, Z. Krolicki, M. Woluntarski, M.H. Buschmann. Transfer processes in the thermosyphon employing graphene oxide and silica nanofluids. In: *25th IIR International Congress of Refrigeration*, August, 24-30, 2019, Montreal, Canada.

5. **A. Kujawska**, B. Zajaczkowski, M.H. Buschmann. On the double peak structure of thermosyphon geysering. In: *5th World Congress on Mechanical, Chemical, and Material Engineering (MCM'19)*, August, 15-17, 2019, Lisbon, Portugal.

6. **A. Kujawska**, B. Zajaczkowski, M.H. Buschmann. How to detect geysering of nanofluid in thermosyphon?. In: *1st International Conference on Nanofluids (ICNf) and the 2nd European Symposium on Nanofluids (ESNf)*, June, 26-28, 2019, Castellon de la Plana, Spain.

7. **A. Kujawska**, B. Zajaczkowski, M. Woluntarski, M.H. Buschmann. Determination of geyser events in a thermosyphon working with graphene oxide nanofluid. *MTM Machines. Technologies. Materials.*, 13 (2019), 74-77.

8. **A. Wlazlak**, B. Zajaczkowski, M. Woluntarski, M.H. Buschmann. Effect of various nanofluids on thermal performance of the thermosyphon. In: *16th International Heat Transfer Conference (IHTC16)*, August, 10-15, 2018, Beijing, China.

9. **A. Wlazlak**, B. Zajaczkowski, M. Woluntarski, M.H. Buschmann. Impact of graphene oxide addition to the working fluid on thermal behavior of the thermosyphon. In: *Joint 19th International Heat Pipe Conference and the 13th International Heat Pipe Symposium, (19th IHPC & 13th IHP)*, June, 10-14, 2018, Pisa, Italy.

10. K. Wojtasik, **A. Wlazlak**, B. Zajaczkowski. The influence of geyser boiling on performance of two-phase-closed thermosyphon filled with R134a. In: *Joint 19th International Heat Pipe Conference and the 13th International Heat Pipe Symposium, (19th IHPC & 13th IHP)*, June, 10-14, 2018, Pisa, Italy.

11. **A. Wlazlak**, B. Zajaczkowski, M. Woluntarski, M.H. Buschmann. Thermosyphon performance in dependence of carbon-based nanofluids. In: *3rd Thermal and Fluids Engineering Conference (TFEC)*, March, 4-7, 2018, Fort Lauderdale, USA.

12. **A. Wlazlak**, B. Zajaczkowski, S. Barison, F. Agresti, L.M. Wilde, M.H. Buschmann. Nanofluids as working fluid in thermosyphon. In: *1st European Symposium on Nanofluids (ESN2017)*, October, 8-10, 2017, Lisbon, Portugal.

13. K. Wojtasik, **A. Wlazlak**, B. Zajaczkowski, S. Sandler. Analiza możliwosci zastosowania czynników HFO w termosyfonowych wymiennikach ciepła stosowanych do odzyskiwania ciepła odpadowego z instalacji sanitarnych. *Ciepłownictwo, Ogrzewnictwo, Wentylacja*, 47 (2016) 9:365-369.

14. **A. Wlazlak**. Wpływ dodatku nanoczastek do medium grzewczego na współczynnik wnikania ciepła w parowaczu płytowym. *Zeszyty Energetyczne. T. 3, Nowe kierunki rozwoju energetyki cieplnej*, 13-22, Wroclaw, 2016.

15. **A. Wlazlak**, B. Zajaczkowski, A. Mrowiec, K. Pralat, Z. Krolicki. The thermal conductivity of nanofluids measurements - a review of available methods. *Inżynieria wytwarzania*, 267-276, Kalisz, 2016. 9:365-369.

16. **A. Wlazlak**, B. Zajaczkowski, Z.Krolicki. Termosyfonowe rury ciepła systemów klimatyzacyjnych: analiza możliwosci zastosowania czynnikow R1234yf oraz R1234ze(E). *Chłodnictwo i klimatyzacja*, 19 (2015) 22-26.

Bibliography

[1] ISO/TS 80004-2:2015 Nanotechnologies — Vocabulary — Part 2: Nano-objects, 2015.

[2] A. Acharya and A. Pise. A review on augmentation of heat transfer in boiling using surfactants/additives. *Heat and Mass Transfer*, 53(4):1–21, 2016.

[3] E.O. Agunlejika, P. Langston, B.J. Azzopardi, and B.N. Hewakandamby. Flow instabilities in a horizontal thermosyphon reboiler loop. *Experimental Thermal and Fluid Science*, 78(January 2017):90–99, 2016.

[4] M.H. Ahmadi, A. Mirlohi, M.A. Nazari, and R. Ghasempour. A review of thermal conductivity of various nanofluids. *Journal of Molecular Liquids*, 265:181–188, 2018.

[5] H.S. Ahn, J.M. Kim, and M.H. Kim. Experimental study of the effect of a reduced graphene oxide coating on critical heat flux enhancement. *International Journal of Heat and Mass Transfer*, 60(1):763–771, 2013.

[6] A.A. Alammar, R.K. Al-Dadah, and S.M. Mahmoud. Effect of inclination angle and fill ratio on geyser boiling phenomena in a two-phase closed thermosiphon – Experimental investigation. *Energy Conversion and Management*, (156):150–166, 2018.

[7] A.A. Alammar, R.K. Al-Dadah, and S.M. Mahmoud. Experimental investigation of the influence of the geyser boiling phenomenon on the thermal performance of a two-phase closed thermosyphon. *Journal of Cleaner Production*, 172:2531–2543, 2018.

[8] H.M. Ali, M.M. Generous, F. Ahmad, and M. Irfan. Experimental investigation of nucleate pool boiling heat transfer enhancement of TiO2-water based nanofluids. *Applied Thermal Engineering*, 113:1146–1151, 2017.

[9] T. Ambreen and M.H. Kim. Heat transfer and pressure drop correlations of nanofluids: A state of art review. *Renewable and Sustainable Energy Reviews*, 91(March):564–583, 2018.

[10] A. Amiri, R. Sadri, M. Shanbedi, G. Ahmadi, B.T. Chew, S.N. Kazi, and M. Dahari. Performance dependence of thermosyphon on the functionalization approaches: An experimental study on thermo-physical properties of graphene nanoplatelet-based water nanofluids. *Energy Conversion and Management*, (92):322–339, 2015.

[11] A. Amiri, M. Shanbedi, H. Amiri, S.Z. Heris, S.N. Kazi, B.T. Chew, and H. Eshghi. Pool boiling heat transfer of CNT/water nanofluids. *Applied Thermal Engineering*, 71(1):450–459, 2014.

[12] S.A. Angayarkanni and J. Philip. Review on thermal properties of nanofluids: Recent developments. *Advances in Colloid and Interface Science*, 225:146–176, 2015.

[13] L.G. Asirvatham, S. Wongwises, and J. Babu. Heat Transfer Performance of a Glass Thermosyphon Using Graphene–Acetone Nanofluid. *Journal of Heat Transfer*, 137(11):111502, 2015.

[14] Attension and Biolin Scientific. Static and dynamic contact angles and their measurement techniques - theory note 1. Technical report.

[15] D. Attinger, C. Frankiewicz, A.R. Betz, T.M. Schutzius, R. Ganguly, A. Das, C.J. Kim, and C.M. Megaridis. Surface engineering for phase change heat transfer: A review. *MRS Energy & Sustainability*, 1, 2014.

[16] M. Azizi, M. Hosseini, S. Zafarnak, M. Shanbedi, and A. Amiri. Experimental analysis of thermal performance in a two-phase closed thermosiphon using graphene/water nanofluid. *Industrial and Engineering Chemistry Research*, (52):10015–10021, 2013.

[17] R. Azizian. Overview of Nanofluid Research at MIT – Focus on boiling. In *Presentation 1st Nanouptake Training School, Castellon de la Plana, Spain, 2016*, number October, 2016.

[18] W.H. Azmi, K.V. Sharma, R. Mamat, G. Najafi, and M.S. Mohamad. The enhancement of effective thermal conductivity and effective dynamic viscosity of nanofluids - A review. *Renewable and Sustainable Energy Reviews*, 53:1046–1058, 2016.

[19] I.C. Bang and S. Heung Chang. Boiling heat transfer performance and phenomena of Al2O3–water nano-fluids from a plain surface in a pool. *International Journal of Heat and Mass Transfer*, 48(12):2407–2419, 2005.

[20] J. Barber, D. Brutin, and L. Tadrist. A review on boiling heat transfer enhancement with nanofluids. *Nanoscale Research Letters*, 6(1):280, 2011.

[21] I.H. Bell, J. Wronski, S. Quoilin, and V. Lemort. Pure and pseudo-pure fluid thermophysical property evaluation and the open-source thermophysical property library coolprop. *Industrial and engineering chemistry research*, 53(6):2498–2508, 2014.

[22] J.D. Berry, M.J. Neeson, R.R. Dagastine, D.Y.C. Chan, and R.F. Tabor. Measurement of surface and interfacial tension using pendant drop tensiometry. *Journal of Colloid and Interface Science*, 454:226–237, 2015.

[23] A. Bianco, H.M. Cheng, T. Enoki, Y. Gogotsi, R.H. Hurt, N. Koratkar, T. Kyotani, M. Monthioux, C.R. Park, J.M.D Tascon, and J. Zhang. All in the graphene family - A recommended nomenclature for two-dimensional carbon materials. *Carbon*, 65:1–6, 2013.

[24] V. Bianco, O. Manca, S. Nardini, and K. Vafai. *Heat Transfer Enhancement with Nanofluids*. CRC Press, 2015.

[25] C.D. Bruce, M.L. Berkowitz, L. Perera, and M.D.E. Forbes. Molecular Dynamics Simulation of Sodium Dodecyl Sulfate Micelle in Water: Micellar Structural Characteristics and Counterion Distribution. *The Journal of Physical Chemistry B*, 106(15):3788–3793, 2002.

[26] J. Buongiorno, D.C. Venerus, N. Prabhat, T. McKrell, J. Townsend, R. Christianson, Y.V. Tolmachev, P. Keblinski, L.W. Hu, J.L. Alvarado, I.C. Bang, S.W. Bishnoi, M. Bonetti, F. Botz, A. Cecere, Y. Chang, G. Chen, H. Chen, S.J. Chung, M.K. Chyu, S.K. Das, R. Di Paola, Y. Ding, F. Dubois, G. Dzido, J. Eapen, W. Escher, D. Funfschilling, Q. Galand, J. Gao, P.E. Gharagozloo, K.E. Goodson, J. Gustavo Gutierrez, H. Hong, M. Horton, K.S. Hwang, C.S. Iorio, S.P. Jang, A.B. Jarzebski, Y. Jiang, L. Jin, S. Kabelac, A. Kamath, M.A. Kedzierski, L.G. Kieng, C. Kim, J.H. Kim, S. Kim, S.H. Lee, K.C. Leong, I. Manna, B. Michel, R. Ni, H.E. Patel, J. Philip, D. Poulikakos, C. Reynaud, R. Savino, P.K. Singh, P. Song, T. Sundararajan, E. Timofeeva, T. Tritcak, A.N. Turanov, S. Van Vaerenbergh, D. Wen, S. Witharana, C. Yang, W.H. Yeh, X.Z. Zhao, and S.Q. Zhou. A benchmark study on the thermal conductivity of nanofluids. *Journal of Applied Physics*, 106(9):1–14, 2009.

[27] J.E. Burkhalter, R.H. Sforzini, and C.R. Tinsley. Investigations of geysering in vertical tubes. *Journal of Spacecraft and Rockets*, 5(7):854–857, 1968.

[28] M.H. Buschmann. Thermal conductivity and heat transfer of ceramic nanofluids. *International Journal of Thermal Sciences*, 62:19–28, 2012.

[29] M.H. Buschmann. Nanofluids in thermosyphons and heat pipes: Overview of recent experiments and modelling approaches. *International Journal of Thermal Sciences*, 72:1–17, 2014.

[30] M.H. Buschmann. Heat Pipes and Thermosyphons Operated With Nanofluids. In V. Bianco, O. Manca, S. Nardini, and K. Vafai, editors, *Heat Transfer Enhancement with Nanofluids*, chapter 14, pages 391 – 409. CRC Press, 2015.

[31] M.H. Buschmann, R. Azizian, T. Kempe, J.E. Juliá, R. Martínez-Cuenca, B. Sundén, Z. Wu, A. Seppälä, and T. Ala-Nissila. Correct interpretation of nanofluid convective heat transfer. *International Journal of Thermal Sciences*, 129(September 2017):504–531, 2018.

[32] M.H. Buschmann and U. Franzke. Improvement of thermosyphon performance by employing nanofluid. *International Journal of Refrigeration*, 40:416–428, 2014.

[33] D. Cabaleiro and A. Navas, H.and Desforges. Dynamic Viscosity and Surface Tension of Stable Graphene Oxide and Reduced Graphene Oxide Aqueous Nanofluid. *Journal of Nanofluids*, 7(June):1–8, 2018.

[34] K. Cacua, R. Buitrago-Sierra, B. Herrera, E. Pabón, and S.M.S. Murshed. Nanofluids' stability effects on the thermal performance of heat pipes. *Journal of Thermal Analysis and Calorimetry*, 5, 2018.

[35] C. Casarosa, E. Latrofa, and A. Shelginski. The geyser effect in a two-phase thermosyphon. *International Journal of Heat and Fluid Flow*, 26(6):933–941, 1982.

[36] J. Chen, S. Yang, S. Liao, and X. Cao. Experimental investigation of effective parameters on geyser periodicity in a vertical heated system. *Experimental Thermal and Fluid Science*, 68:163–176, 2015.

[37] L. Cheng, D. Mewes, and A. Luke. Boiling phenomena with surfactants and polymeric additives: A state-of-the-art review. *International Journal of Heat and Mass Transfer*, 50(13-14):2744–2771, 2007.

[38] S. Choi and J.A. Eastman. Enhancing thermal conductivity of fluids with nanoparticles. In *ASME International Mechanical Engineering Congress&Exoisition, San Francisco*, 1995.

[39] M. Chopkar, A.K. Das, I. Manna, and P.K. Das. Pool boiling heat transfer characteristics of ZrO2-water nanofluids from a flat surface in a pool. *Heat and Mass Transfer/Waerme- und Stoffuebertragung*, 44(8):999–1004, 2008.

[40] J.T. Cieslinski. Effect of nanofluid concentration on two-phase thermosyphon heat exchanger performance. *Archives of Thermodynamics*, 37(2):23–40, 2016.

[41] J.T. Cieśliński and T.Z. Kaczmarczyk. Pool boiling of water-Al2O3 and water-Cu nanofluids on horizontal smooth tubes. *Nanoscale Research Letters*, 6(220):3–7, 2011.

[42] J.T. Ciesliński and T.Z. Kaczmarczyk. Pool boiling of water-Al2O3 and water-cu nanofluids outside porous coated tubes. *Heat Transfer Engineering*, 36(6):553–563, 2015.

[43] D. Ciloglu. An Experimental Investigation of Nucleate Pool Boiling Heat Transfer of Nanofluids From a Hemispherical Surface. *Heat Transfer Engineering*, 38(10):919–930, 2017.

[44] M. Dadjoo, N. Etesami, and M.N. Esfahany. Influence of orientation and roughness of heater surface on critical heat flux and pool boiling heat transfer coefficient of nanofluid. *Applied Thermal Engineering*, 124:353–361, 2017.

[45] S.K. Das, S.U.S Choi, W. Yu, and T. Pradeep. *Nanofluids: Science and Technology*. 2007.

[46] S.K. Das, N. Putra, and W. Roetzel. Pool boiling characteristics of nano-fluids. *International Journal of Heat and Mass Transfer*, 46(5):851–862, 2003.

[47] J. Drelich, C. Fang, and C.L. White. Measurement of interfacial tension in Fluid-Fluid Systems, 2002.

[48] A. Ehle, S. Feja, and M.H. Buschmann. Temperature Dependency of Ceramic Nanofluids Shows Classical Behavior. *Journal of Thermophysics and Heat Transfer*, 25(3):378–385, 2011.

[49] M.S. El-Genk and H.H. Saber. Heat transfer correlations for small, uniformly heated liquid pools. *International Journal of Heat and Mass Transfer*, 41(2):261 – 274, 1998.

[50] M.R.S. Emami, S.H. Noie, M. Khoshnoodi, M.T.H. Mosavian, and A. Kianifar. Investigation of Geyser Boiling Phenomenon in a Two-Phase Closed Thermosyphon. *Heat Transfer Engineering*, 30(5):408–415, 2009.

[51] P. Estellé, D. Cabaleiro, G. Żyła, L. Lugo, and S.M.S. Murshed. Current trends in surface tension and wetting behavior of nanofluids. *Renewable and Sustainable Energy Reviews*, 94(November 2017):931–944, 2018.

[52] A. Faghri. Heat Pipes: Review, Opportunities and Challenges. *Frontiers in Heat Pipes*, 5(1), 2014.

[53] X. Fang, Y. Chen, H. Zhang, W. Chen, A. Dong, and R. Wang. Heat transfer and critical heat flux of nanofluid boiling: A comprehensive review. *Renewable and Sustainable Energy Reviews*, 62:924–940, 2016.

[54] S. Feja and M. H. Buschmann. Nanofluids - potentials and illusions. In *12th Int. Conf. On Simulation and Experiments in Heat Transfer and Their Applications*, Split, Croatia, 2012.

[55] G. Ferrer, C. Barreneche, A. Solé, I. Martorell, and L.F. Cabeza. New proposed methodology for specific heat capacity determination of materials for thermal energy storage (TES) by DSC. *Journal of Energy Storage*, 11:1–6, 2017.

[56] E. Forrest, E. Williamson, J. Buongiorno, L.W. Hu, M. Rubner, and R. Cohen. Augmentation of nucleate boiling heat transfer and critical heat flux using nanoparticle thin-film coatings. *International Journal of Heat and Mass Transfer*, 53(1-3):58–67, 2010.

[57] T. Fukano, S.J. Chen, and C.L. Tien. Operating limits of the closed two-phase thermosyphon. In W.J. Mori, Y.and Yang, editor, *ASME JSME Thermal Engineering Joint Conference Proceedings*, pages 95–102, Honolulu, Hawaii, 1983.

[58] T. Fukano, K. Kadoguchi, and C.L. Tien. Oscillation phenomena and operating limits of the closed two-phase thermosyphon. In *Proceedings of 8th International Heat Transfer Conference*, pages 2326 – 2330, San Francisco, USA, 1986.

[59] J. Ghaderian, N.A.C. Sidik, A. Kasaeian, S. Ghaderian, A. Okhovat, A. Pakzadeh, S. Samion, and W.J. Yahya. Performance of copper oxide/distilled water nanofluid in evacuated tube solar collector (ETSC) water heater with internal coil under thermosyphon system circulations. *Applied Thermal Engineering*, 121:520–536, 2017.

[60] A. Gimeno-Furio, N. Navarrete, R. Mondragon, L. Hernandez, R. Martinez-Cuenca, L. Cabedo, and J.E. Julia. Stabilization and characterization of a nanofluid based on a eutectic mixture of diphenyl and diphenyl oxide and carbon nanoparticles under high temperature conditions. *International Journal of Heat and Mass Transfer*, 113:908–913, 2017.

[61] M.N. Golubovic, H.D. Madhawa Hettiarachchi, W.M. Worek, and W.J. Minkowycz. Nanofluids and critical heat flux, experimental and analytical study. *Applied Thermal Engineering*, 29(7):1281–1288, 2009.

[62] H.R. Goshayeshi, M. Goodarzi, and M. Dahari. Effect of magnetic field on the heat transfer rate of kerosene/Fe2O3 nanofluid in a copper oscillating heat pipe. *Experimental Thermal and Fluid Science*, 68:663–668, 2015.

[63] T. Grab, U. Gross, U. Franzke, and M.H. Buschmann. Operation performance of thermosyphons employing titania and gold nanofluids. *International Journal of Thermal Sciences*, 86:352–364, 2014.

[64] P. Griffith. Geysering in liquid-filled lines. *ASME Paper 62-HT-39*, 1962.

[65] A. Grimm. Powdered aluminum-containing heat transfer fluids., 1993.

[66] F. Haaf, A. Sanner, and F. Straub. Polymers of n-vinylpyrrolidone: Synthesis, characterization and uses. *Polymer Journal*, 17(1):143–152, 1985.

[67] Z. Haddad, C. Abid, H.F. Oztop, and A. Mataoui. A review on how the researchers prepare their nanofluids. *International Journal of Thermal Sciences*, 76:168–189, 2014.

[68] R.N. Hegde, S.S. Rao, and R.P. Reddy. Experimental studies on CHF enhancement in pool boiling with CuO-water nanofluid. *Heat and Mass Transfer/Waerme- und Stoffuebertragung*, 48(6):1031–1041, 2012.

[69] S.Z. Heris, F. Mohammadpur, and A. Shakouri. Effect of electric field on thermal performance of thermosyphon heat pipes using nanofluids. *Materials Research Bulletin*, 53:21–27, 2014.

[70] S.Z. Heris, H. Salehi, and S.H. Noie. The effect of magnetic field and nanofluid on thermal performance of two-phase closed thermosyphon. *Internal Journal of the Physical Sciences*, 7(4):534–543, 2012.

[71] M. Hernaiz, V. Alonso, P. Estellé, Z. Wu, B. Sundén, L. Doretti, S. Mancin, N. Çobanoğlu, Z.H. Karadeniz, N. Garmendia, M. Lasheras-Zubiate, L. Hernández López, R. Mondragón, R. Martínez-Cuenca, S. Barison, A. Kujawska, A. Turgut, A. Amigo, G. Huminic, A. Huminic, M.-R. Kalus, K.-G. Schroth, and M.H. Buschmann. The contact angle of nanofluids as thermophysical property. *Journal of Colloid and Interface Science*, 547:393–406, 2019.

[72] G. Hetsroni, M. Gurevich, A. Mosyak, R. Rozenblit, and L.P. Yarin. Subcooled boiling of surfactant solutions. *Inernational Journal of Multiphase Flow*, 28:347–361, 2002.

[73] A. Huminic, G. Huminic, M.H. Buschmann, and A. Kujawska. Nanofluid suitable for heat transfer in heat pipes. In *Proceedings of 1st Internation Conference on Nanofluids (ICNf2019) and 2nd European Symposium on Nanofluids (ESNf2019)*, Castelló, Spain, 2019.

[74] G. Huminic and A. Huminic. Heat transfer characteristics of a two-phase closed thermosyphons using nanofluids. *Experimental Thermal and Fluid Science*, 35(3):550–557, 2011.

[75] G. Huminic and A. Huminic. Hybrid nanofluids for heat transfer applications – A state-of-the-art review. *International Journal of Heat and Mass Transfer*, 125:82–103, 2018.

[76] H. Imura, K. Sasaguchi, H. Kozai, and S. Numata. Critical Heat Flux in a closed two-phase thermosyphon. *International Journal of Heat and Mass Transfer*, 26(8):1181–1188, 1983.

[77] F.P. Incropera and D.P. DeWitt. *Fundamentals of heat and mass transfer*. Wiley, 1996.

[78] D. Jafari, S. Filippeschi, A. Franco, and P. Di Marco. Unsteady experimental and numerical analysis of a two-phase closed thermosyphon at different filling ratios. *Experimental Thermal and Fluid Science*, 81:164–174, 2017.

[79] D. Jafari, A. Franco, S. Filippeschi, and P. Di Marco. Two-phase closed thermosyphons: A review of studies and solar applications. *Renewable and Sustainable Energy Reviews*, 53:575–593, 2016.

[80] C.G. Jothi Prakash and R. Prasanth. Enhanced boiling heat transfer by nano structured surfaces and nanofluids. *Renewable and Sustainable Energy Reviews*, 82(July 2017):4028–4043, 2018.

[81] H. Jouhara, B. Fadhl, and L.C. Wrobel. Three-dimensional CFD simulation of geyser boiling in a two-phase closed thermosyphon. *International Journal of Hydrogen Energy*, 41(37):16463–16476, 2015.

[82] J.Y. Jung, E.S. Kim, and Y.T. Kang. Stabilizer effect on CHF and boiling heat transfer coefficient of alumina/water nanofluids. *International Journal of Heat and Mass Transfer*, 55(7-8):1941–1946, 2012.

[83] R. Kamatchi, S. Venkatachalapathy, and C. Nithya. Experimental investigation and mechanism of critical heat flux enhancement in pool boiling heat transfer with nanofluids. *Heat and Mass Transfer*, 52(11):2357–2366, 2015.

[84] M.S. Kamel, F. Lezsovits, A.M. Hussein, O. Mahian, and S. Wongwises. Latest developments in boiling critical heat flux using nanofluids: A concise review. *International Communications in Heat and Mass Transfer*, 98:59–66, 2018.

[85] A. Kamyar, K.S. Ong, and R. Saidur. Effects of nanofluids on heat transfer characteristics of a two-phase closed thermosyphon. *International Journal of Heat and Mass Transfer*, 65:610–618, 2013.

[86] M. Karimzadehkhouei, M. Shojaeian, K. Şendur, M.P. Mengüç, and A. Koşar. The effect of nanoparticle type and nanoparticle mass fraction on heat transfer enhancement in pool boiling. *International Journal of Heat and Mass Transfer*, 109:157–166, 2017.

[87] A. Karthikeyan, S. Coulombe, A.M. Kietzig, R.S. Stein, and T. Van de Ven. Interaction of oxygen functionalized multi-walled carbon nanotube nanofluids with copper. *Carbon*, 140:201–209, 2018.

[88] R. Kathiravan, R. Kumar, A. Gupta, and R. Chandra. Preparation and pool boiling characteristics of copper nanofluids over a flat plate heater. *International Journal of Heat and Mass Transfer*, 53:1673–1681, 2010.

[89] R. Kathiravan, R. Kumar, A. Gupta, and R. Chandra. Preparation and pool boiling characteristics of silver nanofluids over a flat plate heater. *Heat Transfer Engineering*, 33(2):69–78, 2012.

[90] R. Kathiravan, R. Kumar, A. Gupta, R. Chandra, and P.K. Jain. Pool boiling characteristics of multiwalled carbon nanotube (CNT) based nanofluids over a flat plate heater. *International Journal of Heat and Mass Transfer*, 54(5-6):1289–1296, 2011.

[91] S. Khandekar, Y.M. Joshi, and B. Mehta. Thermal performance of closed two-phase thermosyphon using nanofluids. *International Journal of Thermal Sciences*, 47(6):659–667, 2008.

[92] I. Khazaee, R. Hosseini, and S.H. Noie. Experimental investigation of effective parameters and correlation of geyser boiling in a two-phase closed thermosyphon. *Applied Thermal Engineering*, 30(5):406–412, 2010.

[93] D.E. Kim, D.I. Yu, D.W. Jerng, M.H. Kim, and H.S. Ahn. Review of boiling heat transfer enhancement on micro/nanostructured surfaces. *Experimental Thermal and Fluid Science*, 66:173–196, 2015.

[94] H. Kim, J. Kim, and M.H. Kim. Effect of nanoparticles on CHF enhancement in pool boiling of nano-fluids. *International Journal of Heat and Mass Transfer*, 49(25-26):5070–5074, 2006.

[95] J.M. Kim, S.C. Park, B.T. Kong, H.B.R. Lee, and H.S. Ahn. Effect of porous graphene networks and micropillar arrays on boiling heat transfer performance. *Experimental Thermal and Fluid Science*, 93(December 2017):153–164, 2018.

[96] K.M. Kim and I.C. Bang. Effects of graphene oxide nanofluids on heat pipe performance and capillary limits. *International Journal of Thermal Sciences*, 100:346–356, 2016.

[97] S.J. Kim, I.C. Bang, J. Buongiorno, and L.W. Hu. Study of pool boiling and critical heat flux enhancement in nanofluids. *Bulletin of the Polish Academy of Sciences*, 55(2):211–216, 2007.

[98] K.M. Koczkur, S. Mourdikoudis, L. Polavarapu, and S.E. Skrabalak. Polyvinylpyrrolidone (PVP) in nanoparticle synthesis., 2015.

[99] K. Kouloulias, A. Sergis, Y. Hardalupas, and T.R. Barrett. Visualisation of sub-cooled pool boiling in nanofluids. *Fusion Engineering and Design*, (December):13–16, 2018.

[100] A. Kujawska, B. Zajaczkowski, L.M. Wilde, and M.H. Buschmann. Geyser boiling in a thermosyphon with nanofluids and surfactant solution. *International Journal of Thermal Sciences*, 139(May):195–216, 2019.

[101] H. Kuncoro, Y.F. Rao, and K. Fukuda. An experimental study on the mechanism of geysering in a closed two-phase thermosyphon. *International Journal of Multiphase Flow*, 21(6):1243–1252, 1995.

[102] S.M. Kwark, R. Kumar, G. Moreno, J. Yoo, and S.M. You. Pool boiling characteristics of low concentration nanofluids. *International Journal of Heat and Mass Transfer*, 53(5-6):972–981, 2010.

[103] A. Kyrychenko, O.M. Korsun, I.I. Gubin, S.M. Kovalenko, and O.N. Kalugin. Atomistic simulations of coating of silver nanoparticles with poly(vinylpyrrolidone) oligomers: Effect of oligomer chain length. *Journal of Physical Chemistry C*, 119(14):7888–7899, 2015.

[104] C.Y. Lee, B.J. Zhang, and K.J. Kim. Morphological change of plain and nanoporous surfaces during boiling and its effect on nucleate pool boiling heat transfer. *Experimental Thermal and Fluid Science*, 40:150–158, 2012.

[105] J.H. Lee, T. Lee, and Y.H. Jeong. Experimental study on the pool boiling CHF enhancement using magnetite-water nanofluids. *International Journal of Heat and Mass Transfer*, 55(9-10):2656–2663, 2012.

[106] X. Li, L. Colombo, and R.S. Ruoff. Synthesis of Graphene Films on Copper Foils by Chemical Vapor Deposition. *Advanced Materials*, (28):6247–6252, 2016.

[107] X. Li, S.C. Pok Cheung, and J. Tu. Nucleate boiling of dilute nanofluids - Mechanism exploring and modeling. *International Journal of Thermal Sciences*, 84:323–334, 2014.

[108] G. Liang and I. Mudawar. Review of pool boiling enhancement with additives and nanofluids. *International Journal of Heat and Mass Transfer*, 124:423–453, 2018.

[109] T.F. Lin, W.T. Lin, Y.L. Tsay, J.C. Wu, and R.J. Shyu. Experimental investigation of geyser boiling in an annular two-phase closed thermosyphon. *International Journal of Heat and Mass Transfer*, 38(2):295–307, 1995.

[110] H.Z. Liu and L. Liao. Sorption and agglutination phenomenon of nanofluids on a plain heating surface during pool boiling. *International Journal of Heat and Mass Transfer*, 51(9-10):2593–2602, 2008.

[111] H.Z. Liu, G.J. Xiong, and R. Bao. Boiling heat transfer characteristics of nanofluids in a flat heat pipe evaporator with micro-grooved heating surface. *International Journal of Multiphase Flow*, 33(12):1284–1295, 2007.

[112] S.H. Liu, W.A. Saidi, Y. Zhou, and K.A. Fichthorn. Synthesis of {111}-faceted au nanocrystals mediated by polyvinylpyrrolidone: Insights from density-functional theory and molecular dynamics. *Journal of Physical Chemistry C*, 119(21):11982–11990, 2015.

[113] Z. Liu, X. Yang, G. Wang, and G. Guo. Influence of carbon nanotube suspension on the thermal performance of a miniature thermosyphon. *International Journal of Heat and Mass Transfer*, 53(9-10):1914–1920, 2010.

[114] Z.H. Liu, X.F. Yang, and J.G. Xiong. Boiling characteristics of carbon nanotube suspensions under sub-atmospheric pressures. *International Journal of Thermal Sciences*, 49(7):1156–1164, 2010.

[115] G.A. Loraine. Oxidation of Polyvinylpyrrolidone and an Ethoxylate Surfactant in Phase-Inversion Wastewater. *Water Environment Research*, 80(4):373–379, 2008.

[116] M. Lotya, A. Rakovich, J.F. Donegan, and J.N. Coleman. Measuring the lateral size of liquid-exfoliated nanosheets with dynamic light scattering. *Nanotechnology*, 265703(24):1–6, 2013.

[117] O. Mahian, L. Kolsi, M. Amani, P. Estellé, G. Ahmadi, C. Kleinstreuer, J.S. Marshall, M. Siavashi, R.A. Taylor, H. Niazmand, S. Wongwises, T. Hayat, A. Kolanjiyil, A. Kasaeian, and I. Pop. Recent advances in modeling and simulation of nanofluid flows-Part I: Fundamentals and theory. *Physics Reports*, 790:1–48, 2018.

[118] Malvern. Industrial intsruction of DLS measurements. Dynamic Light Scattering: An Introduction in 30 Minutes.

[119] L.L. Manetti, M.T. Stephen, P.A. Beck, and E.M. Cardoso. Evaluation of the heat transfer enhancement during pool boiling using low concentrations of Al2O3-water based nanofluid. *Experimental Thermal and Fluid Science*, 87:191–200, 2017.

[120] F. Mashali, E. Languri, G. Mirshekari, J. Davidson, and D. Kerns. Nanodiamond nanofluid microstructural and thermo-electrical characterization. *International Communications in Heat and Mass Transfer*, 101:82–88, 2019.

[121] F. Mashali, E.M. Languri, J. Davidson, D. Kerns, W. Johnson, K. Nawaz, and G. Cunningham. Thermo-physical properties of diamond nanofluids: A review. *International Journal of Heat and Mass Transfer*, 129:1123–1135, 2019.

[122] B. M'hamed, N.A.C. Sidik, M.N.A.W.M. Yazid, R. Mamat, G. Najafi, and G.H.R. Kefayati. A review on why researchers apply external magnetic field on nanofluids. *International Communications in Heat and Mass Transfer*, 78:60–67, 2016.

[123] N. Miljkovic and E.N. Wang. Modeling and optimization of hybrid solar thermoelectric systems with thermosyphons. *Solar Energy*, 85(11):2843–2855, 2011.

[124] N. Monirimanesh, S.M. Nowee, S. Khayyami, and I. Abrishamchi. Performance enhancement of an experimental air conditioning system by using TiO2/methanol nanofluid in heat pipe heat exchangers. *Heat and Mass Transfer/Waerme- und Stoffuebertragung*, 52(5):1025–1035, 2016.

[125] P. Montes-Navajas, N.G. Asenjo, R. Santamaría, R. Menéndez, A. Corma, and H. García. Surface area measurement of graphene oxide in aqueous solutions. *Langmuir : the ACS journal of surfaces and colloids*, 29(44):13443–8, 2013.

[126] M. Moradgholi, S. Mostafa Nowee, and A. Farzaneh. Experimental study of using Al2O3/methanol nanofluid in a two phase closed thermosyphon (TPCT) array as a novel photovoltaic/thermal system. *Solar Energy*, 164(March):243–250, 2018.

[127] G. Moreno, J.R. Jeffers, and S. Narumanchi. Effects of Pressure and a Microporous Coating on HFC-245fa Pool Boiling Heat Transfer. *Journal of Heat Transfer*, 136(10):101502, 2014.

[128] S.D. Morgan and H.F. Brady. Elimination of the geysering effect in missiles. In K.D. Timmerhaus, editor, *Advances in cryogenic engineering*, volume 7, pages 206–213. Springer Science + Business Media, LCC, 1962.

[129] S. Mori, F. Yokomatsu, and Y. Utaka. Enhancement of critical heat flux using spherical porous bodies in saturated pool boiling of nanofluid. *Applied Thermal Engineering*, 144(135):219–230, 2018.

[130] S. Mostafa Ghiaasiaan. *Two-Phase Flow, Boiling and Condensation in Conventional and Miniature Systems*. Cambridge University Press, Georgia Institute of Technology, 2007.

[131] A. Mourgues, V. Hourtané, T. Muller, and M. Caron-Charles. Boiling behaviors and critical heat flux on a horizontal and vertical plate in saturated pool boiling with and without ZnO nanofluid. *International Journal of Heat and Mass Transfer*, 57(2):595–607, 2013.

[132] M.G. Mousa. Thermal Performance of Thermosyphon Charged by Nanofluid for Cooling Electronic Component. *International Journal of Scientific & Engineering Research, Volume 2, Issue 6, June-2011*, 2(6):1–9, 2011.

[133] D.W. Murphy. An experimental investigation of geysering in vertical tubes. In *Advances in Cryogenic Engineering*, volume 10, pages 353–359, 1964.

[134] S.M.S. Murshed and P. Estellé. A state of the art review on viscosity of nanofluids. *Renewable and Sustainable Energy Reviews*, 76(February):1134–1152, 2017.

[135] S.M.S. Murshed, D. Milanova, and R. Kumar. An Experimental Study of Surface Tension-Dependent Pool Boiling Characteristics of Carbon Nanotubes-Nanofluids. In *ASME 2009 7th International Conference on Nanochannels, Microchannels, and Minichannels*, pages 75–80, 2009.

[136] S.M.S. Murshed, C. Nieto De Castro, M.J.V. Loureno, M.L.M. Lopes, and F.J.V. Santos. A review of boiling and convective heat transfer with nanofluids. *Renewable and Sustainable Energy Reviews*, 15(5):2342–2354, 2011.

[137] S. Nabati Shoghl, M. Bahrami, and M. Jamialahmadi. The boiling performance of ZnO, α-Al2O3 and MWCNTs/water nanofluids: An experimental study. *Experimental Thermal and Fluid Science*, 80:27–39, 2017.

[138] A. Najim, V. More, A. Thorat, S. Patil, and S. Savale. Enhancement of pool boiling heat transfer using innovative non-ionic surfactant on a wire heater. *Experimental Thermal and Fluid Science*, 82:375–380, 2017.

[139] K. Negishi. A blowup phenomenon of the working fluid in a two-phase closed thermosyphon. In *Proc. of the Symp. on Mechanics for Space Flight*, volume 1, pages 69–74, 1984.

[140] K. Negishi and T. Sawada. Performance de transfert thermique d'un thermosyphon incline, ferme et diphasique. *International Journal of Heat and Mass Transfer*, 26(8):1207–1213, 1983.

[141] S.H. Noie, S.Z. Heris, M. Kahani, and S.M. Nowee. Heat transfer enhancement using Al2O3/water nanofluid in a two-phase closed thermosyphon. *International Journal of Heat and Fluid Flow*, 30(4):700–705, 2009.

[142] S.H. Noie, M.R. Sarmasti Emami, and M. Khoshnoodi. Effect of Inclination Angle and Filling Ratio on Thermal Performance of a Two-Phase Closed Thermosyphon under Normal Operating Conditions. *Iranian Journal of Science & Technology*, 32(July 2017):39–51, 2008.

[143] K.S. Novoselov, V.I. Fal, L. Colombo, P.R. Gellert, M.G. Schwab, and K. Kim. REVIEW A roadmap for graphene. *Nature*, 490(7419):192–200, 2012.

[144] M. Ozawa, S. Nakanishi, S. Ishigai, Y. Mizuta, and H. Tarui. Flow instabilities in boiling channels. Part 2: Geysering. *Bulletin of the JSME, Paper no. 170-11*, 22(170):1119 – 1126, 1979.

[145] C. Pagura, S. Barison, C. Mortalo, N. Comisso, and M. Schiavon. Large scale and low cost production of pristine and oxidized single wall carbon nanohorns as material for hydrogen storage. *Nanoscience and Nanotechnology Letters*, 4(2):160–164, 2012.

[146] T. Parametthanuwat, S. Rittidech, and A. Pattiya. A correlation to predict heat-transfer rates of a two-phase closed thermosyphon (TPCT) using silver nanofluid at normal operating conditions. *International Journal of Heat and Mass Transfer*, 53(21-22):4960–4965, 2010.

[147] K.J. Park, D. Jung, and S.E. Shim. Nucleate boiling heat transfer in aqueous solutions with carbon nanotubes up to critical heat fluxes. *International Journal of Multiphase Flow*, 35(6):525–532, 2009.

[148] S. Park and R.S. Ruoff. Synthesis and characterization of chemically modified graphenes. *Current Opinion in Colloid and Interface Science*, 20:322–328, 2015.

[149] S.D. Park, S.B. Moon, and I.C. Bang. Effects of thickness of boiling-induced nanoparticle deposition on the saturation of critical heat flux enhancement. *International Journal of Heat and Mass Transfer*, 78:506–514, 2014.

[150] S.D. Park, S. Won Lee, S. Kang, I.C. Bang, J.H. Kim, H.S. Shin, D.W. Lee, and D. Won Lee. Effects of nanofluids containing graphene/graphene-oxide nanosheets on critical heat flux. *Applied Physics Letters*, 97(2), 2010.

[151] D.D. Paul and S.I. Abdel-Khalik. Saturated nucleate pool boiling bubble dynamics in aqueous drag-reducing polymer solutions. *International Journal of Heat and Mass Transfer*, 27(12):2426–2428, 1984.

[152] G. Paul, M. Chopkar, I. Manna, and P.K. Das. *Renewable and Sustainable Energy Reviews*.

[153] Q.T. Pham, T.I. Kim, S.S. Lee, and S.H. Chang. Enhancement of critical heat flux using nano-fluids for Invessel Retention-External Vessel Cooling. *Applied Thermal Engineering*, 35(1):157–165, 2012.

[154] H.T. Phan, N. Caney, P. Marty, S. Colasson, and J. Gavillet. Surface coating with nanofluids: The effects on pool boiling heat transfer. *Nanoscale and Microscale Thermophysical Engineering*, 14(4):229–244, 2010.

[155] R.V. Pinto, F. Augusto, and S. Fiorelli. Review of the mechanisms responsible for heat transfer enhancement using nanofluids. *Applied Thermal Engineering*, 108:720–739, 2016.

[156] E. Pop, V. Varshney, and A.K. Roy. Thermal properties of graphene: Fundamentals and applications. *MRS Bulletin*, 37(12):1273–1281, 2012.

[157] L.M. Poplaski, S.P. Benn, and A. Faghri. Thermal performance of heat pipes using nanofluids. *International Journal of Heat and Mass Transfer*, 107:358–371, 2017.

[158] J. Qu and H. Wu. Thermal performance comparison of oscillating heat pipes with SiO2/water and Al2O3/water nanofluids. *International Journal of Thermal Sciences*, 50(10):1954–1962, 2011.

[159] X. Quan, D. Wang, and P. Cheng. An experimental investigation on wettability effects of nanoparticles in pool boiling of a nanofluid. *International Journal of Heat and Mass Transfer*, 108:32–40, 2017.

[160] M. Ramezanizadeh, M. Alhuyi Nazari, M.H. Ahmadi, and E. Açıkkalp. Application of nanofluids in thermosyphons: A review. *Journal of Molecular Liquids*, 272:395–402, 2018.

[161] M. Ramezanizadeh, M. Alhuyi Nazari, M.H Ahmadi, and K.W. Chau. Experimental and numerical analysis of a nanofluidic thermosyphon heat exchanger. *Engineering Applications of Computational Fluid Mechanics*, 13(1):40–47, 2019.

[162] M.L.V. Ramires, C.A. Nieto De Castro, R.A. Perkins, Y. Nagasaka, A. Nagashima, M.J. Assael, and W.A. Wakeham. Reference data for the thermal conductivity of saturated liquid toluene over a wide range of temperatures. *Journal of Physical and Chemical Reference Data*, 29(2):133–139, 2000.

[163] A. K. Rasheed, M. Khalid, W. Rashmi, T.C.S.M Gupta, and A. Chan. Graphene based nanofluids and nanolubricants - Review of recent developments. *Renewable and Sustainable Energy Reviews*, (63):346–362, 2016.

[164] D.A. Reay and P.A. Kew. *Heat Pipes. Theory, Design and Applications*. Fifth edit edition, 2015.

[165] G. Rice. Thermopedia a-to-z guide to thermodynamics, heat & mass transfer, and fluids engineering, 2011.

[166] R. Riehl. Utilization of Passive Thermal Control Technologies for Electronics Cooling: A Brief Review. *Journal of Applied Mechanical Engineering*, 5(4):161–184, 2016.

[167] W.M. Rohsenow. A method of correlating heat transfer data for surface boiling of liquids. Technical report, MIT, 1962.

[168] W.M. Rohsenow, J.P. Hartnett, and E.N. Ganic. *Handbook of heat transfer fundamentals*. New York, McGraw-Hill Book Co., 1985.

[169] F. Rostamian and N. Etesami. Pool boiling characteristics of silica/water nanofluid and variation of heater surface roughness in domain of time. *International Communications in Heat and Mass Transfer*, 95(May):98–105, 2018.

[170] N.M. Rouai and S.I. Abdel-Khalik. Pool boiling of drag-reducing polymer solutions. *Applied Scientific Research*, 40(3):209–222, 1983.

[171] E. Sadeghinezhad, M. Mehrali, R. Saidur, M. Mehrali, S. Tahan Latibari, A.R. Akhiani, and H.S.C. Metselaar. A comprehensive review on graphene nanofluids: Recent research, development and applications. *Energy Conversion and Management*, 111:466–487, 2016.

[172] M.U. Sajid and H.M. Ali. Thermal conductivity of hybrid nanofluids: A critical review. *International Journal of Heat and Mass Transfer*, 126:211–234, 2018.

[173] H. Sakashita. CHF and near-wall boiling behaviors in pool boiling of water on a heating surface coated with nanoparticles. *International Journal of Heat and Mass Transfer*, 55(23-24):7312–7320, 2012.

[174] H. Sakashita. Pressure effect on CHF enhancement in pool boiling of nanofluids. *Journal of Nuclear Science and Technology*, 53(6):797–802, 2016.

[175] E. Salari, S.M. Peyghambarzadeh, M.M. Sarafraz, F. Hormozi, and V. Nikkhah. Thermal behavior of aqueous iron oxide nano-fluid as a coolant on a flat disc heater under the pool boiling condition. *Heat and Mass Transfer/Waerme- und Stoffuebertragung*, 53(1):265–275, 2017.

[176] M.M. Sarafraz and F. Hormozi. Experimental study on the thermal performance and efficiency of a copper made thermosyphon heat pipe charged with alumina-glycol based nanofluids. *Powder Technology*, 266:378–387, 2014.

[177] M.M. Sarafraz and F. Hormozi. Pool boiling heat transfer to dilute copper oxide aqueous nanofluids. *International Journal of Thermal Sciences*, 90:224–237, 2015.

[178] M.M. Sarafraz, F. Hormozi, and S.M. Peyghambarzadeh. Thermal performance and efficiency of a thermosyphon heat pipe working with a biologically ecofriendly nanofluid. *International Communications in Heat and Mass Transfer*, 57:297–303, 2014.

[179] M.M. Sarafraz, F. Hormozi, M. Silakhori, and S.M. Peyghambarzadeh. On the fouling formation of functionalized and non-functionalized carbon nanotube nanofluids under pool boiling condition. *Applied Thermal Engineering*, 95:433–444, 2016.

[180] C. Seo, D. Jang, J. Chae, and S. Shin. Altering the coffee-ring effect by adding a surfactant-like viscous polymer solution. *Scientific Reports by Nature*, 7(1):500, 2017.

[181] M. Shanbedi, S.Z. Heris, M. Baniadam, A. Amiri, and M. Maghrebi. Investigation of heat-transfer characterization of EDA-MWCNT/DI-water nanofluid in a two-phase closed thermosyphon. *Industrial and Engineering Chemistry Research*, 51(3):1423–1428, 2012.

[182] M. Shiraishi, K. Kikuchi, and T. Yamanishi. Investigation of heat transfer characteristics of a two-phase closed thermosyphon. *Journal of Heat Recovery Systems*, 1(4):287 – 297, 1981.

[183] S.N. Shoghl and M. Bahrami. Experimental investigation on pool boiling heat transfer of ZnO, and CuO water-based nanofluids and effect of surfactant on heat transfer coefficient. *International Communications in Heat and Mass Transfer*, 45:122–129, 2013.

[184] K. Smith. *Two phase flow and heat transfer in reflux thermosyphons*. PhD thesis, University of Dublin, Trinity College, 2016.

[185] K. Smith, A. J. Robinson, and R. Kempers. Confinement and vapour production rate influences in closed two-phase reflux thermosyphons Part B: Heat transfer. *International Journal of Heat and Mass Transfer*, 120:1241–1254, 2018.

[186] K. Smith, A.J. Robinson, and R. Kempers. Confinement and vapour production rate influences in closed two-phase reflux thermosyphons Part A: Flow regimes. *International Journal of Heat and Mass Transfer*, 120:1241–1254, 2018.

[187] M. Soleymaniha, A. Amiri, M. Shanbedi, B.T. Chew, and S. Wongwises. Water-based graphene quantum dots dispersion as a high-performance long-term stable nanofluid for two-phased closed thermosyphons. *International Communications in Heat and Mass Transfer*, 95(May):147–154, 2018.

[188] S. Soltani, S.G. Etemad, and J. Thibault. Pool boiling heat transfer performance of Newtonian nanofluids. *Heat and Mass Transfer*, 45(12):1555–1560, 2009.

[189] S. Soltani, S.G. Etemad, and J. Thibault. Pool boiling heat transfer of non-Newtonian nanofluids. *International Communications in Heat and Mass Transfer*, 37(1):29–33, 2010.

[190] B. Stutz, C.H.S. Morceli, M.F. da Silva, S. Cioulachtjian, and J. Bonjour. Influence of nanoparticle surface coating on pool boiling. *Experimental Thermal and Fluid Science*, 35(7):1239–1249, 2011.

[191] R. Sureshkumar, S. Tharves Mohideen, and N. Nethaji. Heat transfer characteristics of nanofluids in heat pipes: A review. *Renewable and Sustainable Energy Reviews*, 20:397–410, 2013.

[192] M.M. Tawfik. Experimental studies of nanofluid thermal conductivity enhancement and applications: A review. *Renewable and Sustainable Energy Reviews*, 75(July 2016):1239–1253, 2017.

[193] R.A. Taylor and P.E. Phelan. Pool boiling of nanofluids: Comprehensive review of existing data and limited new data. *International Journal of Heat and Mass Transfer*, 52(23-24):5339–5347, 2009.

[194] C. Tecchio, J.L.G. Oliveira, K.V. Paiva, M.B.H. Mantelli, R. Galdolfi, and L.G.S. Ribeiro. Geyser boiling phenomenon in two-phase closed loop-thermosyphons. *International Journal of Heat and Mass Transfer*, 111:29–40, 2017.

[195] M. Tetreault-Friend, R. Azizian, M. Bucci, T. McKrell, J. Buongiorno, M. Rubner, and R. Cohen. Critical heat flux maxima resulting from the controlled morphology of nanoporous hydrophilic surface layers. *Applied Physics Letters*, 108(24), 2016.

[196] L. Tong, J. Chen, X. Cao, S. Yang, S. Liao, J. Deng, and W. Zeng. Visualization experiments on the geyser boiling-induced instability in vertical circular tube at low-pressures. *Annals of Nuclear Energy*, 77:487–497, 2015.

[197] W.L. Tong, M.K. Tan, J.K. Chin, K.S. Ong, and Y.M. Hung. Coupled effects of hydrophobic layer and vibration on thermal efficiency of two-phase closed thermosyphons. *RSC Advances*, 5(14):10332–10340, 2015.

[198] B. Truong, W.L. Hu, J. Buongiorno, and T. McKrell. Modification of sandblasted plate heaters using nanofluids to enhance pool boiling critical heat flux. *International Journal of Heat and Mass Transfer*, 53(1-3):85–94, 2010.

[199] R.I. Vachon, G.H. Nix, and G.E. Tanger. Evaluation of Constants for the Rohsenow Pool-Boiling Correlation. *Journal of Heat Transfer*, May:239–246, 1968.

[200] S. Vafaei and T. Borca-Tasciuc. Role of nanoparticles on nanofluid boiling phenomenon: Nanoparticle deposition. *Chemical Engineering Research and Design*, 92(5):842–856, 2014.

[201] VascoFlex and Cordouan-Technologies. Industrial intsruction of DLS measurements. Dynamic Light Scattering - instruction guide.

[202] P. Vassallo, R. Kumar, and S. D'Amico. Pool boiling heat transfer experiments in silica-water nano-fluids. *International Journal of Heat and Mass Transfer*, 47(2):407–411, 2004.

[203] D.M. Vazquez and R. Kumar. Surface effects of ribbon heaters on critical heat flux in nanofluid pool boiling. *International Communications in Heat and Mass Transfer*, 41:1–9, 2013.

[204] D. Wang, X. Quan, C. Liu, and P. Cheng. An experimental investigation on periodic single bubble growth and departure from a small heater submerged in a nanofluid containing moderately hydrophilic nanoparticles. *International Communications in Heat and Mass Transfer*, 95(May):1–8, 2018.

[205] J. Wang, F.C. Li, and X.B. Li. Bubble explosion in pool boiling around a heated wire in surfactant solution. *International Journal of Heat and Mass Transfer*, 99:569–575, 2016.

[206] J. Wang, F.C. Li, and X.B. Li. On the mechanism of boiling heat transfer enhancement by surfactant addition. *International Journal of Heat and Mass Transfer*, 101:800–806, 2016.

[207] W. Wang, G. Duan, J. Li, W. Zhao, C. Li, and Z. Liu. The preparation and thermal performance research of spherical Ag-H2O nanofluids & applied in heat pipe. *Applied Thermal Engineering*, 116:811–822, 2017.

[208] X. Wang, Y. Wang, H. Chen, and Y. Zhu. A combined CFD/visualization investigation of heat transfer behaviors during geyser boiling in two-phase closed thermosyphon. *International Journal of Heat and Mass Transfer*, 121:703–714, 2018.

[209] X.Q. Wang and A.S. Mujumdar. Heat transfer characteristics of nanofluids: a review. *International Journal of Thermal Sciences*, 46(1):1–19, 2007.

[210] Y. Watanabe, K. Enoki, and T. Okawa. Nanoparticle layer detachment and its influence on the heat transfer characteristics in saturated pool boiling of nanofluids. *International Journal of Heat and Mass Transfer*, 125:171–178, 2018.

[211] J.W. Weber, V.E. Calado, and M.C.M. Van De Sanden. Optical constants of graphene measured by spectroscopic ellipsometry. *Applied Physics Letters*, 97(9):1–4, 2010.

[212] D. Wen, M. Corr, X. Hu, and G. Lin. Boiling heat transfer of nanofluids: The effect of heating surface modification. *International Journal of Thermal Sciences*, 50(4):480–485, 2011.

[213] D. Wen and Y. Ding. Experimental investigation into the pool boiling heat transfer of aqueous based γ-alumina nanofluids. *Journal of Nanoparticle Research*, 7(2-3):265–274, 2005.

[214] S. Witharana. *Thermal Transport in Nanofluids : Boiling heat transfer*. Doctoral thesis, The University of Leeds, 2011.

[215] A. Wlazlak, B. Zajaczkowski, S. Barison, F. Agresti, L.M. Wilde, and M.H. Buschmann. Nanofluids as working fluid in thermosyphon. In *1st European Symposium on Nanofluids, Abstract Collection*, pages 172–177, Lisbon, 2017.

[216] A. Wlazlak, B. Zajaczkowski, and M.H. Buschmann. Characterization of graphene oxide nanofluids. In L.L. Hernández and O. Manca, editors, *Book of abstracts, 28-29.05.2018 Naples, 4th Working Group Meetings Workshop on Nanofluids in Energy Systems, Nanouptake COST Action (CA15119)*, pages 73–74, Naples, Italy, 2018.

[217] A. Wlazlak, B. Zajaczkowski, A. Mrowiec, K. Pralat, and Z. Krolicki. The thermal conductivity of nanofluids measurements - A review of available methods. In D. Kasprzak, A. Mrowiec, and K. Talaska, editors, *Inzynieria wytwarzania*, pages 267–276. Wydawnictwo Państwowej Wyższej Szkoły Zawodowej im. Prezydenta Stanisława Wojciechowskiego w Kaliszu, Kalisz, 2016.

[218] A. Wlazlak, B. Zajaczkowski, M. Woluntarski, and M.H. Buschmann. Influence of graphene oxide nanofluids and surfactant on thermal behaviour of the thermosyphon. *Journal of Thermal Analysis and Calorimetry*, 3456789, 2018.

[219] K. Wojtasik, A. Wlazlak, B. Zajaczkowski, and S. Sandler. Analiza możliwości zastosowania czynników HFO w termosyfonowych wymiennikach ciepła stosowanych do odzysku ciepła odpadowego instalacji sanitarnych. *Cieplownictwo, Ogrzewnictwo i Wentylacja*, 47(9):365–369, 2016.

[220] W.T. Wu, Y.M. Yang, and J.R. Maa. Nucleate pool boiling enhancement by means of surfactant additives. *Experimental Thermal and Fluid Science*, 18(3):195–209, 1998.

[221] G. Xia, W. Wang, L. Cheng, and D. Ma. Visualization study on the instabilities of phase-change heat transfer in a flat two-phase closed thermosyphon. *Applied Thermal Engineering*, 116:392–405, 2017.

[222] X.F. Yang and Z.H. Liu. Application of Functionalized Nanofluid in Thermosyphon. *Nanoscale Research Letters*, 6(1):494, 2011.

[223] X.F. Yang and Z.H. Liu. Pool boiling heat transfer of functionalized nanofluid under sub-atmospheric pressures. *International Journal of Thermal Sciences*, 50(12):2402–2412, 2011.

[224] Y.M. Yang and J.R. Maa. Boiling of suspension of solid particles in water. *International Journal of Heat and Mass Transfer*, 20(1):145–147, 1984.

[225] S.M. You, J.H. Kim, and K.H. Kim. Effect of nanoparticles on critical heat flux of water in pool boiling heat transfer. *Applied Physics Letters*, 83(16):3374–3376, 2003.

[226] B. Zajaczkowski and A. Wlazlak. Rury cieplne w systemie biernego ogrzewania infrastruktury drogowej. *Ciepłownictwo, Ogrzewnictwo i Wentylacja*, 9:337–344, 2015.

[227] S. Zeinali Heris, M. Fallahi, M. Shanbedi, and A. Amiri. Heat transfer performance of two-phase closed thermosyphon with oxidized CNT/water nanofluids. *Heat and Mass Transfer*, 52(1):85–93, 2016.

[228] A. Zendehboudi, R. Saidur, I.M. Mahbubul, and S.H. Hosseini. Data-driven methods for estimating the effective thermal conductivity of nanofluids: A comprehensive review. *International Journal of Heat and Mass Transfer*, 131:1211–1231, 2019.

[229] J. Zhang and R.M. Manglik. Nucleate pool boiling of aqueous polymer solutions on a cylindrical heater. *Journal of Non-Newtonian Fluid Mechanics*, 125(2-3):185–196, 2005.

[230] J. Zhang and Y. Meng. Stick-slip friction of stainless steel in sodium dodecyl sulfate aqueous solution in the boundary lubrication regime. *Tribology Letters*, 56(3):543–552, 2014.

[231] Y. Zhu, S. Murali, W. Cai, X. Li, J.W. Suk, J.R. Potts, and R.S. Ruoff. Graphene and graphene oxide: Synthesis, properties, and applications. *Advanced Materials*, 22(35):3906–3924, 2010.

[232] B. Zohuri. *Heat Pipe Design and Technology. A practical approach*, volume 13. CRC Press, 2011.

[233] A. Zuchowska, M. Chudy, A. Dybko, and Z. Brzozka. Graphene as a new material in anticancer therapy-in vitro studies. *Sensors and Actuators, B: Chemical*, 243:152–165, 2017.

[234] G. Żyła and M. Wanic. Nanotension – results of surface tension measurements performed on Rzeszow University of Technology, Poland. Technical report, Rzeszów University of Technology, 2019.